The mechanisms of HIF-2α action in the carotid body

Maria Prange-Barczyńska
St Edmund Hall
University of Oxford



Supervised by Dr Tammie Bishop and Professor Sir Peter Ratcliffe

A thesis submitted to the examination
for the degree of Doctor of Philosophy

Trinity Term 2022

Abstract

The carotid body (CB) is an arterial chemoreceptor central to ventilatory adaptations to reduced oxygen arterial pressure (hypoxia) and responds both rapidly, by increasing ventilation within seconds of the drop in O_2 saturation, and chronically, by potentiating the acute hypoxic ventilatory response (HVR), which is associated with CB hyperplasia. Mechanisms behind these adaptations are not fully understood, but the Hypoxia Inducible Factor (HIF) signalling pathway has been implicated in mediating the CB chronic response to hypoxia. Indeed, HIF-2α isoform has been found to be very highly expressed in the CB.

Using a recently developed pharmacological HIF-2α inhibitor (PT2385), we demonstrate that HIF-2α is necessary for the CB-mediated acclimatisation to chronic hypoxia, and plays a major role in acute HVR (Chapter 2). The response to PT2385 was blocked in mice with HIF-2α S305M mutation, obstructing binding of allosteric inhibitors without altering the HIF transcriptional function, demonstrating that the PT2385 effects are on-target to HIF-2α (Chapter 3). Further, a hypomorphic ventilatory phenotype was found in S305M mutants (Chapter 3), suggesting a potential HIF-β-independent role of HIF-2α in CB function. This was investigated in *Arnt1/2*dKO mice, which showed incomplete loss of CB responses to chronic hypoxia with *Arnt1/2* loss in adulthood (Chapter 4). The role of G-protein signalling regulators: RGS4 and RGS5, which are highly CB-enriched and reportedly HIF-target genes, was further investigated using genetic models, and demonstrated a function of RGS5 in ventilatory acclimatisation to hypoxia, uncovering a potential HIF-2α downstream mediator (Chapter 5).

Finally, the role of HIF-2α in sympathoadrenal tumours was investigated by developmental, tyrosine-hydroxylase-expressing cell-restricted *Phd2* inactivation (Chapter 6). This study showed that HIF-2α stabilisation (due to *Phd2* inactivation) preserves the chromaffin cells in an 'immature', noradrenergic state, with induction of CB-specific genes, and is sufficient to preserve acute oxygen sensitivity of chromaffin cells, typically only found in neonates.

Together, presented results demonstrate that HIF-2α is both necessary and sufficient for oxygen sensitivity in the carotid body and related tissues, and provides insight into the possible transcriptional and HIF-β-independent mechanisms of HIF-2α action in hypoxia.

Table of Contents

Abstract i

List of Figures ix

List of Tables xiv

Acknowledgements xv

Abbreviations xvii

1 Introduction 21

1.1 Ventilatory responses to hypoxia 22

1.2 The carotid body 25

1.2.1 Carotid body structure and morphology 27

1.2.2 Carotid body acute oxygen sensing 29

1.2.3 Carotid body in long-term adaptations to hypoxia 37

1.3 Hypoxia Inducible Factors: master regulators of the hypoxic response 40

1.3.1 Oxygen sensing by the HIF/PHD pathway 40

1.3.2 Diversity of HIF and PHD isoforms 42

1.4 HIF-2α in carotid body responses to hypoxia 45

1.5 HIF-2α in carotid body pathology – paragangliomas 49

1.6 Pharmacological HIF-2α inhibitors 52

1.7 Research aims 53

2 The marked and rapid effects of pharmacological HIF-2α antagonism on hypoxic ventilatory control. 55

2.1 Introduction 55

2.2 Results 58

2.2.1 PT2385 treatment prevents ventilatory acclimatisation to hypoxia in wild-type mice. 58

2.2.2 PT2385 abolishes ventilatory acclimatisation to hypoxia established through sustained hypoxic exposure 63

2.2.3 PT2385 abolishes enhanced ventilatory responses in pseudo-hypoxic mice with genetic PHD2 inactivation 66

2.2.4 HIF-2α inhibition with PT2385 rapidly reduces acute ventilatory responses to hypoxia in unacclimatised mice 69

2.2.5 HIF-2α inhibition with PT2385 abolishes carotid body proliferation in response to hypoxia 74

2.3 Discussion 76

3 Specificity of the effects of pharmacological HIF-2α inhibition with PT2385 on hypoxic ventilatory control and carotid body proliferation. 81

3.1 Introduction 81

3.2 Results 83

3.2.1 Mice homozygous for the S305M mutant HIF-2α have normal expression levels of *Hif-2α* and HIF-2 target gene: *Vegfa*, in the CB 83

3.2.2 HIF-2α S305M mutation prevents PT2385 effects on ventilatory acclimatisation to hypoxia 85

3.2.3 HIF-2α S305M mutant mice are resistant to PT2385 effects on hypoxic CB proliferation 90

3.2.4 *Epas1*$^{S305M/S305M}$ mutant mice have a reduced polycythaemic response to hypoxia 91

3.2.5 Dissection of the mechanisms of HIF-2α involvement in acute oxygen sensing 93

3.3 Discussion 103

4 The role of HIF-β subunits in HIF-2 function in the carotid body. 108

4.1 Introduction 108

4.2 Results 110

4.2.1 Expression of ARNT isoforms in the carotid body and the kidneys 110

4.2.2 *Arnt*$^{f/f}$;*Arnt2*$^{f/f}$;*RosaCreER* mouse model generation 114

4.2.3 Experimental design and confirmation of *Arnt/Arnt2* inactivation 117

4.2.4 Effects of Arnt inactivation on HIF-2-dependent erythropoiesis 121

4.2.5 Ventilatory acclimatisation to hypoxia in mice with *Arnt* and *Arnt2* inactivation 123

4.2.6 Ventilatory acclimatisation to hypoxia in mice with either *Arnt* or *Arnt2* inactivation in adulthood 129

4.2.7 Carotid body proliferation in response to hypoxia in mice with *Arnt* and *Arnt2* inactivation. 137

4.2.8 Carotid body proliferation in response to hypoxia in mice with either *Arnt* or *Arnt2* inactivation 138

4.3 Discussion 140

5 Role of regulators of G-protein signalling in the carotid body response to hypoxia 145

5.1 Introduction 145

5.2 Results 148

5.2.1 Expression of *Rgs4* and *Rgs5* in the carotid body and mouse model validation 148

5.2.2 Validation of *Rgs4* and *Rgs5* KO mouse models and experimental design 153

5.2.3 Effects of *Rgs4* and *Rgs5* inactivation on acute ventilatory responses to hypoxia 157

5.2.4 Ventilatory acclimatisation to hypoxia in mice lacking *Rgs4* or *Rgs5* in carotid body type 1 cells 160

5.2.5 Carotid body proliferation in mice with *Rgs4* or *5* inactivation 165

5.2.6 Effects of acute *Rgs4* and *Rgs5* inactivation on carotid body responses to chronic hypoxia. 166

5.2.7 Carotid body proliferation in mice with acute *Rgs4* or *5* inactivation 173

5.3 Discussion 175

6 Developmental role of PHD2/HIF-2α in the pathogenesis of pheochromocytomas and paragangliomas 180

6.1 Introduction 180

6.2 Results 182

6.2.1 Constitutive *Phd2* inactivation in the adrenal medulla results in pseudohypoxic PPGL-like transcriptomic profile and abnormal morphology 182

6.2.2 *Phd2* inactivation alters AM transcriptome towards a CB-like profile 190

6.2.3 Testing acute oxygen sensitivity in *Phd2$^{f/f}$;THCre* adrenal medulla 194

6.2.4 Spatial heterogeneity in adrenal medulla acute oxygen sensitivity 202

6.2.5 Abdominal Organ of Zuckerkandl paragangliomas in mice with developmental *Phd2* inactivation 206

6.2.6 Investigating the molecular mechanisms behind increased oxygen sensitivity in *Phd2$^{f/f}$;THCre* chromaffin cells. 215

6.3 Discussion 218

7 Concluding remarks 226

8 Materials and methods 231

8.1 Materials and chemicals 231

8.2 Ethical approval 231
8.3 Animals 231
8.4 Genotyping 232
8.5 Substance administration 234
8.5.1 Tamoxifen 234
8.5.2 BrdU 234
8.5.3 HIF-2α inhibitors 235
8.6 Plethysmography 235
8.7 Chronic hypoxia 236
8.8 Blood measurements 236
8.8.1 Haematocrit measurement 237
8.8.2 Plasma catecholamine measurement 237
8.9 Immunohistochemistry 237
8.9.1 Tyrosine Hydroxylase and Chromogranin A IHC 238
8.9.2 BrdU immunohistochemistry 238
8.10 *In situ* hybridisation 239
8.11 IHC/ISH imaging and quantification 240
8.12 RNA extraction 240
8.12.1 Small tissues: CBs, SCGs, AMs 240
8.12.2 Large tissues (kidneys) 241
8.13 Quantitative Real-Time RT-PCR 241
8.14 RNA Sequencing 243
8.15 Ca^{2+} imaging in live tissues 243

8.15.1 Tissue preparation 243

8.15.2 Fluorescent imaging 244

8.15.3 Ca^{2+} imaging data analysis 245

8.16 Statistical analysis 247

Bibliography 249

List of Figures

Figure 1-1. Hypoxic ventilatory response. 24

Figure 1-2. The fine structure of a human carotid body. 26

Figure 1-3. Respiratory and blood pressure responses to hypoxia depend on intact carotid body innervation. 27

Figure 1-4. Carotid body glomerulus. 29

Figure 1-5. Transduction of the hypoxic stimulus in carotid body type I cells. 31

Figure 1-6. HIF domain structure. 41

Figure 1-7. Post-translational modification of HIF-α by the PHD/VHL signalling pathway. 42

Figure 2-1. Experimental design. 59

Figure 2-2. PT2385 treatment causes anaemia in normoxic mice, but does not prevent CH-induced polycythaemia. 60

Figure 2-3. PT2385 ablates VAH in wild-type mice. 62

Figure 2-4. PT2385 reverses VAH established in acclimatised mice. 65

Figure 2-5. Pharmacological HIF-2α inhibition abolishes enhanced HVRs in pseudo-hypoxic mice with genetic PHD2 inactivation. 68

Figure 2-6. Rapid reduction in ventilatory sensitivity to hypoxia in unacclimatised PT2385-treated mice. 71

Figure 2-7. Changes in TVb and RR in unacclimatised PT2385-treated mice. 73

Figure 2-8. Effects of PT2385 on cellular responses to hypoxia in wild-type CBs. 75

Figure 3-1. Validation of CB morphology and gene expression in hypoxic *Epas1*$^{S305M/S305M}$ mice. 85

Figure 3-2. *Epas1*$^{S305M/S305M}$ mice are resistant to PT2385 effects on VAH. 88

Figure 3-3. *Epas1*$^{S305M/S305M}$ mice have reduced VAH relative to wild-type littermates. 90

Figure 3-4. Effects of PT2385 on cellular responses to hypoxia in *Epas1*$^{S305M/S305M}$ CBs. 91

Figure 3-5. Polycythaemic response to hypoxia in wild-type and *Epas1*$^{S305M/S305M}$ mice. 92

Figure 3-6. HVRs in animals treated with the maximum safe dose of PT2385. 95

Figure 3-7. The effects of PT2385 on MVb changes in response to hypoxic stimuli with varying CO_2 compensation. 98

Figure 3-8. The effects of PT2399 on HVR in unacclimatised mice. 101

Figure 3-9. The effects of PT2977 on HVR in unacclimatised mice. 102

Figure 4-1. *Arnt* and *Arnt2* compared with *Epas1* expression in the mouse carotid bifurcation. 111

Figure 4-2. *Arnt* and *Arnt2* expression in the kidney. 113

Figure 4-3. *Arnt*$^{f/f}$ mouse model construct. 115

Figure 4-4. Generation of the *Arnt2*^{flox} animal model. 116

Figure 4-5. Testing *Arnt2* loxP site recombination by genomic PCR. 117

Figure 4-6. Experimental design for testing CB function in mice with acute *Arnt/Arnt2* inactivation. 118

Figure 4-7. *Arnt* and *Arnt2* mRNA expression in the kidneys of *Arnt1/2*dKO and *Arnt* or *Arnt2* single knock-out mice. 120

Figure 4-8. Targeted *Arnt* and *Arnt2* inactivation in the *Arnt*$^{f/f}$*;RosaCreER* and *Arnt2*$^{f/f}$*;RosaCreER* CBs. 121

Figure 4-9. Hypoxia-induced polycythaemia in mice with adult-onset *Arnt* and *Arnt2* inactivation. 123

Figure 4-10. VAH in mice with acute genetic ARNT and ARNT2 inactivation. 125

Figure 4-11. VAH in *Arnt1/2*dKO mice measured by changes in TVb. 128

Figure 4-12. VAH in mice with either *Arnt* or *Arnt2* inactivation in adulthood. 132

Figure 4-13. VAH in *Arnt1/2* single knock-out mice measured by changes in TVb.... 136

Figure 4-14. CB proliferation and hypertrophy in acclimatised *Arnt*$^{f/f}$*;Arnt2*$^{f/f}$*;RosaCreER* mice. 138

Figure 4-15. CB proliferation and hyperplasia in acclimatised *Arnt*$^{f/f}$*;RosaCreER* and *Arnt2*$^{f/f}$*;RosaCreER* mice. 139

Figure 5-1. G-protein signalling mechanism. 146

Figure 5-2. Post-translational modification of RGS4/5 via the N-degron pathway. 147

Figure 5-3. Expression of the HIF/PHD and RGS/ADO pathway components in the CB. 151

Figure 5-4. HIF/PHD and RGS/ADO pathways components expression in the hypoxic CB. 153

Figure 5-5. Confirmation of specific *Rgs4* and *Rgs5* mRNA loss in mice with RGS4 and RGS5 inactivation. 155

Figure 5-6. CB volume and morphology in mice with RGS4 or RGS5 inactivation. .. 156

Figure 5-7. Experimental design for testing CB function in mice with constitutive *Rgs4* or *Rgs5* inactivation. 157

Figure 5-8. HVR in mice with constitutive *Rgs4* or *Rgs5* inactivation in TH^+ cells.... 159

Figure 5-9. VAH in mice with *Rgs4* or *Rgs5* inactivation in TH^+ cells. 162

Figure 5-10. Acute responses to 10% O_2 in acclimatised mice with *Rgs4* inactivation in TH^+ cells. 164

Figure 5-11. CB proliferation in acclimatised *Rgs4*$^{f/f}$*;THCre* and *Rgs5*$^{f/f}$*;THCre* mice. 166

Figure 5-12. Experimental design for testing CB function in mice with acute *Rgs5* inactivation. 167

Figure 5-13. Confirmation of *Rgs4* or *Rgs5* mRNA loss in mice with acute *Rgs4* and *Rgs5* inactivation in adulthood. 169

Figure 5-14. VAH in mice with acute *Rgs4* or *Rgs5* inactivation in adulthood. 171

Figure 5-15. CB proliferation in acclimatised *Rgs4$^{f/f}$;RosaCreER* and *Rgs5$^{f/f}$;RosaCreER* mice. 175

Figure 6-1. *Phd2* inactivation in chromaffin cells results in pseudohypoxic PCC-like transcriptomic and catecholaminergic profiles, as well as abnormal morphology..... 185

Figure 6-2. Spatial gene expression in the *Phd2$^{f/f}$;THCre* AM. Population switch in noradrenergic/adrenergic chromaffin cells. 189

Figure 6-3. RNA Sequencing of *Phd2$^{f/f}$;THCre* vs *Phd2$^{f/f}$* AM and CB. 192

Figure 6-4. Acute hypoxia causes graded Ca^{2+} influx into the CB and SCG. 198

Figure 6-5. Ca^{2+} fluorescence imaging showing acute oxygen sensitivity in the *Phd2$^{f/f}$;THCre* AM..... 201

Figure 6-6. Spatial distribution of chromaffin cells responsive to hypoxia and hyperkalaemia in wild-type and *Phd2*KO AM. 205

Figure 6-7. Heterogeneity of acute responses to hypoxia in *Phd2$^{f/f}$;THCre vs* wild-type AM. 206

Figure 6-8. Abdominal paraganglioma in *Phd2$^{f/f}$;THCre* mice..... 207

Figure 6-9. Organ of Zuckerkandl in neonatal wild-type *vs Phd2$^{f/f}$;THCre* mice..... 209

Figure 6-10. Neonatal Organ of Zuckerkandl and abdominal PGL volume in wild-type and *Phd2*KO mice. 210

Figure 6-11. Gene expression in the OZ paraganglioma, compared with wild-type CB and *Phd2*KO AM. 212

Figure 6-12. Expression of catecholamine-synthesising enzymes in the *Phd2*KO OZ paraganglioma. 213

Figure 6-13. Acute oxygen sensitivity in the OZ paraganglioma..... 214

Figure 6-14. *Phd2* inactivation induces Ca^{2+} influx into chromaffin cells in response to hypercapnic acidosis and K^{+} ion channel inhibition. 217

List of Tables

Table 2-1. PT2385 effects on hypoxic and hypercapnic AVRs in acclimatised mice. .. 63

Table 2-2. PT2385 abolishes VAH in wild-type acclimatised mice. 66

Table 2-3. Acute ventilatory responses in *Phd2*$^{+/-}$ mice treated with PT2385. 69

Table 3-1. Effects of PT2385 on VAH in wild-type and *Epas1*$^{S305M/S305M}$ mice. 89

Table 4-1. AVRs in animals with acute genetic *Arnt* and *Arnt2* inactivation. 126

Table 4-2. AVRs in *Arnt1/2*dKO mice measured as changes in TVb. 129

Table 4-3. AVRs in animals with acute *Arnt* inactivation in adulthood. 134

Table 4-4. AVRs in animals with acute *Arnt2* inactivation in adulthood. 135

Table 5-1. Hypoxic and hypercapnic AVRs in acclimatised *Rgs4*$^{f/f}$*;THCre* mice. 163

Table 5-2. Hypoxic and hypercapnic AVRs in acclimatised *Rgs5*$^{f/f}$*;THCre* mice. 164

Table 5-3. Hypoxic and hypercapnic AVRs in acclimatised *Rgs4*$^{f/f}$*;RosaCreER* mice. 172

Table 5-4. Hypoxic and hypercapnic AVRs in acclimatised *Rgs5*$^{f/f}$*;RosaCreER* mice. 173

Table 6-1. Genes with expression dysregulated in pseudohypoxic PPGLs. 183

Table 6-2. Top 20 genes upregulated in the *Phd2*$^{f/f}$*;THCre*, relative to wild-type AM. 193

Table 8-1. Primer sequences used for PCR genotyping of mice. 232

Table 8-2. RNAScope and BaseScope probes..... 239

Table 8-3. TaqMan gene expression assays used for RT-qPCR 242

Table 8-4. Composition of gases used to bubble test solutions for Ca^{2+} imaging of fresh tissues. 245

Table 8-5. Criteria used to classify AM ROIs as Hpx-responsive or non-responsive.. 247

Acknowledgements

During my time in Oxford, I have met many friends and colleagues, all of whom played a role in the process of writing this Thesis. I am grateful for all their support, even if the list might be too long to contain here.

I would like to thank my supervisors, Dr Tammie Bishop and Professor Sir Peter Ratcliffe for giving me the opportunity to pursue this work and their continued support throughout the past four years. I have learnt many valuable lessons thanks to you: in Science, work, life and how to combine the three.

I would like to thank Professor Keith Buckler and Dr Thomas Keely for their input into the work during our weekly 'CB meetings', teaching me about the world of microscopy and electrophysiology, helping develop imaging techniques and providing very useful comments and criticism on experiment design and data analysis.

Completion of the animal work would not be possible without the support of Professor Christopher Pugh, responsible for our animal licence. Thank you for putting up with all the administrative issues and for all the insightful comments about my work in the context of the wide field of hypoxia as well as the sailing chat.

Special thanks go to Dr Gloria Cheng, Dr James Fielding, Dr Luise Eckardt, and Dr Emma Hodson, who completed all the pioneering work preceding my thesis and taught me the fine art of animal work and histology, as well as providing continued support with experiments during my time in the lab.

I would also like to thank all the other members of the Ratcliffe group for their help in practical matters and all the interesting conversations, scientific and other: Catherine,

Norma, Tom, David and Julie, and in particular all the youngest members of the lab for not letting me go insane: Olivia, Jess, Joanna, Samvid, George, Virginia, it's been great to have you. Special thanks also go to Isobel and Ela, who helped complete many of the immunohistochemical studies presented.

I would further like to thank all members of the University who taught me different laboratory techniques, answered my questions and provided continued support, particularly Dr Indrika Ratnyaka, for sectioning hundreds of my paraffin blocks and helping me perfect my embedding technique, Dr Richard Lisle, for his help with imaging various tissues, Dr Francesco Boccellato, for teaching me how to slice fresh tissues, Dr Gillian Douglas, for her help with finding the Organ of Zuckerkandl, Dr Minghao Zhang and Professor Fraydoon Rastinejad for their help with *in vitro* validation of the S305M mutation and many interesting discussions about the ARNT proteins, Dr Ben Davies, for creating the *Arnt2*^{flox} mouse model, and all the staff at the Wellcome Functional Genetics Facility, especially Mr Douglas Dos Santos Passos, Miss Jade Harris, Mr Luke Harris, Mrs Heather Chandler and Mrs Viv Clark for all their help with planning and carrying out animal experiments to the best standards and in compliance of the Home Office regulations.

Finally, I would like to thank my parents and my family for putting up with my move abroad and all the missed birthdays, holiday celebrations and parties, your support means a lot!

I will finish by thanking Whitney Houston's mother, because I promised my best friend and partner I would. I know you wanted me to finish in three years, but I wouldn't have done it in four without you.

Abbreviations

5-HT – 5-hydroxytryptamine (serotonin)

ADO – 2-aminoethanethiol dioxygenase

AM – adrenal medulla

ARNT – aryl hydrocarbon receptor nuclear translocator

ATP – adenosine triphosphate

AVR – acute ventilatory response

bHLH – basic Helix Loop Helix domain

b.i.d. – bis in die (twice a day)

BrdU – 5-bromo-2'-deoxyuridine

$[Ca^{2+}]_i$ – intracellular Ca^{2+} concentration

cAMP – 3',5'-cyclic adenosine monophosphate

CB – carotid body

ccRCC – clear cell renal cell carcinoma

CH – chronic hypoxia

CNS – central nervous system

DCV – dense core vesicle

dKO – double knock-out

E(11) – embryonic day (11)

EGLN – egg-laying nine

ETC – electron transport chain

FIH – factor inhibiting HIF

GAP – GTPase activating protein

GCaMP6f – Green Fluorescent Protein (GFP)-calmodulin (CaM) fusion protein 6 fast

GDI – guanine nucleotide dissociation inhibitor

GDP – guanine diphosphate

GEF – guanine nucleotide exchange factor

GFAP – glial fibrillary acidic protein

GFP – green fluorescent protein

GPCR – G-protein coupled receptor

GTP – guanine triphosphate

HIF – hypoxia inducible factor

HRE – hypoxia response element

HVR – hypoxic ventilatory response

IHC – immunohistochemistry

IP_3 – inositol triphosphate

ISH – *in situ* hybridisation

KO – knock-out

MVb – minute ventilation breathing

NADH – nicotinamide adenine dinucleotide + hydrogen

OZ – organ of Zuckerkandl

P(0) – post-natal day (0)

$P_{O2/CO2}$ – oxygen/ carbon dioxide partial pressure

PAS – Per-Arnt-Sim domain

PCA – principle component analysis

PCC – pheochromocytoma

PGL – paraganglioma

PHD – prolyl hydroxylase domain-containing protein

PLC – phospholipase C

PNMT – phenylethanolamine N-methyltransferase

PPGL – pheochromocytoma and paraganglioma

RGS – regulator of G-protein signalling

ROI – region of interest

RR – respiratory rate

RT-qPCR – quantitative reverse transcription polymerase chain reaction

SCG – superior cervical ganglion

SDH – succinate dehydrogenase

SEM – standard error of the mean

TASK – TWIK-related acid sensitive K^+ (channel)

TCA – tricarboxylic acid

TH – tyrosine hydroxylase

TPM – transcripts per million

TVb – tidal volume breathing

VAH – ventilatory acclimatisation to hypoxia

VEGFA – vascular endothelial growth factor A

vs - versus

pVHL – Von Hippel-Lindau protein

1 Introduction

Oxygen is essential to life and over the course of evolution, many different mechanisms developed to counteract hypoxia, caused either by environmental conditions or different pathologies. In multicellular organisms, adaptations to low oxygen aim to either reduce oxygen consumption by utilising anaerobic respiration, increasing glucose transporter expression or inducing cellular senescence, or by increasing oxygen input, by stimulating ventilation, vasodilation, erythropoiesis and angiogenesis. Physiological responses to hypoxia occur over different time-scales, with the most rapid, including the acute ventilatory response (AVR), developing within seconds, while others, such as hypoxia-stimulated erythropoiesis, requiring hours to days, or even spanning generations, with natural selection among hypoxia-related genes evident in high altitude populations.

Deleterious effects of oxygen deprivation as an explanation for altitude sickness were first described by Paul Bert in his book La Pression Barometrique (Bert, 1878), presenting studies on animals placed under bell jars and exposed to normobaric and hypobaric hypoxia (West, 2012). Early efforts to describe adaptations to high altitude in animals and men were confounded by the difficult access and conditions in the high-

altitude laboratories built on Mont Blanc and Monte Rosa in the 1890s (West, 2012). The first comprehensive study of human respiratory and cardiovascular adaptations to altitude was during the 1911 Anglo-American expedition to Pike's Peak, which was served by the railway and had a hotel at the summit, allowing to observe the effects of altitude without confounding factors of cold and discomfort (Douglas et al., 1913). Data collected during this expedition showed a rapid decrease, followed by a gradual recovery, of the P_{O2} in Douglas's and others' blood, as well as a rapid fall and continued reduction in P_{CO2} during the 5 weeks at the summit, which was credited to the hyperventilation on ascent to altitude (Douglas et al., 1913). This was later termed ventilatory acclimatisation to hypoxia (VAH). Concurrently with the Pike's Peak expedition, Mabel FitzGerald made a series of measurements whilst visiting mining camps in Colorado, and described a linear, inverse relationship between barometric pressure and alveolar P_{O2}/P_{CO2}, as well as a direct linear relationship with haemoglobin (West, 2012). Together, these observations showed that the body adapts to altitude by VAH and polycythaemia, overturning the widely held belief at that time that oxygen delivery is a 'fixed' process that does not adapt to hypoxia. This introduction focuses on these ventilatory responses to low oxygen and provides an overview of the subsequent discoveries in the field.

1.1 Ventilatory responses to hypoxia

Continuous ventilation can be measured using body plethysmography – a technique utilising Boyle's law, which states that the pressure and volume of gas are inversely related at a constant temperature. The body plethysmograph originally designed for human studies consists of a sealed box, inside of which a subject respires, with an increase in the pressure inside the box caused by the altered volume of the lung (and reduced airway pressure) during each inspiration, used to derive the volume of the lung

(West, 2004). In animals, this is simplified in that an awake animal is placed in a sealed chamber and changes in pressure inside the chamber, caused by an increase in the volume of expired air as it gets warmed and humidified to body temperature during inspiration, are measured by pressure sensors to derive the breathing depth and frequency (Lim et al., 2014). Together, these methods provide quantitative measurement of tidal volume (total volume of air exchanged with each breath, TVb) and respiratory rate (RR), and the product of these two parameters is called minute ventilation (MVb).

Ventilatory responses to hypoxia constitute several reflex stimuli mediated by different mechanisms and over different time-scales. Within seconds of reduction in arterial PO_2, there is an increase in ventilation, termed hypoxic ventilatory response (HVR), caused by an increase in both the RR and TVb (reviewed in Powell et al., 1998, Figure 1-1A) and a hyperbolic relationship exists between the increased ventilation and arterial P_{O2} decline (Pamenter and Powell, 2016, Duffin, 2007). This acute increase in ventilation is rapidly suppressed due to the fall in arterial carbon dioxide saturation caused by hyperventilation in preparations without CO_2 adjustment, termed short-term depression or hypoxic ventilatory decline (HVD)(Weiskoff and Gabel, 1975, Khamnei and Robbins, 1990, Figure 1-1A). Many studies, therefore, adjust CO_2 levels to produce ‘isocapnic hypoxia', (either by clamping end-tidal CO_2 levels or enriching the hypoxic stimulus with CO_2) allowing assessment of ventilatory response to low oxygen alone (Weil et al., 1970, Khamnei and Robbins, 1990, Duffin, 2007, Figure 1-1B). Elevated ventilation is rapidly reversed back to basal levels upon return to normoxia, followed by a short-term depression (STD), with reduced basal ventilation, observed particularly in the RR recordings (Figure 1-1A).

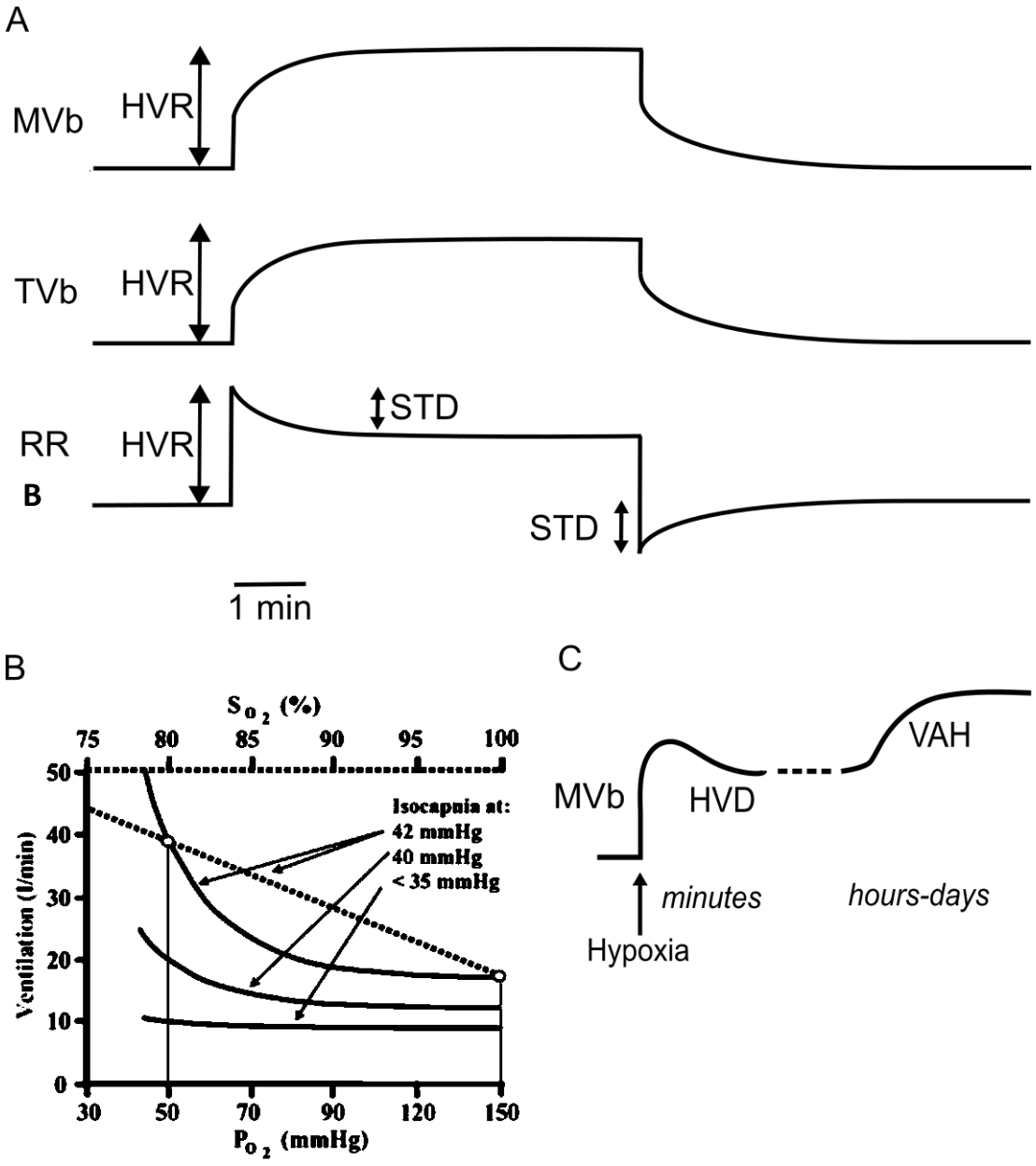


Figure 1-1. Hypoxic ventilatory response.

(**A**) Schematic representation of changes in minute ventilation (MVb), tidal volume (TVb) and respiratory rate (RR) under short hypoxic exposure. HVR – hypoxic ventilatory response, STD – short-term depression. Adapted from Powell et al., 1998. (**B**) Hyperbolic relationship between ventilation and oxygen partial pressure (P_{O2}), under different P_{CO2}, and a linear relationship between ventilation and oxygen saturation (S_{O2}). From Duffin, 2007. (**C**) Schematic representation of changes in MVb over long-term adaptation to hypoxia. HVD – Hypoxic Ventilatory Decline, VAH – ventilatory acclimatisation to hypoxia. Adapted from Powell et al., 1998.

When hypoxia persists for minutes, a progressive HVD is observed, which is independent of the hypocapnia-induced decline (Weil and Zwillich, 1976, Figure 1-1C). Further prolonged exposure to hypoxia, for hours to days, initiates VAH, characterised by the time-dependent fall in arterial P_{CO2} (Douglas et al., 1913), indicating progressive hyperventilation, and by an increase in the acute HVR (Sato et al., 1992, Howard and Robbins, 1995a, Howard and Robbins, 1995b, Robbins, 2007, Figure 1-1C), with the contribution of increased TVb and RR to the overall increase in ventilation varying between species (Forster et al., 1974, Aaron and Powell, 1993, Engwall and Bisgard, 1990, Tatsumi et al., 1995). Duration of hypoxic exposure required to elicit VAH is also species-dependent, varying from 4-6 hours in goats to more than 10 days in humans and rats (Powell et al., 1998, Dempsey and Forster, 1982).

Both the acute and chronic ventilatory responses to hypoxia are initiated by the arterial chemoreceptors: carotid bodies. The structure and mechanisms behind carotid body response to oxygen deprivation will now be reviewed.

1.2 **The carotid body**

Carotid body (CB) is an arterial chemoreceptor located bilaterally at the bifurcation of the carotid artery. Original drawings and microphotographs by Fernando de Castro in the 1920s showed this tissue to be highly vascularized and innervated by projection from the superior cervical ganglion, with glandular cells (later termed 'glomus' or 'Type I' cells) forming small glomeruli surrounded by glossopharyngeal fibres (Type II cells)(Figure 1-2). Based on its high vascularisation, the CB has been proposed to be ‘sampling the blood’. Indeed, the CB is extremely highly perfused, with the blood flow around 1-2 L/min/100 g tissue weight, around ten times more than within the brain (Prabhakar, 2016).

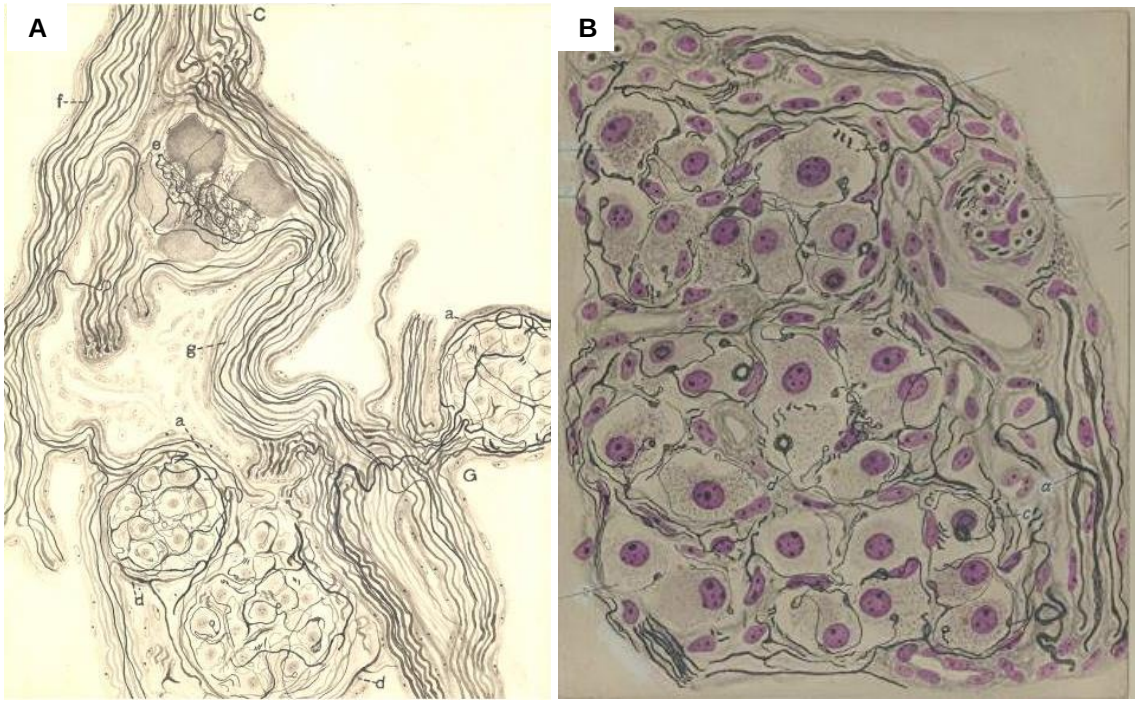


Figure 1-2. The fine structure of a human carotid body.
From de Castro, 2009b, as originally published in 1926. (**A**) Inter-carotid nerve (c) arriving into the CB (d) (**B**) Glomerular structure of the CB of a young man.

Following this hypothesis, work by De Castro and Heymans described the CB as a chemoreceptor, detecting changes in the arterial blood concentration of H^+, carbon dioxide and oxygen to trigger a reflex response (De Castro, 2009a), in a series of experiments with isolation of carotid sinus circulation in anaesthetised dogs and cross-perfusion between hypoxic and normoxic animals. These showed that altering oxygen partial pressure (or $[H^+]$) within the carotid sinus circulation (whilst maintaining normoxia in systemic circulation) was sufficient to cause changes in respiration and blood pressure. Further, the increase in respiration under hypoxaemia was blocked upon sectioning of the carotid sinus nerve (Figure 1-3). Together, this demonstrated the role of the CB as a chemosensor, leading to the award of the Nobel Prize in Physiology in 1938 to Corneille Heymans, *for the discovery of the role played by the sinus and aortic mechanisms in the regulation of respiration* (NobelPrize.org).

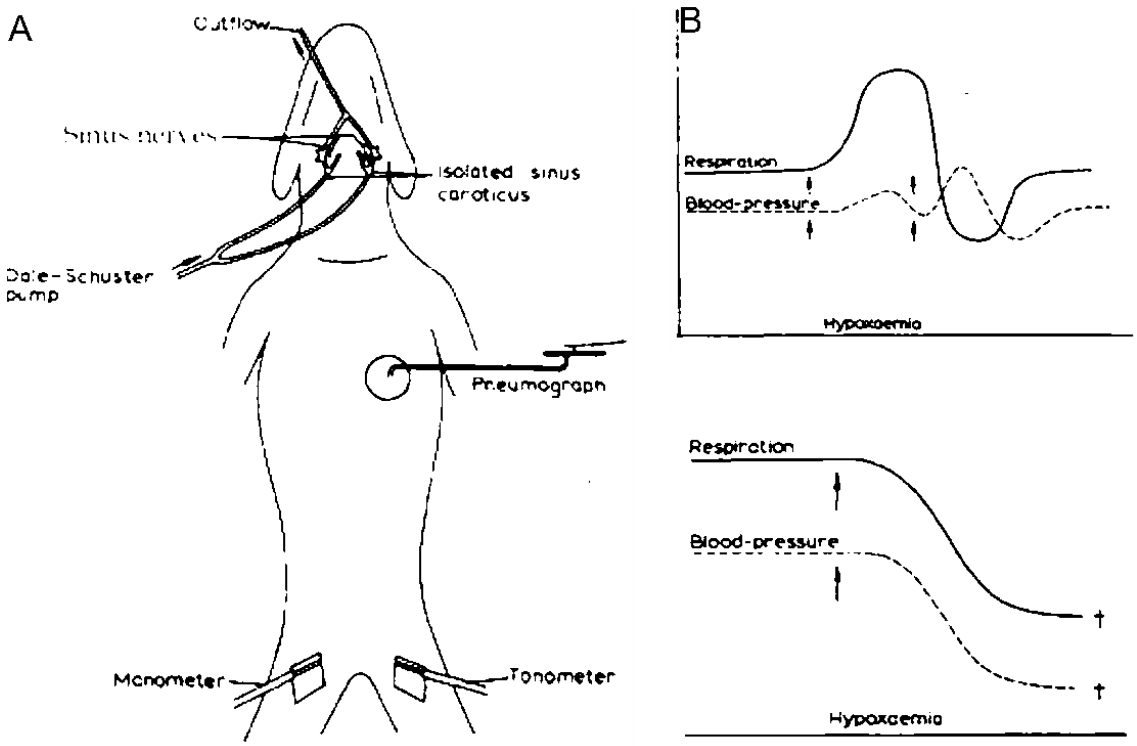


Figure 1-3. Respiratory and blood pressure responses to hypoxia depend on intact carotid body innervation.

(**A**) Diagram of the procedure involving an anaesthetised dog with isolated perfusion of the carotid sinus with intact nervous connection and systemic circulation. (**B**) Increased respiration and blood pressure under hypoxaemia in a dog with intact (top) and cut chemo-sensitive nerves from the aortic and carotid sinus areas (bottom). From Heymans, 1945.

1.2.1 *Carotid body structure and morphology*

The CB is located at the bifurcation of the carotid artery, in close proximity to the superior cervical ganglion (SCG), which provides sympathetic innervation of the CB blood vessels (Fitzgerald et al., 2016), with afferent innervation provided by the carotid sinus nerve, while efferent innervation most likely originating from the glossopharyngeal nerve (Campanucci and Nurse, 2007). The high vascular supply of the carotid chemoreceptor originates from the carotid artery, with a network of convoluted and straight capillaries allowing fine regulation of blood flow (Fitzgerald et al., 2016). The majority of cells in the CB are the type I (glomus) and type II (sustentacular) cells (with the type I cells dominating, typically in a 4/5:1 ratio, Kumar and Prabhakar,

2012), surrounded by a protective capsule of connective tissue providing the characteristic, glomerular structure (Figure 1-4, Kobayashi, 1968, de Castro, 2009b, De Kock, 1954). Both type I and type II cells originate from the neural crest, as demonstrated by the implanation of quail primordia, able to take up L-Dopa, into chick embyros to follow the fate of morphologically distinct cells from the two species (Pearse et al., 1973) and with the Cre/LoxP genetic neural crest marker *Wnt1* recombination in mice (Pardal et al., 2007).

CB chemosensory function is primarily mediated by the type I cells, which are oval, with a diameter of ~8-15 μm in rats (~10 μm in mice) and with a large, spherical nucleus (Kumar and Prabhakar, 2012). One of the most established markers of CB type I cells in histology is their high expression of tyrosine hydroxylase, the rate-limiting enzyme in catecholamine synthesis (Karasawa et al., 1982, Chou et al., 1998). Electron microscopic studies show that a distinctive type I cell feature is their high ratio of dense- to clear-core synaptic vesicles (not found, for instance, in the ontogenically related SCG), with varying size (and neurotransmitter contents) between and within species (Kobayashi, 1968, Kobayashi and Uehara, 1970, Lever and Boyd, 1957). These cells are electrically excitable, with neurotransmitter secretion triggered by reduced P_{O2} (see section 1.2.2).

The glia-like CB type II cells have a characteristic flattened, sickle-like appearance (Figure 1-4) with kidney-shaped nuclei and densely packed chromatin. These cells do not possess cytoplasmic granulations or dense core vesicles (DCVs) characteristic of the type I cells (De Kock, 1951, Duchen et al., 1988). Type II cells are typically identified immunohistochemically by expression of the glial fibrillary acidic protein (GFAP) (Nurse and Fearon, 2002) and the presence of the calcium-binding, acidic protein S100 (Kondo et al., 1982). These cells do not mount an action potential under step

depolarisation (Duchen et al., 1988) and do not show O_2-sensitivity of the outward current (Lopez-Lopez et al., 1989).

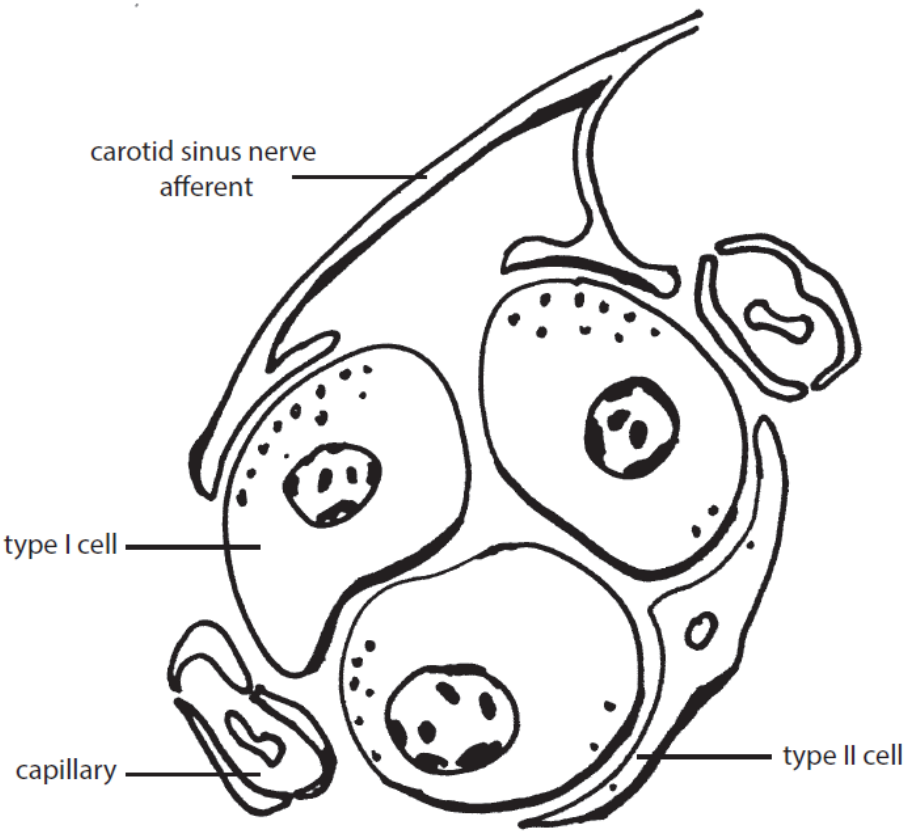


Figure 1-4. Carotid body glomerulus.
Diagram shows the large, neurosecretory type I cells, arranged into a glomerulus with surrounding, glia-like type II cells and a network of capillaries. Type I cells secrete DCV-stored neurotransmitters onto the carotid sinus nerve afferent. Diagram drawn by Dr Emma Hodson.

1.2.2 *Carotid body acute oxygen sensing*

Carotid body sensitivity to acute hypoxic stimuli has been demonstrated *in vivo*, in the original preparations by Heymans (Heymans and Bouckaert, 1930), in whole-mount *ex vivo* preparations (Pardal and Lopez-Barneo, 2002), as well as in isolated type I cells (Lopez-Barneo et al., 2001, Peers and Buckler, 1995, Vidruk et al., 2001), showing a hyperbolic relationship between P_{O2} and CB neurosecretory activity (Lahiri et al., 1993, Peng et al., 2003, Montoro et al., 1996).

CB type I cells are electrically excitable, such that increased extracellular [K^+] alters membrane potential to cause neurotransmitter release in an extracellular Ca^{2+}-dependent manner (Gonzalez et al., 1994, see overview in Figure 1-5). This has been demonstrated by patch-clamping rat type I cells, showing P_{O2}-responsive K^+ currents (Lopez-Lopez et al., 1998, Peers, 1990, Stea and Nurse, 1991) and by the demonstration of increased intracellular [Ca^{2+}] ([$Ca^{2+}]_i$, using fluorescent dyes) upon hypoxic exposure, concurrent with increased membrane potential, but completely ablated by removal of extracellular Ca^{2+} (Buckler and Vaughan-Jones, 1994). Detailed studies of the K^+ currents in isolated rat type I cells predicted that the O_2-sensitive channels are characterised by background conductance and are outwardly rectifying (Buckler, 1997). These characteristics are found in K_{2P} family channels, which maintain the negative membrane potential of excitable cells. Indeed, subsequent work identified expression of members of the K_{2P} family: TWIK-related acid-sensitive K^+ (TASK) channels 1 and 3, in the CB type I cells (Buckler et al., 2000, Yamamoto et al., 2002) and demonstrated that TASK-1/3 heteromers are responsible for the predominant background K^+ current in these cells and that this current is inhibited by hypoxia to induce membrane depolarisation (Turner and Buckler, 2013, Ortega-Saenz et al., 2010).

Disruption of the resting membrane potential by hypoxic K^+ channel inhibition in type I cells results in opening of the voltage-gated ($Ca^{2+}{}_v$) channels and subsequent increase in $[Ca^{2+}]_i$, as demonstrated by the loss of hypoxia-induced Ca^{2+} influx in cells with voltage-clamped membrane potential (Buckler and Vaughan-Jones, 1994) and attenuation of hypoxia-induced catecholamine secretion by L- and T-type $Ca^{2+}{}_v$ channel blockers (Caceres et al., 2009). Increased $[Ca^{2+}]_i$ leads to neurotransmitter release onto the sinus nerve afferents. This was originally demonstrated for dopamine (Urena et al., 1994, Montoro et al., 1996), but many other neurotransmitters have been reported to be

stored in and released from the type I cell vesicles, including acetylcholine, ATP, noradrenalin and serotonin (Nurse, 2005).

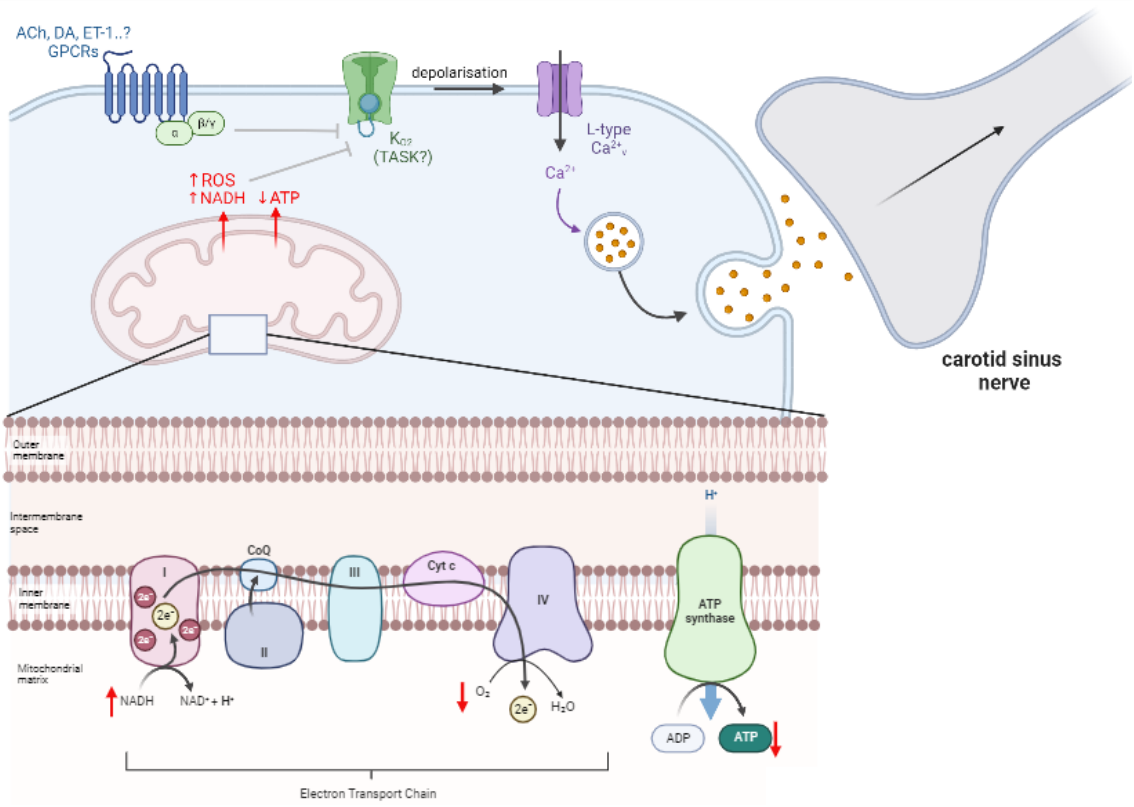


Figure 1-5. Transduction of the hypoxic stimulus in carotid body type I cells. Schematic overview of the proposed transduction mechanisms causing membrane depolarisation and neurotransmitter release under hypoxia. Oxygen-sensing K^+ channels (such as the TASK channels) are inhibited in the absence of oxygen, either directly or by signals from G-protein coupled receptors (GPCRs) and mitochondria, including elevated NADH and ROS caused by electron build-up in the electron transport chain (shown in detail at the bottom of the figure), or reduction in ATP levels due to inhibition of the ATP synthase in the absence of protons in the mitochondrial intermembrane space. Figure generated with biorender.com, based on illustrations from Holmes et al., 2018 and Bishop and Ratcliffe, 2020.

Acute oxygen sensitivity can be tested *ex vivo* using multiple different readouts, as different parts of the sensing mechanism are investigated experimentally (Figure 1-5). Direct measurements of mitochondrial electron transport chain activity can be made by recording NADH autofluorescence (Buckler and Turner, 2013). Electrophysiological techniques can be used to measure ion channel activity and membrane potential (Lopez-

Barneo et al., 1988, Peers, 1990, Buckler et al., 2000), while changes in [Ca^{2+}] can be detected with fluorescent dies or genetically encoded reporters (Buckler and Turner, 2013, Chang et al., 2015). Finally, secretory events can be measured by detecting catecholamines with amperometric recordings and by measuring electrical activity at the sinus nerve (Ortega-Saenz et al., 2010, Vidruk et al., 2001, Pardal and Lopez-Barneo, 2002).

Although there is a consensus on the sequence of events leading to CB neurotransmitter release due to hypoxia-induced K^+ channel inhibition, the mechanism transducing hypoxic stimulus to membrane depolarisation is a subject of debate. Early studies suggested that K^+ channels may sense P_{O2} directly and there have been attempts to prove direct oxygen-sensitivity of the TASK channels by transfection of non-oxygen-sensitive HEK293 cells with recombinant human TASK-1 channel, which showed marked reduction of the pH-sensitive K^+ current under hypoxia (Lewis et al., 2001). However, no oxygen-sensitivity was found in channels isolated from their intracellular environment in an excised patch (Buckler et al., 2000), suggesting that TASK channels cannot sense oxygen independently of the cellular environment. Current thinking now leads towards the metabolic hypothesis, which proposes that oxygen sensing is linked to oxidative phosphorylation (Prabhakar, 2016), as outlined below.

1.2.2.1 Metabolic hypothesis of carotid body hypoxic chemotransduction

Mitochondrial oxidative phosphorylation is the main source of energy in cells. Electron transport chain (ETC) complexes I-IV, spanning across the inner mitochondrial membrane, oxidise NADH produced in the TCA cycle, causing a build-up of protons in the inter-membrane space. The resulting mitochondrial potential is then utilised by the ATP synthase. The forward rate of electron transport across this chain is dependent on many factors, including the availability of oxygen at the cytochrome c oxidase, which

reduces oxygen to water capturing the utilised electrons. Reduction in oxygen tension has been shown to increase NADH autofluorescence, as well as mitochondrial potential, in rat type I cells (Mills and Jobsis, 1972, Duchen and Biscoe, 1992a, Duchen and Biscoe, 1992b) and these changes can be mimicked with application of ETC inhibitors: rotenone (blocking complex I), myxothiazol (blocking complex III) and cyanide (blocking complex IV), as well as with ATP synthase inhibitor: oligomycin (Duchen and Biscoe, 1992b, Wyatt and Buckler, 2004). ETC inhibition further blocks the effects of hypoxia on K^+ current, suggesting a non-additive effect of oxygen deprivation and metabolic inhibition (Wyatt and Buckler, 2004). Based on these studies, hypoxic ETC inhibition has been proposed to signal via increased NADH or ROS, due to the build-up of electrons, or due to reduced ATP availability.

However, uncouplers, such as fluoromethoxyphenylhydrazone, which would decrease NAD^+/NADH ratio by allowing electrons to bypass the ATP synthase, also block type I cell K^+ currents, suggesting the role of reduced ATP levels, rather than increased NADH or ROS, in hypoxic chemotransduction (Wyatt and Buckler, 2004, Buckler and Turner, 2013). One way in which this could mediate oxygen-sensitivity is via AMPK signalling: Reduction in ATP levels increases ADP available for conversion into AMP by the adenylate kinase, thus increasing AMPK-mediated signalling. In line with this, activators of AMPK have been shown to increase $[Ca^{2+}]_i$ in the same way as hypoxia, and AMPK inhibition prevents hypoxia-induced Ca^{2+} influx in CB type I cells (Evans et al., 2005, Wyatt et al., 2007).

Whether this metabolic signalling pathway underlies oxygen-dependent K^+ channel inhibition has been contested due to the very high affinity of cytochrome c oxidase for oxygen, such that a reduction in oxygen availability observed in physiological contexts (and sufficient to induce HVR), would not alter mitochondrial metabolism (Buckler and

Turner, 2013). However, transcriptomic studies of the carotid body type I cells showed high differential expression of "atypical" mitochondrial subunits: *Cox4i2, Ndufa4l2* and *Cox8b*, compared with non-oxygen-sensitive neuronal cells and most other tissues (Zhou et al., 2016), and COX4i2 isoform has been found to have a two-fold higher P_{50} for oxygen than the dominant isoform in most tissues, COX4i1 (Pajuelo Reguera et al., 2020). Based on this, hypoxic inhibition of cytochrome c oxidase, causing electron build-up along the ETC to accumulate NADH and ROS, which in turn signal to the K^+ channels, has been proposed as the new oxygen sensing mechanism in the CB (Moreno-Dominguez et al., 2019, see Figure 1-5). However, studies on the effects of NADH and ROS accumulation on TASK channel currents and CB function under hypoxia are inconclusive, with both increase and reduction of ROS reported in the hypoxic CB (Bernardini et al., 2015).

1.2.2.2 G-protein signalling modulation of carotid body hypoxic chemotransduction

In addition to the uniquely high expression of atypical mitochondrial subunits outlined above, transcriptomic studies of the CB have identified components of the G-protein signalling cascade among the most highly expressed genes in the CB type I cell (Zhou et al., 2016) and highly differentially expressed in the CB compared to non-oxygen-sensitive sympathetic ganglia and adrenal medulla (Gao et al., 2017, Chang et al., 2015). Among these are genes encoding the $G_{\alpha s}$ and $G_{\alpha i}$, as well as $G_{\alpha q}$ subunits, $G_{\alpha s}$ – (*Olfr78, Adora2a, Adcyap1r*), $G_{\alpha i}$ – (*P2ry12, Cnr1*) and $G_{\alpha q}$ – coupled (*Agtr1a, Ednra*) GPCRs and regulators of G-protein signalling/GTPase activating proteins: *Rgs4/5* (Zhou et al., 2016).

The function of the olfactory receptor-78 in oxygen sensitivity was subsequently tested in *Olfr78*$^{-/-}$ mice and, with some initial controversy due to discrepancy in results under different protocols, it has been concluded that OLFR78 can contribute to the hypoxic

response, but this varies depending on the severity of hypoxic stimulus (Chang et al., 2015, Peng et al., 2020, Torres-Torrelo et al., 2018).

Another $G_{\alpha s}$-coupled GPCR upregulated in the CB is adenosine receptor 2A (encoded by *Adora2a*). Exogenous adenosine has been shown to cause an acute increase in ventilation in rats and humans (Monteiro and Ribeiro, 1987, Tubek et al., 2016) and caffeine, an inhibitor of adenosine 2A and 2B receptors, reduces carotid sinus nerve activity under hypoxia (Conde et al., 2006). Adenosine is both a precursor and breakdown product of ATP, generated via the TCA cycle, thus adenosine signalling could also complement the metabolic hypothesis with signalling via reduced ATP synthesis during hypoxia (Aldossary et al., 2020, see Figure 1-5 and section 1.2.2.1).

While the link between downstream mediators of $G_{\alpha s}$ subunit and the excitatory pathway stimulating CB neurosecretion is unclear, more direct signalling could occur between $G_{\alpha q}$-coupled GPCRs and Ca^{2+}-dependent neurotransmitter release, as $G_{\alpha q}$ subunits activate phospholipase C to generate IP_3, which in turn causes Ca^{2+} release from intracellular stores. In line with this, serotonin (5-HT), acting on $G_{\alpha q}$-coupled 5-HT2 receptors, has been shown to potentiate hypoxia-induced $[Ca^{2+}]_i$ increase in isolated type I cells with the effects blocked by a 5-HT2-specific antagonist (Yokoyama et al., 2015). However, as the hypoxia-induced increase in $[Ca^{2+}]_i$ is dependent on external Ca^{2+} availability (Buckler and Vaughan-Jones, 1994), $G_{\alpha q}$-coupled GPCRs are more likely to modulate hypoxia-induced secretion potentiation, than to participate in the acute signalling cascade itself.

Both $G_{\alpha i}$ and $G_{\alpha q}$ are substrates of RGS4 and RGS5, members of the R4 regulators of G-protein signalling (RGS) family, which are highly expressed in the type I cells and highly CB-enriched compared to related, non-oxygen-sensitive tissues (Zhou et al.,

2016, Gao et al., 2017, Chang et al., 2015). RGS proteins function as GTPase-activating proteins (GAPs), accelerating hydrolysis of GTP at the G_{α} subunit, which causes the G-protein heterotrimeric complex to reform following activation by a GPCR ligand (reviewed in Kimple et al., 2011). RGS4 and RGS5 could therefore potentially negatively regulate $G_{\alpha i}$ and $G_{\alpha q}$ signalling in the CB, impacting ATP/cAMP levels and intracellular Ca^{2+} release.

RGS4 and 5 are post-translationally regulated by arginylation of N-terminal cysteine and subsequent degradation via the N-degron pathway (Lee et al., 2005) and recently, the initial step leading to RGS4/5 degradation has been found to be mediated by an oxygen-dependent amino-terminal cysteine dioxygenase, ADO (Masson et al., 2019). ADO inhibition by a reduction in oxygen availability causes RGS4 and RGS5 stabilisation within 4 hours (unpublished data, Keeley et al., manuscript in preparation), these RGS proteins could therefore mediate some of the previously described effects of GPCRs on CB hypoxic acclimatisation.

1.2.2.3 Acute oxygen sensing in other tissues

Identification of key cellular components of acute oxygen sensitivity has been attempted by looking at features conserved across different oxygen-sensitive cells and across species.

In addition to the CB type I cells, rapid neurosecretory responses to hypoxia in mammals have previously been described in the pulmonary artery smooth muscle cells (Murray et al., 1990, Cornfield et al., 1994), neonatal chromaffin cells (Thompson et al., 1997, Mojet et al., 1997, Seidler and Slotkin, 1985) and neuroepithelial bodies found throughout the airway epithelium (Lauweryns et al., 1973). Of particular interest is the parallel between acute oxygen sensing in the CB and hypoxic pulmonary

vasoconstriction, as abnormally elevated expression of *Cox4i2* has been described in both tissues (Zhou et al., 2016, Huttemann et al., 2001) and genetic *Cox4i2* inactivation appears to ablate both HVR and acute hypoxic pulmonary vasoconstriction (Moreno-Dominguez et al., 2019, Sommer et al., 2017).

Peripheral arterial oxygen-sensing chemoreceptors are found throughout different vertebrate taxa and are typically located at the junction of internal and external carotid arteries (Milsom and Burleson, 2007). The presence of tyrosine hydroxylase, 5-HT and O_2-sensitive K^+ channels has been demonstrated in the neuroepithelial cells of the fish gill, suggesting high similarity with the mammalian CB (Milsom and Burleson, 2007). More recently, single-cell RNA sequencing has been performed on zebrafish ventilatory chemoreceptors: neuroepithelial cells, showing high differential expression of several genes previously identified in the mouse CB, including *Epas1*, encoding HIF-2α, atypical mitochondrial subunits *Ndufa4l2* and *Cox8a-like*, regulators of G-protein signalling *Rgs5* and *Rgs4* and voltage-gated K^+ channels *Kcnd2* and *Kcnip3b* (Pan et al., 2022). Conservation of these gene expression patterns across species as well as across different oxygen-sensitive cells suggests that these may play a role in acute oxygen sensing.

1.2.3 *Carotid body in long-term adaptations to hypoxia*

As well as initiating HVR, the CB also plays a role in VAH. This has been demonstrated by abolished VAH in animals with denervated CBs (Forster et al., 1981, Smith et al., 1986), as well as *in vitro* studies showing a progressive increase in afferent CB discharge from goats exposed to prolonged hypoxia (Nielsen et al., 1988). The exact mechanism behind this increased CB activity in chronic hypoxia is unclear (Bisgard, 2000).

Unlike most other tissues, CB cells proliferate under sustained hypoxia. This has been demonstrated by comparing CB volume following long-term (3-4 weeks) hypoxia (Dhillon et al., 1984, Pequignot et al., 1984) and by measuring cellular proliferation with nuclear incorporation of 5-Bromo-2'-deoxyuridine (BrdU) (Pardal et al., 2007, Bishop et al., 2013). Cell lineage tracing technology demonstrates that this CB hypertrophy is associated with an increase in type I, as well as, to a lesser degree, type II cell population (Fielding et al., 2018), with no evidence of trans-differentiation between cell populations, in contrast to the previous theory suggesting that $GFAP^+$ progenitor cells proliferate then differentiate into TH^+ type I cells during sustained hypoxia (Pardal et al., 2007). Increased neovascularization of the hypoxic CB has also been observed, driven by increased expression of Vascular Endothelial Growth Factor A (VEGFA) (Laidler and Kay, 1975, Fielding et al., 2018).

This increased oxygen-sensing type I cell population in the hypoxic CB has been postulated to drive enhanced HVR in acclimatised subjects, especially as the type I cell hypertrophy increases the area available for gap junction connections between type I cells, potentially enhancing hypoxia-stimulated discharge due to coupling of multiple cells (Powell, 2007, Eyzaguirre and Abudara, 1999). However, the onset of VAH precedes CB hypertrophy (Bishop et al., 2013), indicating morpho-physiological changes in the type I cells, including changes in ion channel and neurotransmitter composition, may also contribute to the enhanced neurosecretory activity of the chemoreceptor in this context (Prabhakar et al., 2009, Bisgard, 2000).

Increased Ca^{2+} current and ion channel density have previously been reported in type I cells of hypoxia-acclimatised rats, although this study was done in neonates which do not mount VAH, therefore it is unclear if this mechanism would account for VAH in adults (Hempleman, 1996).

Another hypothesis is that an increase in endothelin-1, acting on ET_A GPCRs in the CB, potentiates the CB neurosecretory output to induce VAH: chronic hypoxia upregulates expression of ET_A receptors (Chen et al., 2002) and treatment with bosentan, a non-specific endothelin-receptor inhibitor, reduces hypoxia-induced CB proliferation and carotid sinus nerve discharge in acclimatised rats (Chen et al., 2007). Intravenous endothelin-1 infusion has further been shown to potentiate ventilation in humans during a 4h exposure to eucapnic hypoxia, mimicking early VAH (Talbot et al., 2008).

Altered dopaminergic signalling has also been contemplated to play a role in hypoxic acclimatisation (Bisgard, 2000). In normoxia, dopamine released from the DCVs acts both pre- and post-synaptically via the $G_{\alpha i}$-coupled D_2 receptors, to inhibit adenylyl cyclase activity and reduce conversion of ATP to cAMP. In hypoxia, increased dopamine release further reduces conversion of ATP and counteracts reduced ATP synthesis caused by oxidative phosphorylation in hypoxia (reviewed in Aldossary et al., 2020, see Figure 1-5). Dopamine is therefore thought to have an autocrine regulatory role to inhibit CB discharges during HVR. Relief of dopaminergic inhibition has been proposed to underly VAH, as treatment with domperidone, a D_2-selective inhibitor unable to cross the blood/brain barrier, mimics VAH in cats, with no further HVR increase with sustained hypoxic exposure in cats treated with domperidone (Tatsumi et al., 1995). This is, however, inconsistent with enhanced dopamine synthesis under chronic hypoxia, due to upregulation of tyrosine hydroxylase – the rate-limiting enzyme in dopamine synthesis (Czyzyk-Krzeska et al., 1992).

Overall, there is no consensus on the molecular or electrophysiological mechanism behind CB-driven VAH, with multiple signalling pathways and morphological changes likely contributing to enhanced type I cell neurosecretory activity and/ or increased sensitivity to changes in P_{O2}.

1.3 **Hypoxia Inducible Factors: master regulators of the hypoxic response**

Many of the cellular responses to hypoxia are regulated by the Hypoxia Inducible Factors (HIFs). These transcription factors are considered master regulators of the hypoxic response, as they can induce changes in the expression of hundreds of genes encoding proteins involved in several different processes, to mediate adaptive responses to hypoxia (reviewed in Keith and Simon, 2007, Ratcliffe, 2013).

1.3.1 *Oxygen sensing by the HIF/PHD pathway*

HIF proteins are basic helix-loop-helix (bHLH) proteins with the bHLH domain at the N-terminus allowing recognition and binding of the Hypoxia Response Element (HRE) in the DNA (Burslem et al., 2017). Two further domains characteristic of this class of proteins: Per-ARNT-AHR-Sim (PAS) domains, allow hetero-dimerisation of HIF-α and HIF-β subunits to form functional transcriptional complexes (Burslem et al., 2017, Card et al., 2005, Erbel et al., 2003, see Figure 1-6). HIF-β subunit also called the Aryl Hydrocarbon Receptor Nuclear Translocator (ARNT), is a Class II bHLH protein and a common heterodimerisation partner for multiple different Class I proteins, which act as the signalling molecules to regulate cellular function (as well as forming homodimers to regulate transcription of some targets) (Kewley et al., 2004). HIF-β is constitutively present in the cell nucleus, with a generally low and ubiquitous expression across tissues in mammals. In contrast, HIF-α proteins are subject to stimulus-dependent post-translational modifications, which control their transcriptional activity.

Proline residues of the HIF oxygen-dependent degradation (ODD) domain are hydroxylated by the prolyl hydroxylase domain (PHD) enzymes in the presence of oxygen, 2-oxoglutarate and Fe^{2+} (Schofield and Ratcliffe, 2004, see Figure 1-6 and Figure 1-7). Hydroxylation of these proline residues increases HIF-α affinity for the Von Hippel Lindau protein (pVHL), an E3 ubiquitin ligase, which in turn marks HIF-α

for proteasomal degradation (Maxwell et al., 1999, Figure 1-7). In hypoxia, reduced oxygen availability prevents HIF-α hydroxylation and allows stabilisation and nuclear translocation of the protein to heterodimerise with HIF-β and subsequently bind HRE to promote expression of HIF-target genes (Figure 1-7). Further control of HIF transcriptional activity is achieved by hydroxylation of the asparagine residue at the HIF-α C-terminus by the Factor Inhibiting HIF (FIH), which prevents recruitment of the transcriptional coactivator and histone acetyltransferase p300/CBP (Dames et al., 2002, Lando et al., 2002, Figure 1-7). The K_m value of FIH is, however, only ~40% that of HIF prolyl hydroxylases (Koivunen et al., 2004), suggesting a much greater reduction in oxygen availability is required to prevent p300/CBP recruitment than what is sufficient to stabilise the HIF-α protein.

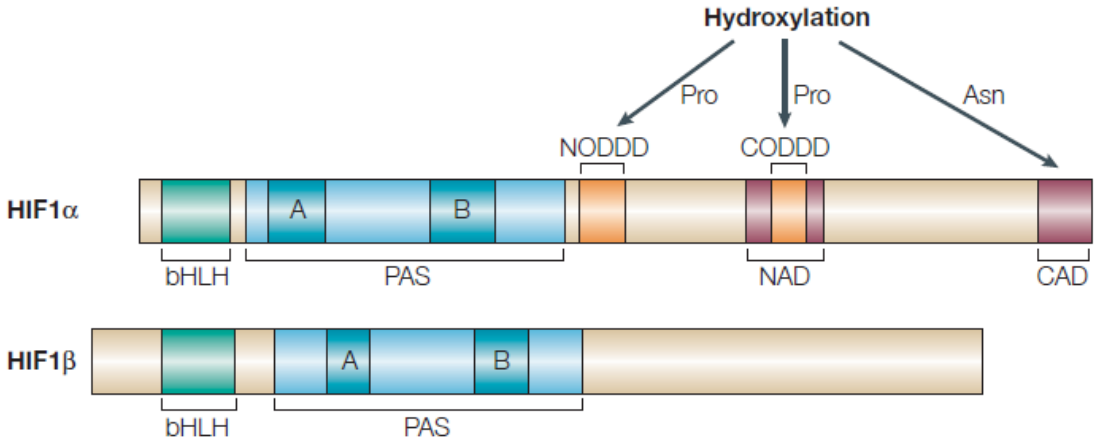


Figure 1-6. HIF domain structure.

N- and C-ODDD – amino- and carboxy-oxygen dependent degradation domains; CAD – carboxy-terminal activation domain. From Schofield and Ratcliffe, 2004.

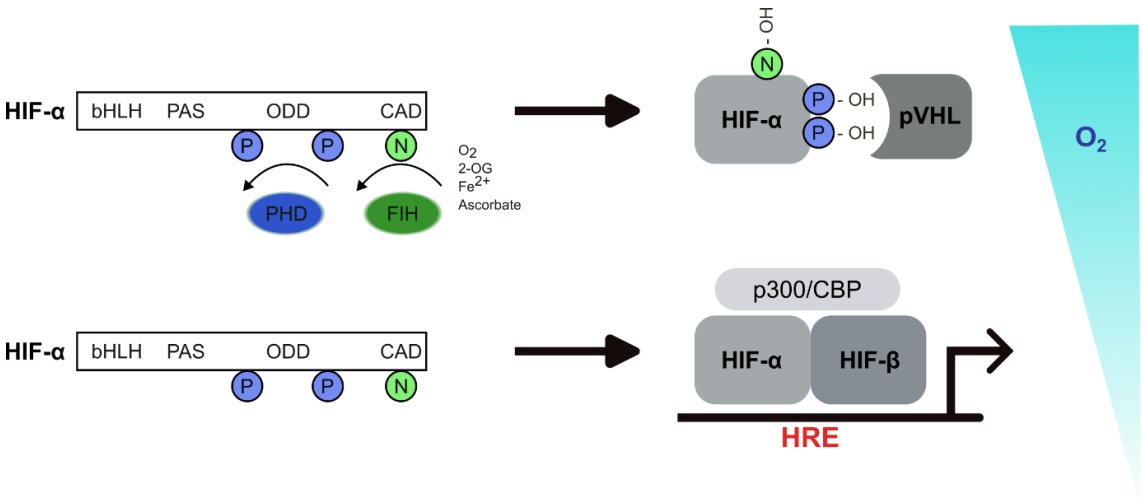


Figure 1-7. Post-translational modification of HIF-α by the PHD/VHL signalling pathway. Proline residues of the Oxygen-Dependent Degradation (ODD) domain are hydroxylated by PHDs to allow recognition of HIF-α by pVHL. In the absence of oxygen, PHD enzymes are inhibited, allowing HIF-α to escape pVHL-dependent degradation and dimerise with HIF-β and DNA hypoxia response element (HRE) to activate gene expression. Further control is achieved by recruitment of p300/CBP at the asparagine residue of the C-terminal activation domain, hydroxylated by FIH (in an oxygen-dependent manner). Adapted from Bishop and Ratcliffe, 2014.

1.3.2 *Diversity of HIF and PHD isoforms*

PHD/HIF pathway is present in some form in all eumetazoa (Mills et al., 2018), however, despite high conservation across the PHD and HIF proteins, multiple genome duplication and deletion events resulted in generation of distinct PHD and HIF-α isoforms in vertebrates (Rytkonen et al., 2011).

In mammals, PHD1, 2 and 3 isoforms have been described, encoded by the Egg Laying Nine (EGLN)-2, 1 and 3 genes respectively (Taylor, 2001) (named after the discovery of the single *Egl-9* PHD isoform in *C. elegans*, responsible for the defective egg-laying phenotype, Trent et al., 1983, which was subsequently shown to mediate *C. elegans* HIF-1α oxygen-dependent degradation, Epstein et al., 2001). Distinct, but overlapping tissue expression patterns have been described for the three PHD isoforms in mammals, with PHD2 found in almost every tissue, but PHD1 and PHD3 expression dominating in

the testis and heart respectively (Wong et al., 2013). In line with its ubiquitous expression, PHD2 is considered to be the principal regulator of HIF-1, with some bias toward the regulation of HIF-2 by PHD3, although this appears to depend on enzyme abundance (Berra et al., 2003, Appelhoff et al., 2004). In further support of PHD2 being the primary HIF regulator in mammals, mice homozygous for *Phd2* die at mid-gestation (Mazzone et al., 2009), whilst *Phd1*$^{-/-}$ and *Phd3*$^{-/-}$ mice survive and appear grossly normal, healthy and viable (Aragones et al., 2008, Bishop et al., 2008).

Similar to the HIF prolyl hydroxylases, there are three mammalian HIF-α isoforms, of which HIF-1 and HIF-2α are the best characterized and most closely related, with 48% primary amino acid sequence identity, while HIF-3α is more distant and may play an inhibitory role antagonizing HRE-dependent gene expression (Lendahl et al., 2009, Ratcliffe, 2007). HIF-1α plays an essential role in embryonic development, as *Hif-1α*$^{-/-}$ mice exhibit mid-gestational lethality by E11 from neural tube defects and cardiovascular malformations (Iyer et al., 1998). On the other hand, embryonic lethality has been reported in some, but not all, *Hif-2α*$^{-/-}$ mice, with one study showing complete litter loss between E12.5 and E15.5 due to a drastic reduction in noradrenaline levels (Tian et al., 1998) and another reporting embryonic lethality between E9.5 and E13.5 due to vascular defects (Peng et al., 2000). Other studies, however, showed incomplete embryonic lethality with early mortality in surviving pups associated with breathing defects (Compernolle et al., 2002) and a further paper reported survival of some *Hif-2α*$^{-/-}$ mice to adulthood but with metabolic defects (Scortegagna et al., 2003). Developmental effects of *Hif-2α* inactivation may therefore depend on the genetic background of the animals studied.

In adults, HIF-1α is ubiquitously expressed throughout the body (Jain et al., 1998, Wenger et al., 1996) and is commonly stabilised in different cancers (Talks et al., 2000),

playing an important role in glucose metabolism (Hu et al., 2003). HIF-2α has a more restricted expression pattern, with high differential expression noted in the endothelial cells, renal fibroblasts, duodenal epithelial cells, and lung type II pneumocytes (Wiesener et al., 2003). Particularly high *Epas1* expression has been observed in the sympathoadrenal system during development, when *Epas1* expression co-localises with tyrosine hydroxylase (Favier et al., 1999) and high expression levels persist in the adult CB, resulting in high differential expression compared to other tissues (including in the sympathoadrenal system)(Tian et al., 1998, Hodson et al., 2016).

While common target genes of both HIF-1α and HIF-2α have been identified, a genome-wide association study showed there are substantially more HIF-1α than HIF-2α-binding loci despite both proteins binding the same HRE motif, with HIF-2-binding loci generally found further away from the promoter than those binding HIF-1 (Mole et al., 2009, Lendahl et al., 2009) and HIF-2α-specific target genes are also known (Patel and Simon, 2008), although the specificity of activation by each isoform may vary between tissues (Rankin et al., 2007).

One particular gene regulated specifically by HIF-2α is *Epo*, encoding erythropoietin (Warnecke et al., 2004) (although the initial discovery of HIF-1α was made based on purification from EPO-producing Hep3B cells, suggesting HIF-1-regulated *Epo* expression in some contexts (Semenza et al., 1991)). This glycoprotein has an essential role in regulating red blood cell synthesis in response to changes in tissue oxygenation. During embryonic development, EPO is mostly secreted from the liver, with some EPO-producing cells remaining in the adult, as shown by positive GFP reactivity in hepatocytes surrounding the central vein in mice with *Epo*-coding sequence replaced by GFP (Obara et al., 2008). In adults, however, EPO is primarily produced by the renal interstitial fibroblasts, as demonstrated in transgenic mice with the SV40 marker gene

inserted into the *Epo* locus (Maxwell et al., 1993). Both the renal interstitial fibroblasts and hepatocytes show high *Epas1* expression (Paliege et al., 2010, Rosenberger et al., 2002, Favier et al., 2001) and indeed, both renal and hepatic hypoxia-induced *Epo* expression is HIF-2α-dependent in mice (Kapitsinou et al., 2010, Rankin et al., 2007). In humans, *EPAS1* gain-of-function mutations are associated with polycythaemia (Pacak et al., 2013, Zhuang et al., 2012) and genetic variation in *EPAS1* across the high-altitude Tibetan and Andean populations has been shown to account for the variation in their haemoglobin concentration as an adaptation to continuous hypoxia (Beall et al., 2010, Bigham and Lee, 2014).

1.4 HIF-2α in carotid body responses to hypoxia

Transcriptomic analyses of the CB have shown that HIF-2α is very highly expressed in type I cells (Zhou et al., 2016) and highly differentially upregulated in the CB compared with other, non-oxygen-sensitive sympathoadrenal tissues (Gao et al., 2017), suggesting it may play a role in hypoxia sensing.

Evidence for the role of HIF signalling in hypoxic ventilatory control first came from the demonstration of increased HVRs in patients with loss-of-function mutations in the main negative regulators of HIF: VHL and PHD2, which stabilise HIF-α in normoxia (termed 'pseudohypoxia'):

Chuvash polycythaemia patients are homozygous for VHL with an R200W mutation, which diminishes the VHL binding affinity for HIF-α. Unlike patients with the VHL syndrome, Chuvash patients do not develop tumours, but have increased erythropoiesis and markedly increased MVb in response to mild and moderate hypoxia (70 and 50 mmHg or 9 and 7% O_2 respectively, with end-tidal carbon dioxide levels clamped at a constant level, Smith et al., 2006). Similarly, 'Chuvash' mice with an R200W VHL

mutation have also been described to have elevated baseline ventilation under normoxia, as well as increased sensitivity to acute 10% O_2 (and 10% O_2/3% CO_2) hypoxia (Slingo et al., 2014), mimicking VAH. This was associated with a high increase in CB size, as measured by the volume of TH^+ tissue (Slingo et al., 2014).

The importance of the PHD2 prolyl hydroxylase isoform in ventilatory control has been suggested by a case report of a polycythaemic patient heterozygous for a single-site, presumed loss-of-function, PHD2 mutation, showing their hypoxic ventilation matched the elevated HVRs observed in Chuvash Polycythaemia patients (Talbot et al., 2017). Loss-of-function of PHD2 has also been shown to elevate ventilation in mice. Initially, this was tested in *Phd2* heterozygotes, which are healthy and viable, unlike the embryonically lethal *Phd2* knock-outs. These *Phd2*$^{+/-}$ mice showed significantly increased 10% O_2 and 10% O_2/3% CO_2 AVRs, as well as an increase in CB volume (Bishop et al., 2013). Studies in mice with acute, tamoxifen-inducible Cre, further showed that the effect of *Phd2* inactivation on ventilatory control is not driven by developmental changes, as mice with acute *Phd2* inactivation in adulthood have elevated HVR, similar to that observed in *Phd2*$^{+/-}$ and hypoxia-acclimatised animals (Hodson et al., 2016), whilst their CB morphology remains unaffected. On the other hand, inactivation of *Phd2* that is restricted to TH^+ type I cells in *Phd2*$^{f/f}$*;THCre* mice (with conditional *Phd2* inactivation driven by a TH-IRES-Cre), results in grossly dysplastic paraganglioma-like CBs, with morphological characteristics of tumours found in patients with pseudohypoxic mutations and only a mild increase in HVR and CB volume, perhaps due to a portion of these type I cells being dysfunctional (Fielding et al., 2018).

Together, loss-of-function of VHL and PHD2 in both patients and mice results in enhanced responses to acute hypoxia and CB growth (although the latter phenotype

likely requires developmental HIF stabilisation), mimicking the effects of prolonged hypoxic exposure. Since the loss of both PHD2 and VHL results in HIF activation, ventilatory and CB hyperplastic phenotypes in these patients and mice suggest a role of HIFs in CB function.

The first studies to test the role of HIF-α inactivation on HVR used mice heterozygous for either of the two isoforms (due to complete or partial embryonic lethality in the knock-out mice, see above). These studies (performed by the Prabhakar laboratory in Chicago/Cleveland) suggested that HIF-1 mediates VAH, with loss of VAH (induced by 72h exposure to hypobaric hypoxia) in *Hif-1α*$^{+/-}$ mice (as measured by a lack of increase in RR, but not TVb, under 12% O_2) and an almost complete absence of carotid sinus nerve activity in the CBs isolated from *Hif-1α*$^{+/-}$ mice (Kline et al., 2002). A later study by the same laboratory credited this loss of VAH in *Hif-1α*$^{+/-}$ mice to increased expression of *Hif-2α* in the CBs of mice heterozygous for *Hif-1α* (Yuan et al., 2013). The Prabhakar laboratory later showed increased hypoxic AVRs and an increase in sensory discharges from the CBs of unacclimatised *Hif-2α*$^{+/-}$ mice compared to wild-type controls, although VAH was not tested in *Hif-2α*$^{+/-}$ mice (Peng et al., 2011).

This contrasts with subsequent findings published by the Oxford laboratory, which showed that both the VAH established by 7-day normobaric hypoxia and enhanced HVR in *PHD2*$^{+/-}$ mice are lost in *Hif-2α*$^{+/-}$, but not *Hif-1α*$^{+/-}$ mice (Hodson et al., 2016). This result was confirmed when near-complete HIF-1α or HIF-2α inactivation was achieved in the adult using an inducible, ubiquitously expressed Cre recombinase (RosaCreER), further indicating that HIF-2α plays an active role in VAH in adulthood, rather than by altering CB development. Both 7-day hypoxic VAH and enhanced HVR in response to acute PHD2 inactivation was lost in *Hif-2α*$^{f/f}$*;RosaCreER*, but not *Hif-1α*$^{f/f}$*;RosaCreER* mice, compared to tamoxifen-treated *Hif-2α*$^{f/f}$ or *Hif-1α*$^{f/f}$ controls (Hodson et al., 2016).

Further studies using an inducible Cre recombinase with expression restricted to the TH^+ cells (TH-IRES-CreER) also reported a loss of VAH in *Hif-2α$^{f/f}$;THCreER* mice (Fielding et al., 2018), pointing to the role of HIF-2α specifically in the TH^+ O_2-sensing type I cells of the CB.

In addition to its role in mediating responses to chronic hypoxia in the CB, HIF-2α has been found to mediate HVR in unacclimatised mice. Acute *Hif-2α* (but not *Hif-1α)* inactivation reduces 10% O_2/3% CO_2 AVR within 10 days of tamoxifen treatment to induce recombination, in mice with no previous hypoxic exposure (Hodson et al., 2016); a similar trend was also found in *Hif-2α$^{f/f}$;THCreER* and *Hif-2α$^{+/-}$* mice (Fielding et al., 2018, Hodson et al., 2016). More recently, complete inactivation of 10% O_2 HVR with respect to increased RR was shown in unacclimatised mice heterozygous for *Hif-2α* with subsequent loss of the second allele induced in adulthood (Moreno-Dominguez et al., 2019). This was accompanied by the loss of hypoxia-induced Ca^{2+} influx and catecholamine secretion from the isolated CB type I cells and slices respectively (Moreno-Dominguez et al., 2019). Based on these findings, HIF-2α has been proposed to play a role in acute CB function, although the mechanism behind this remains unclear.

In addition to its role in adult function, HIF-2α also plays an important role in CB development, as demonstrated by the complete loss of type I cells during late embryonic development in mice with constitutive HIF-2α inactivation in TH^+ cells, and the resulting inability of these animals to mount an HVR or to survive sustained hypoxia (Macias et al., 2018, Fielding et al., 2018).

Overall, despite the clear importance of the VHL/PHD/HIF signalling axis in VAH, there are discrepancies between the effects of HIF-1 *vs* HIF-2α inactivation on VAH from

different laboratories. Further work using orthogonal approaches is therefore required to confirm which HIF-α isoform drives ventilatory acclimatisation in mammals.

1.5 HIF-2α in carotid body pathology – paragangliomas

The HIF-pathway is commonly activated in different cancers (Wicks and Semenza, 2022), as the proliferative potential of solid tumours exceeds their ability to form sufficient vascular supply, thus depriving the tissue of oxygen. Activation of HIFs is, however, rarely the initiating step in tumorigenesis. One of the exceptions to this are pseudohypoxic pheochromocytomas and paragangliomas (PPGLs): neuroendocrine tumours of neural crest origin, affecting the adrenal medulla (AM - pheochromocytomas) and sympathetic paraganglia, including the CB (paragangliomas).

PPGLs are highly hereditary, with up to 40% of cases caused by germline, or early somatic mutations (Dahia, 2014) – the highest of any endocrine tumour (Crona et al., 2017). 80% of hereditary PPGLs are caused by mutations in the *VHL* or *SDHx* gene, with other most commonly mutated genes including *NF1* and *RET* (Favier et al., 2015). Genetic characterization of TCGA patient samples has identified three main clusters of PPGL-causing mutations in three signalling pathways, termed: pseudohypoxic, Wnt signalling and kinase signalling clusters accordingly (Fishbein et al., 2017). Pseudohypoxic mutations take their name from activating hypoxia signalling pathways under physiological oxygen tensions. Mutations in this cluster include mutations in the HIF pathway components: loss-of-function mutations in *VHL* and *PHDs* and gain-of-function *EPAS1* mutations, as well as mutations in the genes encoding metabolic enzymes: succinate dehydrogenase (*SDHx)*, fumarate hydratase (*FH*), dihydrolipoamide S-succinyltransferase (*DLST*) and malate aspartate shuttle (*MDH2, GOT2, SLC25A11*) (Favier et al., 2015, Buffet et al., 2020).

Loss-of-function mutations in the SDHx genes prevent conversion of succinate to fumarate, resulting in extensive metabolic re-wiring of the affected cells, with multiple possible mechanisms by which this may contribute to carcinogenesis proposed (reviewed in Kluckova and Tennant, 2018). Accumulating metabolites in cells with SDHx mutations may also have a more direct signalling function contributing to abnormal cell proliferation, as high levels of succinate (unable to be converted into fumarate) inhibit 2-oxoglutarate-dependent enzymes, including DNA and histone demethylases (Jumonji domain histone lysine demethylases and ten-eleven translocation methylcytosine dioxygenases), as well as prolyl hydroxylases, leading to HIF-α stabilisation and activation of the HIF transcriptional programme (see Figure 1-7)(Moog et al., 2020, Sullivan et al., 2016, Letouze et al., 2013).

While both the metabolic and direct HIF-pathway mutations lead to HIF-α stabilisation, a fine balance in activation of different HIF-α isoforms appears to be necessary to cause PPGLs. This has been demonstrated by the differences in genotype:phenotype correlation in VHL disease – an inherited condition caused by germline loss of one *VHL* copy, with subsequent somatic mutations predisposing to different cancers depending on the level of HIF-α activation induced (Kaelin, 2008). Type 1 mutations associated with a low risk of pheochromocytoma typically map to the pVHL β-domain hydrophobic core and are predicted to cause complete protein misfolding (resulting in high HIF-α activation) (Stebbins et al., 1999). Type 2 mutations associated with a high risk of pheochromocytoma, on the other hand, show a bias against hydrophobic core mapping, and are thought to only cause partial inactivation of the pVHL ubiquitin ligase (Stebbins et al., 1999). In support of the potential 'dose-dependent' tumorigenic effects of HIF-activation, while *Phd2* inactivation in TH^+ cells has been shown to lead to development of PPGL-like CBs in mice (Fielding et al., 2018), *Vhl* inactivation using

the same Cre driver results in CB atrophy, rather than tumourigenesis (Macias et al., 2014).

In addition to the overall level of HIF-α activation, the HIF-1α:HIF-2α stabilisation ratio is also important in cancer, with protective role of HIF-1α stabilisation reported in some patients with neuroblastomas and renal carcinomas, while HIF-2α thought to be the major driver of VHL loss-induced carcinogenesis in clear cell renal cell carcinoma (ccRCC) (reviewed in Tiburcio et al., 2014). Immunohistochemical analysis of pheochromocytomas and paragangliomas showed very high stabilisation of HIF-2α in majority of the SDH- and VHL-mutant patients, and weak HIF-1α staining in 5/8 SDH- and 1/10 VHL mutant samples, and this appeared to be driven by high *EPAS1* mRNA upregulation (Favier et al., 2009). The dominant role of HIF-2 and not HIF-1α in PPGLs is further supported by identification of mutations in the *EPAS1*, but not *HIF1A* gene: mosaic *EPAS1* mutations have been identified in patients with paragangliomas and somatostatinomas associated with polycythaemia, termed the Pacak and Zhuang syndrome (Zhuang et al., 2012, Pacak et al., 2013).

Despite identification of a variety of pseudohypoxic mutations in PPGL patients, generation of clinically relevant pseudohypoxic PPGL mouse models remains a challenge (Lussey-Lepoutre et al., 2018, Martinelli et al., 2020, Lepoutre-Lussey et al., 2016). As mentioned above, there is a discrepancy in the effects of HIF-α stabilisation on CB development across different genetic interventions: mice with TH^+ cell-specific *Phd2/Hif-1α,* but not *Phd2/Hif-2α,* inactivation develop large, PGL-like CBs (Fielding et al., 2018), as do mice with transgenic over-expression of non-degradable HIF-2α (but not HIF-1α) in TH^+ cells (Macias et al., 2014), supporting the evidence for a specific role of HIF-2α in human PPGL formation. TH^+ cell-specific *Vhl* inactivation, on the other hand, results in CB atrophy (Macias et al., 2014). Finally, introduction of the

A529V mutation in *Epas1* (corresponding to a human A530V mutation identified in a polycythaemic patient with an abdominal Organ of Zuckerkandl paraganglioma, adrenal mass, renal cystic lesion and a somatostatinoma, Pacak et al., 2013), results in polycythaemia, reduced metanephrine/normetanephrine ratio and an elevated number of somatostiatin^{+} cells in the duodenum, consistent with the biochemical profile of Packak-Zhuang patients, but with no paragangliomas or somatostatinomas (Wang et al., 2019).

1.6 Pharmacological HIF-2α inhibitors

The development of small molecules targeting specifically the HIF-2α isoform has recently been enabled by the identification of a specific role of the unique, 290Å pocket in the HIF-2α, but not the HIF-1α, PAS-B domain, which facilitates dimerisation with HIF-β (Rogers et al., 2013, Scheuermann et al., 2013, Scheuermann et al., 2009). Molecules binding within this pocket can allosterically weaken the HIF-2α:HIF-β dimer, thus reducing the HIF-2 transcriptional activity (Rogers et al., 2013, Scheuermann et al., 2013, Wu et al., 2019). Several compounds of this class, developed by Peloton Therapeutics (now Merck), have now been successfully used to reduce the size of tumours in HIF-2α-driven ccRCC mouse xenograft studies (Wallace et al., 2016, Cho et al., 2016, Chen et al., 2016, Xu et al., 2019) and two of them, PT2385 and PT2977, have moved to Phase I&II clinical trials, with promising results on safety and efficacy in ccRCC and other tumours associated with VHL disease (Courtney et al., 2018, Papadopoulos et al., 2018, Strowd et al., 2019). Indeed, in August 2021, the first HIF-2α inhibitor, Belzutifan (PT2977), was approved for clinical use in VHL disease patients with associated renal cell carcinoma, CNS hemangioblastomas or pancreatic neuroendocrine tumours not requiring immediate surgery (U.S. Food and Drug Administration, 2021) and there is an ongoing trial for Belzutifan treatment in pheochromocytomas, paragangliomas and pancreatic neuroendocrine tumours,

including, but not limited to VHL-disease patients (NIH trial NCT04924075). Notably, the early PT2385 studies described hypoxia as a side effect in nearly 20% of treated patients (Courtney et al., 2018). This could be due to the known effects of HIF-2α inactivation on HVR or pulmonary ventilation-perfusion matching (Cowburn et al., 2016). Pharmacological HIF-2α inhibitors therefore provide a perfect orthogonal approach for confirming the importance of HIF-2α in hypoxic CB physiology.

1.7 **Research aims**

Despite strong evidence supporting the role of HIF-2α isoform in ventilatory control, discrepancies between the effects of HIF-1/2α inactivation in different genetic models and protocols/laboratories remain. The first aim of this thesis is therefore to resolve the controversy on the role of HIF-2α in the CB-mediated adaptations to hypoxia using an approach orthogonal to genetic modifications, with HIF-2α inactivation by pharmacological inhibitors (Chapters 2 and 3 and Cheng et al., 2020).

Given the observation that both genetic and pharmacological HIF-2α inactivation diminish HVR, with rapid (within 1h of the first oral dose) inhibition of HVR by pharmacological HIF-2α inhibitors, as well as a hypomorphic phenotype in mice with a mutation in the HIF-2α ligand-binding pocket which does not affect HIF-2 transcriptional activity, subsequent studies investigated the possible mechanisms of HIF-2α action in the CB. Firstly, the potential non-transcriptional (HIF-β-independent) role of HIF-2α in CB-mediated acclimatisation to hypoxia was explored (Chapter 4).

Further, the potential downstream mediators of HIF-2α function in the CB responses to hypoxia were investigated, with a focus on the role of regulators of G-protein signalling: RGS4 and RGS5, which are highly expressed in the CB and have recently

been described to be post-translationally degraded in an oxygen-dependent manner by a novel O_2 sensor: ADO (Chapter 5).

Finally, we looked at the relationship between HIF-2α expression and oxygen-sensitivity in other tissues, by testing whether HIF-(2)α stabilisation in CB-related sympathoadrenal organs may be sufficient to induce acute oxygen sensitivity, as well as driving paraganglioma/pheochromocytoma-like phenotypes (Chapter 6 and Eckardt et al., 2021).

2

The marked and rapid effects of pharmacological HIF-2α antagonism on hypoxic ventilatory control.

2.1 Introduction

Studies in animals and humans using plethysmography or measuring direct electrical output of the CB type I cells *in vitro* have implicated a role of the HIF system in VAH. As described in the main Introduction (1.4), loss-of-function mutations in the main negative regulators of HIF: VHL and PHD2, have been shown to increase hypoxic AVRs without the prolonged exposure to hypoxia in humans (Smith et al., 2006, Talbot et al., 2017). In mice, similar effects of a point R200W mutation diminishing the VHL binding affinity for HIF-α and of heterozygous loss of *Phd2*, have been demonstrated, showing elevated baseline ventilation and markedly increased MVb under hypoxia, mimicking VAH, as well as CB hyperplasia (Slingo et al., 2014, Hickey et al., 2007, Bishop et al., 2013).

Further support for the importance of the HIF-2α isoform in ventilatory control comes from RNA expression studies showing high differential upregulation of *Epas1* mRNA in the CB, compared to other non-oxygen-sensitive sympathoadrenal tissues. This has been demonstrated by ISH in mouse tissue (Tian et al., 1998, Fielding et al., 2018) and by RNA

sequencing of both whole mouse CB (Gao et al., 2017) and single type I cells (Zhou et al., 2016). Compared with the low and fairly ubiquitous expression of the HIF-1α isoform (Fielding et al., 2018, Talks et al., 2000, Jain et al., 1998), the high differential expression of HIF-2α in the type I cells of the CB suggests a specific role of this isoform in the CB function, supporting the results showing HIF-2α importance in VAH and CB proliferation.

In spite of clear evidence to suggest involvement of the HIF pathway in hypoxic ventilatory control, there are conflicting studies as to which HIF-α isoform regulates VAH and/ or acute HVR. Early studies using heterozygous *Hif-1α* and *Hif-2α* mice pointed to the importance of HIF-1, and not HIF-2α in VAH, showing loss of enhanced AVR to 12% O_2 in *Hif-1α*$^{+/-}$ mice acclimatised to 72h hypobaric hypoxia, associated with almost complete absence of carotid sinus nerve activity (Kline et al., 2002). A contradictory result was later published by the Oxford laboratory, showing loss of VAH in 7-day normobaric hypoxia in *Hif-2α*$^{+/-}$, but not *Hif-1α*$^{+/-}$ mice, and in mice with acute *Hif-2α*, but not *Hif-1α* inactivation in the adult (Hodson et al., 2016). Studies using an inducible, TH^{+}-cell restricted Cre recombinase also reported loss of VAH with HIF-2α inactivation in the acutely oxygen-sensitive CB type I cells, supporting the role of HIF-2α in the oxygen chemosensitivity of this tissue (Fielding et al., 2018).

Reasons for the discrepancies between these studies on the effects of HIF-1/2α loss on VAH and acute CB responses to hypoxia remain unknown. As genetic knockouts usually involve removal of only a small portion of the gene encoding the catalytic subunit or the binding domains, some unknown function of the residual protein products and/ or RNA molecules could be contributing to the results observed in the HIF-1α and HIF-2α genetic knockouts. Further, use of different genetic constructs in these studies could also give rise to contradictory results. Thus, an ideal approach to resolve the controversy on which HIF-

α isoform is responsible for VAH would be to use an orthogonal method, such as a pharmacological inhibitor specific to the HIF-1/2α isoform.

Small molecules targeting specifically the HIF-2α isoform have recently been developed, following the identification of a specific role of the unique, 290Å pocket in the HIF-2α PAS-B domain, which facilitates dimerisation with HIF-β (Rogers et al., 2013, Scheuermann et al., 2013, Scheuermann et al., 2009). Molecules binding within this pocket can allosterically weaken the HIF-2α:HIF-β dimer, thus reducing the HIF-2 transcriptional activity (Rogers et al., 2013, Scheuermann et al., 2013, Wu et al., 2019). Compounds of this class reduced the size of tumours in HIF-2α-driven ccRCC mouse xenograft studies (Wallace et al., 2016, Cho et al., 2016, Chen et al., 2016, Xu et al., 2019) and two of them, PT2385 and PT2977, have been tested in Phase I&II clinical trials (Courtney et al., 2018, Papadopoulos et al., 2018, Strowd et al., 2019), followed by the approval of the first HIF-2α inhibitor, Belzutifan (PT2977), for clinical use in VHL disease patients with associated renal cell carcinoma, CNS hemangioblastomas or pancreatic neuroendocrine tumours not requiring immediate surgery (U.S. Food and Drug Administration, 2021).

Given a clear importance of HIF-2α in CB function and ventilatory control is emerging from the genetic studies discussed above, systemic treatment with pharmacological HIF-2α inhibitors has a potential to negatively affect HVR and might pose a risk to patients relying on hypoxic ventilatory drive. In this chapter, pharmacological HIF-2α antagonist: PT2385 will be used to test whether VAH and hypoxia-induced CB proliferation are dependent on pharmacological modulation of HIF-2α, in line with the genetic studies. This can both inform the use of HIF-2α inhibitors in the clinic, and provide an orthogonal approach to confirm that the HIF-2α, and not HIF-1α, isoform is important in CB function in ventilatory control.

2.2 **Results**

2.2.1 *PT2385 treatment prevents ventilatory acclimatisation to hypoxia in wild-type mice.*

To test the effects of pharmacological HIF-2α inhibition with PT2385 on ventilatory responses to hypoxia, 10 $mg \cdot kg^{-1}$ PT2385 was administered orally twice per day. This dose was chosen as it is sufficient to completely abolish tumour growth in mouse ccRCC xenograft studies (Wallace et al., 2016) and it is equivalent to the 800 mg b.i.d. recommended phase II dose in the clinical study (Courtney et al., 2018), for an average patient weight of 80 kg.

VAH was established by housing PT2385- and vehicle-treated mice in an altitude chamber with approximately 10% O_2 for 7 days ('chronic hypoxia', CH, as previously described in Bishop et al., 2013, Hodson et al., 2016), starting 24h after the first PT2385/vehicle treatment (Figure 2-1). Initial 24h treatment in unacclimatised mice was designed to allow for assessment of PT2385 effects on ventilation in unacclimatised mice, as discussed later. Baseline HVRs were established prior to the start of the experiment and VAH was measured by testing HVRs after 2, 5 and 7 days of CH (Figure 2-1), with 2 days being the first time-point at which enhanced HVR (i.e. VAH) can be observed (Bishop et al., 2013).

HVR can be monitored in mice using whole-body plethysmography, which measures pressure changes within a sealed chamber as air entering the lungs is warmed and humidified (see section 1.1, Lim et al., 2014). Acute exposure to 10% O_2, equivalent to approximately 5500 m above sea level, around the same altitude as the highest human settlement in La Rinconada, Peru (Pillman, 2018, Enserink, 2019), results in a poorly sustained increase in MVb, owing to the HVR suppression by hyperventilation-induced hypocapnia (see section 1.1). In this Thesis, the primary hypoxic test gas was therefore

10% O_2/3% CO_2. Nevertheless, responses to 10% O_2 alone were also measured, and 3% CO_2 stimulus was used to assess possible effects of PT2385 on the hypercapnic response.

MVb under 5 min challenges with each of the test gases was measured in the mornings, prior to the first daily PT2385 treatment, before the start of the experiment (Baseline) and after 2, 5 and 7 days of CH. To quantify the effects of each challenge, hypoxic and hypercapnic AVRs were calculated as the difference between the MVb during the first minute of stable gas challenge and the last minute at room air (Bishop et al., 2013, Hodson et al., 2016).

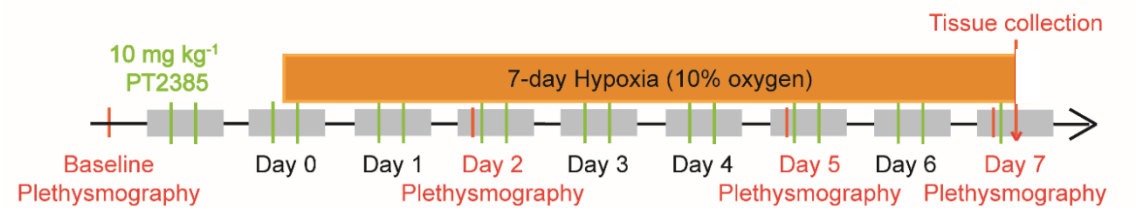


Figure 2-1. Experimental design.
Wild-type mice were treated with 10 mg·kg^{-1} PT2385 (or vehicle) b.i.d., as indicated by the green marks. After the first 3 treatments, mice were placed in the normobaric altitude chamber with oxygen levels gradually reduced to 10% over the first 20h. Mice then remained in the chamber for 7 days, during which twice-daily treatments with PT2385 continued. HVR was measured before the start of the experiment (Baseline) and after 2, 5 and 7 days of hypoxic exposure, as indicated by the red marks. After Day 7 plethysmography, mice received the final PT2385 treatment and were returned to the hypoxic chamber for another hour, after which the experiment was terminated and tissues collected.

Mice tolerated PT2385 treatment well, with no apparent discrepancy in the body weight loss induced by hypoxic exposure between vehicle- and PT2385-treated animals (data not shown). In line with anaemia reported in PT2385-treated patients at sea level (Courtney et al., 2018), there was a significant reduction in haematocrits of unacclimatised mice treated with 10 mg·kg^{-1}, compared with their vehicle-treated

littermates (Figure 2-2). CH exposure, however, caused increased haematocrits (% of blood volume occupied by red blood cells) in both vehicle- and PT2385 treated mice (Figure 2-2), suggesting pharmacological HIF-2α inhibition is not sufficient to prevent hypoxia-induced polycythaemia. This is in contrast to the reduced *Epo* mRNA and serum levels in mice treated with PT2399, a similar HIF-2α inhibitor (Feng et al., 2018) and could suggest EPO-independent stimulation of erythropoiesis drives polycythaemia in PT2385-treated mice.

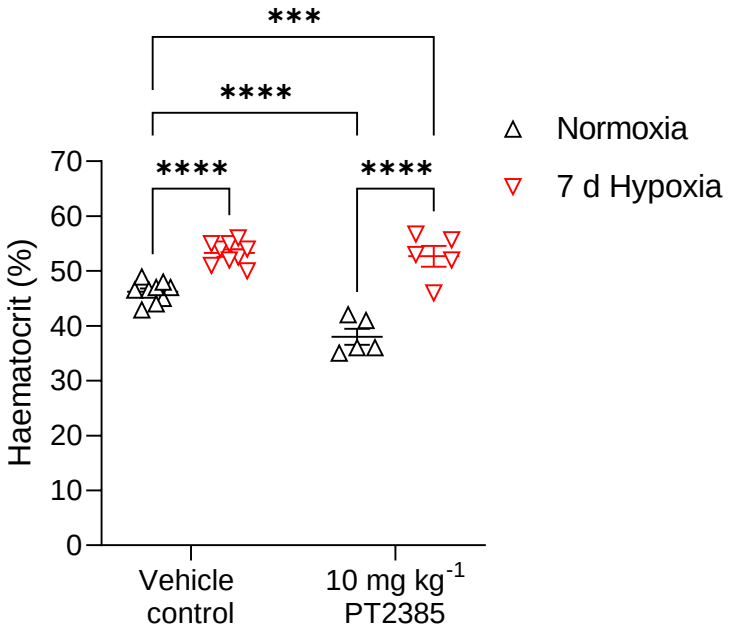


Figure 2-2. PT2385 treatment causes anaemia in normoxic mice, but does not prevent CH-induced polycythaemia.[1]

Haematocrits of mice treated with 10 mg·kg^{-1} PT2385 or equivalent volume of vehicle for 7 days, with concurrent exposure to 10% O_2 in the 7d Hypoxia cohort. Data were analysed by two-way ANOVA, followed by Holm-Sidak's multiple comparisons tests, ***$P < 0.001$, ****$P < 0.0001$.

Mice treated with vehicle developed VAH as expected (Bishop et al., 2013), with enhanced 10% O_2/3% CO_2 AVR after 2d H, which further increased after 5-7-day H

[1] Data as published in Cheng et al., 2020.

(Figure 2-3, Table 2-1). Enhanced HVRs in acclimatised mice were also observed with respect to responses to 10% O_2 alone (Table 2-1). There was no significant change in 3% CO_2 AVRs over time (Table 2-1), suggesting that VAH is specific to the hypoxic response.

In contrast to the vehicle-treated mice, almost no VAH was observed in animals receiving 10 mg·kg^{-1} PT2385 (Figure 2-3, Table 2-1). PT2385-treated mice had overall significantly lower AVRs to 10% O_2/3% CO_2 than the vehicle-treated group (Table 2-1, ANOVA $P < 0.001$), and individual comparisons at specific time-points revealed a significantly reduced AVR to 10% O_2/3% CO_2 in mice treated with 10 mg·kg^{-1} PT2385 compared to the vehicle-treated group after 5 and 7-day CH (Figure 2-3). This ablation of VAH was also observed with respect to the 10% O_2 AVRs, which were significantly lower in PT2385-treated mice compared to vehicle controls, similar to the Baseline values (Table 2-1). A small, borderline-significant difference in 3% CO_2 AVRs was observed between vehicle- and PT2385-treated cohort, but there was no significant effect at any one time-point throughout CH (Table 2-1).

Overall, HIF-2α inhibition with PT2385, at doses effective in reducing tumour growth, prevents VAH by reducing hypoxic, but not hypercapnic AVRs, in a similar manner to genetic HIF-2α inactivation (Hodson et al., 2016).

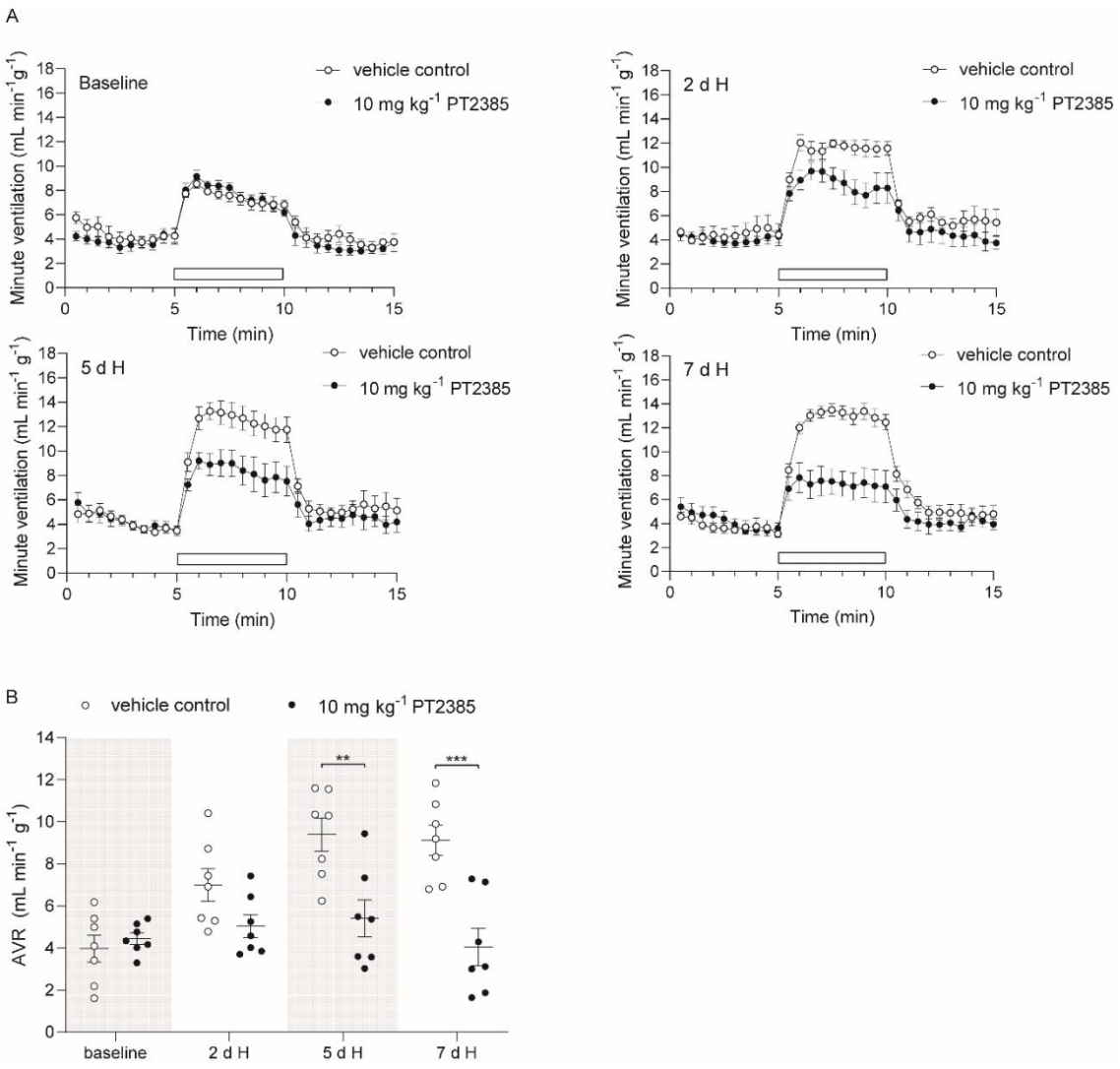


Figure 2-3. PT2385 ablates VAH in wild-type mice.[2]

(**A**) Graphs show MVb in response to 5 min challenge with 10% O_2/ 3% CO_2 (open bars) before (Baseline) and after the indicated exposure to 7-day hypoxia (H, 10% O_2). Mice were treated with 10 mg·kg^{-1} PT2385 (or vehicle) b.i.d., beginning 24h before 7d exposure to hypoxia and continuing throughout (to a total of 8d treatment)($n = 7$). (**B**) Graph shows 10% O_2/3% CO_2 AVRs quantified from the MVb in (A). Data were analysed by two-way repeated measures ANOVA with Baseline recordings removed from statistical analyses (*P* values in Table 1), followed by Holm-Sidak's multiple comparisons tests for individual time-point comparisons, with significance reported in the graph, $^{**}P < 0.01$, $^{***}P < 0.001$. For details of ANOVA analysis, see Table 2-1.

[2] Data as published in Cheng et al., 2020, generated together with Dr Xiaotong Cheng.

Table 2-1. PT2385 effects on hypoxic and hypercapnic AVRs in acclimatised mice.
AVRs of wild-type mice before (Baseline) and following treatment with b.i.d. 10 mg·kg^{-1} PT2385 (or vehicle), beginning 24h before 7d hypoxia (H, 10% O_2) and continuing throughout (to a total of 8d treatment). Data from each hypoxic/hypercapnic challenge are analysed by two-way repeated measures ANOVA (right hand column *P* value = time factor; bottom row *P* value = drug factor; right column, bottom row *P* value = time/ drug interaction factor); followed by Holm-Sidak's multiple comparisons *t*-tests; Baseline (prior to PT2385 treatment) recordings are excluded from ANOVA analysis and compared with an unpaired *t*-test; $n = 6$. $P < 0.05$ comparisons are highlighted in bold.

		vehicle		10 mg·kg^{-1} PT2385			
	Time-point	Mean	SEM	Mean	SEM	*t*-test *P* value	Time/ Interaction *P* value
10% O_2/3% CO_2	Baseline	4.8	0.9	4.3	0.7	*0.645*	
	2d H	8.6	0.9	2.7	0.3	***<0.0001***	
	5d H	9.4	1.0	2.4	0.4	***<0.0001***	*0.757*
	7d H	9.1	1.0	2.0	0.6	***<0.0001***	
	PT2385 *P* value		***<0.0001***				*0.366*
10% O_2	Baseline	0.8	0.6	-0.1	0.6	*0.313*	
	2d H	2.2	0.5	0.6	0.3	***0.016***	
	5d H	2.9	0.4	0.6	0.3	***0.002***	*0.458*
	7d H	3.3	0.7	0.2	0.4	***<0.0001***	
	PT2385 *P* value		***0.001***				*0.073*
3% CO_2	Baseline	3.6	0.5	4.5	0.6	*0.330*	
	2d H	3.3	0.5	1.9	0.4	*0.079*	
	5d H	2.2	0.4	2.2	0.2	*0.983*	*0.541*
	7d H	3.0	0.5	1.9	0.5	*0.124*	
	PT2385 *P* value		*0.054*				*0.200*

2.2.2 *PT2385 abolishes ventilatory acclimatisation to hypoxia established through sustained hypoxic exposure*

To further establish the role of the HIF-2α isoform in VAH, the next experiment tested if pharmacological HIF-2α inhibition could also ablate already established VAH. This

was achieved by exposing mice to 7-day hypoxia as before, and commencing the twice-daily oral 10 $mg \cdot kg^{-1}$ PT2385 treatment on the 7^{th} (rather than 1^{st}) day of hypoxic exposure, while mice continued to reside in hypoxia. To establish the time-course for PT2385 effects on HVR, MVb under the hypoxic and hypercapnic stimuli was measured prior to the start of hypoxic pre-conditioning (Baseline) and 1, 5 and 24h after the first PT2385 treatment. As the effects of PT2385 treatment were only analysed once the VAH was established, no changes to MVb of vehicle-treated mice with time were expected. Therefore, rather than by two-way ANOVA, AVRs were analysed using multiple *t*-tests with Holm-Sidak's correction to adjust for multiple comparisons (Table 2-2). Vehicle-treated mice had a marked increase in the 10% O_2/3% CO_2 AVR after 7-day exposure to hypoxia (Figure 2-4B, Table 2-2, compare vehicle-treated mice at 1, 5 and 24h with Baseline), confirming successful establishment and maintenance of VAH. Treatment with 10 $mg \cdot kg^{-1}$ PT2385 resulted in a less sustained ventilatory response to 10% O_2/3% CO_2 within 5h after the first dose (Figure 2-4A), although with similar AVR to vehicle-treated mice (Figure 2-4B, Table 2-2). Enhanced 10% O_2/3% CO_2 AVR was completely reversed to baseline (prior to acclimatisation) levels 24h after the first PT2385 dose (Figure 2-4, Table 2-2). A marked reduction in 10% O_2 AVRs was also observed in one of the PT2385-treated mice, but overall, there was no significant effect of PT2385 treatment on this response (Figure 2-4B, Table 2-2). As the 10% O_2 AVRs are much smaller and unstable than under 10% O_2/3% CO_2, PT2385 effects on this response may be more difficult to measure. As before, no changes to 3% CO_2 AVRs were observed with PT2385 treatment (Figure 2-4B, Table 2-2), suggesting that the effects of HIF-2α inhibition are specific to the hypoxic AVR. Thus, in addition to preventing VAH establishment, pharmacological HIF-2α inhibition can also reverse an already established enhanced ventilatory response in acclimatised mice.

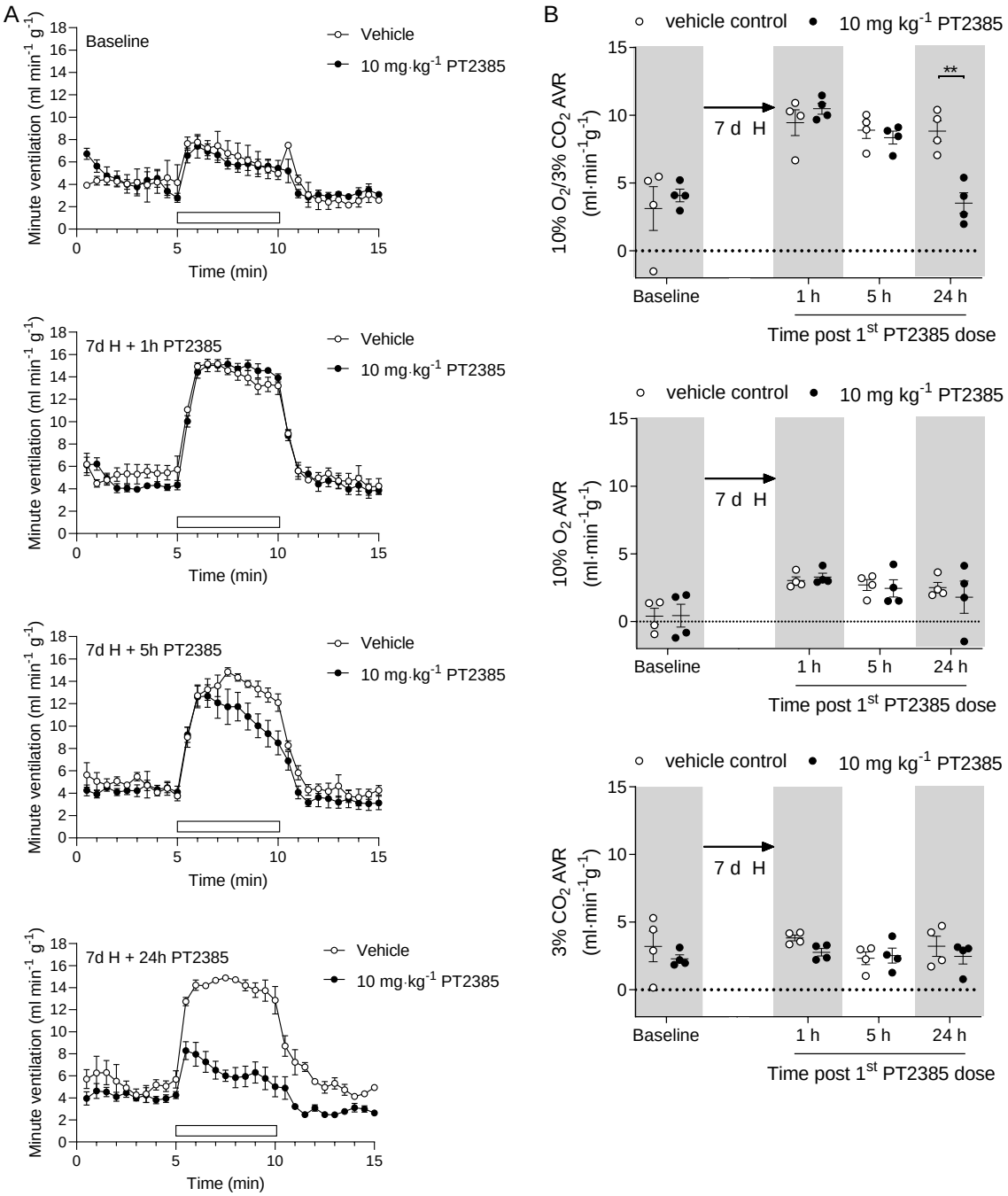


Figure 2-4. PT2385 reverses VAH established in acclimatised mice.[3]

Wild-type mice were pre-exposed to 7d hypoxia (H, 10% O_2), then treated with 10 mg·kg^{-1} PT2385 (or vehicle) in continuing hypoxia ($n = 4$). (**A**) Graphs illustrate changes in MVb under 5 min challenges with 10% O_2/3% CO_2 (open bars) before (Baseline) and 1, 5 and 24h after the first treatment with 10 mg·kg^{-1} PT2385. (**B**) Summary of AVRs calculated from data shown in A (and from challenges with 10% O_2 and 3% CO_2, MVb data not shown). Data from **B** were

[3] As published in Cheng et al., 2020, experiments carried out by Dr Xiaotong Cheng.

analysed by Holm-Sidak's multiple comparisons two-tailed tests, with significance reported in the graphs, $**P < 0.01$.

Table 2-2. PT2385 abolishes VAH in wild-type acclimatised mice.

Hypoxic and hypercapnic AVRs in wild-type mice before (Baseline) and following 7-day CH and 1, 5 and 24h after the first dose of twice daily treatment with 10 mg·kg^{-1} PT2385 (or vehicle) (second dose of PT2385 followed immediately after the 5h recording). Data were analysed by Holm-Sidak's multiple comparisons *t*-tests within each genotype and gas exposure; $n = 4$. $P < 0.05$ comparisons are highlighted in bold.

		vehicle control		10 mgkg^{-1} PT2385		
	Time-point	Mean	SEM	Mean	SEM	*P* value
10% O_2/3% CO_2	Baseline	3.1	± 1.6	4.1	± 0.5	*0.753*
	1h	9.5	± 0.9	10.5	± 0.4	*0.738*
	5h	8.9	± 0.6	8.4	± 0.5	*0.753*
	24h	8.8	± 0.8	3.5	± 0.8	***0.010***
10% O_2	Baseline	0.4	± 0.6	0.4	± 0.8	*0.969*
	1h	3.0	± 0.3	3.3	± 0.3	*0.957*
	5h	2.7	± 0.4	2.5	± 0.6	*0.957*
	24h	2.5	± 0.4	1.8	± 1.2	*0.957*
3% CO_2	Baseline	3.2	± 1.1	2.3	± 0.3	*0.839*
	1h	3.8	± 0.2	2.8	± 0.3	*0.094*
	5h	2.3	± 0.5	2.5	± 0.6	*0.839*
	24h	3.2	± 0.7	2.5	± 0.6	*0.839*

2.2.3 *PT2385 abolishes enhanced ventilatory responses in pseudo-hypoxic mice with genetic PHD2 inactivation*

To further test if pharmacological HIF-2α inhibition could ablate the enhanced HVRs in *Phd2*$^{+/-}$ mice (which mimic VAH in having exaggerated HVR without hypoxic acclimatisation, see section 1.4), *Phd2*$^{+/-}$ mice housed in normoxia were treated with 10 mg·kg^{-1} PT2385 for 7 days, as in the VAH abolishment experiment (Figure 2-1), and HVRs were tested before (Baseline) and after 2 and 7 days from the start of PT2385 treatment (Figure 2-5).

As previously described (Bishop et al., 2013), *Phd2*$^{+/-}$ mice had enhanced 10% O_2/3% CO_2 (Figure 2-4) and 10% O_2 AVRs (Figure 2-5, Table 2-3) compared to their wild-type littermates. Treatment with 10 mg·kg^{-1} PT2385 reduced the enhanced 10% O_2/3% CO_2 AVR in *Phd2*$^{+/-}$ to the level seen in vehicle-treated wild-type mice (Table 2-3, Figure 2-5), although this only reached significance after 7 days of treatment (Table 2-3, Figure 2-5) – a markedly longer treatment period than the 24h required to abolish VAH established by chronic hypoxic exposure (Figure 2-4). No significant changes to 10% O_2 or 3% CO_2 AVRs were observed with PT2385 treatment in either wild-type or *Phd2*$^{+/-}$ cohorts (Figure 2-5B, Table 2-3), the latter suggesting that reduction in 10% O_2/3% CO_2 AVR in PT2385-treated mice is specific to the hypoxic response. Together, these results show that, as well as abolishing environmentally-established VAH, pharmacological HIF-2α inhibition with PT2385 reverses enhanced HVRs in mice with genetically induced pseudohypoxia, albeit with a longer time-course.

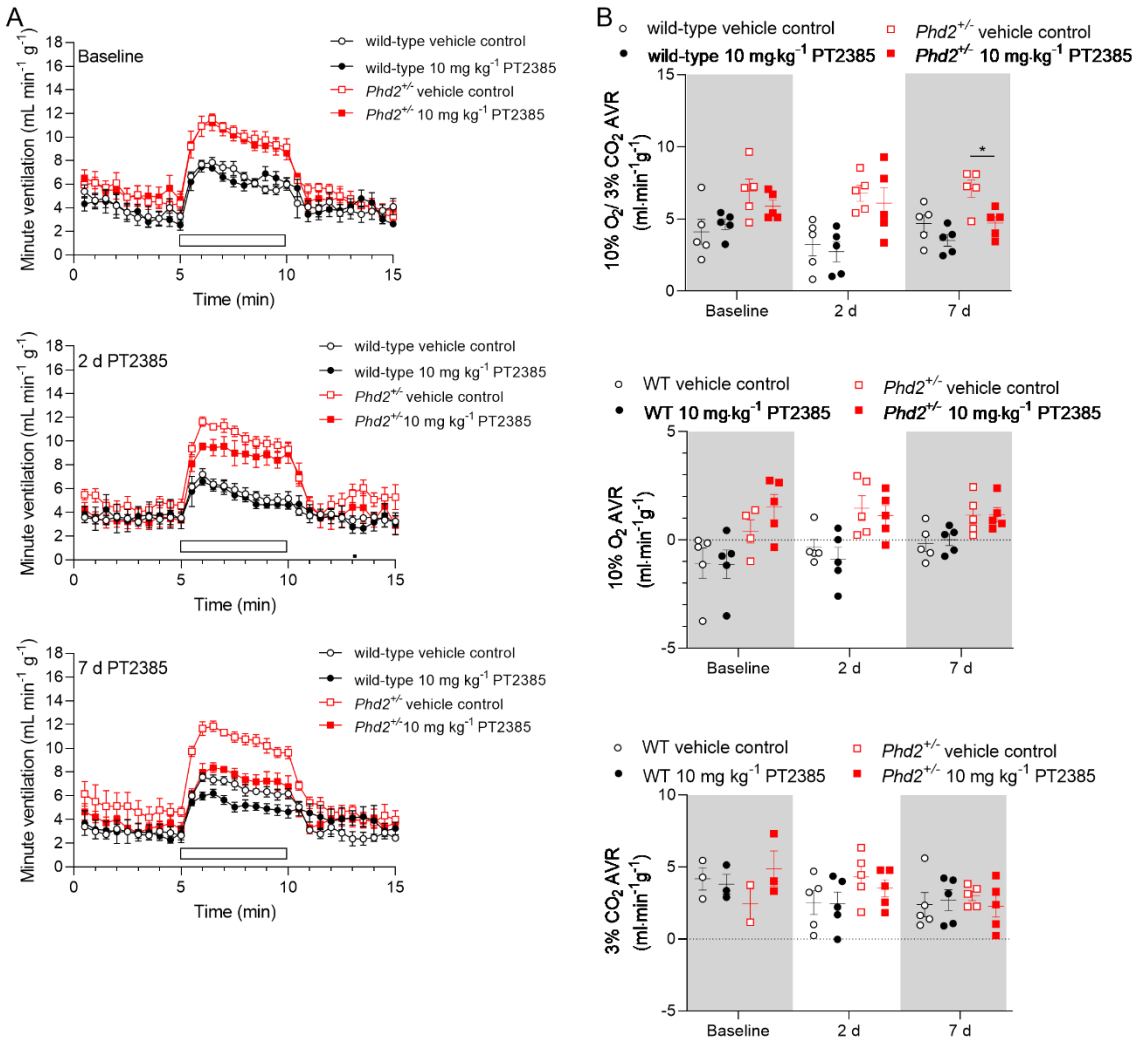


Figure 2-5. Pharmacological HIF-2α inhibition abolishes enhanced HVRs in pseudo-hypoxic mice with genetic PHD2 inactivation.

(**A**) Changes in MVb under 5 min challenge with 10% O_2/3% CO_2 (open bars) before (Baseline) and after 2 and 7 days of b.i.d. treatment with 10 mg·kg^{-1} PT2385 (or vehicle). (**B**) AVRs calculated from data shown in A (and for challenges with 10% O_2 and 3% CO_2 - MVb data not shown). Data were compared between treatment groups within each genotype and at each time-point by Holm-Sidak's multiple comparisons tests, with significance reported in the graphs, $*P < 0.05$.

Table 2-3. Acute ventilatory responses in *Phd2*$^{+/-}$ mice treated with PT2385.
Hypoxic and hypercapnic AVRs in *Phd2*$^{+/-}$ mice and wild-type littermates before (Baseline) and following 2 and 7-day b.i.d. treatment with 10 mg·kg^{-1} PT2385 (or vehicle). Data were analysed by Holm-Sidak's multiple comparisons *t*-tests (for subsequent time-points), within each genotype and gas challenge group; $n = 3$ for 3% CO_2 exposures at Baseline; $n = 5$ for all other groups. $P < 0.05$ comparisons are highlighted in bold.

		wild-type					*Phd2*$^{+/-}$				
		vehicle control		10 mg·kg^{-1} PT2385		*t*-test	vehicle control		10 mg·kg^{-1} PT2385		*t*-test
	Time-point	Mean	SEM	Mean	SEM	*P* value	Mean	SEM	Mean	SEM	*P* value
10% O_2/ 3%CO_2	Baseline	4.12	0.86	4.64	0.38	*0.836*	6.95	0.82	5.89	0.42	*0.486*
	2 d H	3.23	0.77	2.74	0.70	*0.836*	6.80	0.57	6.10	1.07	*0.582*
	7 d H	4.69	0.59	3.52	0.41	*0.375*	7.10	0.60	4.72	0.44	***0.037***
10% O_2	Baseline	-1.07	0.70	-1.12	0.65	*0.959*	0.40	0.54	1.52	0.59	*0.512*
	2 d H	-0.34	0.36	-0.89	0.55	*0.812*	1.47	0.57	1.13	0.46	*0.880*
	7 d H	-0.16	0.36	0.01	0.27	*0.915*	1.15	0.40	1.17	0.33	*0.975*
3%CO_2	Baseline	4.18	0.77	3.81	0.68	*0.982*	2.45	1.29	4.89	1.23	*0.628*
	2 d H	2.54	0.83	2.45	0.80	*0.982*	4.32	0.76	3.53	0.59	*0.646*
	7 d H	2.39	0.84	2.70	0.72	*0.982*	2.99	0.32	2.28	0.75	*0.646*

2.2.4 *HIF-2α inhibition with PT2385 rapidly reduces acute ventilatory responses to hypoxia in unacclimatised mice*

Within the *Phd2*$^{+/-}$ PT2385 treatment experiment, there was a trend towards reduced 10% O_2/3% CO_2 AVRs in unacclimatised PT2385-treated wild-type mice (Figure 2-5), suggesting a possible role for HIF-2α in acute oxygen sensing in the CB. HIF-2α function in HVR in unacclimatised mice has previously been suggested by studies using mice with genetic HIF-2α inactivation, performed both by the Oxford laboratory (Hodson et al., 2016) and more recently by Moreno-Dominguez et al., 2019, with the latter study showing complete ablation of 10% O_2 AVR in mice heterozygous for HIF-2α and with conditional inactivation of the second HIF-2α allele in adulthood.

To further investigate the effects of pharmacological HIF-2α inactivation on acute HVR in wild-type mice, HVRs were analysed 1, 5 and 24h after the start of PT2385 treatment in unacclimatised animals. The 1h time-point was chosen to account for the slow absorption of the compound via the oral route and to accommodate the 30 min acclimatisation of mice to the plethysmograph. The 5h time-point has been chosen as the half-life of the compound after oral administration of 10 mg·kg^{-1} PT2385 in mice has been reported at ~4h (Wallace et al., 2016). Since the acute responses to hypoxia are generally small and easily influenced by behavioural changes during the recording, average MVb during the stimulus was used as the quantification method, rather than AVR, which only measures the initial increase in MVb during the first minute of hypoxia (Figure 2-6B)(Cheng et al., 2020).

Treatment with 10 mg·kg^{-1} PT2385 significantly reduced average MVb under 10% O_2/3% CO_2 compared with vehicle-treated mice within 1h after the first dose (Figure 2-6, 8.72 ± 0.32 *vs* 7.17 ± 0.51 ml·min^{-1}g^{-1} in PT2385- *vs* vehicle-treated mice, adjusted $P = 0.037$). This reduction was sustained 5h after the start of treatment, and was even greater 24h after the first dose, following two PT2385 doses (Figure 2-6).

As described before, the 10% O_2 AVR was small and poorly sustained, and the average MVb during the stimulus was not elevated above resting ventilation (at 21% O_2)(Figure 2-6B). Nevertheless, treatment with 10 mg·kg^{-1} PT2385 significantly reduced average MVb under 10% O_2 5h (3.56 ± 0.13 *vs* 4.04 ± 0.17 in PT2385- *vs* vehicle-treated mice, $P = 0.049$) and 24h after the start of treatment (3.88 ± 0.09 *vs* 4.51 ± 0.13 ml·min^{-1}g^{-1} in PT2385- *vs* vehicle-treated mice, $P = 0.008$, Figure 2-6B). No significant changes to MVb under 3% CO_2 were observed with PT2385 treatment (Figure 2-6B), demonstrating that PT2385 does not alter hypercapnic responses and that PT2385 effects on AVRs are specific to hypoxia.

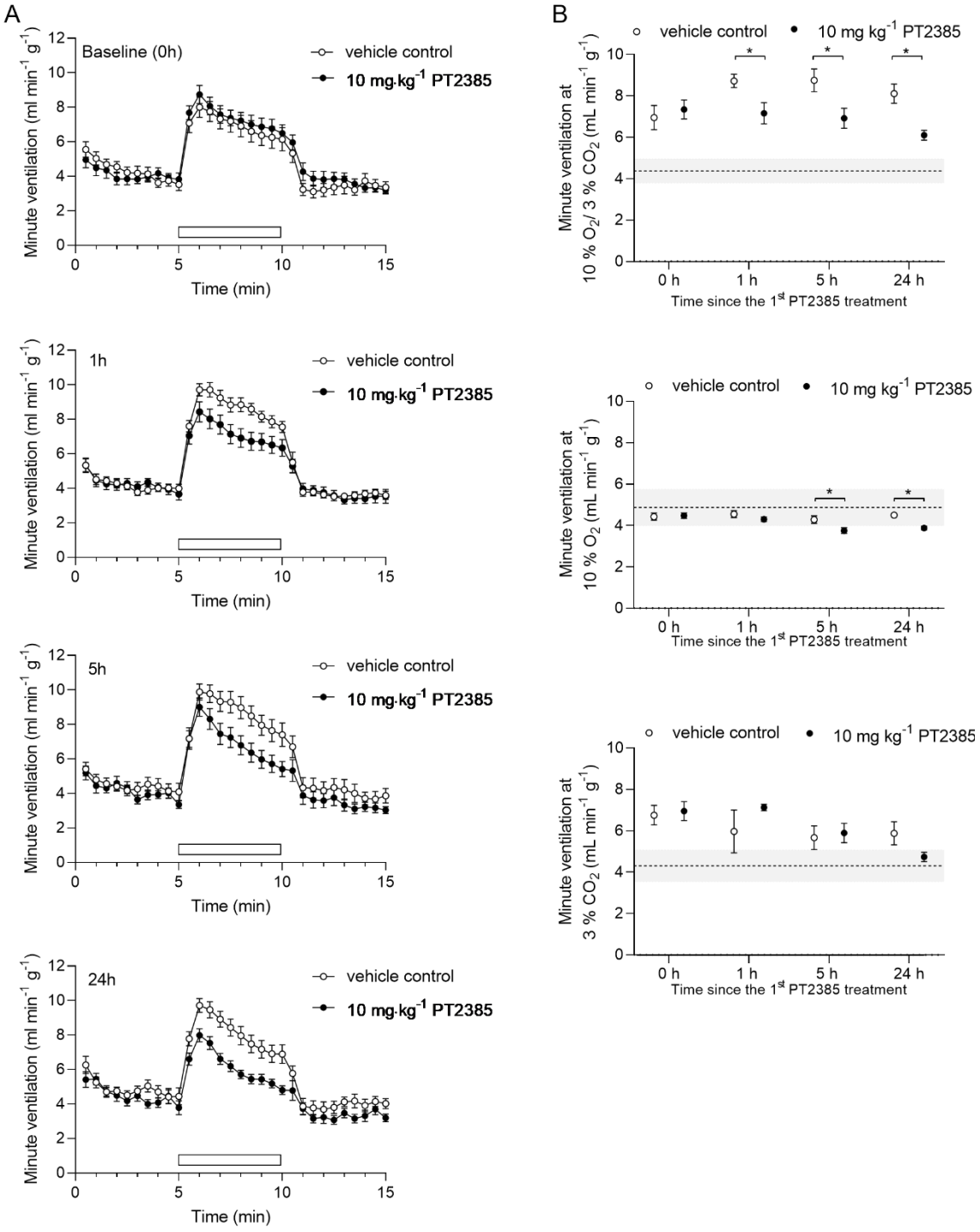


Figure 2-6. Rapid reduction in ventilatory sensitivity to hypoxia in unacclimatised PT2385-treated mice.[4]

(**A**) Changes in MVb in response to 5 min challenge with 10% O_2/3% CO_2 (open bars) before (Baseline, 0h) and 1, 5 and 24h after the first 10 mg·kg^{-1} PT2385 treatment. Second dose was administered immediately after the 5h plethysmography; $n = 15$. (**B**) Average MVb during 5

[4] Figure as published in Cheng et al., 2020. Data collected with Dr Xiaotong Cheng.

min challenges with 10% O_2/3% CO_2 (upper panel), 10% O_2 (middle panel) or 3% CO_2 (lower panel), quantified from recordings shown in A (MVb time-course not shown for 10% O_2 or 3% CO_2). Data were analysed by Holm-Sidak's multiple comparisons tests, with significance reported in the graphs, $*P < 0.05$. Dotted lines show resting MVb in air prior to the challenge, averaged across all time-points and treatment groups, ± SEM (shaded area).

These results showing rapid HVR reduction with pharmacological HIF-2α inhibition may point to a new role of HIF-2α in acute ventilatory control, in addition to its role in VAH.

MVb measurements combine data from both RR and TVb. As the RR measurements are variable with the changing mouse behaviour, analysis of just the changes in TVb could possibly better illustrate effect of HIF-2α inhibition on HVR. Thus, TVb and RR were analysed in unacclimatised mice treated with 10 $mg \cdot kg^{-1}$ PT2385, by averaging TVb or RR during the 5 min stimulus as for MVb above (Figure 2-7).

A clear reduction in the average TVb of PT2385-treated mice under 10% O_2/3% CO_2 was observed 1, 5 and 24h after the first PT2385 treatment, compared to the vehicle-treated group (Figure 2-7). Although some reduction in RR under 10% O_2/3% CO_2 was also observed in PT2385- compared to vehicle-treated mice, this was not statistically significant at any time-point (Figure 2-7). No significant decrease with PT2385 treatment was observed in TVb under 10% O_2 alone, but there was a significant reduction in RR under 10% O_2, 24h after the first 10 $mg \cdot kg^{-1}$ PT2385 dose (Figure 2-7).

In summary, treatment with PT2385, at a ccRCC tumour-reducing dose, results in reduced HVR, but not hypercapnic AVR, in a rapid (1h within start of treatment) manner, and mostly through the effects on TVb.

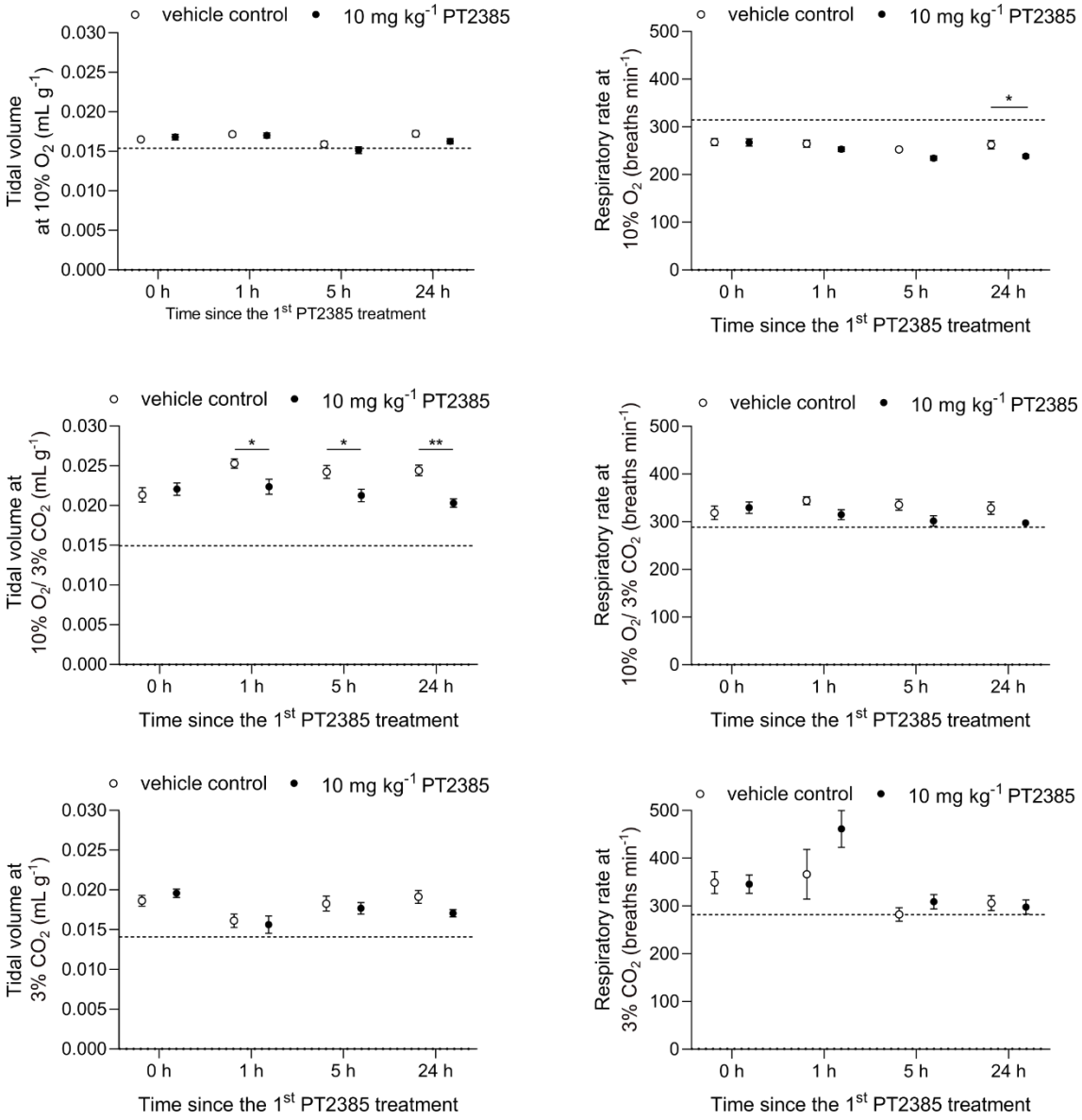


Figure 2-7. Changes in TVb and RR in unacclimatised PT2385-treated mice.[5]

Graphs show average TVb (left) and RR (right) during 5 min challenges with 10% O_2 (top), 10% O_2/ 3% CO_2 (middle) or 3% CO_2 (bottom). Measurements were made before (0 h) and 1, 5 and 24h after the first 10 mg·kg^{-1} PT2385 (or vehicle) dose ($n = 15$; $n = 3$ for 1h at 3% CO_2; $n = 11$ for 0h at 3% CO_2); second dose of PT2385 was given immediately after the 5h measurements. Data were analysed by Holm-Sidak's multiple comparisons tests, $*P < 0.05$, $**P < 0.01$. Dotted line shows resting TVb or RR in air prior to the challenge, averaged across all time-points and treatment groups, ± SEM (shaded area).

[5] As published in Cheng et al., 2020. Data collected with Dr Xiaotong Cheng.

2.2.5 *HIF-2α inhibition with PT2385 abolishes carotid body proliferation in response to hypoxia*

In addition to VAH, CH results in CB proliferation and hypertrophy, associated with increased vascularisation of the organ (Fielding et al., 2018, Pardal et al., 2007). Genetic interventions on the HIF system inactivating HIF-2α either ubiquitously or selectively in the CB type I cells, showed that this proliferative response is HIF-2α-dependent (Hodson et al., 2016, Fielding et al., 2018).

To test if pharmacological HIF-2α inhibition is associated with reduced CB proliferation (in addition to reduced VAH), BrdU incorporation was measured in CBs of mice treated with 10 $mg \cdot kg^{-1}$ PT2385 and exposed to 7-day hypoxia for VAH experiments above (Figure 2-1). BrdU is a modified nucleotide, supplemented in drinking water throughout the hypoxic exposure, which incorporates into the DNA during cell division, thus marking proliferating cells. $BrdU^+$ cell density has been previously established as a reliable measure of hypoxia-induced CB proliferation (Hodson et al., 2016, Fielding et al., 2018, Bishop et al., 2013).

$BrdU^+$ cell density was significantly higher in the CBs of acclimatised vehicle-treated mice, compared with animals residing in normoxia (Figure 2-8), as previously reported (Bishop et al., 2013). This BrdU incorporation was completely abolished in mice treated with 10 $mg \cdot kg^{-1}$ PT2385 (Figure 2-8), confirming the HIF-2α dependence of CB proliferation (Hodson et al., 2016).

To test if loss of CB proliferation in PT2385-treated mice was associated with the loss of CB hypertrophy, CB volume was measured in the CBs of the above mice, with tyrosine hydroxylase (TH) used as a marker of type I cells, as described before (Fielding et al., 2018). As with BrdU incorporation, CB volume also increased in hypoxic,

compared to normoxic mice (Figure 2-8). This mild CB hypertrophy was completely reversed by 10 mg·kg^{-1} PT2385 treatment, with CB volumes of PT2385-treated acclimatised mice similar to those of normoxic, vehicle-treated controls (Figure 2-8).

In summary, pharmacological HIF-2α inhibition with PT2385 results in the loss of CB proliferation and hypertrophy under chronic hypoxia.

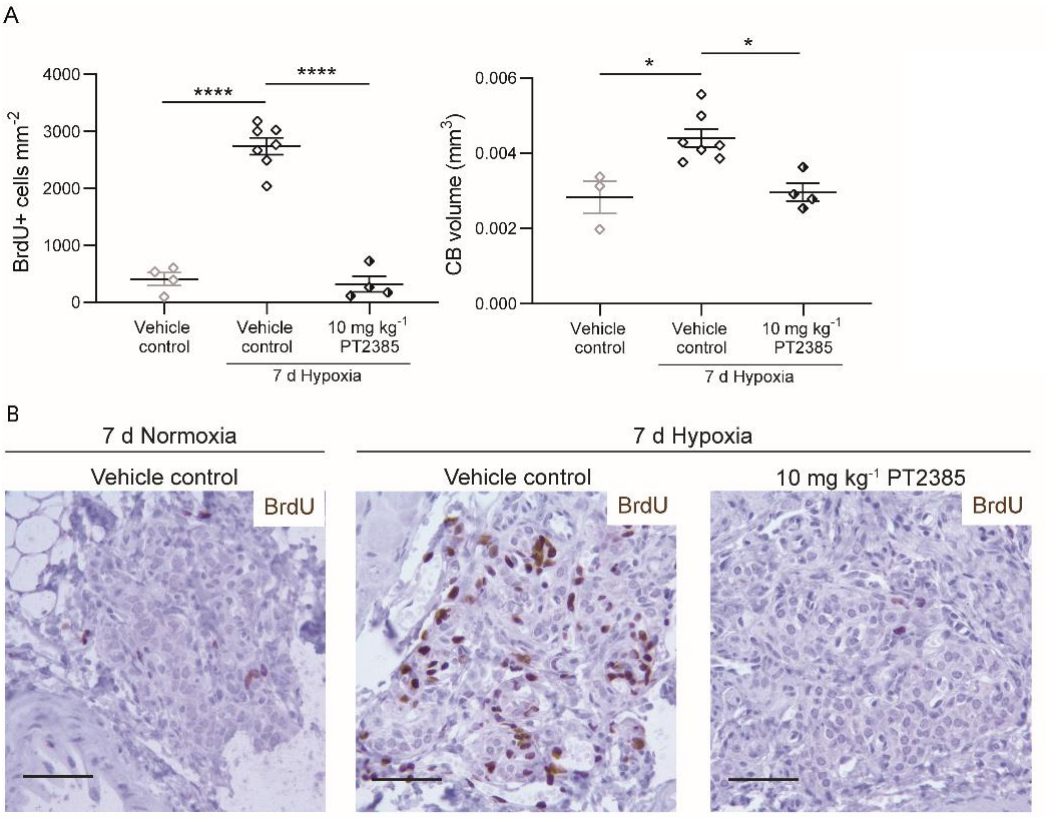


Figure 2-8. Effects of PT2385 on cellular responses to hypoxia in wild-type CBs.[6]
(**A**) Morphometry and (**B**) representative images of wild-type CBs from mice residing in normoxia or exposed to 7-day hypoxia (10% O_2) and treated with b.i.d. 10 mg·kg^{-1} PT2385 (or vehicle), starting one day before 7d exposure to hypoxia (10% O_2) and continuing throughout (to a total of 8d treatment). (**A**) Quantification of BrdU$^+$ cell density (left panel) and CB volumes (right panel). Data were analysed by one-way ANOVAs followed by Tukey's multiple comparisons tests, with significance reported in the graphs, $*P < 0.05$, $****P < 0.0001$. (**B**) BrdU IHC. Scale bars represent 50 μm.

[6] Data as published in Cheng et al., 2020, prepared jointly with Dr James W. Fielding.

2.3 **Discussion**

Experiments in this chapter show that treatment with PT2385, at a dose used to completely abolish ccRCC xenografts in mice, can both prevent and ablate VAH in mice. This is true for both VAH induced by environmental hypoxia, and for enhanced HVRs in *Phd2*$^{+/-}$ mice with genetic inactivation of a negative HIF regulator. In addition to the ablative effects of PT2385 on VAH, treatment with this compound also prevented hypoxia-induced CB proliferation. Last, PT2385 treatment reduced HVRs in unacclimatised mice, pointing to a novel role of HIF-2α in acute oxygen sensing in the CB. All of these results show that pharmacological HIF-2α inhibition mimics the effects of genetic HIF-2α inactivation on the CB function, corroborating the importance of this HIF isoform in the CB-mediated adaptive responses to hypoxia.

Using a method orthogonal to genetic manipulations, experiments presented in this Chapter resolve the discussion on the importance of different HIF isoforms in VAH, showing that HIF-2α is of crucial importance in ventilatory control and other CB functions in oxygen sensing. The importance of HIF-2α in VAH is in line with the results showing high expression of the *Epas1* gene, encoding HIF-2α, in the whole CB and in single-cell analysis of type I cells (Tian et al., 1998, Fielding et al., 2018, Zhou et al., 2016). *Epas1* is also highly up-regulated in the CB compared to other ganglia (Gao et al., 2017), suggesting its specific role in oxygen sensing, which is the primary function of the carotid chemoreceptor.

Although results showing PT2385 mimics the effects of ubiquitous (and TH^{+} cell restricted) genetic HIF-2α inactivation provide a convincing argument for a specific action of this compound on HIF-2α, it should be noted that systemic administration of the drug could still result in off-target effects on other proteins, potentially affecting the function of various physiological systems. Experimental confirmation that PT2385

effects on VAH and CB proliferation are on-target to the HIF-2α PAS-B domain pocket is therefore required to completely resolve the controversy on HIF-2α importance in CB function.

PT2385 ablated CB proliferation in mice exposed to 7-day hypoxia, supporting the results of previous studies inactivating HIF-2 using genetic models (Hodson et al., 2016, Fielding et al., 2018). This was associated with strong reduction in expression of the HIF-2 target gene, *Vegfa* (see Cheng et al., 2020), known to promote neovascularisation in the hypoxic CBs (Fielding et al., 2018), which suggests a possible causative effect of *Vegfa* expression on CB proliferation. This means pharmacological HIF-2α inhibition has a therapeutic potential in PPGLs (CB and AM tumours, see section 1.5), by blocking *Vegfa*, as well as other tumorigenic HIF-2 targets. This is in line with studies suggesting that tyrosine kinase inhibitors, e.g. Sunitinib, which block the VEGFA receptor, might be therapeutically useful in PPGLs (Cassol et al., 2014, Joshua et al., 2009). Indeed, a recent Phase II trial using Sunitinib in patients with recurring PCCs and PGLs showed stable disease in 70% patients in a group of 23 and a partial response in 3 patients (O'Kane et al., 2019). PT2385, which reduces HIF-2-driven *Vegfa* induction, may therefore also be useful in PPGL treatment. Indeed, Belzutifan, a second-generation HIF-2α inhibitor, is currently in clinical trials for the treatment of PPGLs.

Hypoxia-induced CB proliferation, which increases the number of O_2-sensing type I cells and endothelin-expressing vessels within the CB (Fielding et al., 2018), may be responsible for the increase in the O_2-sensitivity of the chemoreceptor leading to VAH, although this relationship is not linear as mice with *Phd2* inactivation in TH^+ cells, which develop large, paraganglioma-like CBs exceeding in size the CBs of mice exposed to hypoxia, only have a mild increase in HVR (Fielding et al., 2018). Similarly,

a small scale study on SDHD mutant CB paraganglioma patients found their HVRs to be within the normal range (Dahan et al., 2007). Indeed, although both CB proliferation and VAH require HIF-2α stabilisation in mice, they could still be driven by independent downstream processes. Experiments in this chapter showed that PT2385 completely reverses VAH within the first 24h of treatment, suggesting that acclimatisation is likely driven by expression of proteins involved in increased oxygen sensitivity or stimulating higher electrical activity of the CB type I cells, rather than structural or morphological changes of the organ. On the other hand, reversal of the enhanced HVRs in *Phd2*$^{+/-}$ mice to the levels observed in wild-type littermates required 7-day PT2385 exposure, suggesting that in the context of constitutive pseudohypoxia, the CB hyperplasia observed in these mice (Bishop et al., 2013) could be more important in driving enhanced HVR. Future studies could investigate this by analysing the time-course of changes in CB volume in acclimatised, and pseudo-hypoxic mice treated with HIF-2α inhibitors.

In addition to the role of HIF-2α in adaptive responses to sustained hypoxia, data in this chapter point to an additional role of HIF-2α in HVR of unacclimatised mice, i.e. in acute oxygen sensing. This was previously proposed by the work of the Oxford laboratory, showing reduced 10% O_2/3% CO_2 HVR in *Hif-2α*$^{f/f}$*;CreER* mice (Hodson et al., 2016) and in a recent report by the López-Barneo group, showing complete ablation of RR increase under 10% O_2 in *Hif-2α*$^{f/-}$*;CreER* mice (Moreno-Dominguez et al., 2019). In line with these studies, pharmacological HIF-2α inhibition with PT2385 significantly reduced 10% O_2/3% CO_2 AVR within 1h after the first treatment, although a complete ablation of this HVR could not be reached, even with 7-day b.i.d. exposure. A reduction in RR under 10% O_2 was seen 24h after the first PT2385 treatment, although average RR during 10% O_2 was below the resting ventilatory rate in

unacclimatised vehicle-treated mice. Thus, the effects of PT2385 on this response are difficult to compare with those reported by Moreno-Dominguez et al., 2019. The difference in the extent of HVR ablation with genetic HIF-2α inactivation observed by the two studies (Moreno-Dominguez et al., 2019, Hodson et al., 2016) has been proposed to be due to the different time of exposure to HIF-2α loss (Moreno-Dominguez et al., 2019). This would indicate the need for the loss of proteins encoded by HIF-2 target genes, with long half-lives, to successfully ablate HVR. However, classically, HIF-2α is rapidly degraded in the presence of oxygen and can only exert its transcriptional effects once stabilised under reduced P_{O2}. A simpler explanation would be that using a *Hif-2α$^{f/-}$;CreER* model results in a greater loss of HIF-2α than in *Hif-2α$^{f/f}$;RosaCreER* mice. This would be in line with the effect of PT2385 on HVR in unacclimatised mice being dose-dependent, as reported in Cheng et al., 2020, with no reduction to HVRs in unacclimatised mice observed under 3 mg·kg^{-1} PT2385 treatment. This hypothesis could be further investigated by testing HVR in mice exposed to higher doses of PT2385, or to the more efficacious second-generation compounds, which will be explored in Chapter 3. Nevertheless, results presented in this Chapter confirm the importance of HIF-2α on ventilatory control in unacclimatised mice. The rapidity of the effect of HIF-2α inhibition on HVR may also point to a novel mechanism of HIF-2α action, beyond the canonical transcription control. This hypothesis remains to be further investigated in subsequent chapters.

In conclusion, demonstrated effects of HIF-2α inhibition of VAH and CB proliferation under sustained hypoxia and in unacclimatised mice are of both biological and clinical importance. First, they confirm the importance of HIF-2α in the CB adaptive responses to hypoxia, resolving previous controversies on the significance of different HIF isoforms in these physiological functions, and shed a new light on additional roles of

HIF-2α in HVR. Second, they raise concerns about the use of pharmacological HIF-2α inhibitors in the clinic. At the doses required for therapeutic benefit in ccRCC, there is a clear inhibition of physiological HIF-2α functions in ventilatory control with PT2385, which may restrict its use in patients relying on hypoxic ventilatory drive. Indeed, clinical trials of PT2385 and PT2977 completed so far reported hypoxia as a relatively common side effect, although details of those cases were not discussed in detail (Courtney et al., 2018, Strowd et al., 2019). Further studies on the specificity of PT2385 effects on VAH to HIF-2α and on the mechanisms of HIF-2α involvement in acute ventilatory control are needed to resolve these concerns about the safe use of HIF-2α inhibitors.

3

Specificity of the effects of pharmacological HIF-2α inhibition with PT2385 on hypoxic ventilatory control and carotid body proliferation.

3.1 Introduction

In the previous chapter, an orthogonal method of pharmacological HIF-2α inhibition was used to corroborate the importance of HIF-2α in VAH. Treatment with HIF-2α inhibitor: PT2385 (which targets the ligand-binding pocket of HIF-2α PAS-B domain to allosterically weaken the HIF-2 transcriptional complex, Rogers et al., 2013), ablated both VAH and CB proliferation in mice exposed to 7-day hypoxia. These effects of HIF-2α inhibition are of high biological and clinical significance, as they provide a starting point to establish the downstream pathway of HIF-mediated oxygen sensing in the CB, as well as revealing a potential for side-effects in the use of Peloton compounds to treat HIF-2-driven cancers. It is therefore important to confirm the specificity of PT2385 actions on HIF-2α.

Traditionally, this would be achieved using an alternative enantiomer of the small molecule that could not bind within the same HIF-2α pocket but could still exert its effects elsewhere. In the absence of such a compound for PT2385, specificity can be best tested using mutant HIF-2α proteins with structural changes occluding the entry to the binding pocket.

Since Peloton compounds allosterically inhibit HIF-2α:ARNT dimerisation (Rogers et al., 2013, Wu et al., 2019, Scheuermann et al., 2009, Scheuermann et al., 2013), a mutant S304M HIF-2α protein has been designed as a negative control to test for specificity of the small molecules binding within the PAS-B domain pocket (Rogers et al., 2013). The substitution of methionine for serine introduces a long aliphatic chain in the PAS-B ligand-binding pocket, preventing the entry of Peloton small molecules, thus significantly reducing the *in vitro* binding affinity of this class of compounds to HIF-2α (Rogers et al., 2013).

An analogous HIF-2α mutation, S305M, has been introduced *in vivo* in *Epas1*$^{S305M/S305M}$ mice and demonstrated the specificity of PT2399 actions on hypoxia-inducible erythropoietin synthesis (Feng et al., 2018). To confirm the S305M mutation prevents weakening of HIF-2α:HIF-β dimers by PT2385, as well as PT2399, *in vitro* assessment of resistance of this mouse mutant S305M HIF-2α PAS-B domain to PT2385 was carried out by Prof Rastinejad at the University of Oxford (Cheng et al., 2020). This showed ~60-fold reduction in the S305M HIF-2α affinity for PT2385, compared to the wild-type mouse protein, but no changes to thermal stability of S305M compared to wild-type HIF-2α alone or in complex with HIF-β (Cheng et al., 2020). Together, these data suggest that the HIF-2α S305M mutation in the mouse should provide a good model to study PT2385 on-target specificity to HIF-2α, as the mutation prevents PT2385 binding to HIF-2α without affecting its structural integrity.

Work in this chapter aims to confirm the specificity of PT2385 effects on adaptive responses to long-term hypoxia to HIF-2α. This will be achieved by testing if *Epas1*$^{S305M/S305M}$ mice are resistant to PT2385 effects on VAH and CB proliferation following a 7-day exposure to 10% O_2.

3.2 **Results**

3.2.1 *Mice homozygous for the S305M mutant HIF-2α have normal expression levels of Hif-2α and HIF-2 target gene: Vegfa, in the CB*

To test if the effects of PT2385 on VAH are on-target to HIF-2α, *Epas1*$^{S305M/S305M}$ mice were treated with 10 mg·kg^{-1} PT2385 and exposed to 7-day hypoxia as per the wild-type mice in Chapter 2 (Figure 2-1). *Epas1* expression and CB morphology following sustained hypoxia were assessed in the mutant mice, since a change in either of these parameters would invalidate the usefulness of the mouse model for confirmation that the PT2385 effects on VAH and CB proliferation are on target to HIF-2α.

Staining against tyrosine hydroxylase (TH), a common marker of neuronal and neuron-like cells, including the CB type I cells, was used for this purpose (Wang and Bisgard, 2002, Macias et al., 2018, Fielding et al., 2018). As expected, high density of TH$^+$ cells was observed in the CBs of wild-type CH mice (Figure 3-1A). No marked differences between the density or appearance of the type I cells were observed in the CBs of *Epas1*$^{S305M/S305M}$ mice, compared to the wild-type littermates, suggesting normal development and morphology of this chemoreceptor in mice homozygous for the S305M HIF-2α (Figure 3-1A).

To further confirm that the S305M mutation does not affect *Hif-2α* expression *in vivo*, *Hif-2α* mRNA levels were measured in the CBs of hypoxic mutant mice by RT-qPCR and the *Hif-2α* distribution within the CB assessed by ISH (Figure 3-1B). This showed

no significant difference in the relative levels of total *HIF-2α* mRNA between wild-type and S305M animals (Student's two-tailed *t*-test $P = 0.990$)(Figure 3-1B). High *Hif-2α* expression was observed in both wild-type and *Epas1*$^{S305M/S305M}$ hypoxic CBs by ISH, with no changes in cellular distribution of gene expression between the two genotypes (Figure 3-1B).

To confirm that HIF-2α is transcriptionally functional in the *Epas1*$^{S305M/S305M}$ mice, expression of a HIF-2 target gene, *Vegfa*, was also assessed in the CBs of CH-exposed wild-type and mutant animals (Figure 3-1B). Quantification of *Vegfa* mRNA by RT-qPCR in CBs pooled from five animals per genotype in three separate experiments did not show a reduction in *Vegfa* expression in *Epas1*$^{S305M/S305M}$ mice compared to wild-type controls, despite high variability in the relative *Vegfa* mRNA levels in the S305M mutants, as noted for *Hif-2α* (Figure 3-1B). High *Vegfa* expression was also confirmed in both wild-type and S305M mutant CBs by ISH, in line with previous studies demonstrating hypoxic induction of this gene (Fielding et al., 2018).

Together, S305M mutation does not disrupt expression of HIF-2α or HIF-2 target gene *Vegfa*, in hypoxic CBs and mice homozygous for the S305M mutant develop normal CBs. Therefore, *Epas1*$^{S305M/S305M}$ mice can be used as a model to test PT2385 on-target efficacy with respect to the effects on CB-mediated responses to hypoxia.

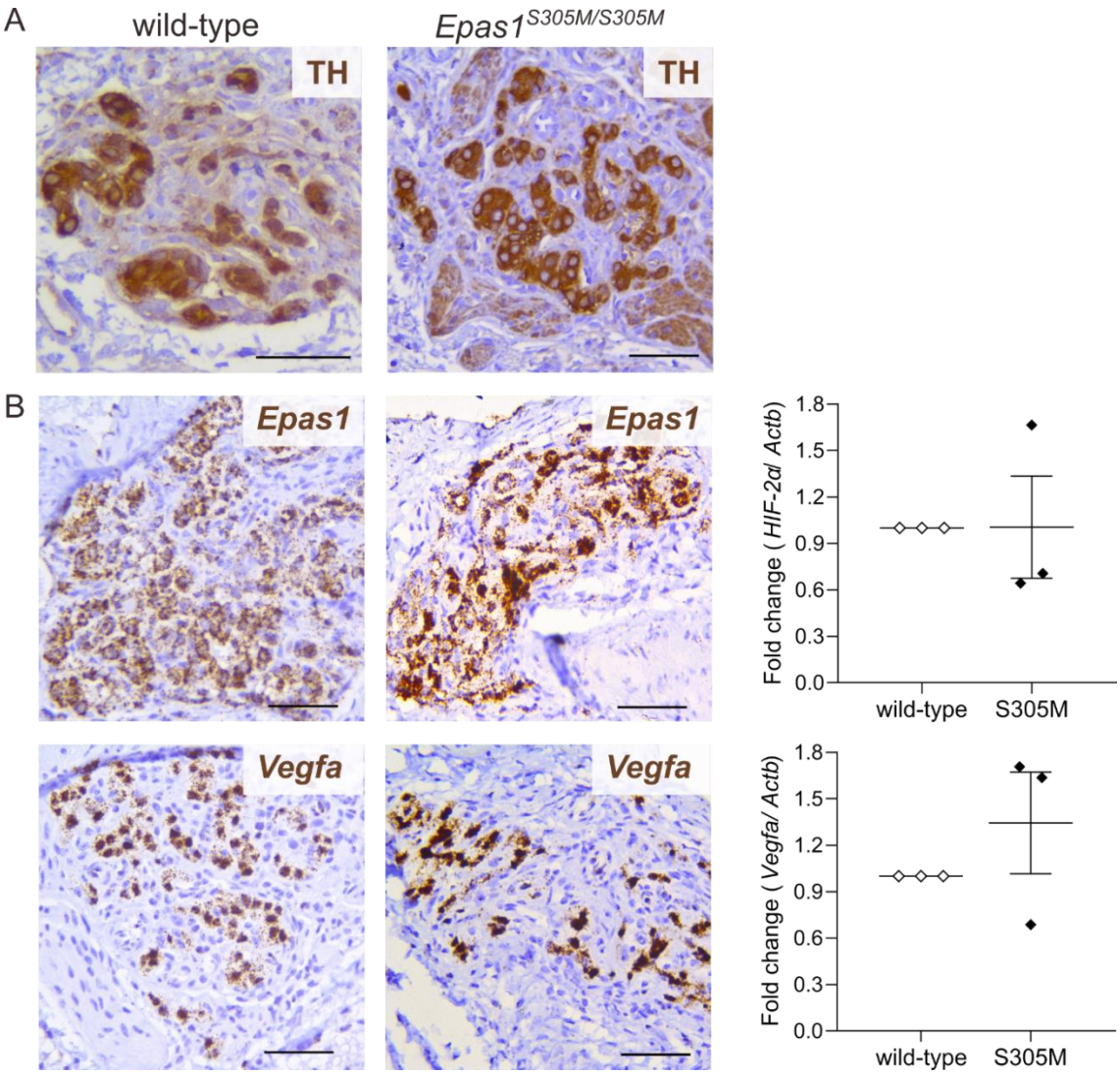


Figure 3-1. Validation of CB morphology and gene expression in hypoxic *Epas1*$^{S305M/S305M}$ mice.

(**A**) TH IHC, marking CB type I cells in wild-type and *Epas1*$^{S305M/S305M}$ mice exposed to 7-day 10% O_2. (**B**) Expression of *Epas1* and *Vegfa* mRNA in the CBs (as in A), assessed by ISH (left) and RT-qPCR (right). Values are the mean fold change of *Epas1* or *Vegfa* mRNA relative to *Actb* mRNA, normalised to wild-type CB expression, from three experiments on CBs pooled from five animals per genotype in each; data analysed by a two-tailed *t*-test, $P > 0.05$. Scale bars show 0.05 mm.

3.2.2 *HIF-2α S305M mutation prevents PT2385 effects on ventilatory acclimatisation to hypoxia*

To assess whether PT2385 effects on VAH are on target to HIF-2α, MVb under 10% O_2, 10% O_2/3% CO_2, and 3% CO_2, was measured before the start of CH (Baseline) and

after 2, 5 and 7 days of hypoxia in 10 mg·kg^{-1} PT2385- or vehicle-treated S305M mice and compared to that of wild-type littermates (Figure 3-2A). In contrast to the wild-type mice, no reduction in MVb during the hypoxic stimulus was observed in *Epas1*$^{S305M/S305M}$ mice treated with 10 mg·kg^{-1} PT2385 at any time-point, suggesting that the S305M mutation provides resistance to the PT2385 effects on VAH (PT2385 effect 2-way ANOVA $P = 0.700$, compared with $P < 0.001$ for wild-type littermates, Table 3-1 and Figure 3-2). Instead, a trend towards increased 10% O_2/3% CO_2 AVRs was observed in some of the PT2385-treated *Epas1*$^{S305M/S305M}$ mice compared to vehicle-treated controls (Figure 3-2, Table 3-1). Similarly, no significant changes to 10% O_2 or 3% CO_2 AVRs with PT2385 treatment were detected in S305M mutant mice (Table 3-1). Therefore, mice homozygous for the S305M allele are resistant to the effects of PT2385 on VAH, suggesting that the effects of the molecule on ventilatory control are on-target to HIF-2α.

Although *Epas1*$^{S305M/S305M}$ mice acclimatised to hypoxia in a similar manner as their wild-type littermates at 2d H (Figure 3-2), direct comparison of vehicle-treated wild-type and *Epas1*$^{S305M/S305M}$ MVb at 10% O_2/3% CO_2 showed a significant reduction in the AVRs of *Epas1*$^{S305M/S305M}$ mice compared to their wild-type littermates after 7, but not 2-day Hypoxia (Figure 3-3). There was also a trend towards reduced 10% O_2 AVRs in *Epas1*$^{S305M/S305M}$ mice compared to wild-type littermates at 7d H, but this did not reach statistical significance (Table 3-1, Student's two-tailed *t*-test $P = 0.094$). No significant difference between 3% CO_2 AVRs in *Epas1*$^{S305M/S305M}$ *vs* wild-type mice was observed (Table 3-1, Student's two-tailed *t*-test $P = 0.815$). Interestingly, a small trend towards reduced 10% O_2/3% CO_2 AVRs in unacclimatised (Baseline) *Epas1*$^{S305M/S305M}$ mice compared with wild-type littermates was also observed (Figure 3-3, 3.74 ± 0.27 *vs* 4.21 ± 0.34 ml·min^{-1}g^{-1}, Student's two-tailed *t*-test $P = 0.273$). Overall, this suggests

that mice homozygous for the S305M allele have a hypomorphic ventilatory phenotype in hypoxia.

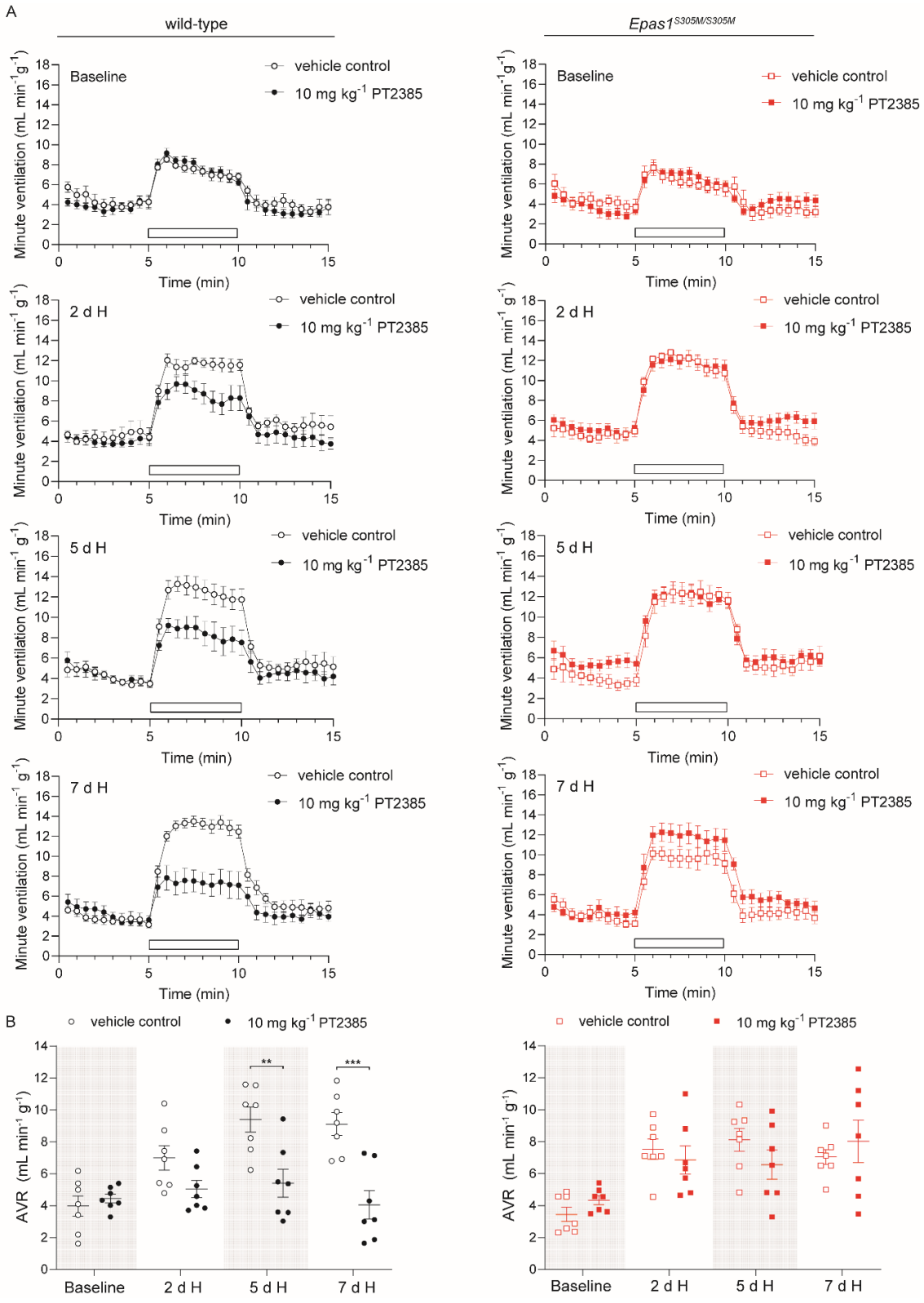


Figure 3-2. *Epas1*$^{S305M/S305M}$ mice are resistant to PT2385 effects on VAH.[7]

Comparison of VAH in wild-type and *Epas1*$^{S305M/S305M}$ mice treated with 10 mg·kg^{-1} PT2385 (or vehicle) b.i.d., beginning 24h before the start of 7d Hypoxia (10% oxygen, H) and continuing

[7] As published in Cheng et al., 2020.

throughout (to a total of 8d treatment)($n = 7$). (**A**) Graphs show MVb during 5 min challenges with 10% O_2/3% CO_2 (open bars) before (Baseline) and after the indicated exposure to hypoxia. (**B**) 10% O_2/3% CO_2 AVRs quantified from the MVb data in A. Data from each genotype were analysed by a two-way repeated measures ANOVA with Baseline recordings removed from statistical analyses (*P* values in Table 2), followed by Holm-Sidak's multiple comparisons tests for individual time-point comparisons, with significance reported in the graphs, $^{**}P < 0.01$, $^{***}P < 0.001$. Data from wild-type mice are reprinted from Figure 2-3 for comparison.

Table 3-1. Effects of PT2385 on VAH in wild-type and *Epas1*$^{S305M/S305M}$ mice.[8]

AVRs of wild-type and *Epas1*$^{S305M/S305M}$ mice before (Baseline) and following twice daily treatment with 10 mg·kg^{-1} PT2385 (or vehicle), beginning 24h before 7d hypoxia (H, 10% oxygen) and continuing throughout (to a total of 8d treatment). Two-way repeated measures ANOVAs within each genotype group (right hand column *P* = time factor; bottom row *P* = drug factor; right column, bottom row *P* = time/ drug interaction factor), with the Baseline (prior to PT2385) recordings excluded from statistical analysis; $n = 7$ for each drug/ genotype group. $P < 0.05$ comparisons are highlighted in bold.

		wild-type					*Epas1* $^{S305M/S305M}$				
		Vehicle control		10 mg·kg^{-1} PT2385		Time/ Interaction	Vehicle control		10 mg·kg^{-1} PT2385		Time/ Interaction
	Time-point	Mean	SEM	Mean	SEM	*P* value	Mean	SEM	Mean	SEM	*P* value
10% O_2/3% CO_2	Baseline	4.0	± 0.6	4.4	± 0.3		3.5	± 0.4	4.0	± 0.3	
	2 d H	7.0	± 0.8	5.0	± 0.5		7.5	± 0.6	6.9	± 0.9	
	5 d H	9.4	± 0.8	5.4	± 0.9	*0.144*	8.1	± 0.7	6.6	± 0.9	*0.821*
	7 d H	9.1	± 0.7	4.1	± 0.9		7.0	± 0.5	8.0	± 1.3	
	PT2385 P value	***<0.001***				*0.087*	*0.700*				*0.080*
10% O_2	Baseline	0.1	± 0.5	-0.6	± 0.4		-1.2	± 0.7	-0.3	± 0.4	
	2 d H	2.4	± 0.3	1.1	± 0.5		1.5	± 0.6	1.0	± 0.6	
	5 d H	2.7	± 0.3	0.8	± 0.5	*0.830*	1.6	± 0.6	2.5	± 0.5	*0.121*
	7 d H	3.0	± 0.4	0.1	± 0.6		2.1	± 0.3	2.0	± 0.5	
	PT2385 P value	***0.001***				*0.113*	*0.889*				*0.253*
3% CO_2	Baseline	2.3	± 0.6	2.6	± 0.6		2.7	± 0.7	1.3	± 0.5	
	2 d H	2.3	± 0.7	1.4	± 0.4		2.7	± 0.8	2.4	± 0.5	
	5 d H	3.5	± 0.5	2.7	± 0.7	*0.058*	2.9	± 0.4	2.5	± 0.3	*0.450*
	7 d H	2.8	± 0.4	2.3	± 0.4		2.7	± 0.2	1.4	± 0.3	
	PT2385 P value	*0.212*				*0.913*	*0.062*				*0.641*

[8] As published in Cheng et al., 2020.

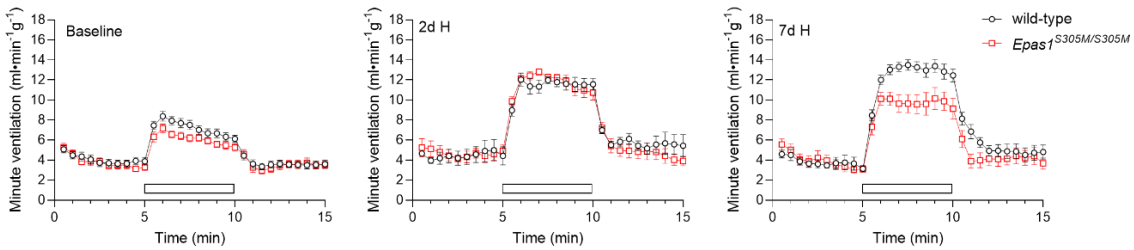


Figure 3-3. *Epas1*$^{S305M/S305M}$ mice have reduced VAH relative to wild-type littermates. Comparison of 10% O_2/3% CO_2 HVR in vehicle-treated wild-type and *Epas1*$^{S305M/S305M}$ mice before (Baseline) and after 2 and 7-day hypoxia (H). For Baseline comparison, measurements were pooled from all treatment groups per genotype ($n = 14$). Data at 2 and 7d are replotted from (Figure 3-2A), to provide direct comparison ($n = 7$). AVRs were compared by a mixed model two-way ANOVA, time $P < 0.0001$, with Sidak's multiple comparisons $P = 0.749$ at Baseline, $P = 0.749$ at 2d H and $P = 0.0325$ at 7d H.

3.2.3 *HIF-2α S305M mutant mice are resistant to PT2385 effects on hypoxic CB proliferation*

To confirm PT2385 effects on CB proliferation and hyperplasia in response to hypoxia are (like VAH) on-target to HIF-2α PAS-B domain, BrdU incorporation was assessed in the CBs of mice carrying the HIF-2α S305M mutation exposed to 7-day hypoxia and treated with 10 mg·kg^{-1} twice daily, as used in the ventilatory experiments above. In contrast to the striking reduction in BrdU incorporation observed in PT2385-treated wild-type mice, BrdU^{+} cell density was similar between the CBs of PT2385- and vehicle-treated *Epas1*$^{S305M/S305M}$ mice, although with a higher variability in the *Epas1*$^{S305M/S305M}$ cohort (Figure 3-4). In line with this, and in contrast to the loss of CB hyperplasia observed in PT2385-treated wild-type mice (Figure 2-8A and Figure 3-4A), CB volumes were similar between PT2385- and vehicle-treated *Epas1*$^{S305M/S305M}$ mice (Figure 3-4A). However, there was a trend towards reduced CB volumes of vehicle-treated *Epas1*$^{S305M/S305M}$ mice exposed to 7-day hypoxia compared to wild-type controls (Figure 3-4A).

In summary, *Epas1*$^{S305M/S305M}$ mice are resistant to the PT2385 effects on hypoxia-induced CB proliferation and hyperplasia. Further, a trend towards a hypomorphic phenotype with respect to the hypoxic CB proliferative response was observed in the mutant mice.

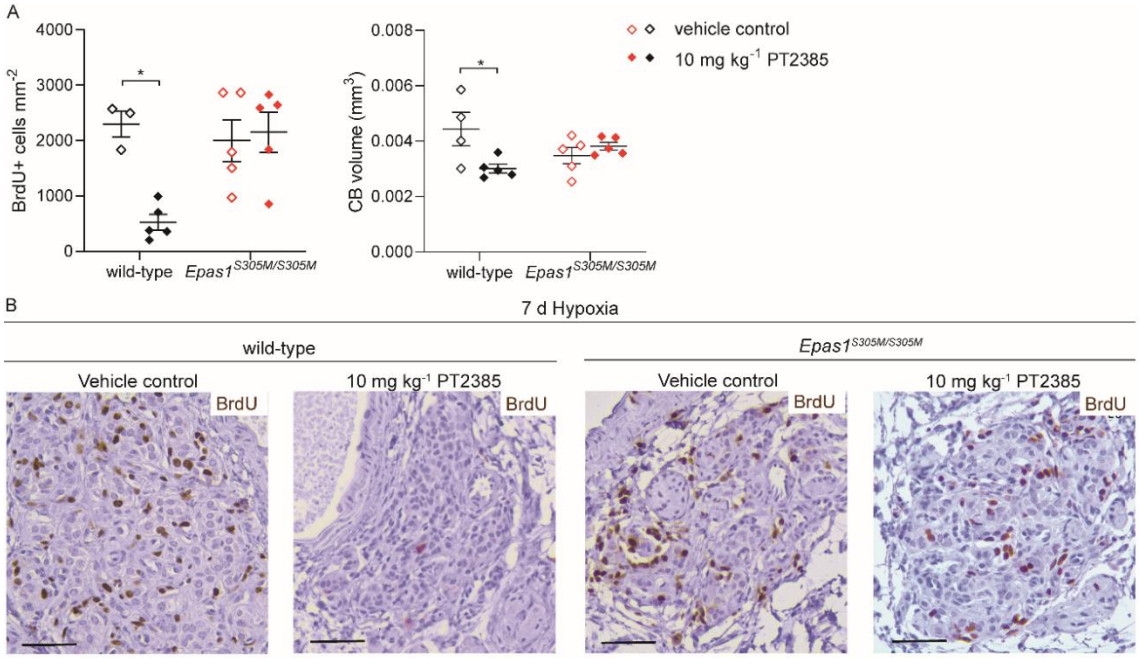


Figure 3-4. Effects of PT2385 on cellular responses to hypoxia in *Epas1*$^{S305M/S305M}$ CBs.[9] (**A**) Quantification of BrdU^{+} cell density (left panel) and CB volumes (right panel) in wild-type and *Epas1*$^{S305M/S305M}$ mice treated b.i.d. with 10 mg·kg^{-1} PT2385 (or vehicle), starting one day before 7-day exposure to hypoxia (10% O_2) and continuing throughout (to a total of 8d treatment). Data were analysed by two-way ANOVAs followed by Holm-Sidak's multiple comparisons tests, with significance reported in the graphs, $*P < 0.05$. (**B**) Representative images of BrdU IHC used for quantification in A. Scale bars represent 50 μm.

3.2.4 *Epas1*$^{S305M/S305M}$ *mutant mice have a reduced polycythaemic response to hypoxia*

Previous work on the *Epas1*$^{S305M/S305M}$ mice suggested that the mutation filling the cavity of the HIF-2α PAS-B domain results in a hypomorphic phenotype with respect to

[9] As published in Cheng et al., 2020

hypoxia-induced erythropoietin synthesis (Feng et al., 2018). To test if the polycythaemic response driven by increased erythropoietin secretion under hypoxia is also reduced in *Epas1*$^{S305M/S305M}$ mice, haematocrits of vehicle- and PT2385-treated mutant and wild-type mice were compared (Figure 3-5). In spite of data presented in the previous chapter (Figure 2-2) showing no reduction in hypoxia-induced polycythaemia with PT2385 treatment, there was a small, but not statistically significant trend towards reduced haematocrits in PT2385-treated wild-type mice in this cohort (Figure 3-5). In contrast, there was no difference in haematocrits between vehicle- and PT2385-treated *Epas1*$^{S305M/S305M}$ mice, supporting resistance of S305M mutant mice to the effects of HIF-2α inhibition on hypoxic polycythaemia (Figure 3-5). Further, there was a small reduction in haematocrits of vehicle-treated S305M mutant mice, compared with wild-type littermates, although this was not statistically significant with multiple comparisons adjustment ($P = 0.0898$, Figure 3-5). Two-way ANOVA analysis of wild-type and PT2385-treated wild-type *vs* *Epas1*$^{S305M/S305M}$ mice, however, showed a significant difference with respect to the S305M mutation across the PT2385-treatment cohorts (S305M factor $P = 0.0465$, Figure 3-5).

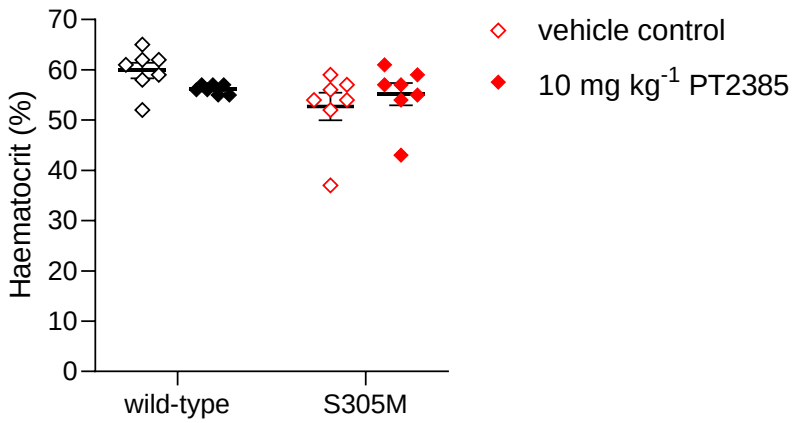


Figure 3-5. Polycythaemic response to hypoxia in wild-type and *Epas1*$^{S305M/S305M}$ mice.
% Haematocrits were calculated in blood collected from wild-type (black) and *Epas1*$^{S305M/S305M}$ (red) mice treated with vehicle (open rhombi) or b.i.d. 10 mg·kg^{-1} PT2385 (closed rhombi) and

exposed to 7-day 10% O_2. Data were analysed by a two-way ANOVA, with interaction $P = 0.126$, PT2385 $P = 0.743$ and S305M $P = 0.047$; followed by Holm-Sidak's multiple comparisons test, with no significant differences ($P < 0.05$) detected between individual groups.

3.2.5 *Dissection of the mechanisms of HIF-2α involvement in acute oxygen sensing*

The finding of a hypomorphic phenotype in mice homozygous for the HIF-2α PAS-B domain S305M mutation, which does not interfere with ARNT heterodimerisation, suggests a HIF-β-independent action of HIF-2α, such as through a ligand interacting with the PAS-B domain to modulate VAH independently of ARNT. Additionally, treatment with PT2385 in Chapter 2 showed rapid (within 1h) effects of PT2385 on HVR in unacclimatised mice, suggesting that HIF-2α may have a rapid, non-transcriptional role in modulating hypoxic ventilatory control such as via binding of an endogenous ligand. However, these effects of PT2385 in unacclimatised mice were small and did not completely abolish HVR. This contrasts to a published report where complete inhibition of HVR was observed with genetic *Hif-2α* inactivation (Moreno-Dominguez et al., 2019) and also to the complete loss of VAH by PT2385 noted in Chapter 2. Thus, it is possible that while partial HIF-2α inactivation can ablate VAH, inhibition of the acute responses in unacclimatised mice requires a higher degree of HIF-2α loss. The next experiment therefore tested whether hypoxic AVRs could be ablated more completely with increased dose of the pharmacological HIF-2α inhibitors.

To test if treatment with higher doses of PT2385 could completely ablate HVR, a small pilot experiment was designed to match the previous datasets of short-term effects of 10 $mg \cdot kg^{-1}$ PT2385 on HVR (see Figure 2-6). Baseline ventilatory responses were measured the day before starting PT2385 treatment (Baseline) and then mice were treated with a single dose of 10 or 60 $mg \cdot kg^{-1}$ PT2385. The 60 $mg \cdot kg^{-1}$ dose was chosen

as the highest PT2385 dose reported safe in mouse studies (Wallace et al., 2016). 10% O_2/3% CO_2 AVRs (and other gas challenges as before) were then measured 1 and 5h after the first oral PT2385 treatment (Figure 3-6).

As before, treatment with 10 mg·kg^{-1} PT2385 resulted in reduced MVb and TVb under 10% O_2/3% CO_2 and 10% O_2 hypoxia within 1h of PT2385 treatment, compared with Baseline (Figure 3-6). There was high variability between average 10% O_2/3% CO_2 MVb across treatment groups at Baseline, the effects of PT2385 treatment were therefore compared between timepoints rather than between treatment groups. There was a reduction in MVb and TVb from Baseline to 1h and 5h PT2385 treatment across all groups, with the strongest effect observed with 10 mg·kg^{-1} PT2385 treatment (Figure 3-6). Treatment with 60 mg·kg^{-1} did not appear to reduce either MVb or TVb during either of the hypoxic stimuli compared with 10 mg·kg^{-1} or vehicle groups, and the extent of between time-points suppression with this dose was similar or lower than that seen with the 10 mg·kg^{-1} treatment (Figure 3-6). Average MVb under 3% CO_2 varied between animals within groups, but no changes in hypercapnic TVb were observed with 10 mg·kg^{-1} PT2385 treatment, while 60 mg·kg^{-1} PT2385 caused a small suppression in hypercapnic TVb (Figure 3-6).

Based on these results, mice can mount an HVR even at the maximum safe dose of PT2385 with no obvious increase in HVR suppression at higher doses, suggesting that incomplete loss of HVR is not due to insufficient PT2385 dose.

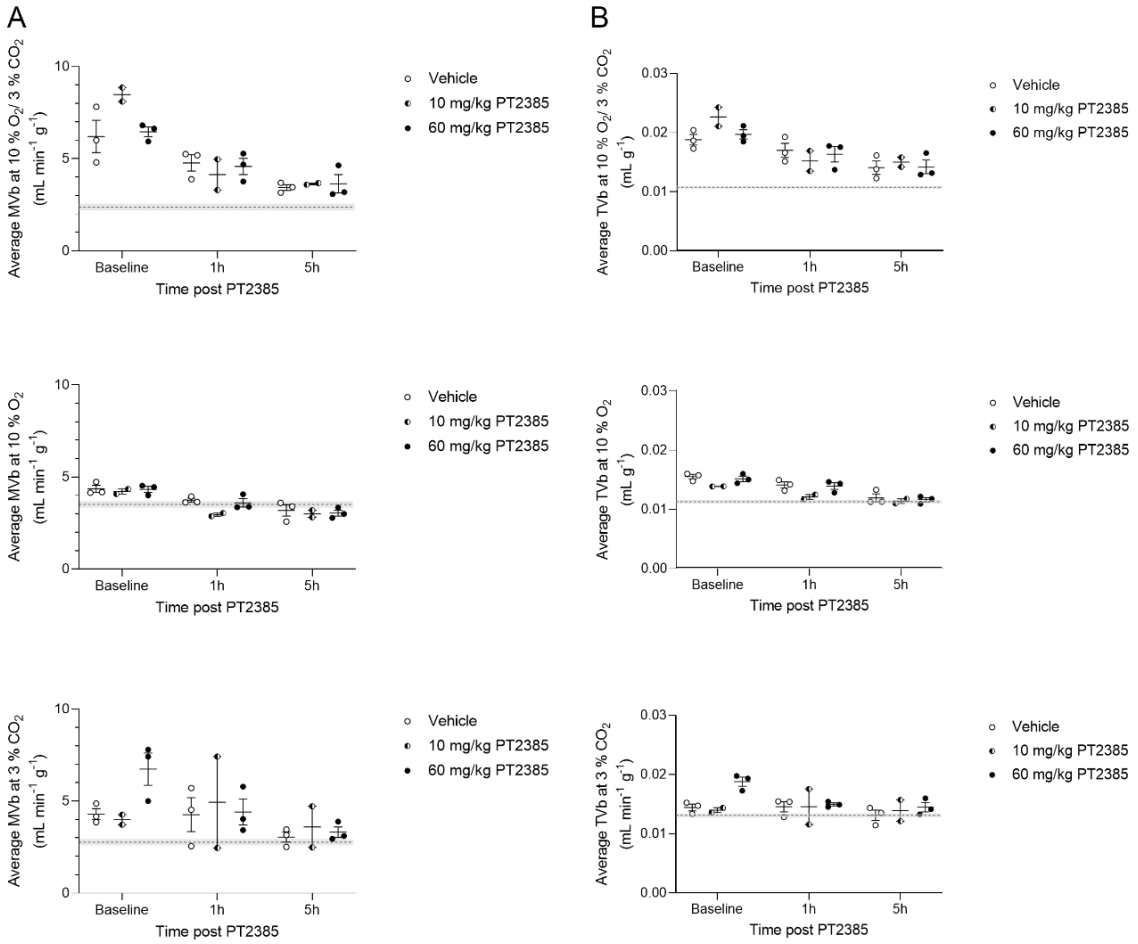


Figure 3-6. HVRs in animals treated with the maximum safe dose of PT2385.
Average MVb (**A**) and TVb (**B**) during a 5 min 10% O_2/3% CO_2 (top row), 10% O_2 (middle row), or 3% CO_2 (bottom row) stimulus, measured the day before (Baseline) and 1 and 5h after the first 10 or 60 mg·kg^{-1} PT2385 treatment in wild-type mice.

Another possible reason for incomplete HVR inhibition with 10 mg·kg^{-1} PT2385 could be overcompensation with carbon dioxide, as treatment with PT2385 can suppress TVb down to baseline levels under stimulation with 10% O_2 alone, but not with 10% O_2/3% CO_2 (Figure 2-7). As explained before, supplementation of the hypoxic gas with 3% CO_2 aims to mimic end-tidal clamping performed in human studies to off-set hypocapnia caused by hyperventilation (Fatemian and Robbins, 1998, also see section 1.1). However, the level of carbon dioxide supplementation has been calculated for experiments primarily investigating AVRs in acclimatised mice (Bishop et al., 2013). It is possible that for measurements in unacclimatised mice, the 3% CO_2 supplementation

could result in overcompensation, thus demonstrating CB sensitivity to hypercapnia, rather than hypoxia.

To investigate if lack of complete AVR inhibition with PT2385 is due to overcompensation with carbon dioxide, MVb, TVb and RR were measured in mice challenged with 10% O_2 with addition of ranging carbon dioxide tensions (0, 1, 1.5 and 2% CO_2). As discussed in Chapter 2, 5 min challenge with 10% O_2 alone resulted in a small spike in MVb that rapidly deteriorated back to resting levels (Figure 3-7A, black circles). Since another small spike was observed upon the switch between the hypoxic and air gases (Figure 3-7A), these spikes most likely result from the reaction of mice to the change in airflow, rather than a hypoxic response.

To test if addition of carbon dioxide at levels between 0 and 3% (as used in the previous experiments (Figure 2-6)) could show a clear AVR that can be completely ablated with PT2385, MVb under 10% O_2/1% CO_2, 10% O_2/1.5% CO_2 and 10% O_2/2% CO_2 was recorded before and 1, 5 and 24h after the treatment with 10 mg·kg^{-1} PT2385 (Figure 3-7).

Addition of 1% CO_2 to the hypoxic challenge did not increase MVb responses beyond that observed with 10% O_2 alone when measured prior to PT2385 or vehicle treatment (Figure 3-7A), however, a small response to 10% O_2/1% CO_2 was observed in vehicle-treated mice 1, 5 and 24h after the start of treatment (Figure 3-7B, left panels). No reduction in the MVb under 10% O_2/1% CO_2 was observed at any time-point during the first 24h of treatment with PT2385, in PT2385- compared to the vehicle-treated mice (Figure 3-7B, left panels).

Addition of 1.5% CO_2 increased the MVb response to between that of 10% O_2 alone and 10% O_2/3% CO_2 (Figure 3-7A). However, treatment with 10 mg·kg^{-1} PT2385 did

not reduce this MVb in response to 10% O_2/1.5% CO_2 (Figure 3-7B, middle panels). This could suggest that mice breathing 10% O_2/1% CO_2 and 10% O_2/1.5% CO_2 are still hypocapnic, thus suppressing HVR, making the effects of HIF-2α inhibition more difficult to observe.

Challenge with 10% O_2/2% CO_2 resulted in a marked increase in MVb compared to resting values, similar to the challenge with 10% O_2/3% CO_2 (Figure 3-7A). A small reduction in the MVb under 10% O_2/2% CO_2 of PT2385-treated mice, compared to vehicle controls, was observed 5 and 24h after the start of PT2385 treatment (Figure 3-7B, right panels). However, this effect was smaller than that observed in PT2385-treated mice challenged with 10% O_2/3% CO_2 (compare Figure 3-7B, right panels with Figure 2-6A). Together, these data suggest that overcompensation with carbon dioxide does not prevent complete ablation of AVR with PT2385.

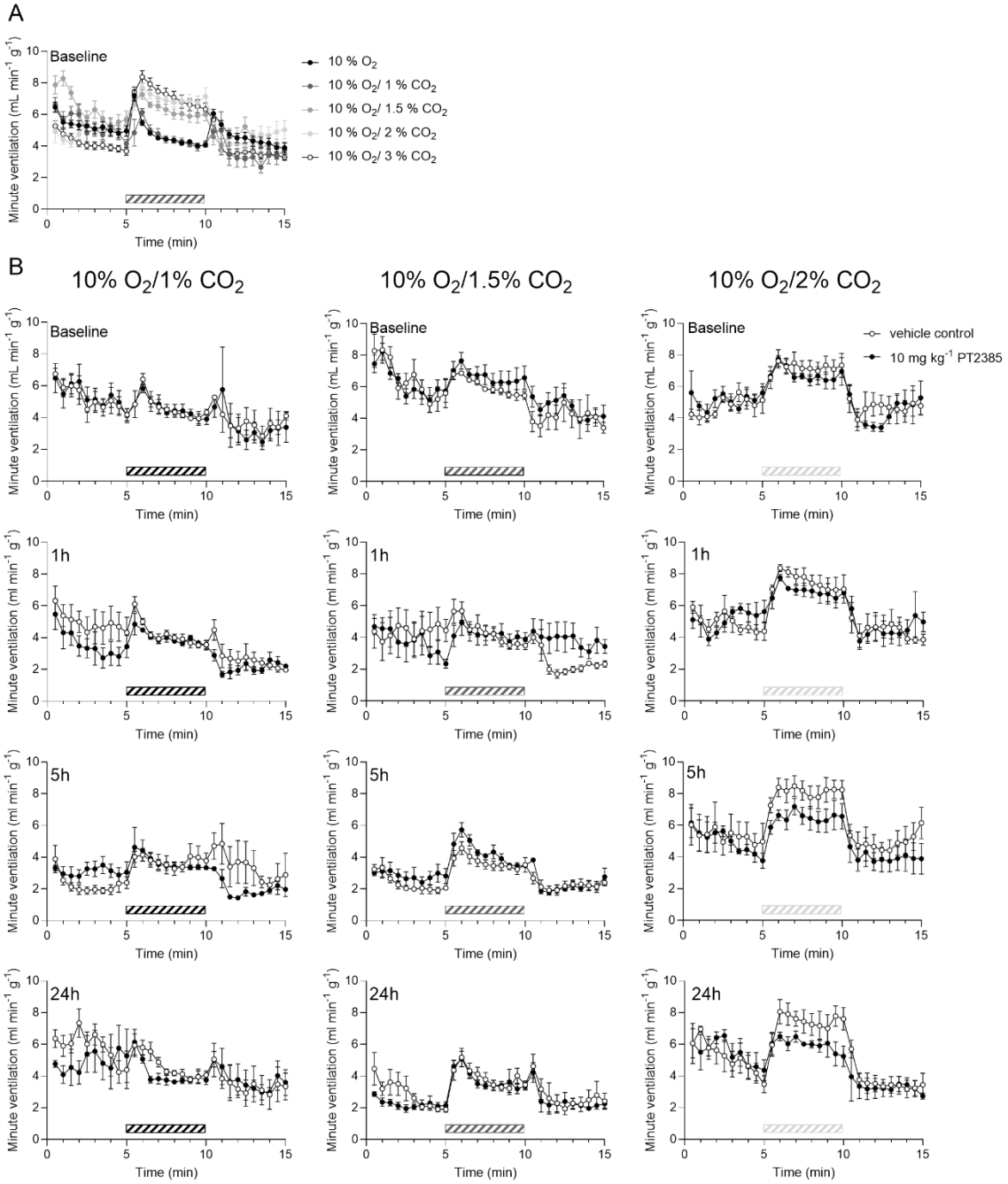


Figure 3-7. The effects of PT2385 on MVb changes in response to hypoxic stimuli with varying CO_2 compensation.

(**A**) Changes in MVb during 5 min challenge (dashed box) with 10% O_2 and increasing (1-3%) CO_2 enrichment in unacclimatised wild-type mice. $n = 30$ for 10% O_2 and 10% O_2/3% CO_2 exposures; $n = 8$ for 10% O_2/ 1% CO_2, 10% O_2/ 1.5% CO_2 and 10% O_2/ 2% CO_2 exposures, with separate mouse cohort for each type of hypoxic challenge. (**B**) Changes in MVb during 5 min challenges with 10% O_2/1% CO_2 (left), 10% O_2/1.5% CO_2 (middle) or 10% O_2/2% CO_2 (right), before (Baseline) and 1, 5 and 24h after the first 10 mg·kg^{-1} PT2385 (or vehicle) dose ($n = 4$); second dose of PT2385 was given immediately after the 5h measurements. Baseline data are replotted from A for separate treatment groups.

With the success of early HIF-2α inhibitor, PT2385, in pre-clinical studies and clinical trials, more compounds of this class have been designed, aiming to improve the pharmacokinetic properties, in particular to extend the short half-life of PT2385 (Wallace et al., 2016). To test if these improved kinetics might increase the inhibitory effects of HIF-2α inhibitors on HVR, the effects of two other compounds of the same class: PT2399 and second-generation PT2977, on unacclimatised AVRs, were tested.

In vitro studies have indicated that PT2399 (compound 10f, MedChemExpress, 2019) has a smaller $EC_{50,}$ as well as a longer half-life than PT2385 (Wehn et al., 2018). PT2399 has been shown to ablate the growth of 786-O xenografts (Cho et al., 2016) and reduce hypoxia-stimulated erythropoiesis in an on-target manner at the dose of b.i.d. 30 $mg{\cdot}kg^{-1}$ in mice (Feng et al., 2018). MVb was therefore measured in response to 10% O_2/3% CO_2 1, 5 and 24h after the start of 30 $mg{\cdot}kg^{-1}$ PT2399 treatment, as before (Figure 2-6). A trend towards reduced MVb 1h after the start of treatment was observed in mice receiving 30 $mg{\cdot}kg^{-1}$ PT2399, compared to vehicle-treated controls (Figure 3-8). This was absent at 5h, but a significant reduction in MVb during the hypoxic challenge was observed 24h after the start of treatment (Figure 3-8A-B). This effect appeared to be more pronounced than that observed with 10 $mg{\cdot}kg^{-1}$ PT2385 treatment (compare Figure 2-6A and Figure 3-8A), although the effects of treatment on MVb at 10% O_2/3% CO_2, 24h after the start of treatment were not statistically significant between the 30 $mg{\cdot}kg^{-1}$ PT2399 and 10 $mg{\cdot}kg^{-1}$ PT2385 groups (Figure 3-8C, two-way ANOVA interaction $P = 0.354$). PT2399 also reduced the 10% O_2 AVR 24h after the start of treatment (Figure 3-8B), but no significant changes to the 3% CO_2 responses were observed (Figure 3-8B), suggesting these PT2399 responses on AVR are specific to hypoxia. PT2399 may therefore be more efficient than PT2385 at blocking the HIF-2α effects on acute oxygen sensing, although it appears to be acting more slowly.

Successful HIF-2α inhibition with PT2385 and PT2399 has prompted generation of the 2nd generation small molecules with higher efficacy, mostly in an attempt to reduce the dosing frequency in human clinical trials. A more efficacious molecule, PT2977, was developed, with improved metabolic profile and longer half-life, allowing for once-daily dosing in mice and humans (Xu et al., 2019). To test if, with its higher bioavailability, HIF-2α inhibition with PT2977 could completely ablate HVR, 10% O_2/3% CO_2 AVRs were measured in mice treated twice-daily with 10 mg·kg^{-1} PT2977 – a dose with reportedly higher exposure than the 10 mg·kg^{-1} PT2385 treatment (Xu et al., 2019). As with the first-generation compound, PT2385, treatment with PT2977 resulted in a rapid reduction in 10% O_2/3% CO_2 AVR (measured as average MVb during stimulus, as before), although this did not reach statistical significance at 1 or 5h after the first dose on a sample of $n = 4$ mice (Figure 3-9A, B). 10% O_2, 3% CO_2 AVR was significantly reduced 24h after the first PT2977 dose (Figure 3-9A, B), and this effect was somewhat greater than in mice treated with PT2385 (Figure 3-9C). As with other HIF-2α inhibitor experiments, 10% O_2 AVRs were small. Nevertheless, a significant reduction in AVR to 10% O_2 was observed 24h after the first PT2977 dose (Figure 3-9B). No significant changes to AVRs to 3% CO_2 were observed with PT2977 treatment (Figure 3-9B), confirming HIF-2α inhibition with PT2977 affects hypoxic, and not hypercapnic AVR.

In summary, neither increasing the dose of PT2385 nor use of second-generation HIF-2α inhibitors: PT2399 or PT2977, completely abolishes HVR in unacclimatised mice.

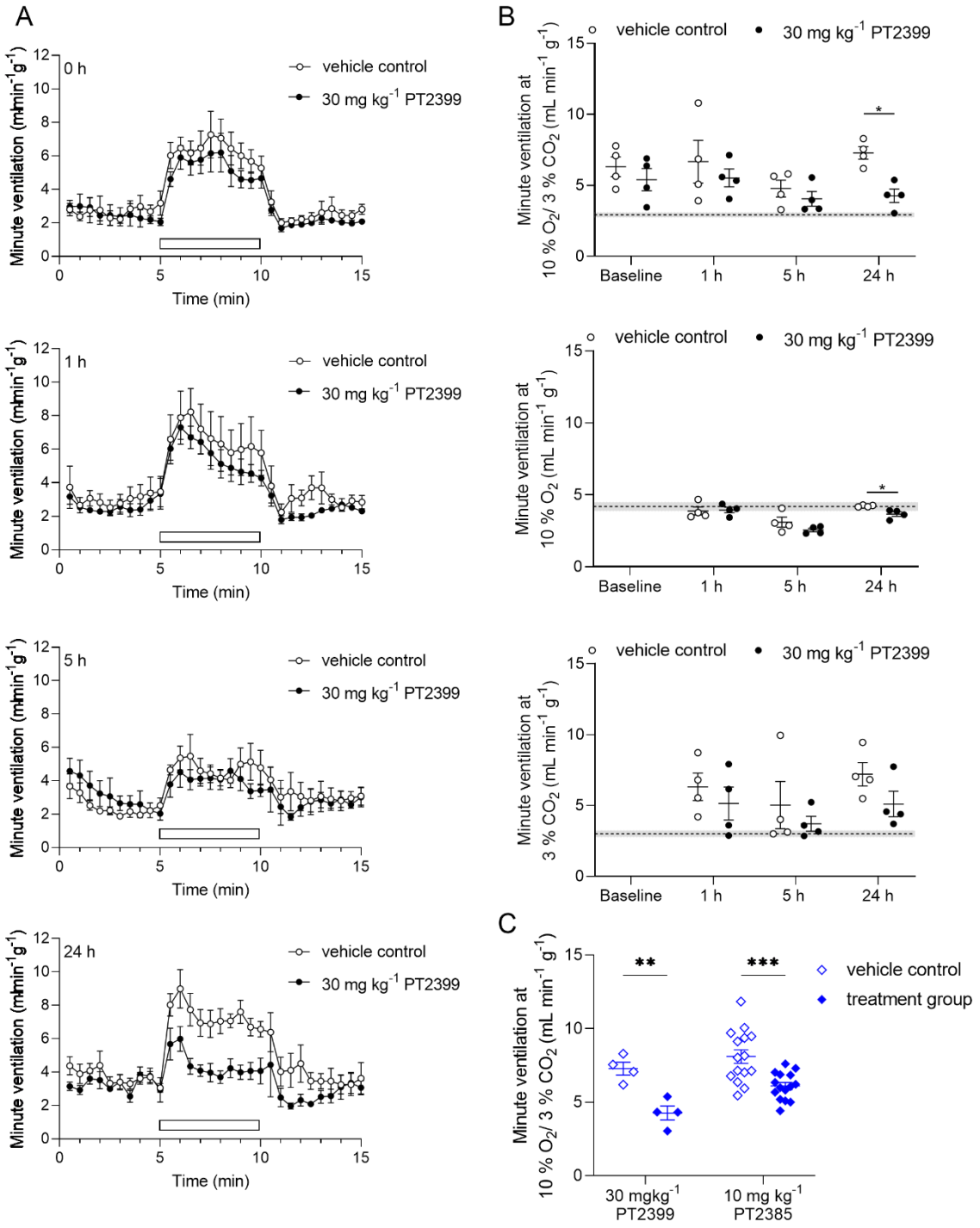


Figure 3-8. The effects of PT2399 on HVR in unacclimatised mice.

(**A**) Changes in MVb during 5 min challenges with 10% O_2/3% CO_2 (open bars) made before (Baseline) and 1, 5 and 24h after the first 30 mg·kg^{-1} PT2399 (or vehicle) oral dose ($n = 4$). PT2399 was administered twice daily, with the second dose given immediately after the 5h plethysmography. (**B**) Average MVb during 5 min challenges with 10% O_2/3% CO_2 (upper panel, quantified from data shown in A), 10% O_2 (middle panel) or 3% CO_2 (lower panel). Data were analysed by Holm-Sidak's multiple comparisons tests, with significance reported in the

graphs, $*P < 0.05$. Dotted lines show the average resting MVb in air prior to the acute gas challenge, across all time-points and treatment groups, ± SEM (shaded area) (**C**) Comparison of average MVb under 10% O_2/3% CO_2 in mice treated with 30 mg·kg^{-1} PT2399 ($n = 4$) or 10 mg·kg^{-1} PT2385 ($n = 15$)(and vehicle), 24h after the start of treatment. 10 mg·kg^{-1} PT2385 data are reproduced from Figure 2-6B for comparison. Data were analysed by a two-way ANOVA, $P = 0.0178$ for different compounds, $P < 0.0001$ for treatment. Comparisons in the graph are Sidak's multiple comparisons tests, $**P < 0.01$, $***P < 0.001$.

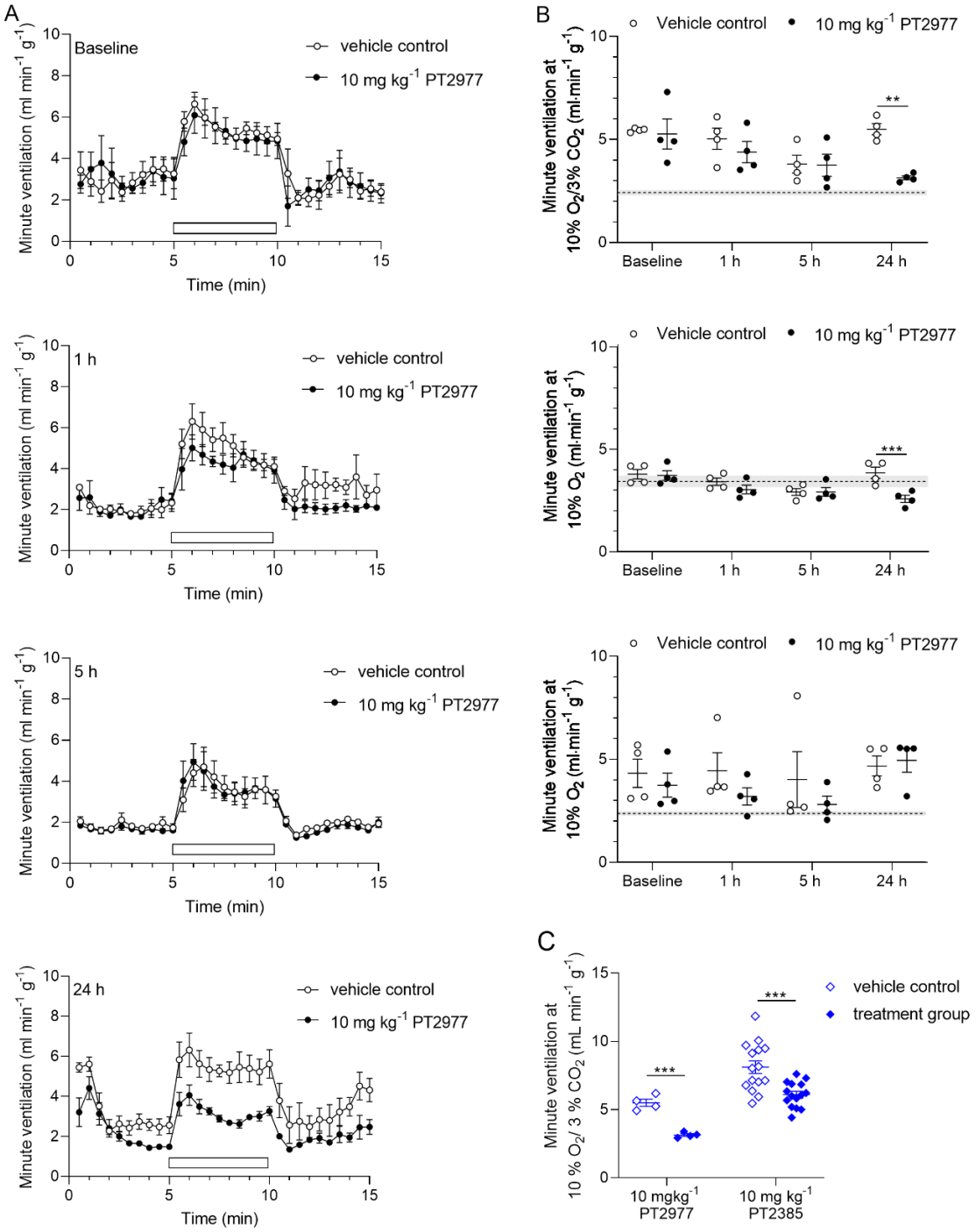


Figure 3-9. The effects of PT2977 on HVR in unacclimatised mice.

(**A**) Changes in MVb in response to a 5 min challenge with 10% O_2/ 3% CO_2 (open bars) made before (Baseline) and 1, 5 and 24h after the first 10 mg·kg^{-1} PT2977 (or vehicle) treatment ($n = 4$). PT2977 was administered orally twice daily, with the second dose given immediately after the 5h plethysmography. (**B**) Average MVb during 5 min challenges with 10% O_2/3% CO_2 (upper panel, quantified form data in A), 10% O_2 (middle panel) or 3% CO_2 (lower panel). Data were analysed by Holm-Sidak's multiple comparisons tests, with significance reported in the graphs, $*P < 0.05$. Dotted lines show the average resting MVb in air prior to the acute gas challenge, across all time-points and treatment groups, ± SEM (shaded area). (**C**) Comparison of average MVb under 10% O_2/3% CO_2 in mice treated with 10 mg·kg^{-1} PT2977 ($n = 4$) or 10 mg·kg^{-1} PT2385 ($n = 15$)(and vehicle), 24h after the start of treatment. 10 mg·kg^{-1} PT2385 data are reproduced from Figure 2-6B for comparison. Data were analysed by a two-way ANOVA, $P < 0.0001$ for different compounds, $P = 0.0002$ for treatment. Comparisons in the graph are Sidak's multiple comparisons tests, $***P < 0.001$.

Together, a complete block of the acute hypoxic response could not be achieved either with increased doses of PT2385, by using compounds with higher binding affinity for HIF-2α, or with lower carbon dioxide supplementations in the hypoxic challenge gas, suggesting HIF-2 inactivation only partially reduces, but is unable to completely ablate HVR, in contrast to published data in mice with HIF-2α genetic inactivation (Moreno-Dominguez et al., 2019).

3.3 Discussion

In this chapter, mice homozygous for the S305M mutant HIF-2α allele, which is resistant to PT2385 binding, were used to confirm on-target specificity of PT2385 actions on VAH and CB proliferation. Treatment with 10 mg·kg^{-1} PT2385, a dose which was previously used to achieve complete ablation of VAH and CB proliferation in wild-type mice (Chapter 2), did not affect either the ventilatory or proliferative responses to 7-day hypoxia in *Epas1*$^{S305M/S305M}$ mice. This confirms that the PT2385 effects on VAH and CB proliferation are on-target to the HIF-2α PAS-B domain pocket, where the

S305M mutation was introduced, resolving the previous controversy on the importance of different HIF-α isoforms in VAH (see section 1.4).

PT2385-treated *Epas1*$^{S305M/S305M}$ mice were not only resistant to the compound, but had had a trend towards increased VAH compared with the vehicle-treated S305M mutant cohort. This could suggest that, at high doses of the compound, the mutation blocking access to the HIF-2α PAS-B domain transforms the antagonist into an agonist. Such an effect has previously been observed for oestrogen receptor point mutations, which convert several oestrogen antagonists to full agonists (Mahfoudi et al., 1995, Moverare-Skrtic et al., 2014). An artificial ligand binding within the HIF-2α PAS-B domain has recently been described to stabilise the HIF-2α:ARNT dimerisation, reflecting a modest agonistic effect (Wu et al., 2019) and while the K_d of PT2385 binding to HIF-2α was significantly reduced in the S305M mutant, some binding was still observed between PT2385 and the mutant protein (Cheng et al., 2020), suggesting an alternative interaction between the mutant PAS-B domain and PT2385 could convert this antagonist into an agonist with respect to some of the HIF-2α functions.

In addition to the PT2385-resistance, a hypomorphic phenotype with respect to VAH and CB proliferation was observed in vehicle-treated *Epas1*$^{S305M/S305M}$ mice. This is in line with previously reported observations of a hypomorphic phenotype with respect to erythropoietin synthesis under sustained hypoxia in these mice (Feng et al., 2018). In this Chapter, haematocrits of *Epas1*$^{S305M/S305M}$ mice were also lower than in wild-type littermates exposed to 7-day hypoxia. However, the reduction in haematocrits was very modest compared to that observed in HIF-2α knock-out mice (Hodson et al., 2016), in line with some residual hypoxic *Epo* induction observed in *Epas1*$^{S305M/S305M}$ mice (Feng et al., 2018).

In vitro analysis found no disruption of S305M mutant HIF-2α:HIF-β heterodimer stability, suggesting intact transcriptional activity of the S305M HIF-2 (Cheng et al., 2020). In line with this, no differences in the expression of *Vegfa*, a HIF-2 target gene, were found between wild-type and *Epas1*$^{S305M/S305M}$ mice. In contrast, Feng et al. reported reduced *Epo* mRNA in S305M mutant mice exposed to hypoxia. Hypoxic *Epo* induction is very transient, with levels suppressed back to basal levels within a few hours of hypoxic treatment (unpublished observation, MPB, TB, PJR). Given this brief activation, which contrasts to other HIF-target genes, such as *Vegfa*, it is possible that some HIF-β-independent regulation of EPO activation is responsible for the reduced *Epo* induction in *Epas1*$^{S305M/S305M}$ mice. Some post-translational HIF-2α modifications have previously been proposed to modulate hypoxic EPO induction (reviewed in Haase, 2010). Future studies could examine whether non-transcriptional, HIF-2-mediated control may also contribute to regulation of EPO secretion.

The hypomorphic ventilatory phenotype of S305M mutant mice, together with the rapid action of PT2385 on HVR, suggest a specific action of the HIF-2α PAS-B domain pocket in acute hypoxic ventilatory control. The ligand hypothesis, proposing endogenous ligands bind within the PAS-B domain to regulate HIF-2α transcriptional activity, has previously been put forward based on structural studies and in relation to the enhanced adipogenesis of S305M mice under metabolic stress (Scheuermann et al., 2009, Feng et al., 2018). Data presented in this Chapter, showing a clear loss of HIF-2α function in VAH with the S305M mutation filling in the PAS-B domain cavity, suggest such a ligand could also mediate non-transcriptional action of HIF-2α in ventilatory control. The different mechanisms of HIF-2α action, with and without the involvement of such a ligand, could explain the difference in sensitivity of acute and acclimatised ventilatory responses to HIF-2α ablation.

Dissection of the mechanism of HIF-2α action in acute HVR is of particular interest as the mechanism of hypoxic chemotransduction in CB type I cells remains unknown (see section 1.2.2). In this study, partial ablation of HVR in unacclimatised mice was achieved with different HIF-2α pharmacological inhibitors, within 1h of the first oral dose, however, complete ablation of HVR could not be achieved, even at maximum safe doses, suggesting HIF-2α only partially mediates HVR.

Genetic studies using *Hif-2α$^{f/-}$;CAGGCreER^{TM}* transgenic mice, on the other hand, showed complete suppression of hypoxia-, but not hypercapnia-stimulated RR (Moreno-Dominguez et al., 2019). This discrepancy could be explained by differences in the plethysmography protocols, or it may suggest that a long-term (since HVR was measured 2 months after tamoxifen treatment to induce HIF-2 loss in this study), or indeed developmental (such as via the constitutive loss of one allele in this model) loss of HIF-2α, is necessary for a more severe phenotype in adult knock-outs. Further, Moreno-Dominguez et al. found a more convincing loss of acute oxygen sensitivity in the *ex vivo* CB preparations from *Hif-2α*KO mice, than in ventilatory phenotype. Systemic effects of HIF-2α inhibitors could therefore be responsible for the incomplete ablation of HVR in this Chapter. Investigation into the effects of pharmacological HIF-2α inhibition in *ex vivo* CBs, or isolated type I cells, is therefore necessary to resolve whether HIF-2α stabilisation is necessary for acute oxygen sensing in the CB.

Although HIF-2α protein is degraded in the presence of oxygen and its levels are expected to be negligible in a highly-perfused tissue such as the CB, loss of several atypical, CB-enriched mitochondrial ETC subunits was reported in normoxic CBs of *Hif-2α$^{f/-}$;CAGGCreER^{TM}* mice, compared to wild-type controls and CB hypoxia-sensitivity proposed to be mediated by *Cox4i2* cytochrome c oxidase subunit, in a HIF-2-dependent manner (Moreno-Dominguez et al., 2019). This may suggest that even low

levels of HIF-2α protein are sufficient to exert some transcriptional changes, or it may be that developmental heterozygosity alters the CB type I cell lineage resulting in different basal expression of these mitochondrial genes. In the next chapter, the potential non-transcriptional HIF-2α actions on CB function will further be explored using mice with genetic inactivation of HIF-β isoforms.

4

The role of HIF-β subunits in HIF-2 function in the carotid body.

4.1 Introduction

Work presented in the previous chapters, using the selective HIF-2α antagonist: PT2385, demonstrated that HIF-2α is necessary for CB-mediated CH responses: VAH, and CB proliferation. Additionally, HIF-2α was also shown to mediate HVR in unacclimatised mice, suggesting a role of HIF-2α in acute oxygen sensing. This was demonstrated using both genetically modified mice (Hodson et al., 2016) and pharmacological inhibitors (Cheng et al., 2020 and Chapters 2-3 of this thesis), with the latter reducing HVR within 1h of the first oral dose, which is a rapid time-frame for transcription-mediated changes to occur, raising the possibility of a non-transcriptional mechanism of HIF-2α action.

Further, mice with a point *Epas1* S305M mutation in the hydrophobic pocket of the PAS-B domain (designed to test the specificity of PT2385 to HIF-2α) had a hypomorphic ventilatory phenotype, with reduced VAH in vehicle-treated animals (Chapter 3 and Cheng et al., 2020). Since this mutation does not alter HIF-2α:HIF-β heterodimerisation *in vitro* (Cheng et al., 2020), this suggests that the HIF-2α PAS-B

domain plays a role in VAH independent of HIF-β dimerisation, e.g. by interaction with an endogenous ligand. Others have also reported a hypomorphic phenotype with respect to hypoxia-induced expression of *Epo* and erythropoietin secretion, but an enhanced S305M HIF-2α activity in adipogenesis (Feng et al., 2018), suggesting that HIF-2α function may depend on the cellular environment, and thus ligand availability.

Both the rapid responses to PT2385 and the hypomorphic phenotype in S305M mutant mice suggest a possible non-transcriptional role of HIF-2α. To test if HIF-2α might function independently of HIF-β heterodimerisation and subsequent gene expression, we set out to test the effects of genetic HIF-β inactivation. Since HIF-2α dimerises with HIF-β in a 1:1 stochiometry, if the role of HIF-2α is entirely dependent on this interaction, inactivation of HIF-β would be expected to phenocopy the HIF-2α genetic or pharmacological inactivation.

To date, two HIF-β isoforms have been described: ARNT and ARNT2 (Johnson et al., 1993, Wines et al., 1998). The two proteins share all the conserved regions crucial for their function as transcription factors and given this high structural similarity, they have previously been proposed to be functionally redundant (Keith et al., 2001). However, there are differences in the pattern of expression of *Arnt* and *Arnt2.* While *Arnt* is ubiquitously and lowly expressed, *Arnt2* expression is more restricted, with enrichment in the neuroepithelium at E9.5 and later in the neural crest derivatives, including the dorsal root ganglia, the AM and the renal cortical tubules, as well as some glomeruli and the thick ascending loop of Henle, during development (Jain et al., 1998, Aitola and Pelto-Huikko, 2003, Freeburg and Abrahamson, 2004) and in the adult CNS and kidney, with renal expression largely constricted to a few cortical and medullary tubules (Drutel et al., 1996, Freeburg and Abrahamson, 2004). Further, *Arnt2*, but not *Arnt*, was found to be mildly enriched in the CB compared to the non-oxygen-sensitive SCG in

bulk RNA sequencing (Gao et al., 2017). To study the importance of HIF-β heterodimerisation in HIF-2α function in the CB, genetic disruption of both *Arnt* isoforms is therefore required.

Constitutive ARNT inactivation results in embryonic lethality (Maltepe et al., 1997, Kozak et al., 1997) or, in the case of ARNT2, perinatal lethality (Keith et al., 2001), therefore mice with conditional ARNT1/2 inactivation using the Cre-LoxP system (Tomita et al., 2000) were used to test ARNT-dependence of physiological responses to hypoxia. Both subunits have been inactivated ubiquitously in adulthood, with a tamoxifen-inducible Rosa26Cre^{ERT2}, to allow for direct comparison with the effects of HIF-2α inactivation on the physiological responses to hypoxia, previously studied using this Cre driver (Hodson et al., 2016), without potential confounding effects of *Arnt*KO in development. *Arnt1/2*dKO mice did not mount a polycythaemic response to hypoxia and had mildly blunted ventilatory and CB-proliferative responses to hypoxia. This was not phenocopied by either single *Arnt1* or *Arnt2* knock-out, suggesting potential redundancy in the function of the two isoforms. Together, this suggests that the effects of hypoxic HIF-2α stabilisation on physiology are at least partly mediated by heterodimerisation with ARNT1/2, but alternative HIF-2α mechanisms of action could also contribute to its role in adaptive responses.

4.2 **Results**

4.2.1 *Expression of ARNT isoforms in the carotid body and the kidneys*

To confirm that both *Arnt* and *Arnt2* isoforms of the HIF-β subunit are expressed in the carotid body, and to test their relative expression levels, *Arnt* and *Arnt2* mRNA were detected by ISH in adjacent carotid bifurcation sections from wild-type normoxic mice, and their expression compared with that of *Epas1* (Figure 4-1). *Arnt* mRNA expression was generally low, with some enrichment in the SCG compared to the CB and no signal

detected in the adjacent carotid artery. Similarly, *Arnt2* mRNA appeared to localise to the neuronal tissues: SCG and CB, with no mRNA detected in the carotid artery or the connective tissue around the CB. This is consistent with the *Arnt2* expression pattern reported in the human protein atlas (Uhlen et al., 2015), showing elevated mRNA and protein levels in neuronal tissues, such as the brain. *Arnt2* mRNA signal was stronger in the CB relative to the SCG, in line with previous bulk RNA Sequencing results (Gao et al., 2017), and matching the expression pattern of *Epas1*, which is highly expressed in the CB and slightly enriched in the SCG compared to adjacent connective tissue and arterial wall (Figure 4-1). Within the CB, *Arnt2* expression was stronger than that of *Arnt*, in line with published RNA Sequencing data identifying *Arnt2*, but not *Arnt*, expression in CB type I cells (Zhou et al., 2016).

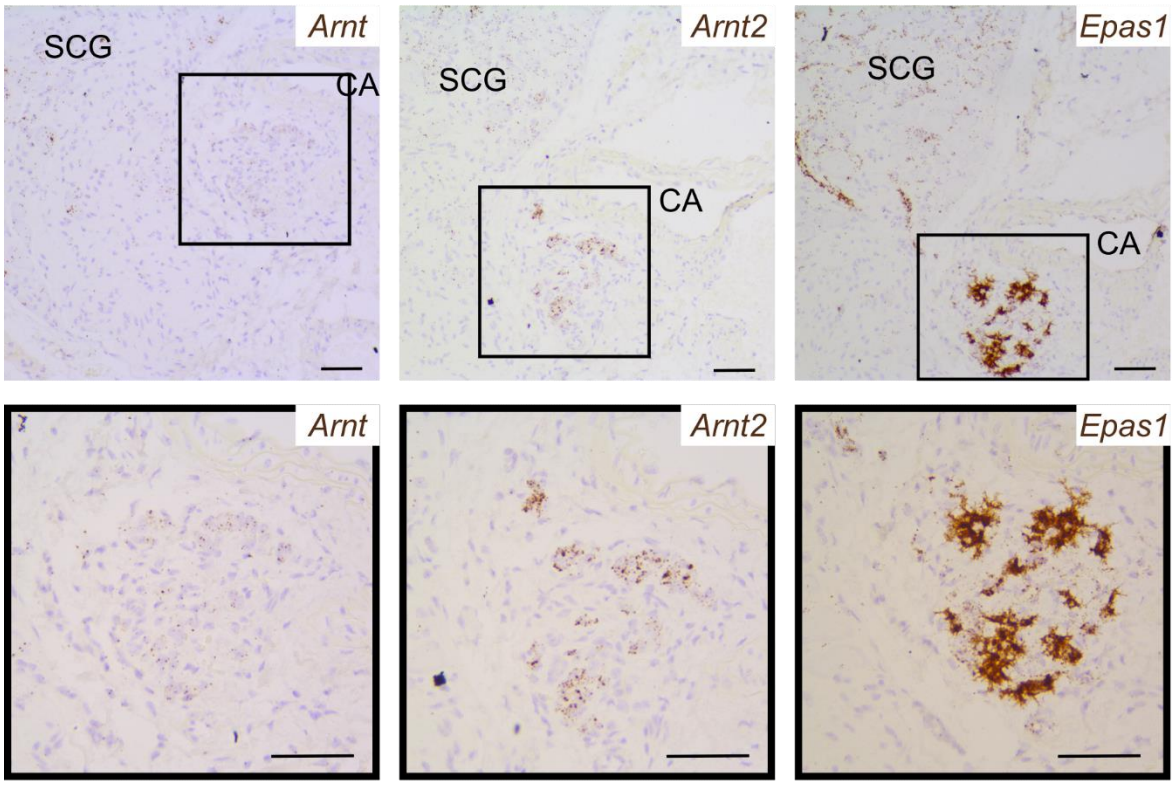


Figure 4-1. *Arnt* and *Arnt2* compared with *Epas1* expression in the mouse carotid bifurcation.

ISH against *Arnt, Arnt2* and *Epas1* mRNA (brown) in wild-type mouse carotid bifurcations (top panels) and CBs (black frames, bottom panels), counterstained with blue Gill hematoxylin. Scale bars represent 50 μm. SCG – superior cervical ganglion, CA – carotid artery.

In addition to regulating ventilation by modulating CB responses to acute and chronic hypoxia, HIF-2α plays a role in physiological adaptations to hypoxia by upregulating the expression of erythropoietin encoding gene: *Epo*, in renal interstitial fibroblasts (Paliege et al., 2010, Kapitsinou et al., 2010). Indeed, ubiquitous *Hif-2α* inactivation in adult mice prevents polycythaemia induced by a 7-day exposure to 10% O_2 (Hodson et al., 2016). *Arnt* and *Arnt2* mRNA expression in the kidneys was therefore compared with that of *Epas1*, encoding HIF-2α (Figure 4-2). *Epas1* is highly expressed in multiple renal structures, including in the glomeruli, identified as the round clusters of densely packed small cells (podocytes) and in the endothelial walls of small blood vessels, which were distinguished from tubules by their smaller lumen and thinner walls (Figure 4-2, top panels). Further, *Epas1* expression marks the interstitial fibroblasts (Figure 4-2, top row), which produce *Epo* in response to hypoxia.

mRNA expression of both *Arnt* and *Arnt2* isoforms was very low compared with *Epas1* (Figure 4-2, compare middle and bottom panels with the top row). *Arnt* mRNA signal appeared to be ubiquitously distributed throughout all cell types in the renal cortex, while *Arnt2* mRNA was enriched in some of the flat and elongated tubules (Figure 4-2), in line with a previous study showing *Arnt2* mRNA expression is much more restricted than that of *Arnt* in the adult murine kidney (Freeburg and Abrahamson, 2004). In contrast to the CB, there appears to be little overlap between the expression of *Arnt2* and *Epas1* in the adult kidney.

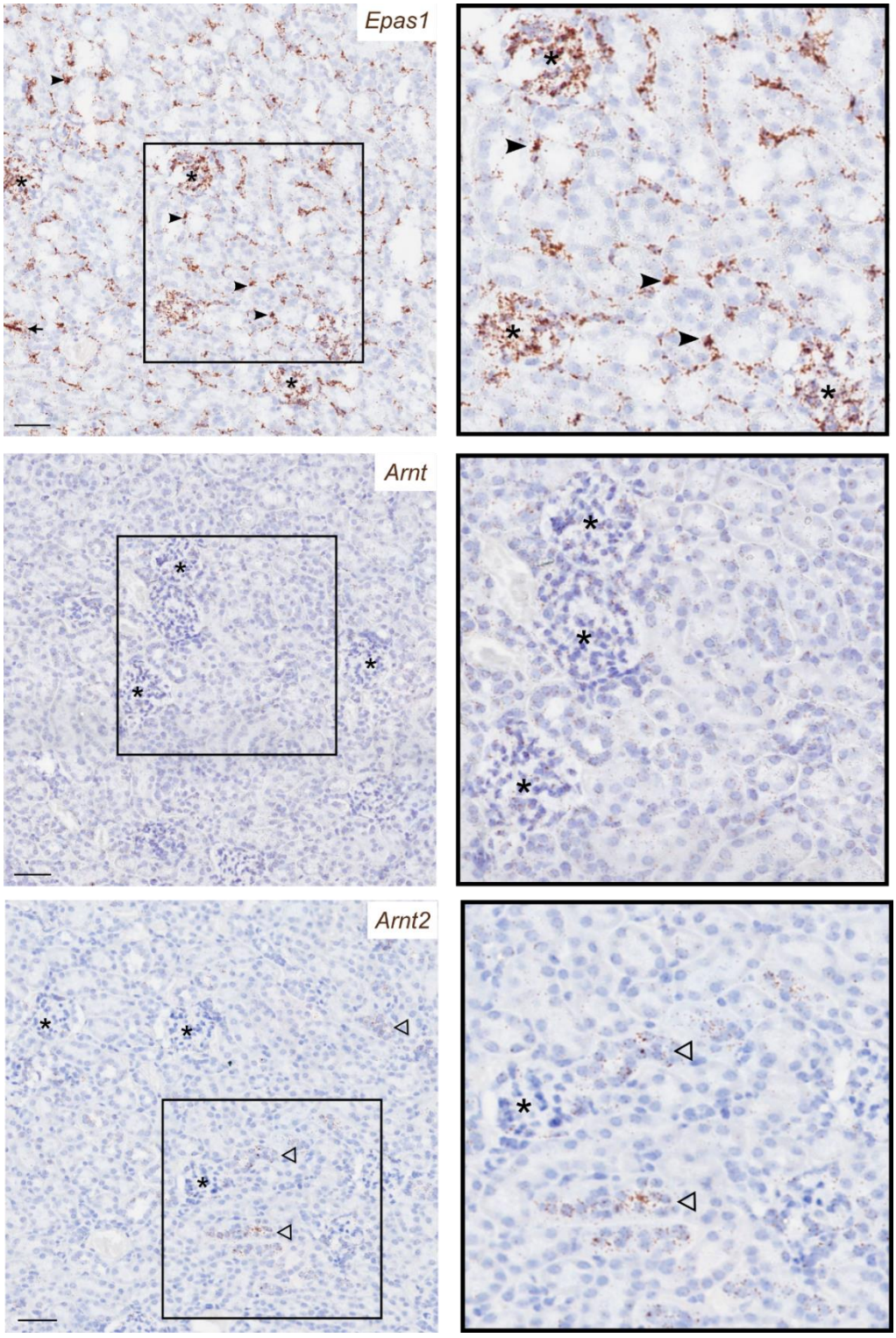


Figure 4-2. *Arnt* and *Arnt2* expression in the kidney.

mRNA expression of *Epas1*, *Arnt* and *Arnt2* in the wild-type murine kidney, detected by ISH. * mark glomeruli, ➤ mark the interstitial fibroblasts, → the *Epas1*$^{+}$ blood vessels and ◁ the *Arnt2*$^{+}$ renal tubules. 0.05 mm scale bars.

Together, in contrast to *Epas1*, *Arnt* and *Arnt2* mRNA appear to be lowly expressed in the tissues with HIF-2-dependent responses to hypoxia: carotid body and renal interstitial fibroblasts. *Arnt2* appears to be more strongly expressed in the CB (but not in the renal interstitial fibroblasts) than *Arnt*, suggesting its importance in mediating the HIF-2α effects in this tissue. Effects of inactivating both ARNT isoforms on the HIF-2α-dependent CB responses to hypoxia, as well as the EPO-induced polycythaemia, will therefore be tested.

4.2.2 *Arnt$^{f/f}$;Arnt2$^{f/f}$;RosaCreER mouse model generation*

To study the effects of ARNT inactivation on physiological responses to hypoxia in adults, *Arnt$^{f/f}$* mice harbouring the floxed *Arnt* gene (as described previously, Tomita et al., 2000) were crossed with transgenic mice expressing an inducible Cre under the ubiquitously expressed Rosa26 promoter (*RosaCreER, Vooijs et al., 2001*) previously used to test effects of HIF-2α inactivation in Hodson et al., 2016, to produce *Arnt$^{f/f}$;RosaCreER* mice. These animals develop normally and can be treated with tamoxifen in adulthood to induce recombination of LoxP sites flanking the *Arnt* exon 6, encoding the conserved basic helix-loop-helix domain of the ARNT protein, responsible for recognising and dimerising with DNA (Figure 4-3), resulting in a non-functional ARNT.

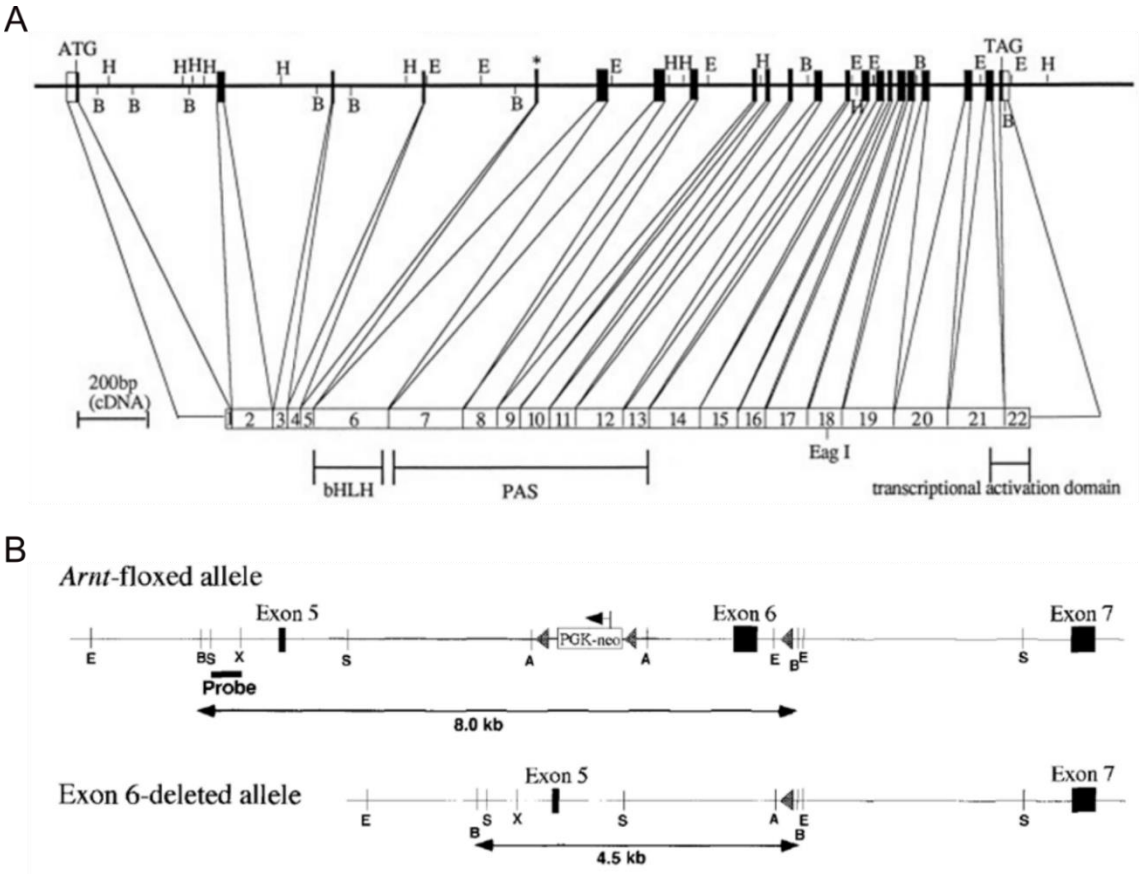


Figure 4-3. *Arnt*$^{f/f}$ mouse model construct.

Diagram shows (**A**) the structure of the mouse *Arnt* gene and resulting protein domains and (**B**) insertion of the loxP sites (hatched triangles) and the PGK neo cassette to flank exon 6 of the *Arnt* gene. Figure adapted from A: Wang et al., 1998 and B: Tomita et al., 2000.

To study the role of *Arnt2* isoform inactivation on physiological responses to hypoxia in adults, Arnt2$^{tm1a(KOMP)Wtsi}$ ES cells were obtained from the UCDavis KOMP Repository (Skarnes et al., 2011)(since a mouse model is not available), from which *Arnt2*$^{f/f}$ mice on a C57BL/6 background were generated by the Wellcome Trust Centre for Human Genetics Transgenics Core Facility, led by Dr Ben Davies. These mice have the L1L2_Bact_P cassette inserted in Chromosome 7, upstream of exon 5 encoding the PAS-1 domain of ARNT2, containing two loxP sites and a neomycin resistance gene, and a third loxP site inserted downstream of the target exon 5 (Figure 4-4). Conditional *Arnt2*$^{f/f}$ animal was then generated by expression of a Flp recombinase. F1 animals were intercrossed with *Arnt*$^{f/f}$*;RosaCreER* mice to generate *Arnt*$^{f/f}$*;Arnt2*$^{f/f}$*;RosaCreER*

(*Arnt1/2*dKO) mice or with mice expressing the *RosaCreER* driver to generate single knock-out *Arnt2*$^{f/f}$*;RosaCreER* mice.

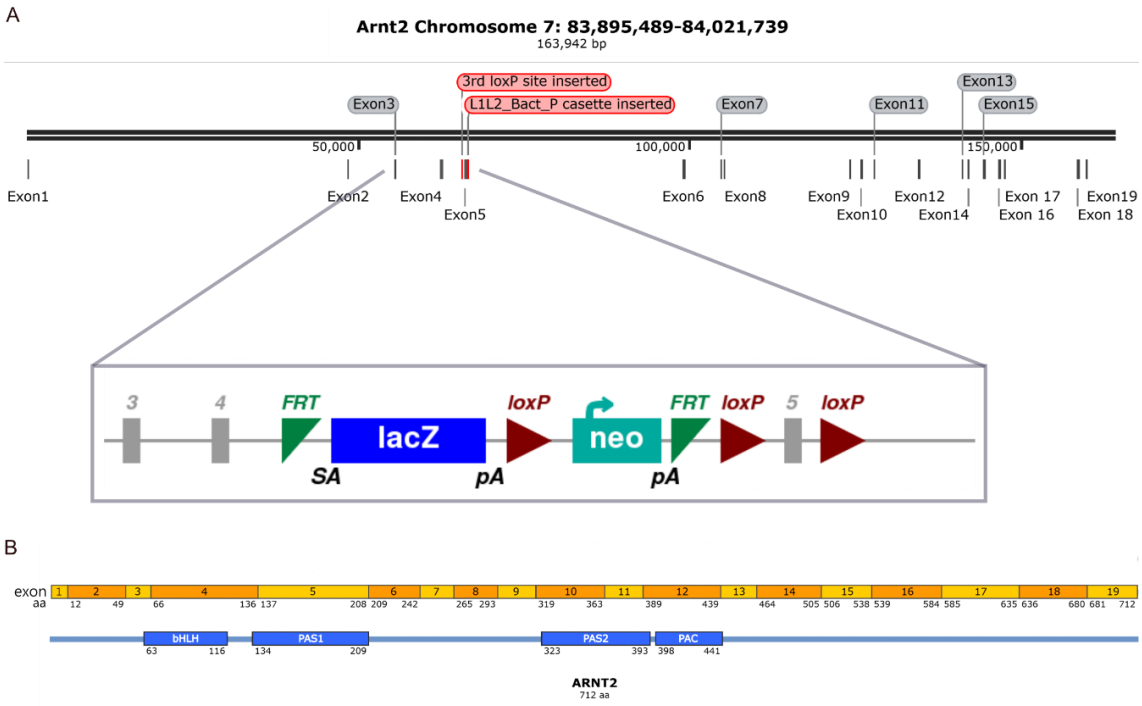


Figure 4-4. Generation of the *Arnt2*^{flox} animal model.
(**A**) Generation of Arnt2$^{tm1a(KOMP)Wtsi}$ ES cell mutation to flank the *Arnt2* exon 5 with loxP sites. Top diagram shows the relative position of the cassette and downstream loxP site insertion within the structure of the gene while the framed diagram shows the structure of the L1L2_Bact_P cassette and the positions of the three loxP sites. (**B**) Exon to protein alignment in the ARNT2 gene product (based on the ENSMUST00000085077.5 transcript and Uniprot Q61324 accessions). Diagrams were generated with SnapGene and adapted from the materials by International Mouse Phenotyping Consortium.

To confirm successful loxP site recombination in this newly generated model, genomic PCR was performed on DNA isolated from ear notches of tamoxifen-treated animals (Figure 4-5). ~500 bp bands corresponding to the expected 506 bp postFlp and postCre fragment amplified using primers flanking the start of the inserted cassette and the 3' loxP site, were identified in all animals homozygous for the *Arnt2*^{floxed} allele and expressing the Rosa26Cre^{ERT2} (Figure 4-5B). This band was absent in Cre^{-} animals, confirming tamoxifen-inducible excision of exon 5 in tamoxifen-treated

Arnt2$^{f/f}$*;RosaCreER* animals. The relative intensity of the floxed and excised fragments varied between animals, with the floxed fragment generally stronger, suggesting incomplete recombination in the sampled tissue.

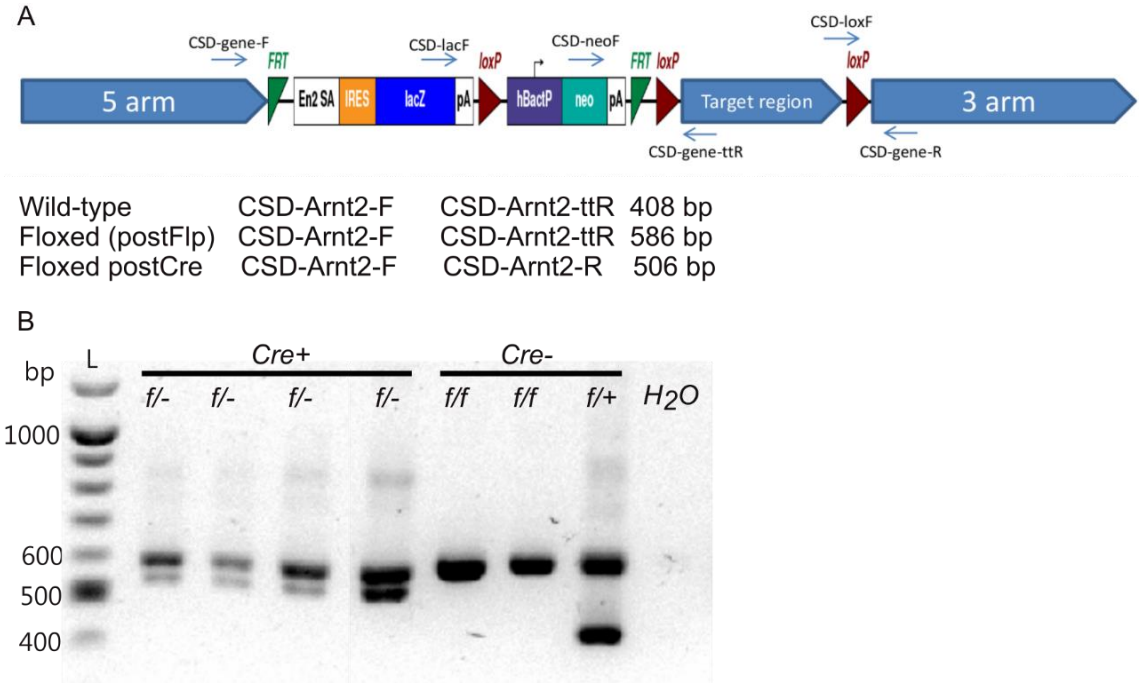


Figure 4-5. Testing *Arnt2* loxP site recombination by genomic PCR.

(**A**) Primers used to amplify the target region flanked by loxP sites in the Arnt2$^{tm1a(KOMP)Wtsi}$ mutant mice. Expected band sizes for wild-type, floxed (postFlp to invert the cassette and orient loxP sites for target excision) and floxed postCre (following tamoxifen-induced target region excision) regions amplified using the given primers pairs. (**B**) Genomic DNA from four *Arnt*$^{f/f}$*;Arnt2*$^{f/f}$*;RosaCreER* (Cre^{+}), and three Cre^{-}: two *Arnt*$^{f/f}$*;Arnt2*$^{f/+}$ and one *Arnt*$^{f/f}$*;Arnt2*$^{f/f}$ animals, separated using agarose electrophoresis, showing presence of the floxed (f) and excised (-) bands in Cre^{+} animals, and floxed or wild-type (+) bands in the Cre^{-} animals. DNA ladder (L) shows relative band sizes in base pairs (bp).

4.2.3 *Experimental design and confirmation of Arnt/Arnt2 inactivation*

To study the HIF-β dependence of physiological responses to sustained hypoxia, animals with inactivation of both ARNT isoforms were studied first, and effects of inactivation of individual *Arnt* or *Arnt2* only studied where a phenotype was observed in *Arnt1/2*dKOs. To allow for direct comparison of the effect of HIF-β inactivation to that

of HIF-α, conditional inactivation and sustained hypoxia protocols previously used in *Hif-2α$^{f/f}$;RosaCreER* mice (Hodson et al., 2016) were applied, namely: *Arnt* and/or *Arnt2* were inactivated in adult (~8 weeks old) mice by 5 consecutive oral doses of 2 mg tamoxifen (Figure 4-6). 10 days after the start of tamoxifen treatment ('post TMX'), ventilation was assessed in unacclimatised mice by plethysmography, followed by overnight acclimatisation to 10% O_2 in a normobaric altitude chamber (Figure 4-6). Further ventilatory assessments were carried out on days 2 and 7 of the chronic hypoxic exposure in the altitude chamber, as VAH has previously been shown to develop by the 2nd and further increase by the 7th day of 10% O_2 exposure (Bishop et al., 2013, Hodson et al., 2016). To assess cellular proliferation, animals were injected with a single intraperitoneal dose of BrdU at the start of hypoxic acclimatisation, and drinking water was supplemented with BrdU for the duration of hypoxia (Figure 4-6, based on Bishop et al., 2013, Hodson et al., 2016, Fielding et al., 2018). On day 7, following the final plethysmography, animals were placed back in the altitude chamber for 1-4 hours and then culled in the hypoxic conditions and tissues were collected for analysis (Figure 4-6).

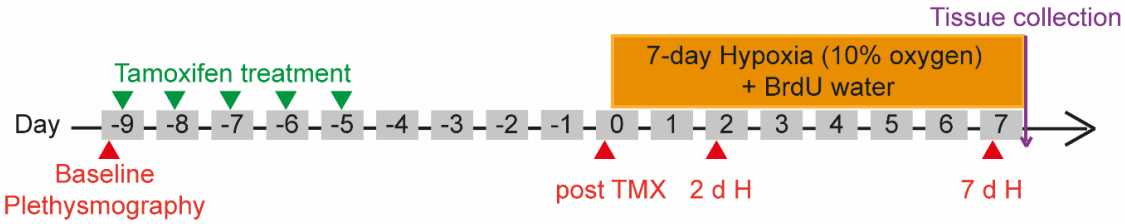


Figure 4-6. Experimental design for testing CB function in mice with acute *Arnt/Arnt2* inactivation.

Animals were treated orally with 5 doses of 2 mg tamoxifen on consecutive days, followed by a 5-day rest period before the start of 10% O_2 hypoxia housing. Immediately before the start of CH, animals received a single intraperitoneal injection of 50 mg·kg^{-1} BrdU and drinking water was supplemented with 1 mg·ml^{-1} BrdU for the rest of the experiment. Hypoxic and hypercapnic AVRs were measured by plethysmography before the start of the experiment (Baseline), following tamoxifen treatment but before the start of chronic hypoxic exposure (post TMX) and

after 2 and 7 days of 10% O_2 exposure (2d and 7d H). Following the 7dH plethysmography, mice were returned to the hypoxia chamber and left for at least 1h before culling and tissue collection.

To confirm successful ARNT and ARNT2 recombination, *Arnt* and *Arnt2* mRNA was compared in Cre^- and littermate-matched Cre^+ animals subjected to all experimental procedures in parallel. Initially, this was completed in the kidneys as they are large organs, providing a high yield of RNA from a single animal, and both isoforms have been reported to be expressed in this tissue in wild-type mice (although low expression was observed by ISH here, Figure 4-2). Kidneys from 3 pairs of *Arnt*$^{f/f}$*;Arnt2*$^{f/f}$*;RosaCreER* animals and *Arnt*$^{f/f}$*;Arnt2*$^{f/f}$ controls subjected to the hypoxia protocol (Figure 4-6), were snap-frozen upon collection at the end of the experiment, then pulverized and homogenized for RNA extraction as described in Chapter 8. *Arnt* and *Arnt2* mRNA were then quantified by RT-qPCR (Figure 4-7). Using a probe recognising specifically exon 6-7 boundary of the *Arnt* gene, *Arnt* mRNA loss was observed in the kidneys of *Arnt1/2*dKO (61 ± 1%) and *Arnt*KO (62.4 ± 0.6%) mice, with some loss also detected in the *Arnt2*KO mice (16 ± 2%)(Figure 4-7). Using a custom-designed probe recognising the exon 5 sequence of the *Arnt2* gene, a milder loss of *Arnt2* mRNA was observed in *Arnt1/2*dKO (19 ± 1%) and in *Arnt2*KO (29 ± 2%) kidneys (Figure 4-7). A small, but significant increase in *Arnt2* mRNA was detected in the *Arnt*KO kidneys (Figure 4-7), suggesting possible compensation for *Arnt* loss in this model.

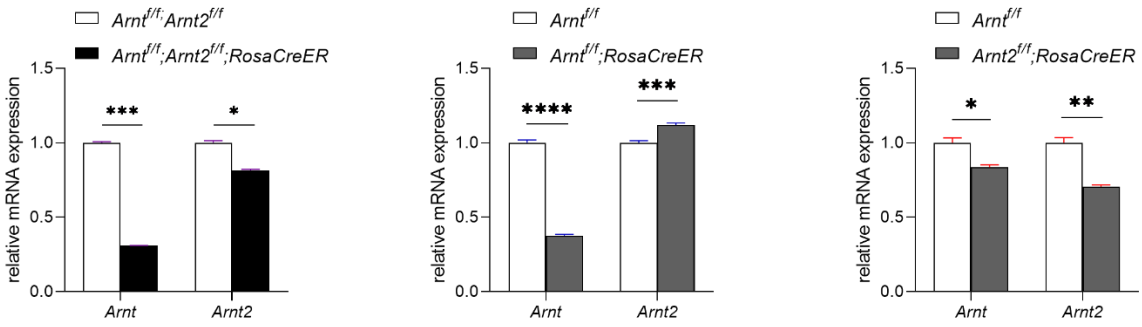


Figure 4-7. *Arnt* and *Arnt2* mRNA expression in the kidneys of *Arnt1/2*dKO and *Arnt* or *Arnt2* single knock-out mice.

Arnt and *Arnt2* mRNA expression in *Arnt1/2*dKO and *Arnt/Arnt2* single knock-out mice exposed to 7-day 10% O_2 hypoxia, quantified by RT-qPCR normalised to *Actb* and presented relative to the Cre^- controls for each gene. Data represent mean ± SEM, $n = 3$ (except for *Arnt1/2*dKO kidneys, $n = 2$), compared between genotypes by a Student's *t*-test, $*P < 0.05$, $**P < 0.01$, $***P < 0.001$, $****P < 0.0001$.

To test ARNT1/2 recombination specifically in the CB, tissues were pooled (due to small CB size resulting in low mRNA yield) across five females of *Arnt*$^{f/f}$*;Arnt2*$^{f/f}$*;RosaCreER, Arnt*$^{f/f}$*;RosaCreER* or *Arnt2*$^{f/f}$*;RosaCreER* mice and matched controls, subjected to the same hypoxia protocol as above, but without ventilatory assessments or BrdU treatment (Figure 4-6). Isoform-specific loss was detected in the CB across all models, with 53.0% *Arnt* and 33.7% *Arnt2* mRNA loss in *Arnt1/2*dKO animals (Figure 4-8A); 52.2% loss of *Arnt* and 17.4% increase in *Arnt2* mRNA in *Arnt*KO animals (Figure 4-8B); and 69.3% loss of *Arnt2*, with 15.2% loss in *Arnt* mRNA, in the *Arnt2*KO mice (Figure 4-8C).

Together, marked loss of *Arnt* and *Arnt2* mRNA was observed in the CBs of both double and single knock-out animals (with isoform specificity as expected). The milder recombination levels observed in the kidneys may therefore be due to lower *Arnt1/2* expression levels in this tissue, or due to differences in the Rosa26Cre expression/recombination efficiency between the CB and kidney.

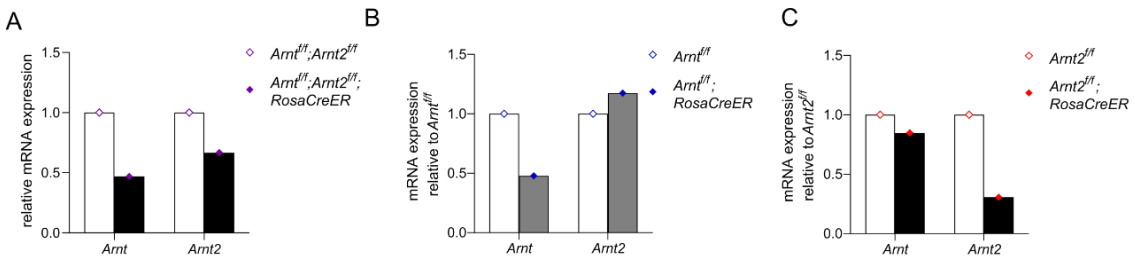


Figure 4-8. Targeted *Arnt* and *Arnt2* inactivation in the *Arnt*$^{f/f}$*;RosaCreER* and *Arnt2*$^{f/f}$*;RosaCreER* CBs.

Arnt and *Arnt2* mRNA normalised to *Actb* and expressed relative to the control (Cre$^-$ animals), quantified by RT-qPCR in tissues pooled from 5 animals per genotype in (**A**) *Arnt1/2*dKO, (**B**) *Arnt*KO and (**C**) *Arnt2*KO, exposed to 10% O_2 for 7 days. Each data-point represents one experiment on RNA extracted from tissues pooled from 5 animals.

4.2.4 *Effects of Arnt inactivation on HIF-2-dependent erythropoiesis*

To test if genetic ARNT or ARNT2 inactivation prevents hypoxia-induced polycythaemia, haematocrits were measured in male and female *Arnt*$^{f/f}$*;Arnt2*$^{f/f}$*;RosaCreER* animals exposed to CH (Figure 4-9A, D). Control *Arnt*$^{f/f}$*;Arnt2*$^{f/f}$ mice of both sexes had high haematocrits after the 7-day CH ($61 \pm 2\%$, $n = 7$ males and $61 \pm 1\%$, $n = 11$ females, Figure 4-9). Inactivation of both ARNT isoforms using the ubiquitously expressed RosaCreER resulted in a significant reduction in haematocrits in both populations ($56 \pm 1\%$, $n = 8$ males, $P = 0.0109$; $54 \pm 1\%$, $n = 11$ females, $P < 0.0001$, Figure 4-9). However, the haematocrits of both male and female hypoxic *Arnt*$^{f/f}$*;Arnt2*$^{f/f}$*;RosaCreER* mice were still higher than the value reported in normoxic wild-type males in the previous studies in this laboratory ($51 \pm 1\%$, Hodson et al., 2016, $46 \pm 1\%$, Cheng et al., 2020), suggesting incomplete loss of the polycythaemic response to hypoxia in mice with ARNT/ARNT2 inactivation.

To test the role of ARNT *vs* ARNT2 in mediating the hypoxia-induced polycythaemia, haematocrits were next measured in *Arnt*$^{f/f}$*;RosaCreER* and *Arnt2*$^{f/f}$*;RosaCreER* mice with single inactivation of each of the isoforms (Figure 4-9B-C and E-F). Single

inactivation of *Arnt* caused only a mild reduction in haematocrits after 7-day hypoxia in males ($57 \pm 1\%$ in *Arnt*$^{f/f}$ *vs* $54 \pm 1\%$ in *Arnt*$^{f/f}$*;RosaCreER*, $P = 0.162$, Figure 4-9B), but a significant loss in haematocrits was observed in *Arnt*$^{f/f}$*;RosaCreER* females relative to littermate *Arnt*$^{f/f}$ controls ($59.0 \pm 0.3\%$ in *Arnt*$^{f/f}$ *vs* $51 \pm 1\%$ in *Arnt*$^{f/f}$*;RosaCreER*, $P = 0.0006$, Figure 4-9E). Note the lower average haematocrit in acclimatised *Arnt*$^{f/f}$ male controls compared to other groups, suggesting possible lower acclimatisation in some of these mice as a factor contributing to the milder effect of ARNT inactivation. Further, male animals were removed from the altitude chamber for plethysmography on days 2 and 7, while female mice remained in the altitude chamber for the duration of the experiment, possibly resulting in a stronger hypoxic drive on erythropoietin synthesis. No changes in haematocrits in acclimatised *Arnt2*$^{f/f}$*;RosaCreER* males or females compared to *Arnt2*$^{f/f}$ littermates were observed (Figure 4-9C, F).

Together, inactivation of ARNT1/2 reduces haematocrits of CH mice, with some evidence that inactivation of just the *Arnt*, but not *Arnt2*, isoform, may be sufficient to prevent hypoxic polycythaemia.

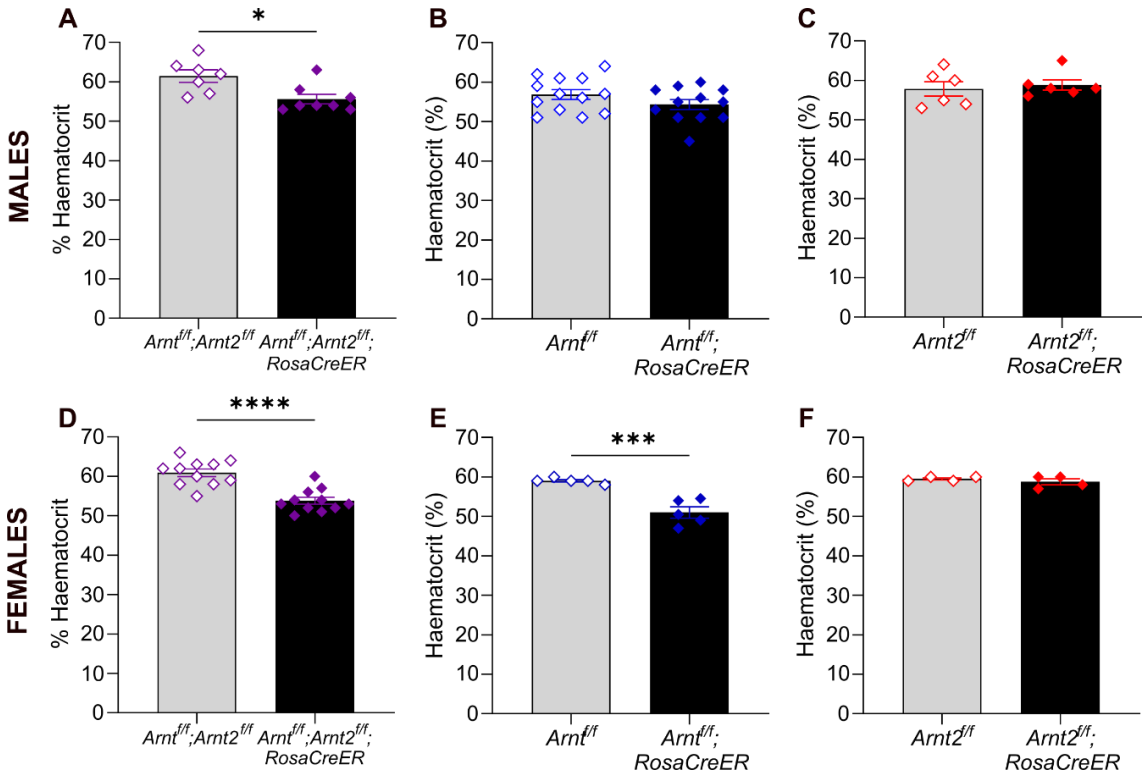


Figure 4-9. Hypoxia-induced polycythaemia in mice with adult-onset *Arnt* and *Arnt2* inactivation.

% Haematocrits in male (A-C) and female (D-F) *Arnt*$^{f/f}$*;Arnt2*$^{f/f}$*;RosaCreER* (A, D), *Arnt*$^{f/f}$*;RosaCreER* (B, E) and *Arnt2*$^{f/f}$*;RosaCreER* (C, F) mice compared with littermate controls, acclimatised to 7-days 10% oxygen. Bars show the mean ± SEM of the individual points plotted. Within each dataset, genotype groups are compared by a Student's *t*-test, $*P < 0.05$, $***P < 0.001$, $****P < 0.0001$.

4.2.5 *Ventilatory acclimatisation to hypoxia in mice with Arnt and Arnt2 inactivation*

To test if inactivation of ARNT1/2 prevents VAH, *Arnt1/2*dKO mice were housed in a normobaric 10% O_2 chamber for 7 days and hypoxic and hypercapnic AVRs were measured prior to the start (post TMX) and after 2 and 7 days of Hypoxia (H) (Figure 4-10). Inactivation of *Arnt* and *Arnt2* did not affect either 10% O_2/3% CO_2 or 10% O_2 AVRs in unacclimatised mice, as evidenced by no significant effect in the two-way ANOVA analysis of *Arnt*$^{f/f}$*;Arnt2*$^{f/f}$ vs *Arnt*$^{f/f}$*;Arnt2*$^{f/f}$*;RosaCreER* mice at Baseline *vs* post TMX (Figure 4-10, Time×genotype interaction $P = 0.0929$ for 10% O_2 and $P =$

0.5309 for 10% O_2/3% CO_2). Note there was a small change in AVRs to 10% O_2, but not 10% O_2/3% CO_2 from Baseline to post TMX recording, which may be due to the stress caused by tamoxifen treatment or small differences in the way animals were acclimatised to the plethysmographs (as responses to 10% O_2 are recorded first).

Chronic exposure to 10% O_2 caused an exacerbation in the HVRs of both control and *Arnt1/2*dKO mice, with significantly increased AVRs to both 10% O_2/3% CO_2 and 10% O_2, as well as 3% CO_2, over the course of 7-day exposure (Figure 4-10 and

Table 4-1, 2-way ANOVA Time $P < 0.0001$, $P = 0.0003$ and $P = 0.0002$ for the 3 types of stimuli respectively). Inactivation of *Arnt* and *Arnt2* did not affect 10% O_2/3% CO_2 AVR following 2 days of sustained hypoxia, but there was a trend towards decreased MVb under 10% O_2/3% CO_2 after 7-day hypoxia (Figure 4-10A). This reduction was not statistically significant in the two-way ANOVA comparison of *Arnt*$^{f/f}$*;Arnt2*$^{f/f}$ *vs Arnt*$^{f/f}$*;Arnt2*$^{f/f}$*;RosaCreER* mice. No significant difference in 10% O_2 AVRs was detected at the 7d H time-point, however, *Arnt*$^{f/f}$*;Arnt2*$^{f/f}$*;RosaCreER* mice had significantly lower responses at 2d H (Figure 4-10B, middle panel).

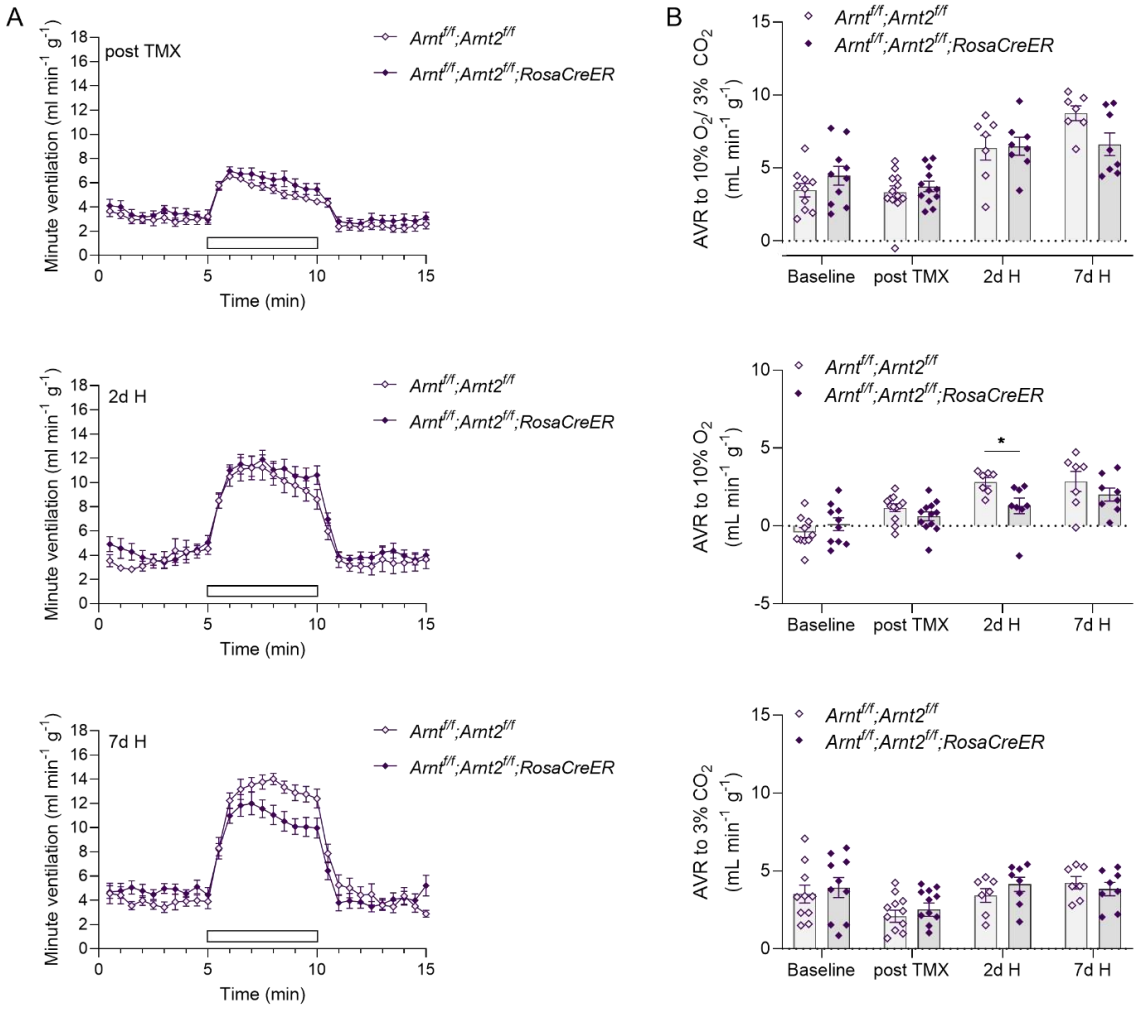


Figure 4-10. VAH in mice with acute genetic ARNT and ARNT2 inactivation.
(**A**) MVb in normal air and in response to 5 min 10% O_2/ 3% CO_2 stimulus (open bars) in *Arnt*$^{f/f}$*;Arnt2*$^{f/f}$*;RosaCreER* mice and *Arnt*$^{f/f}$*;Arnt2*$^{f/f}$ controls 10 days following the start of tamoxifen treatment (post TMX) and after 2 and 7 days of continuous exposure to 10% O_2 hypoxia (H). Data-points represent mean ± SEM, $n = 12$ at post TMX, $n = 8$ at 2 and 7d H. (**B**) AVRs to 10% O_2/ 3% CO_2 (quantified from MVb data in A), 10% O_2 and 3% CO_2. Baseline is d0 prior to the start of tamoxifen treatment. Data are shown as mean ± SEM with individual data-points displayed. For each gas stimulus, data were analysed by a two-way ANOVA, followed by Holm Sidak's *t*-tests, $*P < 0.05$. Details of the two-way ANOVA *P* values are shown in

Table 4-1).

Table 4-1. AVRs in animals with acute genetic *Arnt* and *Arnt2* inactivation.

AVRs to 10% O_2/ 3% CO_2, 10% O_2 or 3% CO_2, quantified as the difference between MVb during the first stable minute of stimulus and the MVb in the last minute of normoxia before the stimulus application, from the recordings in Figure 4-10. Baseline is d0 prior to the start of tamoxifen treatment and post TMX is d10 after the start of tamoxifen treatment, following which animals were exposed to 7-day 10% O_2 hypoxia (H). For each stimulus, data were analysed by a two-way ANOVA, with the Time (right-hand side column), *Arnt*KO (bottom row) and interaction (bottom right corner) *P* values shown; followed by Holm Sidak's *t*-tests (second column from the right). Data for Baseline were excluded from the two-way ANOVA analysis and an unpaired Student's *t*-test was applied instead. $P < 0.05$ values are shown in bold; $n = 10$ for Baseline, $n = 12$ for post TMX and $n = 8$ for 2 and 7d H.

		Arnt$^{f/f}$;*Arnt2*$^{f/f}$		*Arnt*$^{f/f}$;*Arnt2*$^{f/f}$; *RosaCreER*			Time/ Interaction
	Time-point	Mean	SEM	Mean	SEM	*t* -test *P*	*P*
10% O_2/3% CO_2	Baseline	3.5	0.5	4.5	0.6	*0.227*	
	post TMX	3.3	0.4	3.7	0.4	*0.924*	
	2d H	6.4	0.9	6.5	0.6	*0.999*	***<0.0001***
	7d H	8.8	0.5	6.6	0.8	*0.055*	
	ArntKO P		*0.253*				*0.073*
10% O_2	Baseline	-0.4	0.3	0.1	0.4	*0.320*	
	post TMX	1.2	0.2	0.6	0.3	*0.581*	
	2d H	2.8	0.3	1.3	0.5	*0.036*	***0.0003***
	7d H	2.9	0.6	2.0	0.4	*0.412*	
	ArntKO P		***0.004***				*0.416*
3% CO_2	Baseline	3.5	0.6	3.9	0.6	*0.637*	
	post TMX	2.1	0.4	2.5	0.4	*0.806*	
	2d H	3.4	0.4	4.1	0.5	*0.650*	***0.0002***
	7d H	4.2	0.4	3.8	0.4	*0.909*	
	ArntKO P		*0.502*				*0.471*

MVb is a product of respiratory rate and tidal volume. While it provides a more complete measurement of changes in ventilation, it may not be as sensitive as measuring TVb alone, due to the effects of animal behaviour on RR (Bishop et al., 2013). To investigate if the reduction in VAH caused by *Arnt1/2* inactivation may be more evident in TVb measurements, TVb during acute exposures to 10% O_2/3% CO_2 was assessed before the start and after 2 and 7-day H (Figure 4-11A). As described previously (Bishop et al., 2013), chronic exposure to hypoxia caused a progressive increase in TVb HVR in control mice (Figure 4-11A).

Unacclimatised *Arnt1/2*dKO mice had similar changes in TVb in response to acute hypoxia as their littermate controls and showed an increase in the acute 10% O_2/3% CO_2 TVb response after 2-day H (Figure 4-11A). By the 7th day of CH, however, there was a decrease in basal TVb in the *Arnt1/2*dKOs, as well as a reduced 10% O_2/3% CO_2 AVR (Figure 4-11A, bottom row). Despite this, no significant difference between HVRs of *Arnt1/2*dKOs and controls was detected (Figure 4-11B, Table 4-2), due to high variability in the ventilatory data and a mild reduction in baseline ventilation in *Arnt1/2*dKO mice (Figure 4-11A, 7d H). No significant difference between average TVb during 5 min 10% O_2/3% CO_2 (unpaired Student's *t*-test $P = 0.152$) or between average resting TVb prior to hypoxia ($P = 0.847$) were found between control and *Arnt1/2*dKO mice at 7d H either.

Overall, loss of both ARNT isoforms appears to cause a mild VAH reduction, which is more apparent in TVb and may further involve a reduction in baseline ventilation in acclimatised mice.

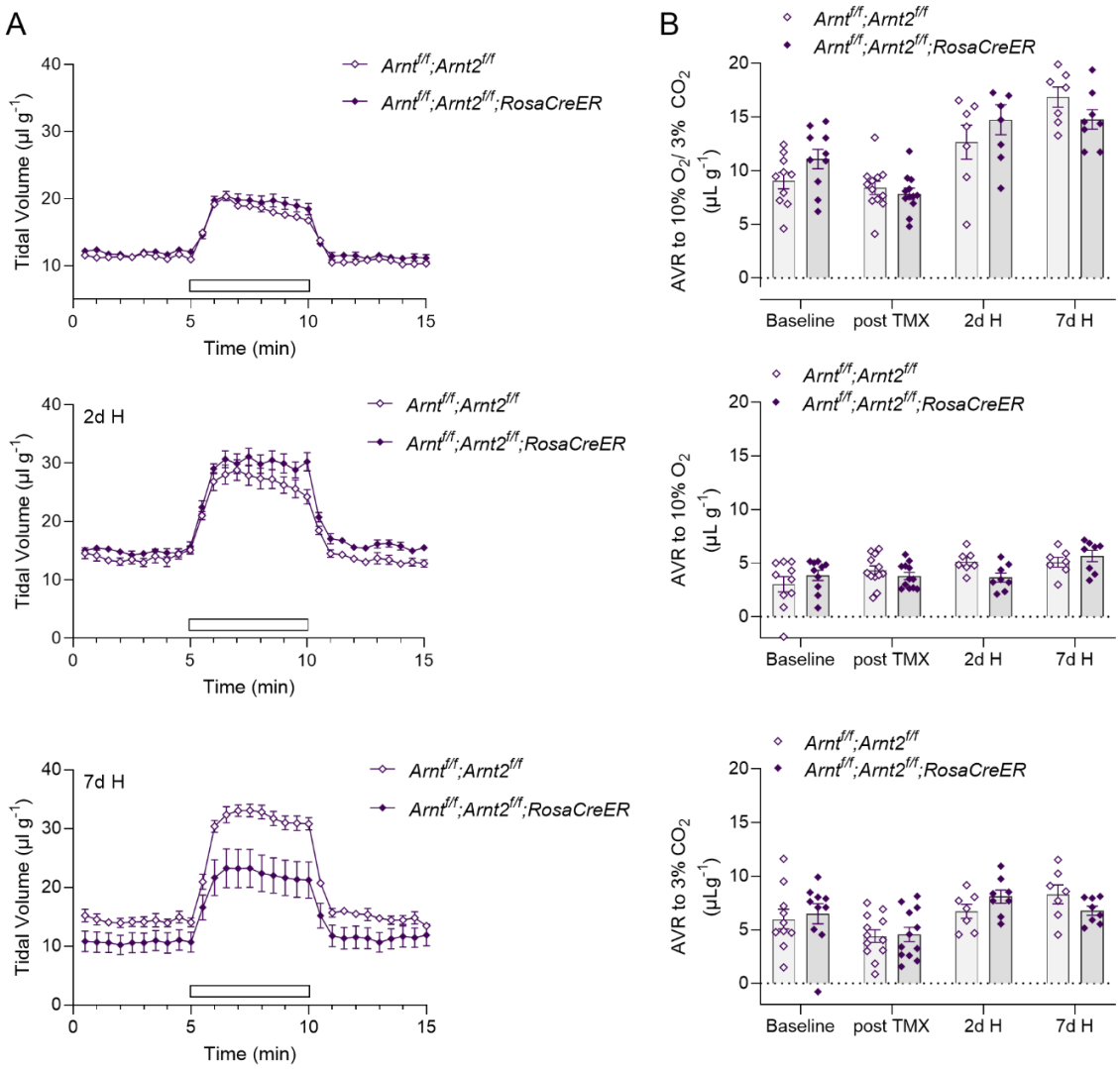


Figure 4-11. VAH in *Arnt1/2*dKO mice measured by changes in TVb.

(**A**) TVb in air and in response to 5 min 10% O_2/3% CO_2 (open bars) in *Arnt*$^{f/f}$;*Arnt2*$^{f/f}$;*RosaCreER* mice and *Arnt*$^{f/f}$;*Arnt2*$^{f/f}$ controls 10 days following the start of tamoxifen treatment (post TMX) and after 2 and 7 days of continuous exposure to 10% O_2 hypoxia (H). Data-points represent mean ± SEM, $n = 12$ at post TMX, $n = 8$ at 2 and 7d H. (**B**) AVRs to 10% O_2/3% CO_2 (quantified from TVb data in A), 10% O_2 or 3% CO_2. Baseline is d0 prior to the start of tamoxifen treatment. Bars represent mean ± SEM with individual data-points displayed. For each gas stimulus, data were analysed by a two-way ANOVA, followed by Holm Sidak's *t*-tests (no $P < 0.05$ detected). Details of the two-way ANOVA *P* values are shown in Table 4-2.

Table 4-2. AVRs in *Arnt1/2*dKO mice measured as changes in TVb.

AVRs to 10% O_2/ 3% CO_2, 10% O_2 or 3% CO_2, quantified from TVb recordings as shown in Figure 4-11. Baseline is d0 prior to the start of tamoxifen treatment and post TMX is d10 after the start of tamoxifen treatment, following which animals were exposed to seven days of 10% O_2 hypoxia (H). For each gas stimulus, data were analysed by a two-way ANOVA, with the Time (right-hand side column), *Arnt1/2*dKO (bottom row) and interaction (bottom right corner) *P* values shown; followed by Holm Sidak's *t*-tests (second column from the right). Data for Baseline were excluded from the two-way ANOVA analysis and a simple Student's *t*-test was applied instead. $P < 0.05$ values are in bold; $n = 10$ for Baseline, $n = 12$ for post TMX and $n = 8$ for 2 and 7d H.

		$Arnt^{f/f};Arnt2^{f/f}$		$Arnt^{f/f};Arnt2^{f/f};RosaCreER$			Time/ Interaction
	Time-point	Mean	SEM	Mean	SEM	*t*-test *P*	*P*
10% O_2/3% CO_2	Baseline	9.1	± 0.8	11.1	± 0.9	*0.106*	
	post TMX	8.4	± 0.6	7.9	± 0.5	*0.953*	
	2d H	12.7	± 1.6	14.8	± 1.4	*0.409*	***<0.0001***
	7d H	16.9	± 0.9	14.8	± 0.9	*0.409*	
	ArntKO P		*0.819*				*0.135*
10% O_2	Baseline	3.0	± 0.7	3.9	± 0.5	*0.347*	
	post TMX	4.3	± 0.4	3.8	± 0.3	*0.694*	
	2d H	5.1	± 0.4	3.7	± 0.4	*0.080*	***0.010***
	7d H	5.1	± 0.5	5.7	± 0.5	*0.767*	
	ArntKO P		*0.185*				*0.094*
3% CO_2	Baseline	6.0	± 0.9	6.5	± 0.9	*0.707*	
	post TMX	4.4	± 0.6	4.6	± 0.7	*0.996*	
	2d H	6.7	± 0.7	8.1	± 0.6	*0.456*	***<0.0001***
	7d H	8.3	± 0.9	6.8	± 0.4	*0.366*	
	ArntKO P		*0.992*				*0.140*

4.2.6 *Ventilatory acclimatisation to hypoxia in mice with either Arnt or Arnt2 inactivation in adulthood*

Given a mild VAH reduction was observed in hypoxic *Arnt1/2*dKO mice (Figure 4-10), the next step was to investigate if this effect requires inactivation of both *Arnt* and *Arnt2*, or if it only depends on one of the isoforms. $Arnt^{f/f}$;*RosaCreER* and $Arnt2^{f/f}$;*RosaCreER* mice

with littermate controls have been subjected to the same CH protocol as above (Figure 4-6) and VAH was assessed by plethysmography (Figure 4-12, Table 4-3,

Table 4-4). There was strong evidence of VAH in both control cohorts, with respect to AVRs to both 10% O_2/3% CO_2, and 10% O_2 alone, but not 3% CO_2 (Figure 4-12, Table 4-3,

Table 4-4). Although a small reduction in MVb under 10% O_2/3% CO_2 was observed in *Arnt*$^{f/f}$*;RosaCreER* mice acclimatised to 7d H (Figure 4-12A), there was no significant difference between 10% O_2/3% CO_2 AVRs of *Arnt*KO and control animals at this time-point (Figure 4-12B and Table 4-3), and the small reduction in the AVR mean was likely caused by one outlier *Arnt*KO mouse with very low HVR at 7d H. 10% O_2 AVRs were lower in acclimatised *Arnt*KO mice than in controls (Table 4-3), although this did not reach statistical significance.

Inactivation of *Arnt2* alone did not cause any changes in VAH, with no significant differences between AVRs to either 10% O_2/3% CO_2 or 10% O_2 alone (Figure 4-12C-D and

Table 4-4).

Since effects of *Arnt1/2* inactivation on VAH were more clearly evident in TVb recordings, TVb under acute 10% O_2/3% CO_2 exposure was assessed in single *Arnt* or *Arnt2*KO mice throughout the acclimatisation protocol (Figure 4-13). No differences in TVb changes under acute hypoxia were found in either unacclimatised or 2 and 7-day acclimatised *Arnt*KO and *Arnt2*KO mice compared with their littermate controls, suggesting that the small MVb decrease at 7d H observed in *Arnt*$^{f/f}$*;RosaCreER* mice (Figure 4-12A, B) was due to behavioural differences in the outlier KO mouse, affecting RR, rather than physiological adaptations in carotid chemoreception.

Overall, inactivation of either *Arnt* or *Arnt2* isoform on its own did not prevent VAH, while co-inactivation of both isoforms caused a mild VAH reduction (more clearly evident in TVb analysis), suggesting some redundancy between *Arnt* and *Arnt2*.

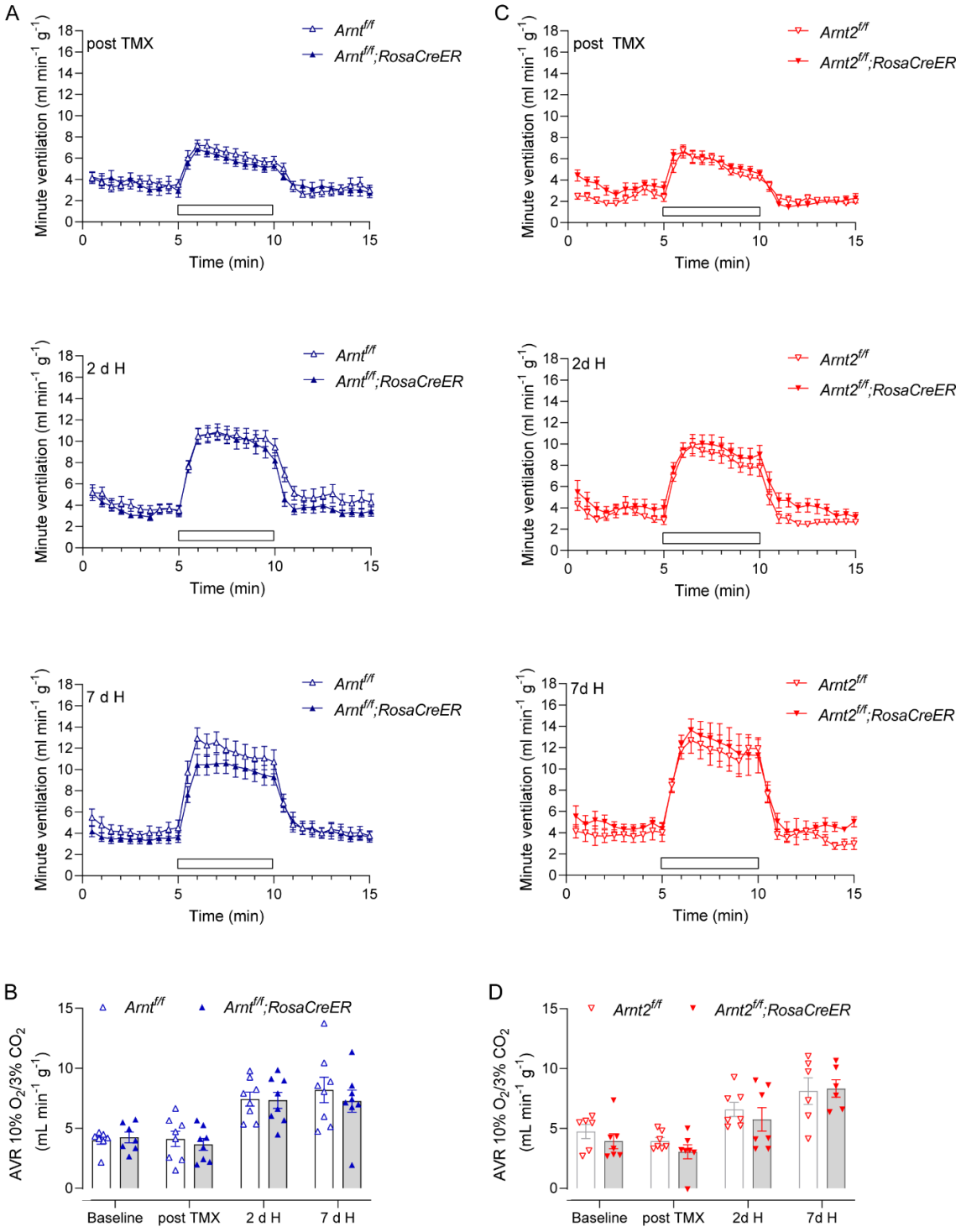


Figure 4-12. VAH in mice with either *Arnt* or *Arnt2* inactivation in adulthood.

(**A, C**) MVb in normal air and in response to 5 min 10% O_2/3% CO_2 stimulus (open bars) in *Arnt*$^{f/f}$*;RosaCreER* (**A**) and *Arnt2*$^{f/f}$*;RosaCreER* (**C**) mice with *Arnt*$^{f/f}$ or *Arnt2*$^{f/f}$ controls respectively, 10 days following the start of tamoxifen treatment (post TMX) and after 2 and 7-day 10% O_2 hypoxia (H). Data-points represent mean ± SEM, $n = 8$ in A, $n = 7$ for Baseline post TMX and 2d H in C, $n = 6$ for 7d H in C. (**B, D**) AVRs to 10% O_2/3% CO_2, quantified from the MVb recordings as shown in A and C respectively. Baseline is d0 prior to the start of

tamoxifen treatment. Data are shown as mean ± SEM with individual data-points displayed. For each genotype, data were analysed by a two-way ANOVA, followed by Holm Sidak's *t*-tests, and no statistically significant ($P < 0.05$) comparisons were detected. Details of the two-way ANOVA *P* values are shown in Table 4-3 and

Table 4-4).

Table 4-3. AVRs in animals with acute *Arnt* inactivation in adulthood.

AVRs to 10% O_2/ 3% CO_2, 10% O_2 or 3% CO_2, quantified as the difference between MVb during the first stable minute of stimulus and the MVb in the last minute of normoxia prior to the stimulus application, from the recordings in Figure 4-12. Baseline is d0 prior to the start of tamoxifen treatment and post TMX is d10 after the start of tamoxifen treatment, following which animals were exposed to seven days of 10% O_2 hypoxia (H). For each gas stimulus, data were analysed by a two-way ANOVA, with the Time (right-hand side column), *Arnt2KO* (bottom row) and interaction (bottom right corner) *P* values shown; followed by a Holm Sidak's *t*-test (second column from the right). Data for Baseline were excluded from the two-way ANOVA analysis and a simple Student's *t*-test was applied instead. $P < 0.05$ values are shown in bold; $n = 7$ for Baseline, post TMX and 2d H, $n = 6$ for 7d H.

		$Arnt^{f/f}$		$Arnt^{f/f}$;*RosaCreER*			Time/
	Time-point	Mean	SEM	Mean	SEM	*t*-test *P*	Interaction *P*
10% O_2/3% CO_2	Baseline	4.0	0.3	4.2	0.4	*0.653*	
	post TMX	4.1	0.6	3.7	0.5	*0.894*	
	2d H	7.4	0.6	7.3	0.7	*0.926*	***<0.0001***
	7d H	8.2	1.1	7.3	0.9	*0.772*	
	ArntKO P		*0.576*				*0.749*
10% O_2	Baseline	0.4	0.4	1.0	0.3	*0.286*	
	post TMX	0.7	0.3	0.6	0.4	*0.922*	
	2d H	2.7	0.4	1.7	0.3	*0.195*	***<0.0001***
	7d H	3.8	0.4	2.5	0.4	*0.141*	
	ArntKO P		*0.058*				*0.229*
3% CO_2	Baseline	2.7	0.2	2.8	0.6	*0.887*	
	post TMX	2.0	0.5	2.2	0.3	*0.792*	
	2d H	2.2	0.5	2.7	0.3	*0.750*	*0.702*
	7d H	2.0	0.8	2.6	0.6	*0.789*	
	ArntKO P		*0.352*				*0.888*

Table 4-4. AVRs in animals with acute *Arnt2* inactivation in adulthood.

AVRs to 10% O_2/ 3% CO_2, 10% O_2 or 3% CO_2, quantified as the difference between MVb during the first stable minute of stimulus and the MVb in the last minute of normoxia prior to the stimulus application, from the recordings in Figure 4-12. Baseline is d0 prior to the start of tamoxifen treatment and post TMX is d10 after the start of tamoxifen treatment, following which animals were exposed to seven days of 10% O_2 hypoxia (H). For each gas stimulus, data were analysed by a two-way ANOVA, with the Time (right-hand side column), *Arnt2KO* (bottom row) and interaction (bottom right corner) *P* values shown; followed by a Holm Sidak's *t*-test (second column from the right). Data for Baseline were excluded from the two-way ANOVA analysis and a simple Student's *t*-test was applied instead. $P < 0.05$ values are shown in bold; $n = 7$ for Baseline, post TMX and 2d H, $n = 6$ for 7d H.

		Arnt2$^{f/f}$		*Arnt2*$^{f/f}$;*RosaCreER*			
	Time-point	Mean	SEM	Mean	SEM	*t* -test *P*	Time/ Interaction *P*
10% O_2/3% CO_2	Baseline	4.7	0.6	3.9	0.6	*0.376*	
	post TMX	3.9	0.3	3.1	0.6	*0.770*	
	2d H	6.6	0.6	5.8	1.0	*0.806*	***<0.0001***
	7d H	8.1	1.1	8.3	0.7	*0.992*	
	Arnt2 KO *P*		*0.562*				*0.541*
10% O_2	Baseline	-0.7	0.7	0.5	0.5	*0.218*	
	post TMX	1.5	0.2	1.0	0.3	*0.697*	
	2d H	1.3	0.5	2.4	0.2	*0.148*	***0.003***
	7d H	2.5	0.4	2.7	0.7	*0.983*	
	Arnt2 KO *P*		*0.548*				*0.057*
3% CO_2	Baseline	0.8	0.5	0.4	0.3	*0.492*	
	post TMX	3.1	0.6	2.6	0.3	*0.930*	
	2d H	2.7	0.7	2.2	0.7	*0.908*	*0.450*
	7d H	3.2	0.4	3.1	0.8	*0.999*	
	Arnt2 KO *P*		*0.565*				*0.921*

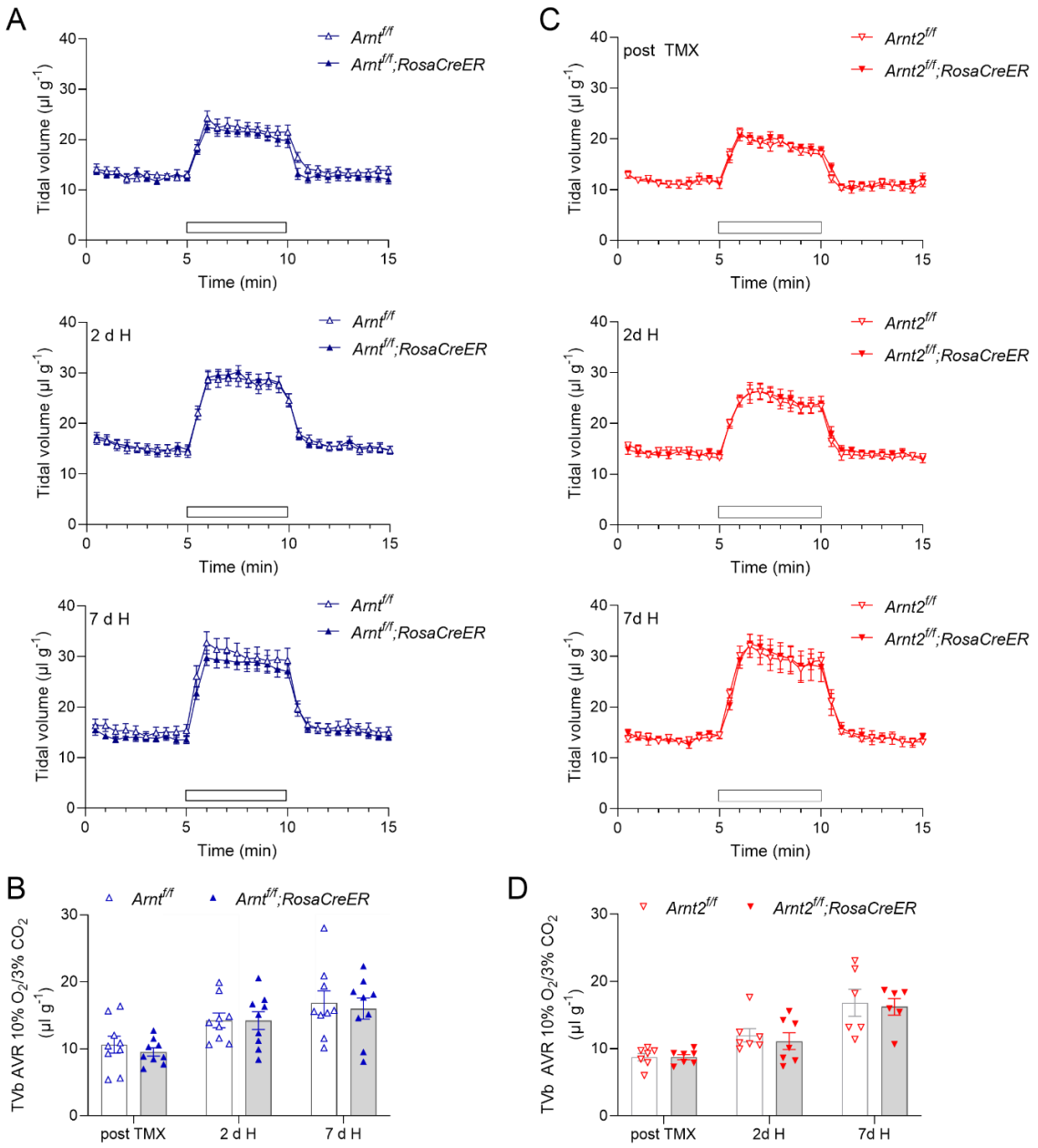


Figure 4-13. VAH in *Arnt1/2* single knock-out mice measured by changes in TVb.

(**A, C**) TVb in normal air and in response to 5 min 10% O_2/ 3% CO_2 stimulus (open bars) in (A) *Arnt*$^{f/f}$*;RosaCreER* and (B) *Arnt2*$^{f/f}$*;RosaCreER* mice and *Arnt*$^{f/f}$ or *Arnt2*$^{f/f}$ controls, 10 days following the start of tamoxifen treatment (post TMX) and after 2 and 7-day 10% O_2 hypoxia (H). Data-points represent mean ± SEM, $n = 9$ in *Arnt*$^{f/f}$*;RosaCreER* cohort, $n = 7$ in *Arnt2*$^{f/f}$*;RosaCreER*, except 7d H, where $n = 6$. (**B, D**) AVRs to 10% O_2/ 3% CO_2 quantified from the TVb recordings shown in A, C respectively. Data are shown as mean ± SEM with individual data-points displayed. For each gas stimulus, data were analysed by a two-way ANOVA, followed by Holm Sidak's *t*-tests. Difference over time $P < 0.0001$ in both datasets but no other significant comparisons.

4.2.7 *Carotid body proliferation in response to hypoxia in mice with Arnt and Arnt2 inactivation.*

To test if the HIF-2α function in hypoxic CB proliferation is mediated by dimerisation with HIF-β and subsequent alteration of gene expression, cellular BrdU incorporation and CB volume were measured in the CBs of *Arnt*$^{f/f}$*;Arnt2*$^{f/f}$*;RosaCreER* mice exposed to 10% O_2 for 7 days (see experimental design in Figure 4-6). There was high BrdU incorporation in the *Arnt*$^{f/f}$*;Arnt2*$^{f/f}$ control CBs (Figure 4-14, top row, 3241 ± 403 BrdU$^+$ cells mm^{-2}, $n = 4$), similar to the levels previously reported in acclimatised mice in the Oxford laboratory (2993 ± 153, Fielding et al., 2018). In contrast, BrdU$^+$ cell density was significantly lower in *Arnt1/2*dKO mice (Figure 4-14, top row, 2067 ± 252 BrdU$^+$ cells mm^{-2}, $n = 4$, Student's *t*-test $P = 0.0363$), although this was still markedly higher than previously reported in normoxic CBs (~250 BrdU$^+$ cells mm^{-2}, Bishop et al., 2013).

Despite this suppression of cellular proliferation in *Arnt*$^{f/f}$*;Arnt2*$^{f/f}$*;RosaCreER* mice, CB volumes were comparable with controls (0.0041 ± 0.0003 mm^3 in KO, *vs* 0.0041 ± 0.0007 mm^3 in control mice, Student's *t*-test $P = 0.960$, Figure 4-14). This may be because 7-day hypoxia only results in a small increase in CB volume (Cheng et al., 2020), with longer (~4 weeks) exposure required to observe marked hypertrophy (Fielding et al., 2018, Pardal et al., 2007).

In sum, ARNT1/2 inactivation reduced cellular proliferation in the CB in response to hypoxia, although marked levels of BrdU incorporation were still observed in *Arnt1/2*dKO CBs (in contrast to near-complete loss of BrdU in *Hif-2α*$^{f/f}$*;RosaCreER* mice, Hodson et al., 2016), suggesting a mild effect of ARNT1/2 inactivation on hypoxia-induced proliferation in the CB.

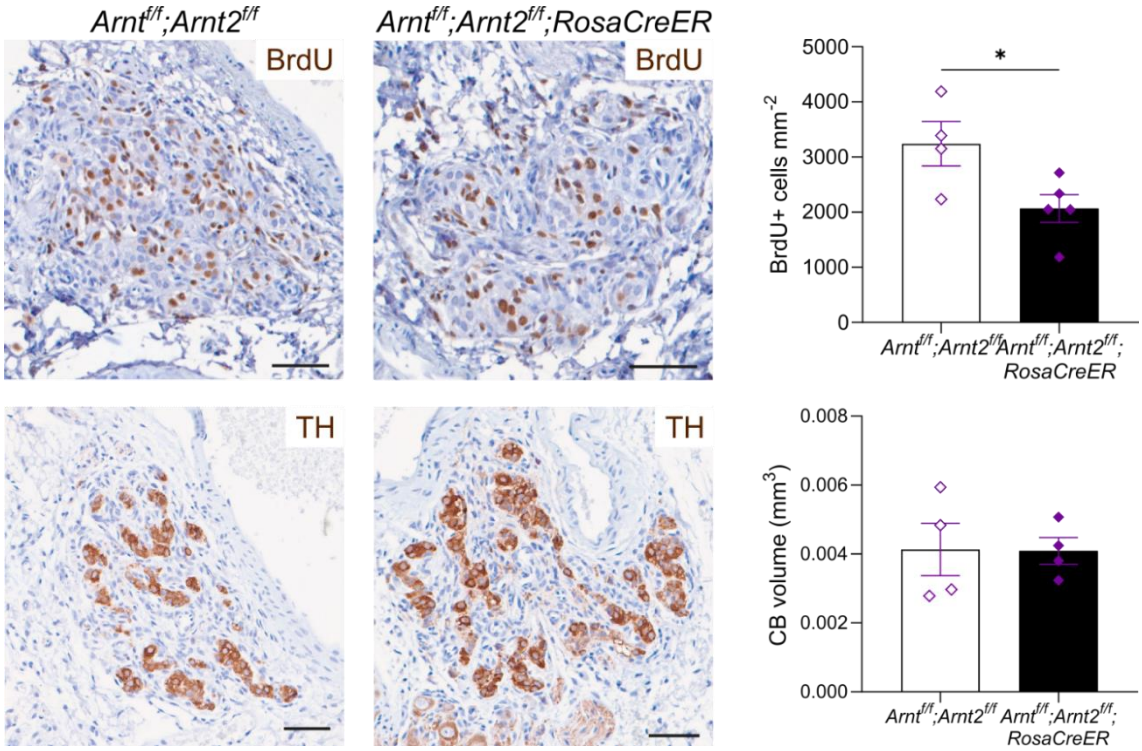


Figure 4-14. CB proliferation and hypertrophy in acclimatised *Arnt$^{f/f}$;Arnt2$^{f/f}$;RosaCreER* mice.

CB proliferation was measured by cellular BrdU incorporation (top row) and CB volume estimated from TH$^+$ areas (bottom row) in *Arnt$^{f/f}$;Arnt2$^{f/f}$;RosaCreER* animals (and littermate Cre$^-$ controls) exposed to 7d 10% O_2. Representative images from each immune stain are shown on the left (0.05 mm scale bars) and BrdU$^+$ cell density and CB volume are quantified in graphs on the right; mean ± SEM are plotted in bars with individual values shown. Data were compared between genotype groups by Student's *t*-test, $*P < 0.05$.

4.2.8 *Carotid body proliferation in response to hypoxia in mice with either Arnt or Arnt2 inactivation*

To test if inactivation of just one of the ARNT isoforms may be sufficient to cause a reduction in CB proliferation under hypoxia, as observed in *Arnt$^{f/f}$;Arnt2$^{f/f}$;RosaCreER* mice (Figure 4-14), BrdU cellular incorporation and CB volume were assessed in *Arnt$^{f/f}$;RosaCreER* and *Arnt2$^{f/f}$;RosaCreER* mice exposed to CH (Figure 4-15). High BrdU incorporation was observed in the CBs of both control and *Arnt*KO or *Arnt2*KO mice exposed to hypoxia, with a small, non-significant trend towards reduced

proliferation in *Arnt2*$^{f/f}$*;RosaCreER* mice (Figure 4-15B, 1869 ± 216 BrdU^{+} cells·mm^{-2} in *Arnt2*KO, compared with 2542 ± 330 in controls, Student's *t*-test $P = 0.163$). As per the *Arnt1/2*dKO animals, no differences in CB volumes were observed (Figure 4-15, unpaired Student's *t*-test $P = 0.555$ for *Arnt*$^{f/f}$*;RosaCreER* and $P = 0.560$ for *Arnt2*$^{f/f}$*;RosaCreER vs* control animals), suggesting inactivation of *Arnt* or *Arnt2* alone does not affect CB hypoxic growth and inactivation of both isoforms is required to achieve a significant reduction in cellular proliferation (Figure 4-14).

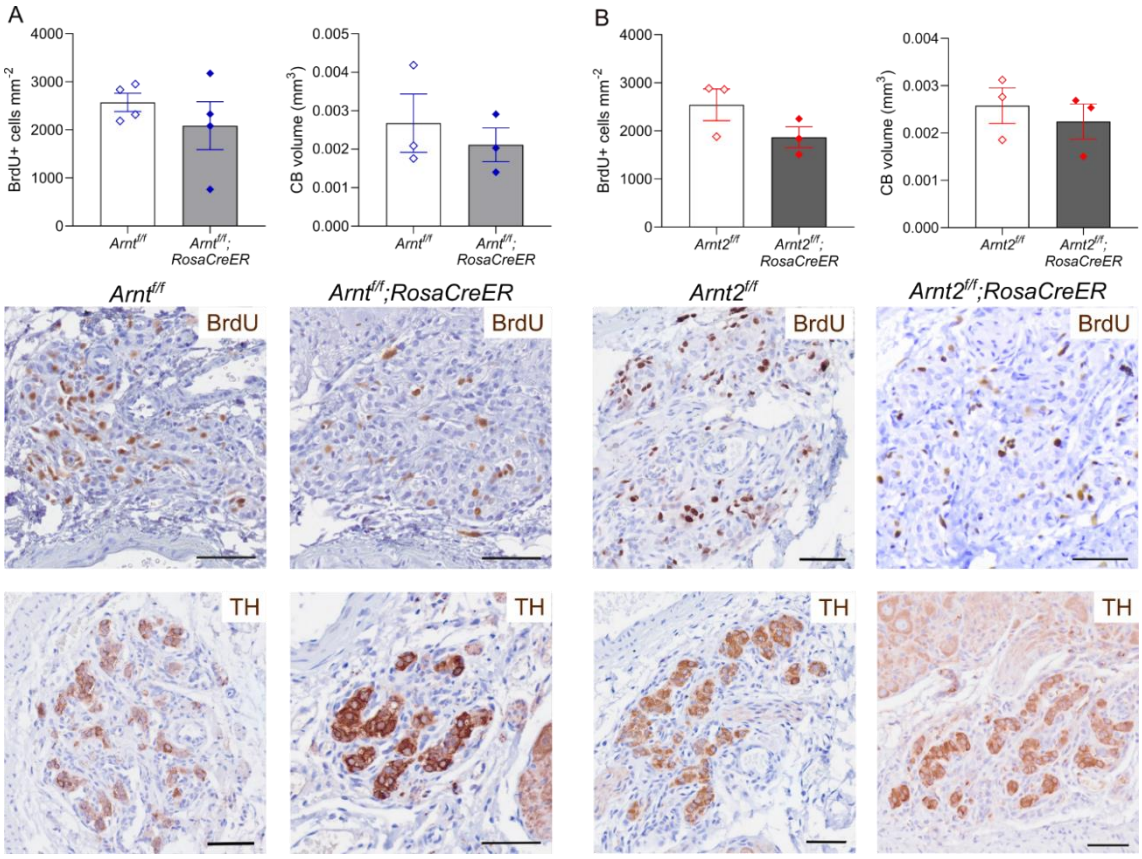


Figure 4-15. CB proliferation and hyperplasia in acclimatised *Arnt*$^{f/f}$*;RosaCreER* and *Arnt2*$^{f/f}$*;RosaCreER* mice.

BrdU^{+} cell density and CB volume quantified in (**A**) *Arnt*$^{f/f}$*;RosaCreER* and (**B**) *Arnt2*$^{f/f}$*;RosaCreER* mice and Cre^{-} controls acclimatised to 7-day CH. Representative images showing BrdU (top panels) and TH (bottom panels) IHC, used to quantify the responses are presented below the graphs. Scale bars represent 0.05 mm. Bars in graphs represent means ± SEM, with individual values displayed. Genotype groups were compared by Student's *t*-test with no statistically significant differences ($P < 0.05$).

4.3 **Discussion**

Earlier work by this and other laboratories suggested a potential non-transcriptional function of HIF-2α in regulating acute and long-term adaptations to hypoxia (Chapter 3, Cheng et al., 2020, Feng et al., 2018). To test this potential HIF-β-independent function of HIF-2α, HIF-α heterodimerisation partners: ARNT and ARNT2, classically considered to be necessary for HIF translocation to the nucleus and stimulation of HIF-target gene expression in response to hypoxia, were inactivated in adult mice.

Inactivation of *Arnt* and *Arnt2* resulted in a mild reduction in CH acclimatisation, with reduced hypoxia-induced polycythaemia, CB hypoxic proliferation and a mild reduction in VAH. Both ventilatory and CB proliferative responses to hypoxia were normal in *Arnt* and *Arnt2* single knock-outs, suggesting inactivation of both isoforms is necessary to prevent HIF-mediated adaptive responses to hypoxia. However, a reduction in hypoxia-induced polycythaemia was observed in female (but not male) *Arnt*KO mice, as well as *Arnt1/2*dKOs, suggesting a potential dominant function of the *Arnt1* isoform in the renal *Epo* stimulation.

Neuronal expression of *Arnt2*, as well as enrichment of *Arnt2 vs Arnt* in the CB (Gao et al., 2017, Zhou et al., 2016 and ISH results presented here), suggests a potential dominant function of the *Arnt2* over the *Arnt* isoform. However, there was no evidence for suppression of VAH or CB proliferation by *Arnt2*KO here and instead, VAH and CB proliferation reduction was only observed in *Arnt1/2*dKO mice. It is therefore possible that while *Arnt1* isoform mediates renal *Epo* stimulation under hypoxia, CB hypoxic phenotypes can be mediated by either of the *Arnt* isoforms, or independently of HIF-β heterodimerisation.

Redundancy between the ARNT and ARNT2 isoforms has been previously suggested in the literature based on their very high amino acid sequence similarity (57% overall, with

95 and 78% amino acid identity in the conserved bHLH and PAS regions respectively, Hirose et al., 1996), and the reports that ARNT2 can form functional complexes with HIF-1α and AHR (Maltepe et al., 2000, Hirose et al., 1996, Keith et al., 2011).
There is some evidence in the published literature that ARNT plays a role in mediating HIF-dependent phenotypes. For example, *Arnt* inactivation in the liver has been reported to result in a mild and selective reduction in HIF-target gene induction under hypoxia (Tomita et al., 2000, Scott et al., 2015) and *Arnt*KO mice repress several HIF-dependent phenotypes in models of wound healing, tissue regeneration and glucose control (Scott et al., 2014, Endo et al., 2020, Lau et al., 2013). Perhaps most convincingly, *Arnt*KO ablates polycythaemia caused by *Vhl* inactivation in the liver (Rankin et al., 2005). Redundancy between the ARNT and ARNT2 isoforms may therefore be phenotype- and/or tissue-specific.

The mild reduction in ventilatory, CB proliferative and hematopoietic adaptations to hypoxia in *Arnt1/*2dKOs reported here contrasts with the near complete loss in hypoxia-induced polycythaemia, VAH and CB proliferation observed in *Hif-2α*KO animals (Hodson et al., 2016). One reason for this could be the incomplete *Arnt* and *Arnt2* recombination with inducible Rosa26Cre^{ERT2}. Successful recombination to induce *Arnt* inactivation was confirmed by measuring *Arnt* mRNA levels. Although only ~50% loss in the CB and 60% loss of *Arnt* in the kidneys was observed, this is a reduction from already very low levels of basal expression in these tissues, and the degree of mRNA loss was comparable with that seen in *Hif-2α$^{f/f}$;RosaCreER* mice previously examined in the Oxford laboratory (Hodson et al., 2016 and unpublished data, EJH, PJR and TB). While *Hif-2α* mRNA levels are much higher than those of *Arnt* in the CB and interstitial fibroblasts, HIF-2α protein is subject to rapid degradation in the cytoplasm. It is therefore possible that, at the protein level, HIF-2α, and not ARNT, is the limiting factor

in the generation of functional HIF-2 heterodimers, thus a more complete loss of *Arnt* mRNA may be required to observe a reduction in hypoxic adaptation in these tissues. In the future, *Arnt1/2$^{f/-}$;RosaCreER* mice with complete, constitutive loss of one allele could be tested to achieve a better level of *Arnt* recombination.

Incomplete *Arnt1/2* recombination is an important caveat of this work and the mild phenotype in *Arnt1/2*dKO mice with respect to CB-mediated responses to hypoxia should be interpreted cautiously. Previous studies in *Arnt* and *Arnt2* knock-out animals have used HIF or AHR target gene expression as a means to validate successful functional inactivation. However, despite the identification of multiple HIF-target genes *in vitro*¸ reduction in HIF-2 target genes mRNA *in vivo* appears to be subtle and time-sensitive (Cheng et al., 2020, Feng et al., 2018, Persson et al., 2020). Due to their small size, quantitation of RNA from isolated CBs is technically challenging and requires pooling of tissues from multiple animals, while ISH technique only provides a semi-quantitative assessment of expression levels. For these reasons, target gene expression was not tested in *Arnt1/2* knock-out animals in this chapter, but testing mRNA levels of HIF-target genes in larger tissues could potentially provide indirect validation of the model.

Another potential reason for the milder reduction in acclimatisation with *Arnt1/2*dKO vs *Hif-2α*KO could be the existence of other bHLH proteins that can heterodimerise with HIF-2α to mediate its transcriptional function. Similar to ARNT1&2, BMAL1&2 are also members of the Class II bHLH protein family, binding different cellular stimuli-sensing transcription factors (Kewley et al., 2004). BMAL1 is primarily considered to heterodimerise with CLOCK to regulate the circadian rhythm (Mohawk et al., 2012), however, the potential interaction between HIF-1α and BMAL1 has previously been reported (although protein-protein heterodimerisation could not be established with co-

immunoprecipitation experiments) (Suyama et al., 2016). To resolve the potential redundancy between HIF-2α heterodimerisation partners as a caveat, a *Hif2-α* mutant mouse with a defective bHLH domain unable to dimerise with DNA could be designed.

In addition to the potential caveats of the *Arnt1/2*dKO mouse model, compensatory mechanisms at the systemic level could also contribute to the milder reduction in ventilatory, CB-proliferative and erythropoietic acclimatisation to hypoxia in *Arnt1/2*dKO compared to *Hif-2α*KO mice. Hypoxia-induced polycythaemia has previously been shown to be abolished in *Hif-2α$^{f/f}$;RosaCreER* mice (Hodson et al., 2016), but not in animals treated with a HIF-2α inhibitor, PT2385 (Cheng et al., 2020). Additionally, studies in mice with tissue-specific HIF-2α inactivation in the sympathoadrenal system showed elevated haematocrits under CH (Fielding et al., 2018) in mice with reduced VAH, suggesting that polycythaemia may act as a compensatory mechanism in hypoxic animals. Indeed, there appeared to be a negative correlation between AVRs to 10% O_2/3% CO_2 at 7d H and the haematocrits after 7 days at 10% O_2, although this was not statistically significant (Pearson's correlation $P = 0.209$, $n = 8$). Further studies of HIF-2α function in adaptive responses to hypoxia in isolated systems, such as the *ex vivo* CB preparations (Moreno-Dominguez et al., 2019), rather than in ubiquitous knock-out animals, may be needed to understand the mechanism of HIF-2α action in different tissues. The possibility of ARNT-independent, non-transcriptional function of HIF-2α has previously been suggested by others based on the differential effects of HIF-2α heterodimerisation inhibition with small molecules and protein loss (Persson et al., 2020), as well as the discovery of a ligand-binding pocket in the HIF-2α PAS-B domain, drawing a parallel with other ligand-regulated PAS domains such as in the xenobiotic-responsive AHR and many bacterial PAS proteins (Scheuermann et al.,

2009). The mild reduction in VAH and CB proliferation in *Arnt*$^{f/f}$*;Arnt2*$^{f/f}$*;RosaCreER* animals acclimatised to hypoxia supports this hypothesis.

Further work using alternative models, such as modifying HIF-2α to inactivate its DNA-binding bHLH domain, while preserving the structure of the PAS-B ligand binding cavity, could help corroborate the results from *Arnt1/2*dKO mice. Nevertheless, the results presented in this chapter, taken together with the hypomorphic phenotypes in *Hif-2α*$^{S305M/S305M}$ mice with obstructed PAS-B ligand binding domain but normal ARNT dimerisation (Cheng et al., 2020, Feng et al., 2018), as well as the rapid effects of PT2385 on HVR (Cheng et al., 2020), suggest the possibility of a non-transcriptional role for HIF-2. Ultimately, the non-transcriptional HIF-2α function would need to be confirmed by identification of an endogenous ligand interacting with the HIF-2α PAS-B domain. Linking such a ligand to the CB function would provide a breakthrough in understanding the role of the HIF-2α protein in the physiology, and pathophysiology of the sympathoadrenal system.

5

Role of regulators of G-protein signalling in the carotid body response to hypoxia

5.1 Introduction

To gain a better understanding of signalling pathways involved in CB oxygen sensing, transcriptomic studies have been performed in whole CBs and type I cells, and gene expression compared with that of non-oxygen-sensitive neuronal tissue, SCG (Gao et al., 2017, Zhou et al., 2016). These studies have identified *Epas1*, encoding HIF-2α, as both highly up-regulated in the CB compared to the SCG (Gao et al., 2017), and the second most abundant gene in the CB type I cells (Zhou et al., 2016). In line with this, high CB-specific expression of *Epas1* mRNA encoding HIF-2α has been shown to play a crucial role in mediating the CB responses to acute and chronic hypoxia using genetic inactivation and pharmacological inhibitors (Hodson et al., 2016, Cheng et al., 2020, Chapters 2 and 3).

Among the genes highly upregulated in the CB compared to the SCG and those highly abundant in the type I cells, several genes encoding components of the G-protein signalling pathway have been identified (Gao et al., 2017, Zhou et al., 2016, see section 1.2.2.2). Among these, the genes encoding RGS4 and RGS5 were particularly highly

upregulated in the CB. In the single-cell transcriptomic study of mouse CB, *Rgs4* was the third most abundantly expressed gene in CB type I cells and *Rgs5* was also very highly expressed (Zhou et al., 2016). In another study, using microarray analysis of whole CB tissue, *Rgs5* was the eighth most up-regulated gene in the CB compared with the oxygen-insensitive SCG (Gao et al., 2017).

RGS proteins are GTPase activating proteins (GAPs), which increase the rate of G_{α} inactivation, thus inhibiting the G_{α} (and by association $G_{\beta\gamma}$) signalling following its dissociation from the GPCR (reviewed in Kimple et al., 2011, see Figure 5-1). RGS4 and RGS5 preferentially target the $G_{\alpha q}$ and $G_{\alpha i}$ forms (Masuho et al., 2020). Activation of $G_{\alpha q}$ subunits causes generation of IP_3 via phospholipase C, which in turn releases Ca^{2+} ions from intracellular stores. RGS4/5 proteins could therefore mediate/alter the Ca^{2+}-stimulated neurotransmitter release within the type I cells, which has been described to occur in response to several GPCR agonists (Aldossary et al., 2020, also see Chapter 1).

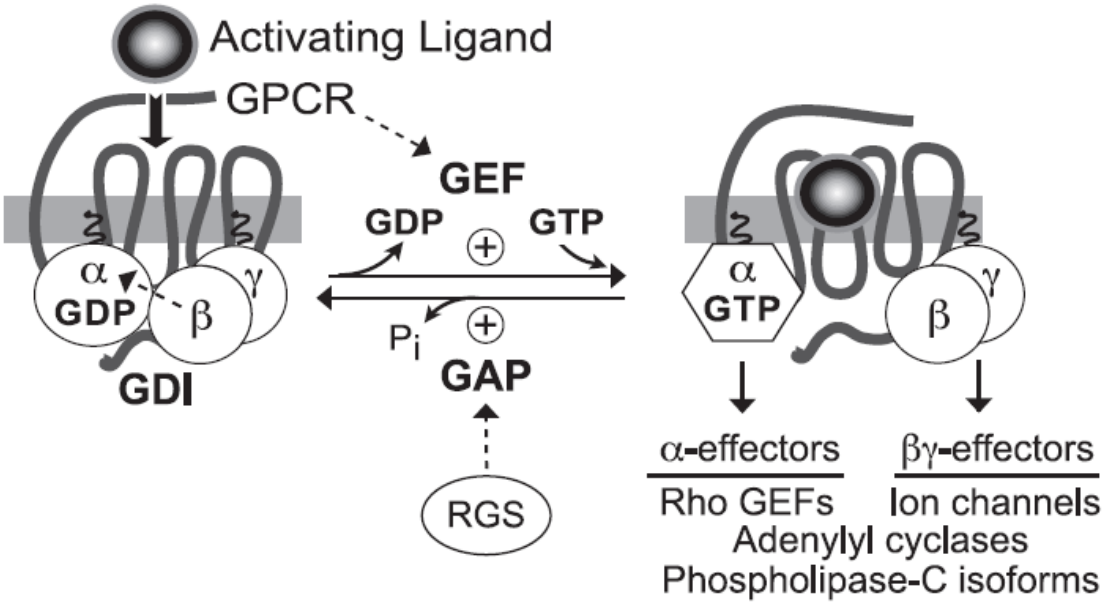


Figure 5-1. G-protein signalling mechanism.

In the inactive state, the $G_{\beta\gamma}$ subunit acts as a guanine nucleotide dissociation inhibitor (GDI), allowing association with GDP-bound G_{α} at the G-protein coupled receptor (GPCR). Binding of the ligand at the transmembrane receptor changes the conformation of the receptor such that it becomes a guanine nucleotide exchange factor, causing GDP dissociation from the G_{α} subunit in exchange for GTP. This results in dissociation of the G_{α}:$G_{\beta\gamma}$ complex and activation of downstream signalling cascades. The signal is terminated by GTP hydrolysis into GDP, either by intrinsic GTPase-activity of the G_{α} subunit or with help from GTPase-accelerating proteins (GAPs), such as regulators of G-protein signalling (RGS). From Kimple et al., 2011.

RGS4 and RGS5 have been reported to play several roles in oxygen sensing. First, as HIF-target genes, with *Rgs4* mRNA expression shown to be hypoxia- and HIF-1α (but not HIF-2α) stabilisation-inducible in the CB-related, chromaffin cell-derived pheochromocytoma PC-12 cell line (Olechnowicz et al., 2012), while *Rgs5* mRNA and protein shown to be hypoxia-inducible in human umbilical vein endothelial cells (an effect which was sensitive to HIF-β inactivation, Jin et al., 2009). In addition to these *in vitro* data, *Rgs4* and *Rgs5* are upregulated in pseudohypoxic PPGLs, caused by mutations in the VHL/HIF pathway components (Burnichon et al., 2011, Waldmann et al., 2010), serving as an *in vivo* evidence for the possible HIF-dependent control of RGS4/5 expression. Second, RGS4 and RGS5 protein levels have recently been described to be post-translationally regulated by a novel oxygen-sensing enzyme: amino-terminal cysteine dioxygenase, ADO, with RGS4/5 stabilisation in hypoxic cells (Masson et al., 2019, see Figure 5-2).

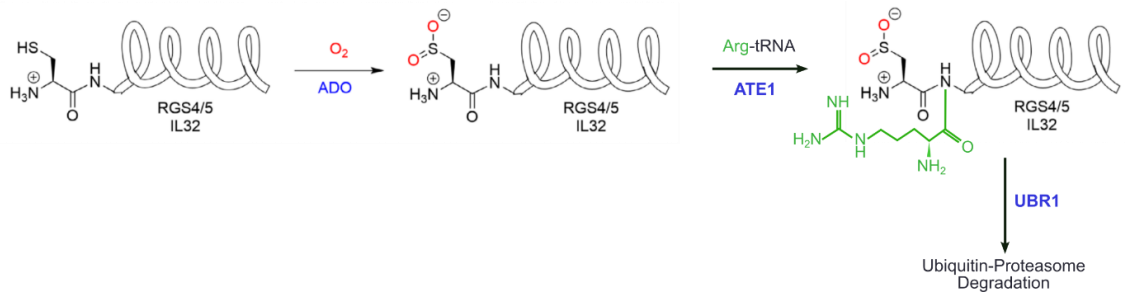


Figure 5-2. Post-translational modification of RGS4/5 via the N-degron pathway.

Diagram shows N-terminal cysteine oxidation via ADO, followed by arginylation by Arginyl-tRNA-protein transferase 1 (ATE1), which allows recognition by the Ubiquitin Protein Ligase E3 Component N-Recognin 1 (UBR1) and proteasomal degradation. Adapted from Gunawardana et al., 2021.

The uniquely high expression of RGS4 and RGS5 mRNA in the CB, together with the reported oxygen-dependent regulation of RGS4/5 levels (either at the mRNA level as HIF-target genes or at the protein level as substrates for the novel ADO oxygen sensor) points to a possible role for RGS4/5 in mediating hypoxic responses in the CB. To test this, mice with genetic *Rgs4* and *Rgs5* inactivation were studied under acute and chronic hypoxia and the effects of RGS4/5 loss on CB responses to low oxygen assessed.

5.2 Results

5.2.1 *Expression of Rgs4 and Rgs5 in the carotid body and mouse model validation*

Transcriptomic studies have shown that *Rgs4* and *Rgs5* mRNA are highly expressed in whole mouse CB and in type I cells (Zhou et al., 2016, Gao et al., 2017). To validate these results, *Rgs5* and *Rgs4* mRNA were detected by ISH in sequential sections of a mouse CB and compared with the expression of *Epas1* (encoding HIF-2α), which is highly CB-enriched and mediates hypoxic responses (Hodson et al., 2016, Fielding et al., 2018, Cheng et al., 2020), as well as the *Hif-1α* isoform, which is lowly expressed and does not appear to be important for CB function (Hodson et al., 2016). Both HIF-1/2α and RGS4/5 are post-translationally regulated by oxygen-sensing enzymes: PHD1/2/3 and ADO respectively (Schofield and Ratcliffe, 2004, Masson et al., 2019), therefore expression of these functional targets was also compared with that of genes encoding their regulatory enzymes, *Egln1* (encoding PHD2, the dominant PHD enzyme in HIFα regulation and in mediating hypoxic ventilatory control; Appelhoff et al., 2004, Bishop et al., 2013) and *Ado* (Figure 5-3).

As previously described, *Epas1* was highly expressed in the type I cells, characterised by circular nuclei and clustering into glomeruli (Figure 5-3, black frame insert), with no signal detected in the adjacent SCG or other tissues, including the carotid artery (Figure 5-3). In contrast, *Hif1a* mRNA signal was very low, with individual molecules detected uniformly throughout the section and with no apparent cell-specific expression (Figure 5-3). This is in line with the importance of HIF-2α, but not HIF-1α, in CB function (Hodson et al., 2016). Expression of *Egln1,* encoding the PHD2 enzyme post-translationally regulating cellular HIF-α levels, was very low and no CB enrichment was observed (Figure 5-3). The discrepancy between the expression of the prolyl hydroxylase and its functional target, HIF-2α, is in line with the post-translational HIF-2α modification mechanism, as high mRNA levels of the target are required to maintain a sufficient protein pool to rapidly increase HIF-2 availability upon PHD2 inactivation in hypoxia.

In contrast to the HIF signalling pathway, in which only the HIF-2α isoform is highly expressed in the CB, both *Rgs5* and *Rgs4* genes were enriched in the CB, with signal localising to the type I cell clusters (as characterised by round cells with larger nuclei than adjacent type II cells with denser hematoxylin staining) (Figure 5-3). Within the CB, *Rgs5* expression was stronger than that of *Rgs4* (Figure 5-3), in line with published ISH data showing higher *Rgs5* than *Rgs4* expression in CB sections (Zhou et al., 2016). While *Rgs5* was not detected outside of the CB (in line with its reported enrichment relative to the SCG (Gao et al., 2017)), *Rgs4* was enriched in both the CB and the SCG (Figure 5-3) relative to the surrounding tissues. Neither *Rgs5* nor *Rgs4* were detected in the CB-adjacent carotid artery. Expression of *Ado,* encoding the oxygen-sensing enzyme regulating RGS4/5 protein levels, was very low throughout the carotid bifurcation, with no CB-enrichment observed (Figure 5-3). Together, this low

expression of ADO/high expression of RGS4/5 - with *Rgs5*, in particular, showing *Epas1*-like specificity to the CB - is similar to the pattern of expression of HIF pathway components *Egln1* and *Epas1*, with very high and CB-enriched *Epas1* expression in contrast to low and diffuse *Egln1* signal throughout the carotid bifurcation (Figure 5-3).

Overall, spatial detection of genes encoding components of the RGS/ADO and HIF pathway confirms high enrichment of the functional targets: RGS4, RGS5 and HIF-2α in the CB, in line with published transcriptomic studies (Zhou et al., 2016, Gao et al., 2017) supporting the hypothesis that RGS4 and/or RGS5 may play a role in CB function. High expression of genes encoding the functional targets *Rgs4*, *Rgs5* and *Epas1*, relative to the oxygen-sensing enzymes marking them for degradation (*Ado* and *Egln1*) is in line with the proposed signalling mechanism in which hypoxic inhibition of the enzymes allows rapid stabilisation of the target proteins. RGS4/5/ADO could therefore be a novel oxygen-sensing pathway regulating the CB function via G-protein signalling cascades.

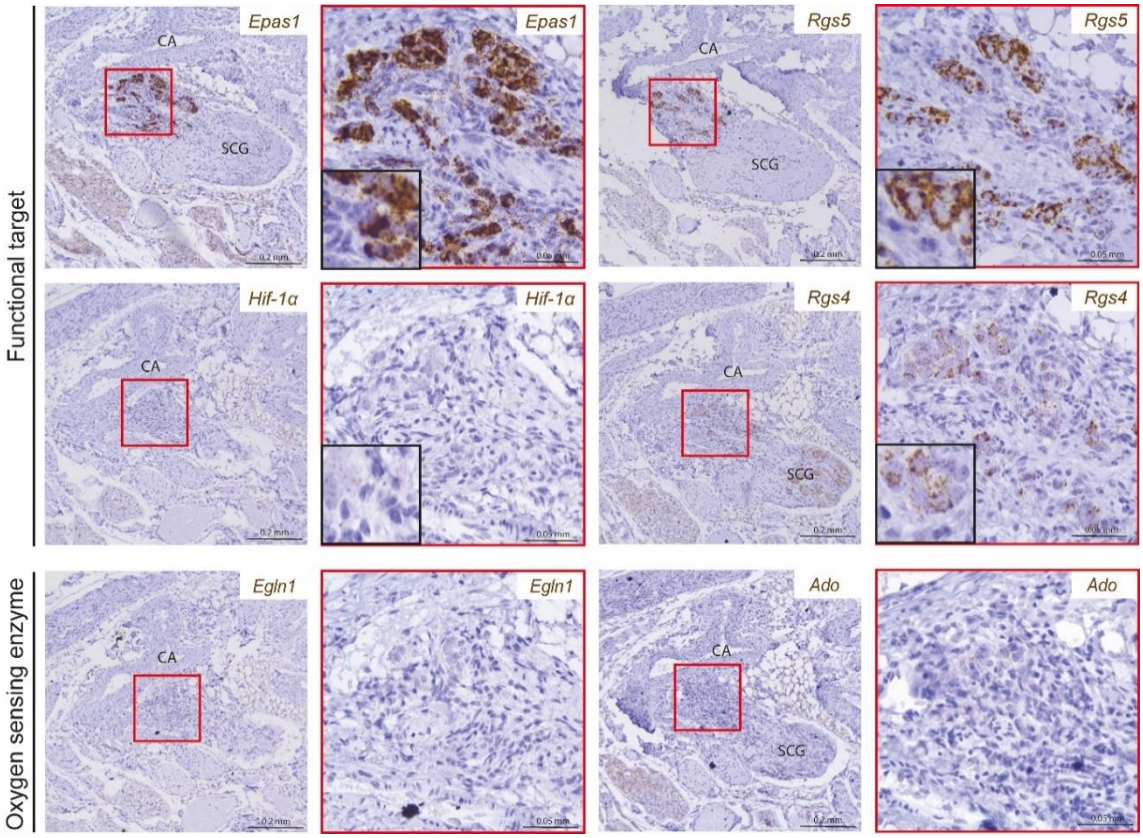


Figure 5-3. Expression of the HIF/PHD and RGS/ADO pathway components in the CB. ISH against *Epas1*, *Hif1a*, *Rgs5*, *Rgs4*, *Egln1* and *Ado* mRNA in sequential sections of a normoxic CB. Lower magnification images on the left show the CB (red frame) in the context of carotid arteries (CA) and SCG. Red frames represent high magnification from the image on the left to illustrate expression in the CB. Black frames represent high magnification (2x greater than the red frame) from the red frame image to illustrate expression in individual cell types.

mRNA levels of *Rgs4* and *Rgs5* have previously been described to be regulated by HIF in an oxygen-dependent manner *in vitro* (Jin et al., 2009, Olechnowicz et al., 2012). To test if the expression of RGS/ADO pathway components is altered in hypoxia, expression of *Rgs4*, *Rgs5*, *Ado*, *Hif-2α*, *Hif-1α* and *Egln1* was also measured in serial CB sections in a wild-type mouse exposed to 7-day 10% O_2, as per the standard CH protocol used in other experiments (Figure 5-4). Hypoxic CBs increase in size (Fielding et al., 2018), resulting in a larger cross-section CB area in the images shown.

Chronic exposure to hypoxia did not appear to cause marked changes in the mRNA expression of the HIF pathway components, with high and CB-specific *Epas1*

expression contrasted with low and ubiquitous pattern of *Hif1a* and *Egln1* hybridisation (Figure 5-4).

In comparison with the expression in normoxic tissue, more *Rgs5*$^{+}$ cell clusters with large, faintly stained nuclei resembling type I cell morphology, were observed in the acclimatised CBs (compare Figure 5-4 and Figure 5-3), in line with CB hyperplasia in response to hypoxia. Additionally, the *Rgs5* mRNA signal intensity appeared higher in the hypoxic than in the normoxic tissue (compare Figure 5-4 and Figure 5-3), suggesting hypoxic *Rgs5* mRNA induction. Even more striking increase in *Rgs4* mRNA was observed, with very high expression in both the CB and SCG of the hypoxic mouse (Figure 5-4, compare with Figure 5-3). Within the CB, *Rgs4* mRNA induction was also restricted to the type I cell-like clusters, although the signal appeared more uniformly distributed within the cells than that of *Rgs5*, with no evidence of low nuclear expression (Figure 5-4). Unlike for the functional RGS targets, *Ado* expression was not changed in the hypoxic *vs* normoxic CB and appeared low and not enriched in any of the tissues within the carotid bifurcation (Figure 5-4).

Together, these data demonstrate that *Rgs4* and *Rgs5* mRNA is enriched in the CB (in the case of *Rgs5*, uniquely within the CB and not in other neuronal tissues), similar to that of *Epas1*. Further, *Rgs4/5* (in particular *Rgs4*) mRNA levels can be induced by chronic exposure to 10% O_2, in line with published *in vitro* results.

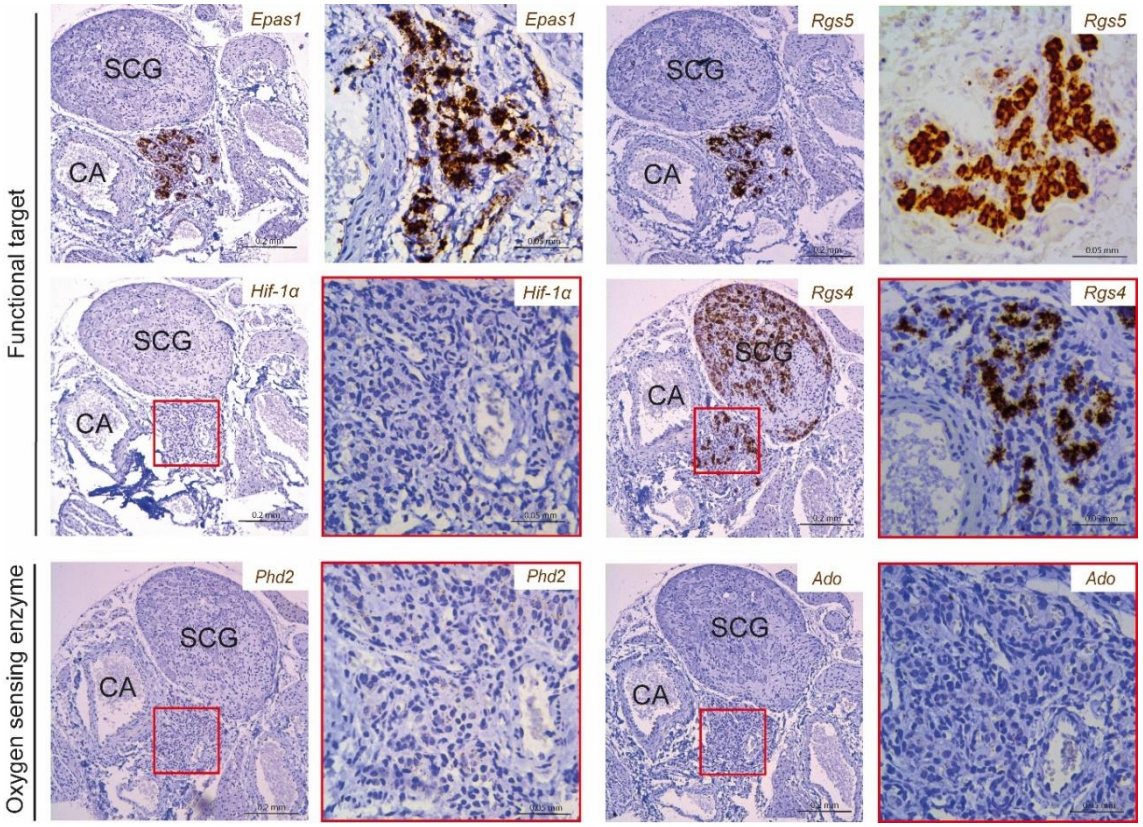


Figure 5-4. HIF/PHD and RGS/ADO pathways components expression in the hypoxic CB. ISH against *Rgs5*, *Rgs4*, *Ado*, *Epas1*, *Hif-1α* and *Phd2* mRNA in sequential sections of the carotid bifurcation from a wild-type mouse exposed to 7-day 10% O_2. Lower magnification images on the left show the CB (red frame) in the context of carotid arteries (CA) and the SCG. Red frames represent high magnification from the image on the left to illustrate expression in the CB.

5.2.2 *Validation of Rgs4 and Rgs5 KO mouse models and experimental design*

To study the involvement of RGS4/5 in CB development and function, mice with floxed *Rgs4* or *Rgs5* alleles (previously described in Pang et al., 2015 and Demirel et al., 2021) were crossed with animals expressing a TH-IRES-Cre, to allow recombination specifically within the TH^+ cells, including the CB type I cells, resulting in the generation of $Rgs4^{f/f}$*;THCre* and $Rgs5^{f/f}$*;THCre* mice. Tissue-restricted inactivation was chosen in the first instance to exclude possible effects of *Rgs4/5* inactivation on other physiological systems mediated by G-protein signalling.

To confirm successful *Rgs4* and *Rgs5* inactivation in the tissue of interest, *Rgs4* and *Rgs5* mRNA levels were assessed by ISH in CB sections from the *Rgs4*$^{f/f}$*;THCre* and *Rgs5*$^{f/f}$*;THCre* mice (and their littermate *Rgs4/5*$^{f/f}$ controls) (Figure 5-5). Although ISH is a semi-quantitative method, it provides a spatial resolution of gene expression and prevents obscuring the results by contamination with TH^- cells.

Rgs4 mRNA was detected in both the CB and adjacent SCG in the *Rgs4*$^{f/f}$ normoxic CB (Figure 5-5, top row). In contrast, very little *Rgs4* mRNA was detected in the *Rgs4*$^{f/f}$*;THCre* CB. Due to the small area of CB in the normoxic sections (and because hypoxic *Rgs4* mRNA was observed in the CBs earlier, Figure 5-3 and Figure 5-4), *Rgs4* mRNA loss was further confirmed in the CBs of *Rgs4*$^{f/f}$*;THCre* animals exposed to 7-day 10% O_2. TH^+-cell-specific *Rgs4* inactivation resulted in near-complete loss of *Rgs4* mRNA in the hypoxic *Rgs4*$^{f/f}$*;THCre* CB (Figure 5-5, bottom row).

In the *Rgs4*$^{f/f}$ mouse model, floxed sites flank a large portion of the gene, including exons 2-5 (The Jackson Laboratory strain #026695). In contrast, in *Rgs5*$^{f/f}$ mice, inactivation is achieved by recombination of a single exon 3 (C57BL/6N-Rgs5$^{tm1a(EUCOMM)Wtsi}$/H strain, MRC Harwell), therefore, transcribed mRNA may still be detected by standard RNAScope probes designed to detect *Rgs5*. A shorter probe detecting the exon 3 region was therefore designed to test loss of *Rgs5* mRNA in *Rgs5*$^{f/f}$*;THCre* mice, and used with the BaseScope assay, compatible with probes targeting shorter regions of interest. There was a marked reduction in *Rgs5* signal intensity in the *Rgs5*$^{f/f}$*;THCre* CB compared with the *Rgs5*$^{f/f}$ control, although some expression was still apparent throughout the type I cells (Figure 5-5). We have encountered technical difficulties when testing *Rgs5* mRNA loss in acclimatised *Rgs5*$^{f/f}$*;THCre* animals and it was not possible to repeat this experiment before the

submission of this thesis. Overall, however, these results confirm successful, albeit incomplete, inactivation of the *Rgs4* and *Rgs5* isoforms in the respective mouse models.

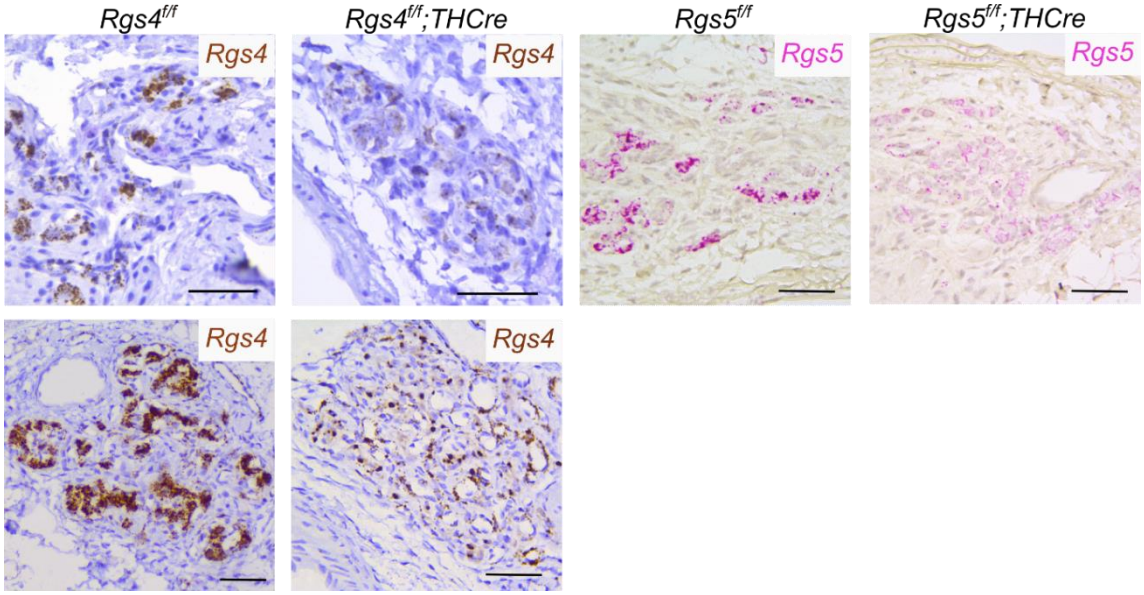


Figure 5-5. Confirmation of specific *Rgs4* and *Rgs5* mRNA loss in mice with RGS4 and RGS5 inactivation.

ISH against *Rgs4* (brown signal against blue Harris hematoxylin) or *Rgs5* (pink signal against grey Gill hematoxylin) mRNA in CBs of normoxic (top row) and hypoxic (bottom row, acclimatised to 7-day 10% O_2) *Rgs4*$^{f/f}$*;THCre* and *Rgs5*$^{f/f}$*;THCre* mice, with matched controls. Scale bars show 0.05 mm.

To test if *Rgs4*$^{f/f}$*;THCre* and *Rgs5*$^{f/f}$*;THCre* mice develop morphologically normal CBs, carotid bifurcation sections of the knock-out and control (normoxic) mice were immunostained against TH, the type I cell marker (Figure 5-6). Both *Rgs4*$^{f/f}$*;THCre* and *Rgs5*$^{f/f}$*;THCre* CBs appeared morphologically normal, with similar TH^+ cell density and no marked discrepancy in CB volumes between *Rgs4/5*KO mice and their littermate controls (Figure 5-6). This is in contrast to *Hif-2α*$^{f/f}$*;THCre* mice, which do not develop functional CBs and have vestigial organs with few TH^+ cells (Macias et al., 2018). The discrepancy between the effects of *Hif-2α* and *Rgs4/5* loss on CB morphology suggests that RGS4 and RGS5 do not play a role in CB development.

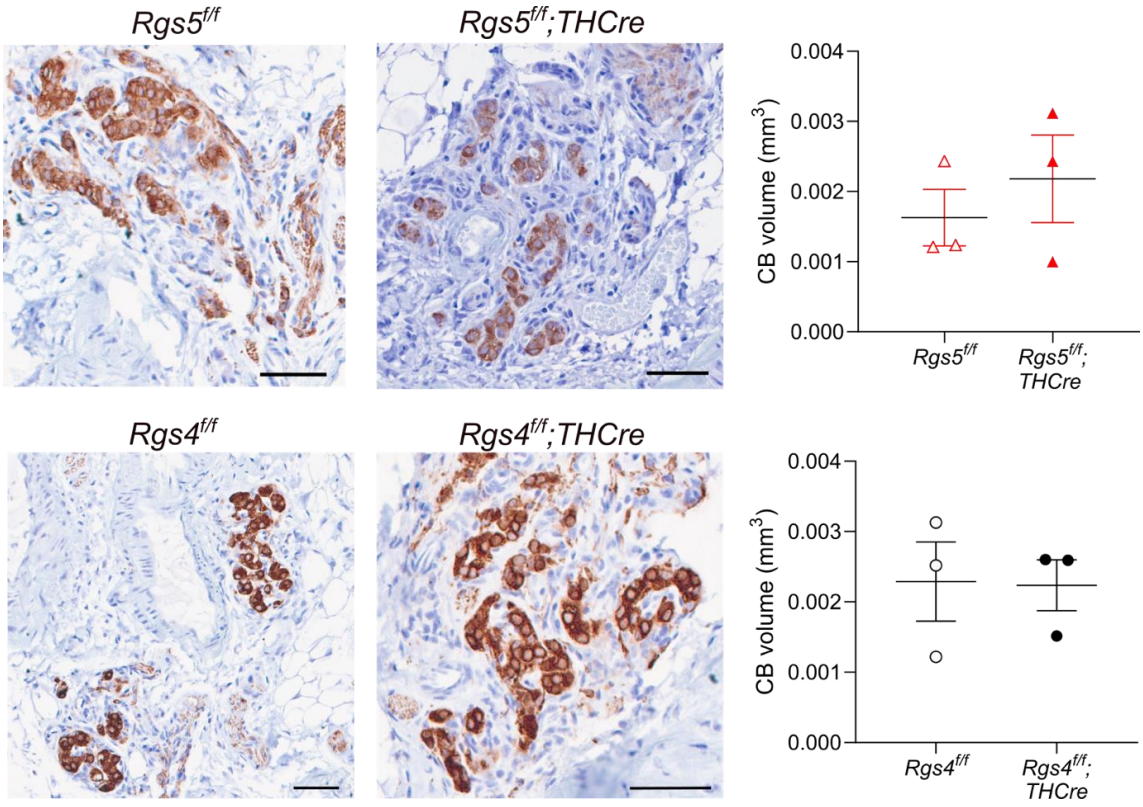


Figure 5-6. CB volume and morphology in mice with RGS4 or RGS5 inactivation.
TH IHC (brown with blue Hematoxylin counterstain), showing the typical glomerular CB structure in *Rgs5*$^{f/f}$*;THCre* (top panels) and *Rgs4*$^{f/f}$*;THCre* (bottom panels) animals and matched *Cre*$^{-}$ controls. Scale bars show 0.05 mm. CB volume was quantified by modelling from the CB area determined using TH IHC. Data show mean ± SEM with individual values. KO mice were compared with controls by an unpaired Student's *t*-test with no statistically significant ($P < 0.05$) differences detected.

The CB mediates responses to both acute and chronic hypoxia, therefore, to characterise the CB function in mice with *Rgs4* and *Rgs5* inactivation, ~2-3 months old *Rgs4*$^{f/f}$*;THCre* and *Rgs5*$^{f/f}$*;THCre* animals were exposed to 7-day 10% O_2 in a normobaric chamber (Chapter 2) and ventilation in response to acute stimuli of 10% O_2/3% CO_2, 10% O_2 or 3% CO_2, was assessed by plethysmography before the start of and after 2 and 7-day hypoxia (Figure 5-7). To assess CB proliferation, mice were injected with 5-Bromo-2'-deoxyuridine (BrdU) before the start of hypoxic exposure, and drinking water was supplemented with BrdU throughout the experiment (Figure 5-7). After the Day 7 plethysmography, mice were returned to hypoxia and, after ~1 h,

animals were culled within the hypoxic conditions and tissues, including the CB, collected and fixed for immunostaining.

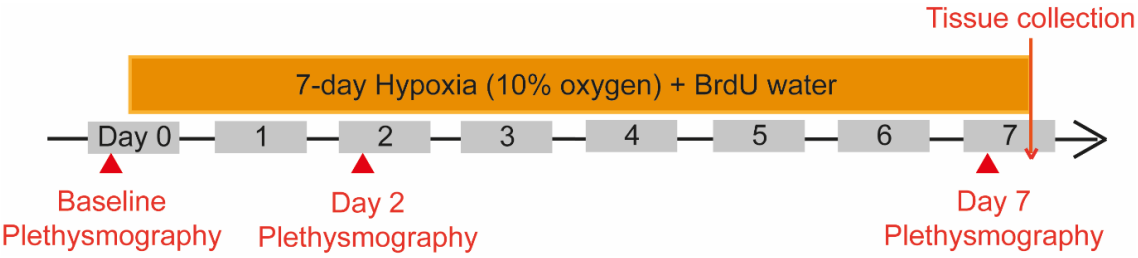


Figure 5-7. Experimental design for testing CB function in mice with constitutive *Rgs4* or *Rgs5* inactivation.

Animals were housed in a 10% O_2 normobaric hypoxia chamber for 7 days. Hypoxic and hypercapnic AVRs were measured by plethysmography before the start of the experiment (Baseline) and after 2 and 7 days of 10% O_2 exposure (2d and 7d H). Immediately before the start of hypoxia housing, animals received a single intraperitoneal injection of 50 $mg \cdot kg^{-1}$ BrdU and drinking water was supplemented with 1 $mg \cdot ml^{-1}$ BrdU for the rest of the experiment. Following the 7d H plethysmography, mice were returned to hypoxia and left for at least 1h before culling and tissue collection.

5.2.3 *Effects of Rgs4 and Rgs5 inactivation on acute ventilatory responses to hypoxia*

First, the effects of RGS4/5 inactivation on HVR were assessed in unacclimatised mice. MVb was measured by whole-body plethysmography in *Rgs4$^{f/f}$;THCre* and *Rgs5$^{f/f}$;THCre* mice, as in previous chapters. Both *Rgs4$^{f/f}$* and *Rgs5$^{f/f}$* control mice showed a rapid increase in MVb in response to 10% O_2 (Figure 5-8A, middle panels), which was quickly suppressed unless 3% CO_2 was added to the stimulating gas to offset ventilatory hypocapnia (Figure 5-8A, top panels). *Rgs4$^{f/f}$;THCre* and *Rgs5$^{f/f}$;THCre* mice responded in the same way as their littermate controls (Figure 5-8A, closed triangles/circles). Acute HVRs were assessed by averaging MVb during the 5 min hypoxic or hypercapnic stimulus (Figure 5-8B), as explained in previous chapters (section 2.2.4). No significant change in hypoxic or hypercapnic responses was noted in

either *Rgs4*$^{f/f}$*;THCre* or *Rgs5*$^{f/f}$*;THCre* mice compared with their littermate controls (Figure 5-8B).

Together, this data shows that unacclimatised mice with conditional *Rgs4* or *Rgs5* inactivation in the TH^+ cells develop morphologically normal CBs and are able to mount an HVR.

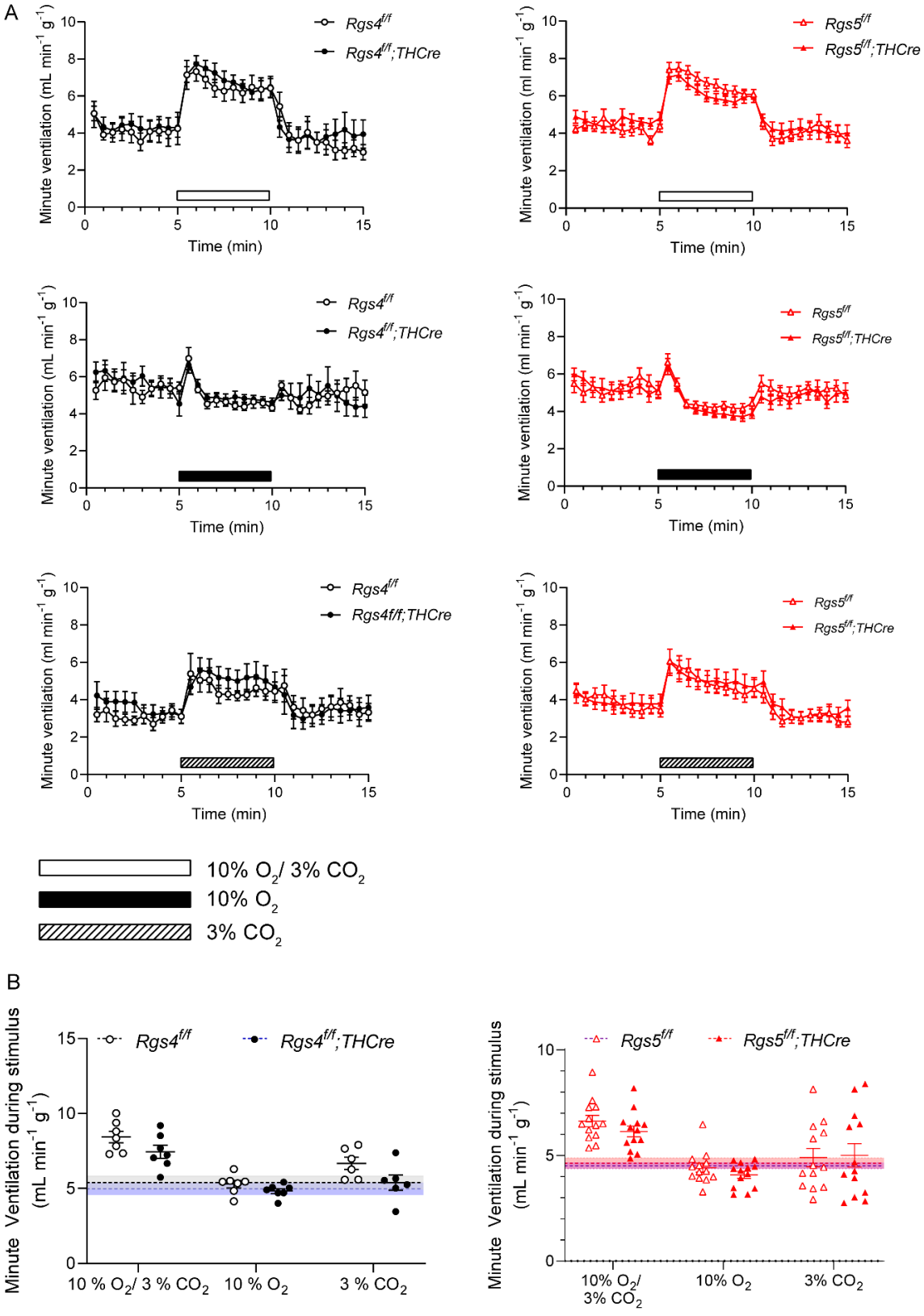


Figure 5-8. HVR in mice with constitutive *Rgs4* or *Rgs5* inactivation in TH⁺ cells.

(**A**) MVb in *Rgs4*$^{f/f}$*;THCre* and *Rgs5*$^{f/f}$*;THCre* mice, compared with *Rgs4*$^{f/f}$ or *Rgs5*$^{f/f}$ controls respectively, under 5 min challenge with 10% O_2/3% CO_2 (open bars), 10% O_2 (filled bars), or 3% CO_2 (dashed bars); $n = 7$ for *Rgs4*$^{f/f}$*;THCre* and $n = 13$ for *Rgs5*$^{f/f}$*;THCre* mice. (**B**)

Average MVb during each stimulus presented in A (dots and triangles), relative to the baseline ventilation under normoxia (dashed lines). Data from knock-out mice were compared with controls under each stimulus using an unpaired Student's *t*-test, with no statistically significant ($P < 0.05$) differences detected.

5.2.4 *Ventilatory acclimatisation to hypoxia in mice lacking Rgs4 or Rgs5 in carotid body type I cells*

To test if RGS4 and RGS5 are involved in VAH, *Rgs4$^{f/f}$;THCre* and *Rgs5$^{f/f}$;THCre* mice (and their littermate controls) were housed in a normobaric chamber ventilated with 10% O_2 for 7 days and their HVRs measured before and after 2 and 7 days since the start of acclimatisation (Figure 5-7). Both *Rgs4$^{f/f}$;THCre* and *Rgs5$^{f/f}$;THCre* mice tolerated hypoxia well, with no marked differences in weight loss compared with their littermate controls (data not shown), suggesting these animals can acclimatise to hypoxic conditions.

As in the Baseline recording, mice were exposed to 10% O_2, 10% O_2/3% CO_2 and 3% CO_2 (Figure 5-9, Table 5-1), but full MVb traces are only shown for 10% O_2/3% CO_2 exposures (Figure 5-9) and responses to all three gases are quantified in Table 5-1. Here, responses to acute hypoxia/hypercapnia are quantified as the difference between the MVb in the first minute of stable hypoxia and the last minute at room air, as used before to quantify VAH (Chapters 2-2, Bishop et al., 2013, Hodson et al., 2016).

Recordings taken prior to the start of acclimatisation (Baseline) are as shown before (Figure 5-8) and no difference between *Rgs4$^{f/f}$;THCre* or *Rgs5$^{f/f}$;THCre* mice and their controls was found (Figure 5-9 and Table 5-1). Two-day 10% O_2 exposure resulted in a marked increase in 10% O_2/3% CO_2 AVR in *Rgs4$^{f/f}$* and *Rgs5$^{f/f}$* control mice, which was sustained at 7d H (Figure 5-9A and Table 5-1). 10% O_2 AVR increased progressively after two and seven-day exposure to hypoxia (2-way ANOVA Time factor $P < 0.0001$,

Table 5-1 for *Rgs4*$^{f/f}$ and $P < 0.001$, Table 5-2 for *Rgs5*$^{f/f}$ mice), and a small increase in the 3% CO_2 AVR after a two-day exposure to 10% O_2 was also observed (2-way ANOVA Time factor $P = 0.004$, Table 5-1 for *Rgs4*$^{f/f}$ and $P = 0.047$, Table 5-2 for *Rgs5*$^{f/f}$ mice). Together, this shows successful VAH in control animals.

Rgs4$^{f/f}$*;THCre* mice showed enhanced 10% O_2/3% CO_2 AVRs both after 2 and 7-day hypoxia, similar to their *Rgs4*$^{f/f}$ controls, suggesting normal VAH (Figure 5-9, left column). Interestingly, increased 10% O_2 AVRs were observed in *Rgs4*$^{f/f}$*;THCre* vs *Rgs4*$^{f/f}$ mice (2-way ANOVA $P = 0.020$, Table 5-1), however, this appeared to be due to increased MVb only during the first minute of 10% O_2 exposure, with MVb during the remaining four minutes of 10% O_2 stimulus similar to that in *Rgs4*$^{f/f}$ controls (Figure 5-10). No differences in the responses to 3% CO_2 (2-way ANOVA $P = 0.960$, Table 5-1) or 10% O_2/3% CO_2 (2-way ANOVA $P = 0.724$, Table 5-1) were observed.

In contrast to animals with *Rgs4* inactivation, *Rgs5*$^{f/f}$*;THCre* mice had markedly reduced 10% O_2/3% CO_2 AVRs after 2 and 7-day CH relative to their controls, suggesting impaired VAH (Figure 5-9A). Although a significant reduction in the AVR was detected in *Rgs5*$^{f/f}$*;THCre* mice relative to *Rgs5*$^{f/f}$ controls (Figure 5-9B), there was no significant interaction between the changes across acclimatisation time-points and those caused by *Rgs5* inactivation (2-way ANOVA Time factor $P < 0.0001$, Time x *Rgs5* interaction $P = 0.148$, Table 5-2), suggesting an incomplete ablation of VAH in mice with *Rgs5* inactivation. No significant difference between AVRs to 10% O_2 or 3% CO_2 in *Rgs5*$^{f/f}$*;THCre vs Rgs5*$^{f/f}$ mice was detected (2-way ANOVA $P = 0.691$ and $P = 0.622$ respectively, Table 5-2), suggesting that the effect of *Rgs5* inactivation on VAH is not strong enough to affect responses to the milder stimuli.

In summary, this data suggests that although both RGS4/5 isoforms are highly expressed in the CB and induced by hypoxia, their function in CB-mediated ventilatory control may be different. Loss of RGS5, but not RGS4, reduces (but does not ablate) VAH, in line with its enrichment in the CB relative to the non-oxygen-sensitive SCG.

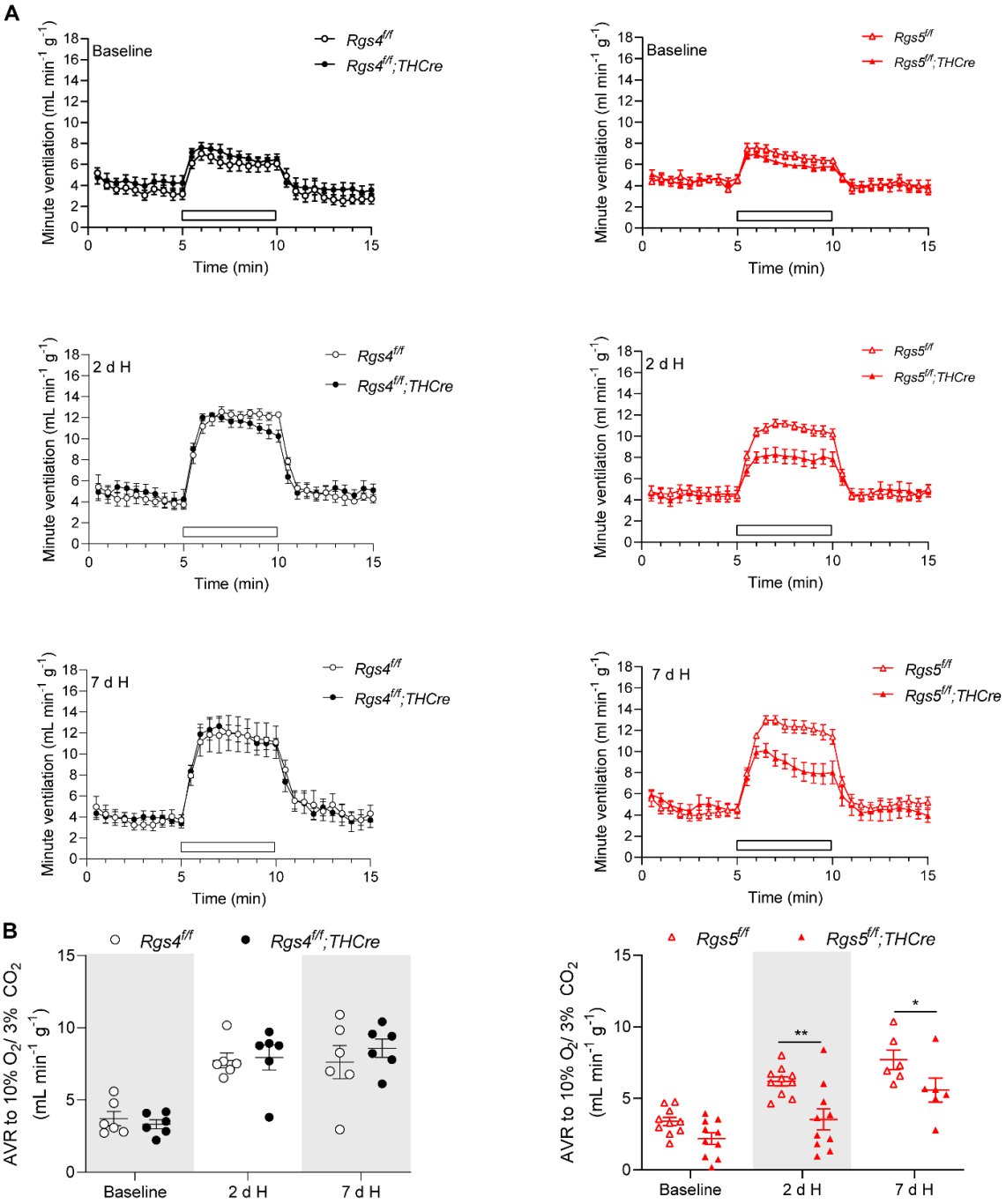


Figure 5-9. VAH in mice with *Rgs4* or *Rgs5* inactivation in TH$^+$ cells.

(**A**) MVb under 5 min 10% O_2/3% CO_2 (open bars) in *Rgs4$^{f/f}$;THCre* and *Rgs5$^{f/f}$;THCre* mice, compared with *Rgs4$^{f/f}$* or *Rgs5$^{f/f}$* controls respectively, exposed to 7-day 10% O_2 (H), measured

before (Baseline) and after 2 and 7-day H. $n = 6$ for *Rgs4$^{f/f}$;THCre* and $n = 10$ (Baseline and 2d H) or $n = 6$ (7d H) for *Rgs5$^{f/f}$;THCre* mice. (**B**) 10% O_2/3% CO_2 AVRs, quantified from data in A. Data from knock-out mice were compared with controls using a 2-way ANOVA (see Table 5-1 and Table 5-2), followed by Holm-Sidak's multiple *t*-tests, with significance shown in the graph: $*P < 0.05$, $***P < 0.001$.

Table 5-1. Hypoxic and hypercapnic AVRs in acclimatised *Rgs4$^{f/f}$;THCre* mice.

Data were analysed by a 2-way ANOVA, with Time *P* shown in the rightmost column, *Rgs4*KO *P* shown below each stimulus section and Interaction *P* shown in the bottom right corner; followed by Holm-Sidak's multiple *t*-tests for each time-point. $P < 0.05$ are in bold; $n = 6$.

		Rgs4$^{f/f}$		*Rgs4$^{f/f}$;THCre*			Time/
	Time-point	Mean	SEM	Mean	SEM	*t*-test *P*	Interaction *P*
10% O_2 / 3% CO_2	Baseline	3.72	0.49	3.32	0.31	*0.859*	
	2 d H	7.74	0.51	7.95	0.87	*0.859*	***<0.0001***
	7 d H	7.62	1.14	8.59	0.63	*0.895*	
	Rgs4 P		*0.724*				*0.553*
10% O_2	Baseline	-0.53	0.37	0.77	0.39	*0.077*	
	2 d H	1.47	0.48	2.20	0.75	*0.433*	***<0.0001***
	7 d H	2.30	0.43	4.11	0.44	***0.044***	
	Rgs4 P		***0.020***				*0.491*
3% CO_2	Baseline	1.75	0.53	2.09	0.65	*0.906*	
	2 d H	3.92	0.88	3.28	0.28	*0.884*	***0.004***
	7 d H	3.35	0.59	3.56	0.47	*0.906*	
	Rgs4 P		*0.960*				*0.555*

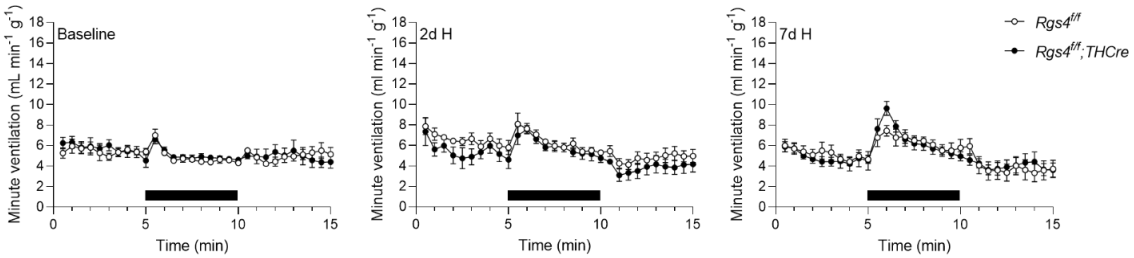


Figure 5-10. Acute responses to 10% O_2 in acclimatised mice with *Rgs4* inactivation in TH^+ cells.

MVb in response to 5 min 10% O_2 (filled bars) in *Rgs4*$^{f/f}$*;THCre* mice, compared with *Rgs4*$^{f/f}$ controls, exposed to 7-day 10% O_2 (H), measured before (Baseline) and 2 and 7 days after the start of hypoxia; $n = 6$.

Table 5-2. Hypoxic and hypercapnic AVRs in acclimatised *Rgs5*$^{f/f}$*;THCre* mice.

Data were analysed by a 2-way ANOVA, with Time *P* shown in the rightmost column, *Rgs5*KO *P* shown below each stimulus section and Interaction *P* shown in the bottom right corner; Data were analysed by mixed-effects 2-way ANOVA, followed by Holm-Sidak's multiple *t*-tests for each time-point. $P < 0.05$ are in bold. $n = 10$ for Baseline and 2d H groups, $n = 6$ for 7d H group.

		Rgs5$^{f/f}$		*Rgs5*$^{f/f}$*;THCre*			Time/
	Time-point	Mean	SEM	Mean	SEM	*t*-test *P*	Interaction *P*
10% O_2 / 3% CO_2	Baseline	3.39	± 0.29	2.20	± 0.41	*0.097*	
	2 d H	6.19	± 0.32	3.54	± 0.74	***0.001***	***<0.001***
	7 d H	7.70	± 0.68	5.58	± 0.84	***0.049***	
	Rgs5 P		***0.004***				*0.148*
10% O_2	Baseline	-0.27	± 0.39	-0.14	± 0.27	*0.972*	
	2 d H	1.51	± 0.53	0.72	± 0.43	*0.519*	***<0.001***
	7 d H	2.26	± 0.75	2.44	± 0.65	*0.972*	
	Rgs5 P		*0.691*				*0.509*
3% CO_2	Baseline	1.96	± 0.57	1.44	± 0.33	*0.660*	
	2 d H	2.63	± 0.48	1.91	± 0.41	*0.603*	***0.047***
	7 d H	2.42	± 0.61	3.10	± 0.50	*0.660*	
	Rgs5 P		*0.622*				*0.3953*

5.2.5 *Carotid body proliferation in mice with Rgs4 or 5 inactivation*

To test the effects of *Rgs4* or *Rgs5* inactivation on CB proliferation and hypertrophy under hypoxia, cell proliferation was assessed by measuring BrdU incorporation and CB volume was modelled based on TH^+ CB area in selected carotid bifurcation sections as in previous chapters (Figure 5-11). High BrdU incorporation was observed within the CBs of acclimatised *Rgs4*$^{f/f}$ mice, suggesting successful induction of CB proliferation by hypoxia (Figure 5-11A). Although there was a trend towards increased $BrdU^+$ cell density in the *Rgs4*KO mice relative to *Cre*$^-$ controls, this did not reach statistical significance (Figure 5-11A, $P = 0.369$). Average CB volume of the control *Rgs4*$^{f/f}$ mice exposed to 7-day hypoxia was similar to the previously published results (Fielding et al., 2018) and no statistically significant difference was detected between *Rgs4*$^{f/f}$*;THCre* and control animals.

High BrdU incorporation was also observed in both *Rgs5*$^{f/f}$ and *Rgs5*$^{f/f}$*;THCre* mice acclimatised to 7-day 10% O_2. Despite this, *Rgs5* inactivation in the TH^+ cells partially prevented the hypoxia-induced hypertrophy, with CB volumes of acclimatised *Rgs5*$^{f/f}$*;THCre* mice significantly lower than those of acclimatised *Rgs5*$^{f/f}$ mice (Figure 5-11B). Nevertheless, the CB volume of hypoxic *Rgs5*KO was on average higher than that in normoxia (0.0030 ± 0.0003 mm^3 in hypoxic *vs* 0.0022 ± 0.0006 mm^3 in normoxic *Rgs5*$^{f/f}$*;THCre* mice, Figure 5-6 and Figure 5-11B), suggesting some hypertrophy in response to sustained hypoxia still occurred in these mice (NB normoxic and hypoxic cohorts are not age-matched).

Together, data presented in this section show that although the CB proliferative response to hypoxia is not affected by RGS4 or RGS5 loss, *Rgs5*$^{f/f}$*;THCre* mice display hypomorphic CB hyperplasia, which may be related to the reduced VAH. Both the

ventilatory and the CB morphological phenotypes are much milder than those observed in mice with HIF-2α loss.

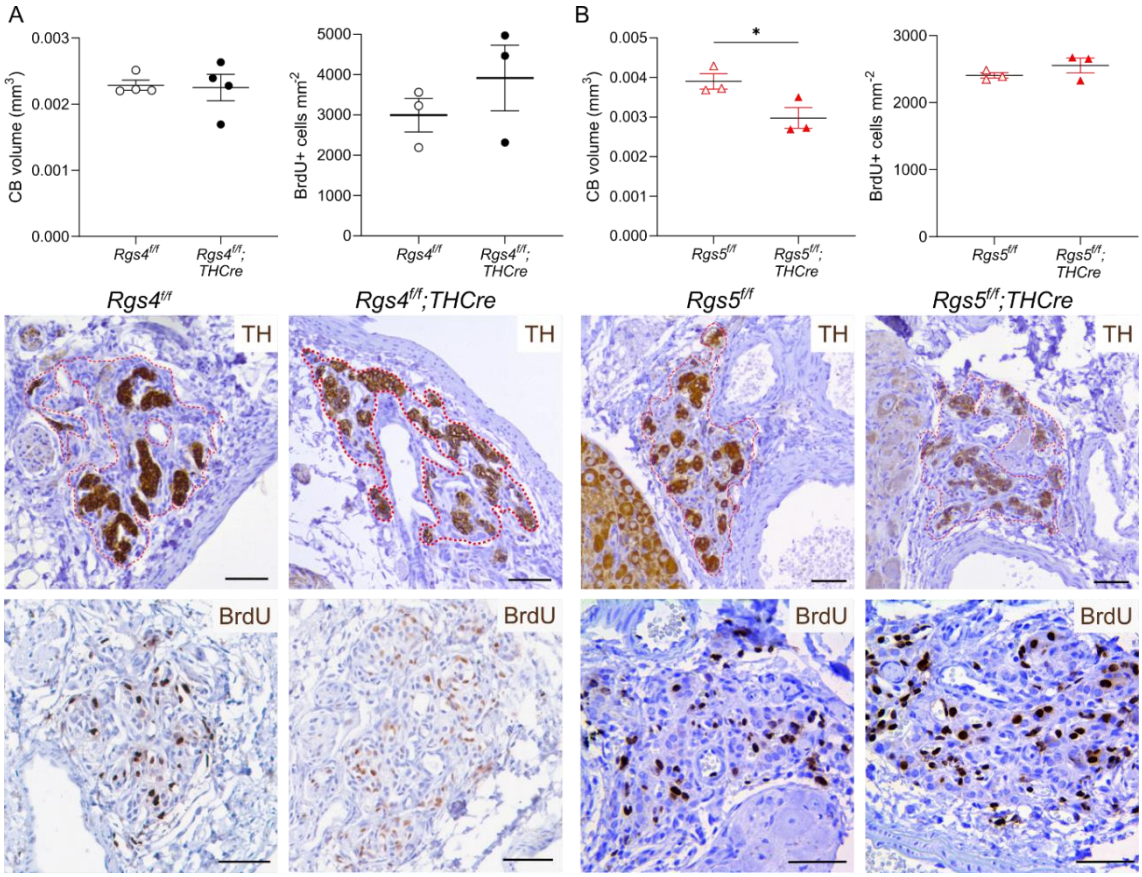


Figure 5-11. CB proliferation in acclimatised *Rgs4$^{f/f}$;THCre* and *Rgs5$^{f/f}$;THCre* mice. (**A**) BrdU^{+} cell density and CB volume in *Rgs4$^{f/f}$;THCre* (left panels) and *Rgs5$^{f/f}$;THCre* (right panels) mice and controls. Data were analysed by Student's *t*-test, $*P < 0.05$. (**B**) Representative images showing immunostaining against TH (top panels, brown) and BrdU (bottom panels, brown), from which quantifications in A were made. Red dashed lines in TH images show CB area used for volume quantification. Scale bars represent 0.05 mm.

5.2.6 *Effects of acute Rgs4 and Rgs5 inactivation on carotid body responses to chronic hypoxia.*

To test if acute *Rgs4* or *Rgs5* inactivation in adulthood mimics the reduced VAH observed in *Rgs5$^{f/f}$;THCre* mice, ~3-month-old animals expressing the tamoxifen-inducible Rosa26Cre^{ERT2} and homozygous for the floxed *Rgs4* or *Rgs5* allele were treated with tamoxifen to induce loxP site recombination and *Rgs4* or *Rgs5* inactivation

(as previously used for testing effects of *Hif-α* inactivation in Hodson et al., 2016 and in Chapter 4). A ubiquitously expressed Cre was chosen to maximise recombination efficiency, as the tamoxifen-inducible TH-restricted Cre has previously been reported to result in incomplete target gene inactivation (Fielding et al., 2018).

Rgs4$^{f/f}$*;RosaCreER* and *Rgs5*$^{f/f}$*;RosaCreER* mice were treated with tamoxifen by oral gavage for 5 consecutive days and 5 more days were allowed before starting the experimental protocol (as in Hodson et al., 2016). Following tamoxifen treatment, animals were housed in a 10% O_2 chamber for 7 days, as in the experiments carried out on *Rgs4/5*$^{f/f}$*;THCre* mice, and HVRs were assessed by plethysmography before tamoxifen treatment (Baseline), 10 days after the start of tamoxifen treatment - immediately before acclimatisation to hypoxia (post TMX), and 2 and 7 days after the CH start (Figure 5-12).

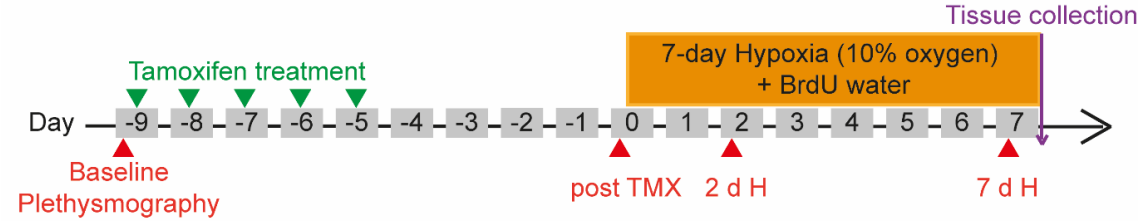


Figure 5-12. Experimental design for testing CB function in mice with acute *Rgs5* inactivation.

Hypoxic and hypercapnic AVRs were measured by plethysmography before the start of the experiment (Baseline), following tamoxifen treatment, but before the start of chronic hypoxic exposure (post TMX) and after 2 and 7 days of 10% O_2 exposure (2d and 7d H). Animals were treated orally with 5 doses of 2 mg tamoxifen on consecutive days, followed by a 5-day rest period before the start of 10% O_2 housing. Immediately before the CH start, animals received a single intraperitoneal injection of 50 mg·kg^{-1} BrdU and drinking water was supplemented with 1 mg·ml^{-1} BrdU for the rest of the experiment. Following the 7d H plethysmography, mice were returned to hypoxia and left for 1h+ before culling and tissue collection.[10]

[10] Figure and legend reused from Chapter 4

To confirm successful *Rgs4* or *Rgs5* inactivation in tamoxifen-treated *Rgs4$^{f/f}$;RosaCreER* and *Rgs5$^{f/f}$;RosaCreER* mice, *Rgs4* and *Rgs5* mRNA was quantified in CBs and adjacent SCGs by RT-qPCR in animals subjected to the same tamoxifen and hypoxia protocol as the mice used for ventilatory assessments (Figure 5-12), but without BrdU treatment or plethysmography. Rosa26Cre^{ERT2} is ubiquitously expressed, RNA can therefore be extracted from whole CBs and target gene loss should be similar across different cell types. RT-qPCR provides a quantitative comparison of RGS4/5 expression and is therefore preferred to the ISH used in the *Rgs4/5$^{f/f}$;THCre* models (Figure 5-5). Due to the small tissue size, RNA was extracted from 5 pairs of CBs and SCGs per genotype, and expression therefore represents an average across multiple animals.

Using a probe designed against the exon 3-4 boundary (within the excised exon 2-5 region), 90.3% loss of *Rgs4* mRNA was detected in the SCGs of *Rgs4$^{f/f}$;RosaCreER*, relative to the *Rgs4$^{f/f}$* mice (Figure 5-13A). Due to poor RNA yield in the control CB preparation in this experiment, RNA from another set of 5 wild-type mice exposed to 7-day hypoxia was used to compare *Rgs4* expression, with internal normalisation to the expression of a 'housekeeping' gene, *Actb.* This showed a 79% loss in *Rgs4* mRNA in *Rgs4$^{f/f}$;RosaCreER* CBs relative to controls (Figure 5-13A). Marked loss of *Rgs5* mRNA was observed in both the CBs (56.7%) and SCGs (58.2%) of *Rgs5$^{f/f}$;RosaCreER* animals (Figure 5-13B), comparable to the mRNA loss observed in other single exon excision models using the Rosa26Cre^{ERT2} (see Chapter 4).

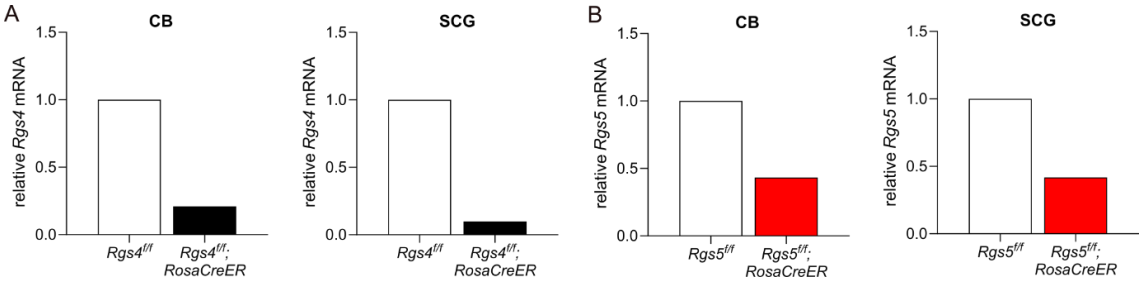


Figure 5-13. Confirmation of *Rgs4* or *Rgs5* mRNA loss in mice with acute *Rgs4* and *Rgs5* inactivation in adulthood.

Relative (**A**) *Rgs4* and (**B**) *Rgs5* mRNA expression in CBs and SCGs pooled from *Rgs4*$^{f/f}$*;RosaCreER* (A) or *Rgs5*$^{f/f}$*;RosaCreER* (B) and *Rgs4/5*$^{f/f}$ control mice exposed to 7-day 10% O_2, analysed by RT-qPCR. Target mRNA was normalised to *Actb* within each genotype and expressed relative to expression in *Cre*$^{-}$ animals. $n = 1$ set of 5 animals per genotype.

To evaluate the effects of acute RGS4/5 inactivation in adulthood on VAH, hypoxic and hypercapnic AVRs were measured in tamoxifen-treated *Rgs4*$^{f/f}$*;RosaCreER* and *Rgs5*$^{f/f}$*;RosaCreER* animals exposed to 7-day 10% O_2. There was a progressive increase in 10% O_2/3% CO_2 (Figure 5-14, Table 5-3, Table 5-4, ANOVA Time $P < 0.01$) and 10% O_2 AVRs (Table 5-3, Table 5-4, ANOVA Time $P < 0.01$) in acclimatised *Rgs4*$^{f/f}$ and *Rgs5*$^{f/f}$ controls, although the 10% O_2/3% CO_2 AVRs at 7d H were lower in *Rgs5*$^{f/f}$ than in *Rgs4*$^{f/f}$ controls (Figure 5-14 and compare Table 5-3 with Table 5-4). Additionally, in the *Rgs4* cohort, a small increase in the 3% CO_2 AVR was observed as mice acclimatised to hypoxia (Table 5-3, ANOVA Time $P = 0.011$).

Acute *Rgs4* inactivation in adult mice did not affect VAH, with no difference detected between the responses of *Rgs4*$^{f/f}$*;RosaCreER* and *Rgs4*$^{f/f}$ mice to any of the acute stimuli (Table 5-3).

Acute *Rgs5* inactivation caused a reduction in VAH (measured as an increase in the amplitude of the response to 10% O_2/3% CO_2) (Table 5-4, ANOVA *Rgs5* $P = 0.002$), with the difference in AVRs between *Rgs5*$^{f/f}$*;RosaCreER* and *Rgs5*$^{f/f}$ mice being most

striking after 2-day CH (Figure 5-14 and Table 5-4). No significant differences between AVRs to 10% O_2 or 3% CO_2 were observed (Table 5-4), although there was a statistically significant interaction between the effect of *Rgs5* inactivation and time under hypoxia with respect to 3% CO_2 AVRs (Table 5-4, ANOVA interaction $P = 0.016$).

Together, this suggests that acute *Rgs5* inactivation in adulthood diminishes VAH, although the effect is less marked than in mice with constitutive *Rgs5* inactivation in TH^+ cells (Figure 5-9), which could be due to the less efficient *Rgs5* recombination in tamoxifen-treated, *vs* TH-IRES-Cre-expressing mice, or it may suggest the hypomorphic VAH in *Rgs5*$^{f/f}$*;THCre* mice is partly due to developmental alterations in CB physiology.

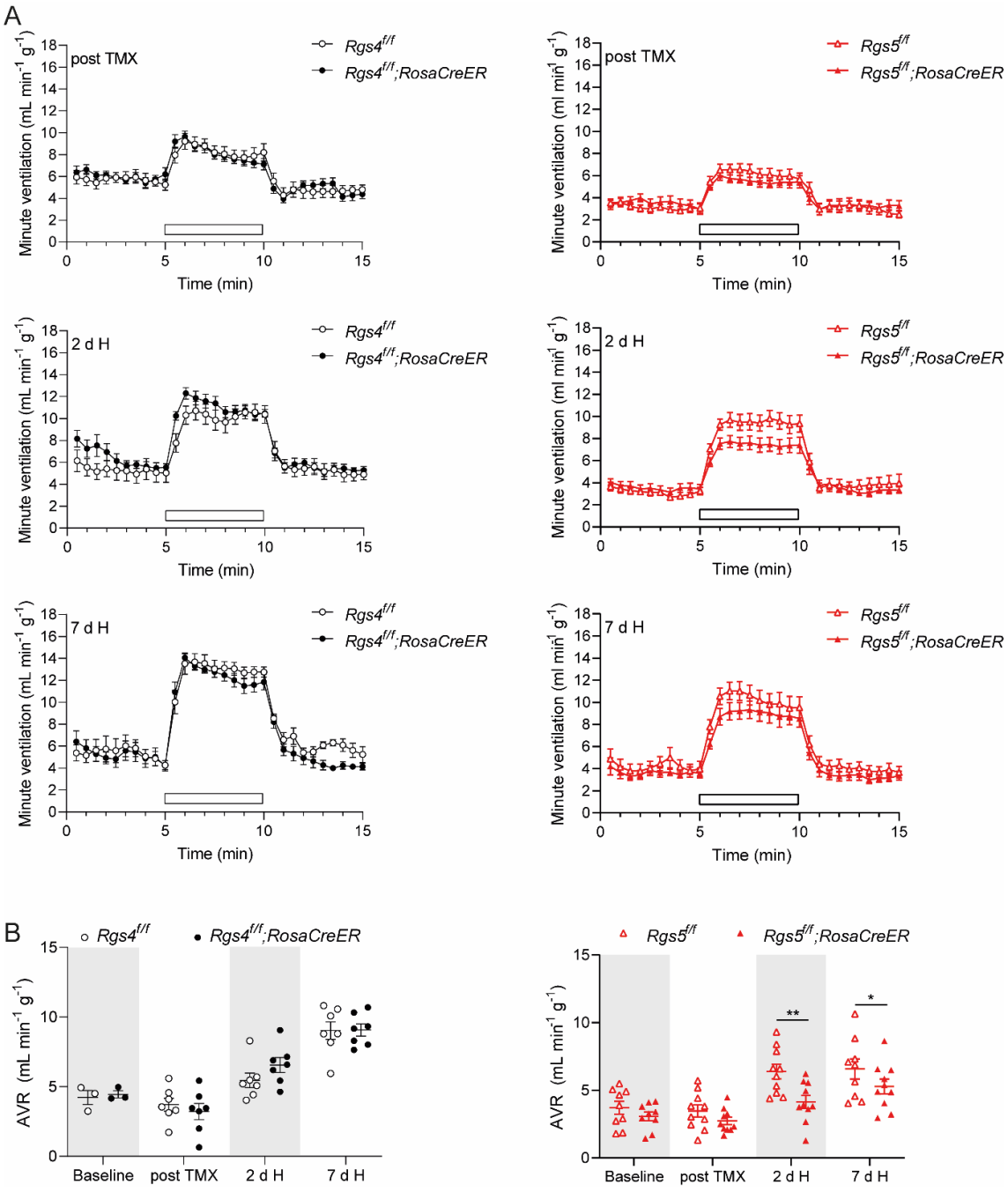


Figure 5-14. VAH in mice with acute *Rgs4* or *Rgs5* inactivation in adulthood.

(**A**) MVb under 5 min 10% O_2/3% CO_2 (open bars) in *Rgs4*$^{f/f}$*;RosaCreER* (black circles) or *Rgs5*$^{f/f}$*;RosaCreER* (red triangles) mice compared with *Rgs4*$^{f/f}$ or *Rgs5*$^{f/f}$ controls (open circles/triangles) exposed to 7-day 10% O_2 (H), measured before (Baseline, not shown) and 10 days after the start of tamoxifen treatment (post TMX), and after 2 and 7 days H; $n = 7$ for *Rgs4*$^{f/f}$*;RosaCreER*, $n = 9$ for *Rgs5*$^{f/f}$*;RosaCreER*. (**B**) 10% O_2/3% CO_2 HVRs quantified from data in A. Data from knock-out mice were compared with controls using a 2-way ANOVA, followed by a Sidak's multiple comparisons test, with significance shown in the graph: $*P < 0.05$, $**P < 0.01$. 2-way ANOVA *P* values are in Table 5-3 and Table 5-4**.**

Table 5-3. Hypoxic and hypercapnic AVRs in acclimatised *Rgs4$^{f/f}$;RosaCreER* mice.
10% O_2/3% CO_2, 10% O_2 and 3% CO_2 AVRs measured before (Baseline) and 10 days after the start of tamoxifen treatment (post TMX) in unacclimatised mice, and after 2 and 7-day 10% O_2 hypoxia (H); $n = 7$ ($n = 3$ for Baseline). Data were analysed by 2-way ANOVA and time, *Rgs4* and interaction (bottom right corner) *P* values are shown; followed by Sidak's multiple comparisons *t*-tests. $P < 0.05$ are bolded. Baseline measurements have been excluded from statistical analyses and compared with an unpaired Student's *t*-test.

		Rgs4$^{f/f}$		*Rgs4$^{f/f}$;RosaCreER*			Time/
	Time point	Mean	SEM	Mean	SEM	*t*-test *P*	Interaction *P*
10% O_2 / 3% CO_2	Baseline	4.23	± 0.51	4.45	± 0.26	*0.719*	
	post TMX	3.71	± 0.46	3.21	± 0.58	*0.766*	
	2d H	5.46	± 0.52	6.56	± 0.53	*0.390*	***<0.0001***
	7d H	9.03	± 0.64	9.07	± 0.44	*0.953*	
	Rgs4 P		*0.649*				*0.303*
10% O_2	Baseline	-0.91	± 0.61	0.04	± 0.24	*0.224*	
	post TMX	-0.21	± 0.49	0.20	± 0.40	*0.738*	
	2d H	1.64	± 0.38	1.16	± 0.38	*0.738*	***<0.0001***
	7d H	2.49	± 0.51	3.62	± 0.64	*0.280*	
	Rgs4 P		*0.481*				*0.166*
3% CO_2	Baseline	3.77	± 1.42	3.15	± 0.74	*0.714*	
	post TMX	1.58	± 0.26	1.60	± 0.32	*0.975*	
	2d H	1.54	± 0.34	2.10	± 0.45	*0.769*	***0.011***
	7d H	2.84	± 0.65	2.46	± 0.53	*0.797*	
	Rgs4 P		*0.900*				*0.390*

Table 5-4. Hypoxic and hypercapnic AVRs in acclimatised *Rgs5$^{f/f}$;RosaCreER* mice.
10% O_2/3% CO_2, 10% O_2 and 3% CO_2 AVRs measured before (Baseline) and 10 days after the start of tamoxifen treatment (post TMX) in unacclimatised mice, and after 2 and 7-day 10% O_2 exposure (H); $n = 10$ ($n = 9$ for Baseline). Data were analysed by 2-way ANOVA and time, *Rgs5* and interaction (bottom right corner) *P* values are shown; followed by Holm-Sidak's multiple *t*-tests. $P < 0.05$ are bolded. Baseline measurements have been excluded from statistical analyses and compared by Student's *t*-test.

		Rgs5$^{f/f}$		*Rgs5$^{f/f}$;RosaCreER*			Time/
	Time point	Mean	SEM	Mean	SEM	*t*-test *P*	Interaction *P*
10% O_2 / 3% CO_2	Baseline	3.70	± 0.47	3.08	± 0.33	0.291	
	post TMX	3.48	± 0.44	2.74	± 0.28	*0.030*	
	2 d H	6.39	± 0.54	4.14	± 0.47	***0.008***	***<0.001***
	7 d H	7.16	± 0.66	5.29	± 0.54	***0.022***	
	Rgs5 P		***0.002***				*0.260*
10% O_2	Baseline	-0.27	± 0.59	0.03	± 0.37	0.668	
	post TMX	0.53	± 0.22	0.08	± 0.44	0.501	
	2 d H	1.47	± 0.39	1.52	± 0.59	0.892	***<0.001***
	7 d H	2.32	± 0.23	1.35	± 0.25	0.054	
	Rgs5 P		*0.106*				*0.179*
3% CO_2	Baseline	1.74	± 0.44	2.08	± 0.43	0.583	
	post TMX	2.34	± 0.41	1.35	± 0.44	0.156	
	2 d H	1.67	± 0.25	2.55	± 0.27	0.156	*0.642*
	7 d H	2.65	± 0.34	1.66	± 0.40	0.156	
	Rgs5 P		*0.234*				***0.016***

5.2.7 *Carotid body proliferation in mice with acute Rgs4 or 5 inactivation*

To test the effect of acute *Rgs4* or *Rgs5* inactivation on hypoxia-induced CB proliferation, CB volume and BrdU incorporation were assessed (Figure 5-15). High cellular BrdU incorporation was observed in the CBs of *Rgs4$^{f/f}$* and *Rgs5$^{f/f}$* controls, with $BrdU^+$ cell density somewhat lower in the latter (Figure 5-15). The discrepancy between the *Rgs4$^{f/f}$* and *Rgs5$^{f/f}$* $BrdU^+$ cell density could be a batch effect, for example due to differences in processing/embedding (highlighting the importance of testing both control and KO mice in parallel in this protocol), but it may illustrate difference in the

degree of acclimatisation of these mice, in line with lower VAH in *Rgs5*$^{f/f}$ mice noted above (Figure 5-14).

Tamoxifen-induced *Rgs4* inactivation resulted in a trend towards lower BrdU incorporation, although this did not reach statistical significance (Figure 5-15, $P = 0.082$, $n = 4$). There was a trend towards increased CB volume in the *Rgs4*$^{f/f}$*;RosaCreER* mice compared to the *Rgs4*$^{f/f}$ controls (Figure 5-15), although the *Rgs4*$^{f/f}$ CBs were smaller than those of *Rgs5*$^{f/f}$ mice (in contrast to higher $BrdU^+$ cell density in *Rgs4*$^{f/f}$ than in *Rgs5*$^{f/f}$ CBs). No significant change in the volume ($P = 0.944$, $n = 4$) or $BrdU^+$ cell density ($P = 0.593$, $n = 4$) was observed in *Rgs5*$^{f/f}$*;RosaCreER* CBs (Figure 5-15), suggesting acute *Rgs5* inactivation does not affect hypoxia-induced CB proliferation.

In summary, no significant changes in either CB proliferation or hyperplasia in 7-day acclimatised mice were found between *Rgs4*$^{f/f}$*;RosaCreER* or *Rgs5*$^{f/f}$*;RosaCreER* mice and their littermate controls, suggesting that reduced VAH in *Rgs5*KO mice occurs despite normal hypoxia-induced CB proliferation.

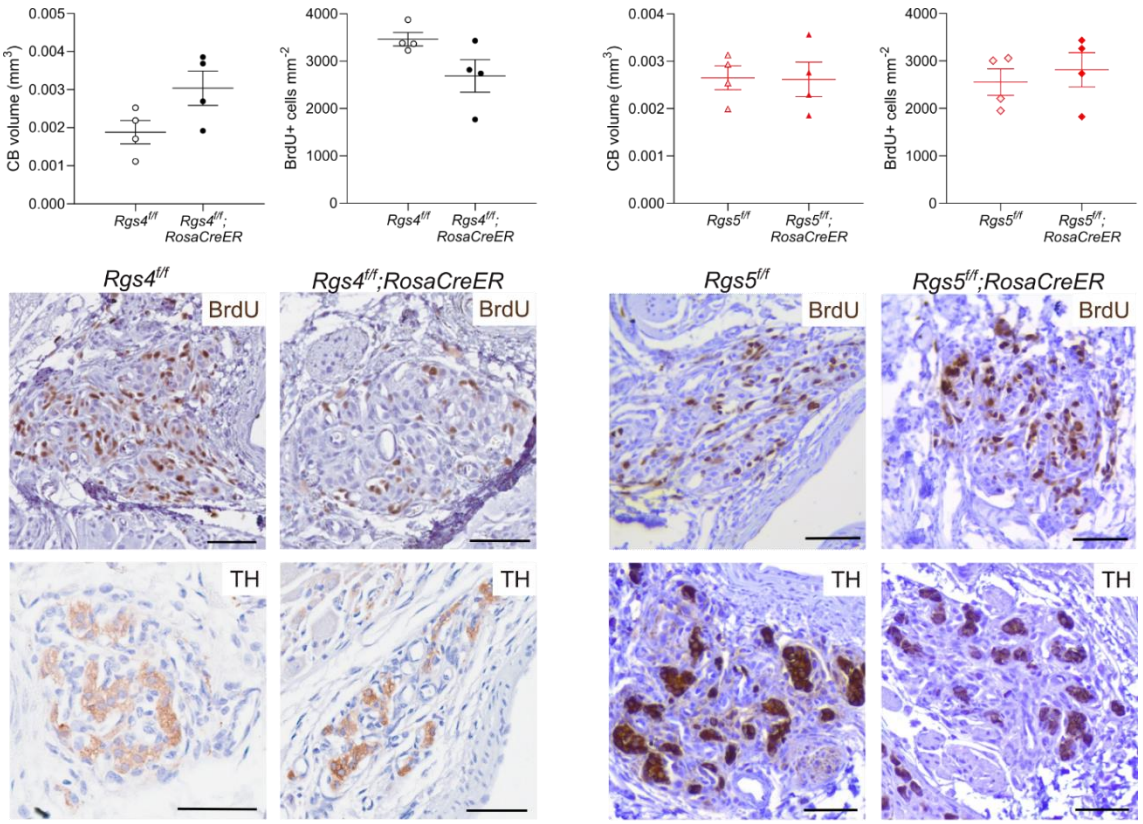


Figure 5-15. CB proliferation in acclimatised *Rgs4$^{f/f}$;RosaCreER* and *Rgs5$^{f/f}$;RosaCreER* mice.

CB volume and BrdU incorporation in *Rgs4$^{f/f}$;RosaCreER* (left panels) and *Rgs5$^{f/f}$;RosaCreER* (right panels) mice and *Rgs4$^{f/f}$* and *Rgs5$^{f/f}$* controls exposed to 7-day 10% O_2. Individual data with means ± SEM are plotted in the graphs. Between-genotype comparisons were made by unpaired Student's *t*-tests, with no $P < 0.05$ detected. Representative images showing BrdU and TH IHC used for the quantification are shown in the bottom panels. Scale bars represent 0.05 mm.

5.3 Discussion

Inactivation of *Rgs5*, but not *Rgs4*, reduced VAH, both in the developmental and acute inactivation in adult models. The effects were more pronounced with *Rgs5* inactivation during development, indicating that *Rgs5* may additionally be involved in CB development. However, no abnormalities in gross CB morphology or volume were found in *Rgs5$^{f/f}$;THCre* mice compared with their *Rgs5$^{f/f}$* littermates. Developmental changes in cellular physiology could still, however, predispose to the hypomorphic

VAH in *Rgs5*KOs. This could be explored further by electron microscopy imaging, which has previously been used to demonstrate a reduction in DCV density and the appearance of atypical, 'eccentric' DCVs in CH CBs and in mice with developmental *Phd2* inactivation (Fielding et al., 2018, Cheng et al., 2020).

Differences in the degree of VAH loss in mice with acute and developmental *Rgs5* inactivation could also be due to the varying efficiency of recombination between the constitutively active TH-IRES-Cre and tamoxifen-inducible Rosa26Cre^{ERT2}. Data presented in this chapter do not allow a direct comparison of recombination efficiency, as *Rgs5* mRNA levels were tested by ISH in the *Rgs5$^{f/f}$;THCre*, whereas quantitative *Rgs5* mRNA assessment by RT-qPCR was performed in *Rgs5$^{f/f}$;RosaCreER* animals. ISH was chosen as the method to confirm *Rgs5* recombination in animals with TH^{+} cell-restricted *Rgs5* inactivation to avoid false-negative results due to contamination with *Rgs5* mRNA from non-CB cells in a bulk mRNA preparation. This might be particularly problematic in *Rgs5* mRNA preparation, as *Rgs5* is highly expressed in the vasculature (Nisancioglu et al., 2008), including in the CB, which would not be targeted by the TH-IRES-Cre recombinase. On the other hand, ISH may lack sensitivity to accurately compare recombination efficiency between the two models, as it only provides a semi-quantitative measurement of mRNA expression (Lee et al., 2008), therefore RT-qPCR was employed in the *Rgs4/5$^{f/f}$;RosaCreER* models.

VAH is typically associated with CB proliferation and hyperplasia and genetic inactivation and pharmacological inhibition of HIF-2α prevents both these adaptive responses to sustained hypoxia (Hodson et al., 2016, Cheng et al., 2020). *Rgs5* inactivation, however, reduced VAH without affecting cellular proliferation in the CB. Although a small reduction in CB volume was observed in acclimatised *Rgs5$^{f/f}$;THCre* mice *vs Rgs5$^{f/f}$* controls, marked changes in CB volume require longer 10% O_2

exposure: 10-28, rather than the 7-day protocol used here (Pardal et al., 2007, Fielding et al., 2018). These data, therefore, point to the possible disconnect between the increased number of TH^+ cells in the CB and the ability to increase ventilation under sustained hypoxia and point to a role of RGS5 specifically in the latter.

Different molecular alterations have been proposed to cause increased CB sensitivity under CH, including changes in the ion channel composition and activity and in the neurotransmitter signalling, particularly via GPCR activation/inhibition (Prabhakar et al., 2009, Bisgard, 2000, see section 1.2.3). RGS5 could act to alter this signalling, thus mediating VAH. RGS5 binds to $G_{\alpha q}$ subunits, which activate PLC to cause Ca^{2+} release from intracellular stores. In line with this, diminished [Ca^{2+}] increase in response to endothelin (a GPCR agonist) stimulation has previously been demonstrated in RGS5-transfected 293T cells (Zhou et al., 2001). Hypoxic chemotransduction in the CB comprises membrane depolarization to open voltage-gated Ca^{2+} channels, resulting in Ca^{2+}-dependent neurotransmitter release (section 1.2.2). RGS5-dependent reduction in intracellular Ca^{2+} release would therefore act in the opposite direction, reducing rather than increasing neurotransmitter release. However, RGS5-mediated inhibition of GPCR-stimulated neurotransmitter release could help preserve a greater neurotransmitter pool available for release upon hypoxia-induced depolarisation and extracellular Ca^{2+} influx, thus contributing to enhanced CB neurosecretion resulting in VAH.

In a more direct signalling mechanism, RGS5-induced GTP hydrolysis at the G_α subunit, which would cause re-assembly of the G-protein heterotrimer, may negatively regulate $G_{\beta\gamma}$ signalling. $G_{\beta\gamma}$ subunits are known to modulate $Ca^{2+}{}_v$ channels by increasing the depolarisation potential required for their opening (reviewed in Zamponi and Currie, 2013). RGS5-mediated increased rate of $G_{\beta\gamma}$ signal termination could

therefore facilitate CB response to hypoxia by reducing the depolarisation potential required to trigger Ca^{2+} influx and subsequent neurotransmitter release.

Finally, RGS5-mediated VAH modulation could be via inhibition of the $G_{\alpha i}$-mediated signalling, as relief of dopamine-dependent inhibition of CB activity via $G_{\alpha i}$-coupled receptors has been proposed to enhance CB neurosecretion in CH (see section 1.2.3). Treatment with a D_2-selective inhibitor, domperidone, mimics VAH in cats, with non-additive effects of domperidone and CH on cat HVR (Tatsumi et al., 1995). D_2 receptors are $G_{\alpha i}$-coupled and could therefore be inhibited by RGS5 stabilisation in hypoxia.

Overall, multiple signalling pathways linking GPCRs to type I cell neurosecretion exist, many of which could be targeted by RGS5. Further *in vitro* studies on Ca^{2+} and K^+ currents, as well as downstream GPCR signalling in CB type I cells, are needed to understand the mechanism of RGS5 function in VAH.

Of note, transcriptomic studies highlighted *Gnas*, encoding a $G_{\alpha s}$ stimulatory subunit (and not the $G_{\alpha i}$ or $G_{\alpha q}$), as the most highly expressed gene in the type I cells (Zhou et al., 2016), suggesting multiple different G-protein signalling pathways might contribute to the modulation of the CB hypoxic response, including independently of RGS5.

Regardless of the mechanism involved, a role for RGS5 in mediating VAH is in line with its uniquely high expression in the CB. This contrasts to the expression of *Rgs4*, which is expressed throughout the neuronal tissues, including the CB (possibly due to the neuronal properties of this chemoreceptor), and inactivation of which does not affect VAH. Interestingly, a recent single-cell RNA sequencing study of the zebrafish gill showed *Rgs5* to be the second most highly differentially expressed in the oxygen-sensing neuroepithelial cells compared to other gill cells, suggesting that this protein is

conserved in oxygen-chemotransducing cells of other species (Pan et al., 2022). Within mammals, *Rgs5* expression also aligns with acute oxygen sensitivity in chromaffin cells (Nurse et al., 2009), with high expression in the O_2-sensitive neonatal (Chan et al., 2019), but not in O_2-insensitive adult AM (Gao et al., 2017). *Rgs5* is also a pericyte marker (Nisancioglu et al., 2008) and these cells have been shown to express CB-enriched atypical mitochondrial subunits, *Ndufa4l2* and *Cox4i2* (Mesa-Ciller et al., 2022), suggesting a possible acute oxygen sensing function of this cell type.

The main site of *Rgs5* expression throughout the body is microvasculature, including in the kidneys (Nisancioglu et al., 2008, Cho et al., 2003), which orchestrate the hematopoietic response to CH by upregulating erythropoietin expression. Although *Epo* is mostly produced by the interstitial fibroblasts, renal pericytes can also secrete EPO in an oxygen-dependent manner (Chang et al., 2016), potentially implicating a role of *Rgs5* in this hypoxic response. However, no reduction in hypoxia-induced polycythaemia was observed in *Rgs5$^{f/f}$;RosaCreER* mice in this Chapter ($58 \pm 1\%$ *vs* $60.0 \pm 0.8\%$ RBCs in whole blood in *Rgs5$^{f/f}$;RosaCreER vs* Cre$^-$ controls, Student's *t*-test $P = 0.271$, $n = 7$).

Overall, there is compelling evidence for the role of RGS5 in VAH and in line with its role in adaptations to chronic hypoxia, RGS5 activity is mediated by two independent oxygen-sensitive signalling pathways (HIF and ADO) and *Rgs5* expression is highly enriched (and conserved) in oxygen-sensitive tissues. Future studies should focus on the role of *Rgs5* in modulating CB hypoxic chemotransduction, and the relationship between *Rgs5* expression and acute oxygen sensitivity in different tissues.

6

Developmental role of PHD2/HIF-2α in the pathogenesis of pheochromocytomas and paragangliomas

6.1 Introduction

Work described in the previous chapters has demonstrated that HIF-2α is necessary to develop VAH and CB proliferation under low oxygen conditions and that it is involved in mediating acute HVR. However, to understand the function of HIF-2α in CB physiology, it is also important to test whether HIF-2α stabilisation alone (in the absence of environmental hypoxia) is sufficient to induce acute oxygen sensing underlying these phenotypes. Indeed, there is clinical evidence suggesting HIF-2α activation affects the CB and related tissues in the sympathoadrenal system in the context of cancer.

Pheochromocytomas and paragangliomas (PPGLs) are tumours affecting the AM and sympathetic ganglia, including the CB (see section 1.5). PPGLs are a rare syndrome of highly familial tumours, with up to 40% of cases caused by germline or post-zygotic but

early somatic mutations (Dahia, 2014, Crona et al., 2017). Among these, three genetic clusters have been identified, with mutations affecting the hypoxia (pseudohypoxic Cluster 1), kinase (Cluster 2) and Wnt (Cluster 3) signalling pathways (Fishbein et al., 2017, Jochmanova and Pacak, 2018). Of the pseudohypoxic mutations, Cluster 1b specifically contains mutations in the HIF pathway components, leading to stabilisation of HIF-2α: loss-of-function mutations in *EGLN1* and *VHL* and gain-of-function mutations in *EPAS1*. PPGLs with these mutations have a characteristic transcriptomic profile, with upregulation of several HIF-target genes, oncogenes, as well as atypical mitochondrial subunits and components of the G-protein signalling pathway (Dahia et al., 2005, Favier et al., 2009, Waldmann et al., 2010, Burnichon et al., 2011, Lorenzo et al., 2013, Toledo et al., 2013, Welander et al., 2014, Yang et al., 2015, Fishbein and Nathanson, 2017). Interestingly, many of these genes are highly expressed in the CB, including *Rgs4* and *Rgs5*, discussed in Chapter 5 and *Cox4i2* and *Ndufa4l2* (Zhou et al., 2016, Moreno-Dominguez et al., 2019).

To test the effects of HIF stabilisation on chromaffin cells and the PPGL formation in mice, the dominant negative regulator of HIF: *Phd2*, was inactivated in TH^+ cells and the effects on chromaffin cells tested. *Phd2*$^{f/f}$*;THCre* mice developed PCC-like morphological abnormalities in the AM, with gene expression altered to match the transcriptomic profile observed in PPGL patients. Further analysis revealed that chromaffin cells exist as a binary population, with *Pnmt*$^+$*/Rgs5*$^-$*/Epas1*$^-$ cells dominating and a minority of *Pnmt*$^-$*/Rgs5*$^+$*/Epas1*$^+$ cells. PHD2 inactivation/HIF-2 activation caused a switch towards predominantly immature/noradrenergic *Pnmt*$^-$*/Rgs5*$^+$*/Epas1*$^+$ cells. Transcriptomic analysis of *Phd2*KO AMs revealed a change in the gene expression profile to resemble that observed in PPGL patients, with upregulation of genes typically

found in developing chromaffin cells and characteristic of adult CB i.e. acutely oxygen sensing cells. Last, acute oxygen sensitivity was therefore tested in *Phd2*KO AMs.

6.2 **Results**

6.2.1 *Constitutive Phd2 inactivation in the adrenal medulla results in pseudohypoxic PPGL-like transcriptomic profile and abnormal morphology*

Based on multiple transcriptomic studies of PPGL patients, a panel of 14 genes dysregulated in pseudohypoxic PPGLs was chosen (Table 6-1) and their expression tested in the AMs of *Phd2*$^{f/f}$*;THCre* mice and *Phd2*$^{f/f}$ controls (Figure 6-1A). In line with human studies, *Phd2* inactivation in chromaffin cells caused an induction in expression of HIF-target genes: *Vegfa, Slc2a1* and *Ldha,* as well as *Hif-2α* (Figure 6-1A). There was a marked and significant increase in expression of the CB-enriched cytochrome c oxidase subunit *Cox4i2* (Gao et al., 2017), but not *Ndufa4l2,* pointing to a possible partial alteration in mitochondrial function of the chromaffin cells. Expression of regulators of G-protein signalling: *Rgs4* and *Rgs5* was induced in *Phd2*KO AMs, as was the expression of a highly CB-enriched GPCR: *Adora2a* (Figure 6-1A) (Zhou et al., 2016).

In line with human transcriptomic studies showing downregulation of *Pnmt* in pseudohypoxic PCCs (Dahia et al., 2005, Welander et al., 2014, Fishbein et al., 2017), *Pnmt* expression was nearly completely abolished in *Phd2*$^{f/f}$*;THCre* AMs. *Pnmt* encodes the phenylethanolamine N-methyltransferase enzyme, which converts noradrenaline to adrenaline. Downregulation of *Pnmt* therefore suggests a switch towards a dominating noradrenergic profile in these knock-out mice. To test this, plasma catecholamine levels were measured in *Phd2*$^{f/f}$*;THCre* and *Phd2*$^{f/f}$ control animals (Figure 6-1B). As expected

from the loss of *Pnmt* expression, *Phd2* inactivation resulted in a reduction in adrenaline and increase in noradrenaline plasma levels (Figure 6-1B).

Table 6-1. Genes with expression dysregulated in pseudohypoxic PPGLs.[11]

The table lists 14 genes with up- or down-regulation (relative to healthy tissue) commonly described in pseudohypoxic paragangliomas and pheochromocytomas, representing several classes of genes including: HIF-pathway components and HIF-target genes, G-protein signalling pathway components, atypical mitochondrial subunits and classical oncogenes. Mutation and type of PPGL in which the expression abnormality has been described, as well as the source, are stated.

Gene	Differential regulation	Mutation and type of PPGL	Reference
VEGFA	Upregulated	*VHL*- and *SDHx*-PCCs	Dahia et al., 2005
		SDHx- and *VHL*-PPGLs	Burnichon et al., 2011
		VHL- and *SDHx*-PPGLs and *HIF-2α*-PCCs	Favier et al., 2012
		HIF-2α-PGLs	Lorenzo et al., 2013
		HIF-2α-PPGLs	Toledo et al., 2013
		HIF-2α-PCCs	Welander et al., 2014
		PHD1- and *PHD2*-PCCs	Yang et al., 2015
SLC2A1	Upregulated	*VHL*- and *SDHx*-PPGLs	Favier et al., 2009
		VHL-PPGLs	Burnichon et al., 2011
		HIF-2α-PGL	Lorenzo et al., 2013
		PHD2-PCCs	Yang et al., 2015
CCND1	Not dysregulated	Pseudohypoxic (*VHL*, *SDHx*) PPGLs	Toledo et al., 2013
		HIF-2α-PCCs	Welander et al., 2014
	Upregulated	*HIF-2α*-PPGLs	Toledo et al., 2013
LDHA	Upregulated	*VHL*- and *SDHx*-PPGLs	Dahia et al., 2005
		VHL- and *SDHx*-PPGLs	Favier et al., 2009
		SDHx- and *VHL*-PPGLs	Burnichon et al., 2011
		PHD1- and *PHD2*-PPGLs	Yang et al., 2015
HIF-2α	Upregulated	*SDHx*- and *VHL*-PPGLs	Burnichon et al., 2011
		VHL- and *SDHx*-PPGLs	Favier et al., 2009
		VHL- and *SDHx*-PPGLs and *HIF-2α*-PCCs	Favier et al., 2012
		HIF-2α-PCCs	Welander et al., 2014
NDUFA4L2	Upregulated	*VHL*- and *SDHx*-PPGLs	Favier et al., 2009
		SDHx- and *VHL*-PPGLs	Burnichon et al., 2011
		Pseudohypoxic (*SDHx/VHL/HIF-2α/PHD2*) PPGLs	Fishbein et al., 2017
COX4I2	Upregulated	*VHL*- and *SDHx*-PPGLs	Favier et al., 2009
		SDHx- and *VHL*-PPGLs	Burnichon et al., 2011
		VHL- and *SDHx*-PPGLs and *HIF-2α*-PCCs	Favier et al., 2012
		HIF-2α-PCCs	Welander et al., 2014

[11] As published in Eckardt et al., 2021.

		Pseudohypoxic (*SDHx/VHL/HIF-2α/PHD2*) PPGLs	Fishbein et al., 2017
RGS4	Upregulated	*SDHx*- and *VHL*-PPGLs	Burnichon et al., 2011
RGS5	Upregulated	PPGLs	Waldmann et al., 2010
ADORA2A	Upregulated	*SDHx*- and *VHL*-PPGLs	Burnichon et al., 2011
PNMT	Downregulated	*VHL*- and *SDHx*-PPGLs	Dahia et al., 2005
		HIF-2α-PCCs	Welander et al., 2014
		Pseudohypoxic (*SDHx/VHL/HIF-2α/PHD2*) PPGLs	Fishbein et al., 2017
STC1	Upregulated	*VHL*- and *SDHx*-PPGLs	Dahia et al., 2005
		SDHx- and *VHL*-PPGLs	Burnichon et al., 2011
IGF2	Upregulated	PPGLs	Waldmann et al., 2010
		HIF-2α-PPGLs	Toledo et al., 2013
RET	Downregulated	*VHL*- and *SDHx*-PPGLs	Dahia et al., 2005
		Pseudohypoxic (*SDHx/VHL/HIF-2α/PHD2*) PPGLs	Fishbein et al., 2017

Both the transcriptomic and catecholaminergic profiles of *Phd2$^{f/f}$;THCre* animals match those observed in pseudohypoxic PPGL patients. To test whether *Phd2*KO mice develop PCCs, AM morphology and volume were assessed (Figure 6-1C). Chromaffin cells were identified by the expression of TH, the rate-limiting enzyme in catecholamine synthesis. Adult wild-type adrenal glands displayed high levels of TH in the AM, enclosed by a layer of TH$^-$ cortical cells (Figure 6-1C). In contrast, *Phd2$^{f/f}$;THCre* AMs extended beyond the cortical barrier with tracks of TH$^+$ cells leading to ectopic chromaffin cell clusters and sympathetic ganglia-like TH$^+$ structures characterized by large, 'ghosted' nuclei (Figure 6-1C). Despite these clear morphological abnormalities observed in 11/14 *Phd2$^{f/f}$;THCre* and 0/15 *Phd2$^{f/f}$* mice, AM volume modelled from TH$^+$ areas in serial sections of adult adrenal glands was unchanged in *Phd2$^{f/f}$;THCre* mice relative to littermate controls (0.08 ± 0.02 *vs* 0.08 ± 0.01 mm^3, $n = 5$, unpaired Student's *t*-test $P = 0.731$). Together, these findings suggest that *Phd2* inactivation

causes PCC-like changes in the AM transcriptome and plasma catecholamines, as well as morphological abnormalities, but not frank tumours.

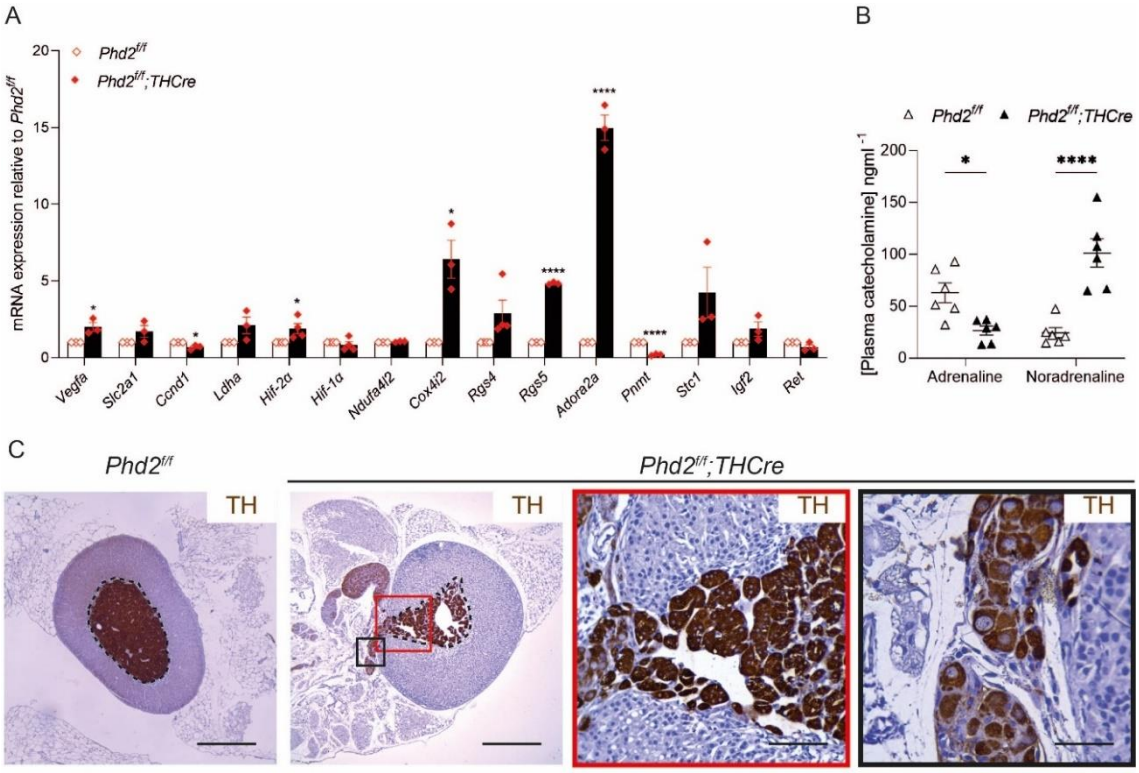


Figure 6-1. *Phd2* inactivation in chromaffin cells results in pseudohypoxic PCC-like transcriptomic and catecholaminergic profiles, as well as abnormal morphology[12].
(**A**) Expression of a panel of genes typically dysregulated in PPGL patients, assessed by qPCR in *Phd2$^{f/f}$;THCre vs Phd2$^{f/f}$* AMs, pooled from five animals per genotype. $n = 3$ biological replicates with each replicate representing an average of 5 animals. Expression of individual genes is compared by unpaired Student's *t*-tests. (**B**) Plasma levels of adrenaline and noradrenaline in *Phd2$^{f/f}$;THCre* and *Phd2$^{f/f}$* control mice, analysed in plasma taken from terminally anaesthetized adults. Data were analysed by a two-way ANOVA, with Sidak's multiple comparisons test *P* values displayed in the graph. $*P < 0.05$, $****P < 0.0001$. (**C**) Representative images of TH immunohistochemistry in *Phd2$^{f/f}$* and *Phd2$^{f/f}$;THCre* AMs. Red and black frame inserts show high magnification images to detail the ectopic TH$^+$ cell tracks and extra-adrenal ganglia in *Phd2*KOs. Scale bars: 0.5 mm (far and middle left panels), 0.1 mm (red frame), 0.05 mm (black frame).

Morphological abnormalities observed in the *Phd2$^{f/f}$;THCre* AMs, with TH$^+$ cells breaking the cortical boundary and forming ectopic tracks extending outside of the

[12] As published in Eckardt et al., 2021.

adrenal gland, resemble neonatal adrenals, with incomplete migration of the chromaffin cells into the medulla (Coupland, 1965). Immature, migrating cells are $PNMT^-$ (noradrenergic) and PNMT is only expressed once the cells reach the cortex, to form two distinct cell populations in the adult: dominant $PNMT^+$ (adrenergic) and minority $PNMT^-$ (noradrenergic) (Coupland and Hopwood, 1966, Verhofstad et al., 1989). Spatial expression of *Pnmt* was therefore analysed in the wild-type and *Phd2$^{f/f}$;THCre* AMs (Figure 6-2) to test if, in addition to arrested migration, *Phd2* inactivation might preserve PNMT status of the chromaffin cells in their immature state.

ISH against *Pnmt* in wild-type AM sections showed >50% of cells to be *Pnmt*$^+$, with the minority *Pnmt*$^-$ cells clustering around the edges near the cortex (Figure 6-2A). In other sections, the ratio of *Pnmt*$^+$:*Pmnt*$^-$ cells was even higher (Figure 6-2B) and the exact proportion likely depends on how deep within the AM the section is cut. This is in line with published reports that $PNMT^+$ cells usually dominate in the adult AM, with ~80% of the AM in the rat and mouse and nearly 100% in the human producing adrenaline (Wong, 2003).

There was a clear difference in the proportion of *Pnmt*$^+$ cells in the *Phd2$^{f/f}$;THCre* AM, with very few *Pnmt*$^+$ regions detected, in line with the change in plasma catecholamine levels (Figure 6-2B). Interestingly, in addition to the reduced number of *Pnmt*$^+$ cell clusters, there was also a change in their spatial distribution, with *Pnmt*$^+$ cells now mostly present at the cortical boundary (Figure 6-2B).

Next, we sought to test whether other genes noted as dysregulated by *Phd2* inactivation (Figure 6-1A) also have a binary expression pattern in the AM. *Epas1* was chosen as it encodes HIF-2α, the downstream mediator of *Phd2* function and previously reported to be highly expressed in the developing adrenal and important for catecholamine

secretion in the mouse embryo (Tian et al., 1998). *Rgs5* has previously been reported as a HIF-target gene *in vitro* (Jin et al., 2009) and has been proposed to play a role in chromaffin cell differentiation (Chan et al., 2019, Hanemaaijer et al., 2021). It was also highly upregulated in bulk mRNA from *Phd2$^{f/f}$;THCre* AM (Figure 6-1A). Finally, expression of a classic HIF-2 target gene, *Vegfa*, was assessed, as it was previously shown to be upregulated *in vivo* in the *Phd2$^{f/f}$;THCre* CB (Fielding et al., 2018).

Comparison of *Pnmt*, *Epas1* and *Rgs5* expression in sequential sections of the wild-type AM showed a binary distribution pattern, with no *Epas1* or *Rgs5* detected in the *Pnmt*$^{+}$ regions, but high *Epas1/Rgs5* mRNA levels present in the *Pnmt*$^{-}$ clusters around the AM edge (Figure 6-2A). This suggests that two distinct chromaffin cell populations exist in the adult wild-type AM: a dominating population of adrenergic *Pnmt*$^{+}$*/Epas1*$^{-}$*/Rgs5*$^{-}$ and a minority population of noradrenergic *Pnmt*$^{-}$*/Epas1*$^{+}$*/Rgs5*$^{+}$ cells. No *Vegfa* mRNA was detected in the wild-type AM, in line with no HIF-2α protein stabilisation in the presence of oxygen to induce target-gene expression, although high *Vegfa* levels were found in the adrenal cortex (together with *Epas1* mRNA) (Figure 6-2A).

To test if the negative correlation between expression of *Pnmt* and *Epas1/Rgs5* would be preserved in *Phd2$^{f/f}$;THCre* AM, expression of all three genes was tested in sequential AM sections (Figure 6-2B). *Phd2* inactivation caused a switch towards a dominating population of *Pnmt*$^{-}$*/Epas1*$^{+}$*/Rgs5*$^{+}$ cells, with the remaining *Pnmt*$^{+}$ cells not expressing/co-localising with *Epas1* or *Rgs5* (Figure 6-2B). There was a high induction in *Vegfa* mRNA levels, in line with *Phd2* inactivation causing a state of pseudohypoxia to activate HIF-target genes, however this *Vegfa* was only expressed in the *Epas1*$^{+}$ regions of the *Phd2*KO AM (Figure 6-2B).

Taken together, this suggests that *Phd2* inactivation alters AM gene expression to a more 'immature', noradrenergic profile, with a switch in proportion of adrenergic, *Pnmt*$^{+}$*/Epas1*$^{-}$*/Rgs5*$^{-}$, towards noradrenergic, *Pnmt*$^{-}$*/Epas1*$^{+}$*/Rgs5*$^{+}$ cells. This change is dependent on HIF-2α, but not HIF-1α, stabilisation, as demonstrated by the reversal of morphological and spatial gene expression changes in *Phd2*$^{f/f}$*;Hif-2α*$^{f/f}$*;THCre*, but not *Phd2*$^{f/f}$*;Hif-1α*$^{f/f}$*;THCre* mice (data not shown, see Eckardt et al., 2021). Further, the dominating 'immature' noradrenergic chromaffin cell population together with ectopic TH^{+} cells in *Phd2*KO AMs, indicative of arrested migration, suggest that the AM abnormalities in *Phd2*$^{f/f}$*;THCre* mice are due to developmental HIF-2α stabilisation. This was confirmed by lack of morphological or spatial gene expression changes in *Phd2*$^{f/f}$*;THCreER* mice, with *Phd2* loss induced by tamoxifen-treatment in adulthood; further, in these mice, induction of HIF-target genes such as *Vegfa*, was only observed in the minority population of *Epas1*$^{+}$ cells (data not shown, see Eckardt et al., 2021).

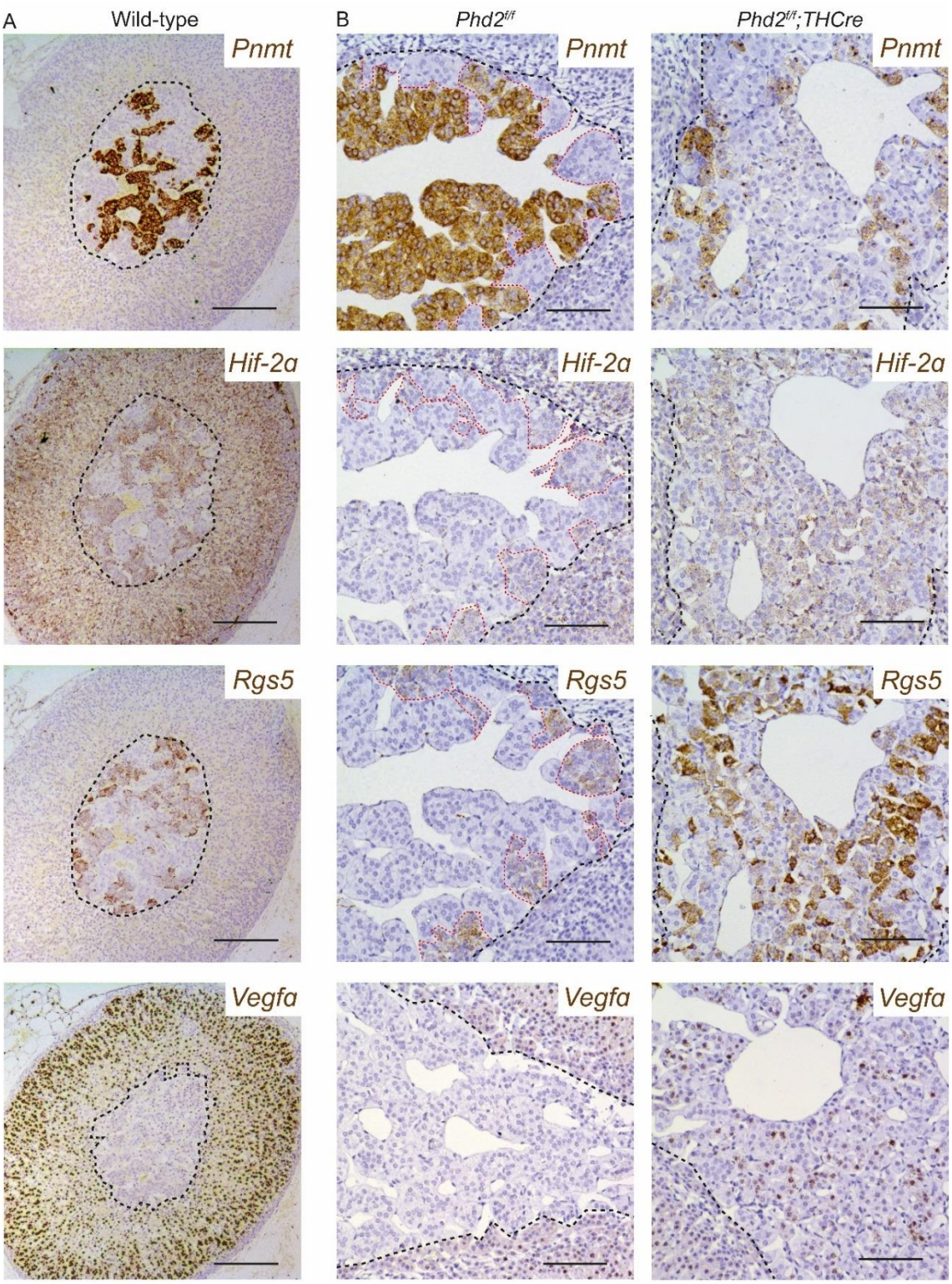


Figure 6-2. Spatial gene expression in the *Phd2$^{f/f}$;THCre* AM. Population switch in noradrenergic/adrenergic chromaffin cells.[13]

(**A**) ISH of *Pnmt, Epas1, Rgs5* and *Vegfa* (brown signal on blue Haematoxylin background) in wild-type AM. (**B**) Binary pattern of *Pnmt* and *Rgs5/Epas1* expression is preserved in

[13]As published in Eckardt et al., 2021. Prepared with Dr Luise Eckardt.

Phd2$^{f/f}$*;THCre* AMs, with a change to dominating *Rgs5*$^{+}$*/Epas1*$^{+}$*/Pnmt*$^{-}$ cell population. As a HIF-target gene, *Vegfa* is only expressed in the *Epas1*$^{+}$ regions of *Phd2*$^{f/f}$*;THCre* AM. AM/cortical boundary is outlined with a black dashed line. Scale bars show 0.05 mm.

6.2.2 *Phd2 inactivation alters AM transcriptome towards a CB-like profile*

To test whether *Phd2* inactivation in the AM alters gene expression towards a more CB-like transcriptomic profile, as suggested from gene dysregulation observed above, bulk RNA was extracted from AMs and CBs pooled from five *Phd2*$^{f/f}$*;THCre* and five *Phd2*$^{f/f}$ control animals and three biological replicates were submitted for RNA sequencing (Figure 6-3).

Principal component analysis (PCA) showed distinct clustering of samples from the same tissues and/or genotypes, with CBs lying along the same region of the PC1, but separated along the PC2 axis, while AM samples separated from the CBs along the PC1 axis (Figure 6-3A, PC1 and PC2 are the two components best explaining variability in gene expression across the samples). As expected, there was a much greater separation between tissue types than between individual genotypes, with PC1 explaining 80%, while the PC2 only explaining 10% of sample variability. Overall, therefore, there were clear differences between samples of the same tissue with a different genotype, but *Phd2* inactivation did not appear to shift the AM transcriptomic profile towards that of the CB (Figure 6-1A). Thus, further analysis focused on subsets of tissue-specific genes to test whether there is any selective upregulation of CB-specific genes in the *Phd2*$^{f/f}$*;THCre* AM.

To identify CB- and AM-specific genes, RNA expression was compared between wild-type CBs and AMs and genes with significantly different expression between the two tissues (false discovery rate (FDR) < 0.1) and above 1.5-fold upregulation were assigned as CB-specific (1827 out of 12067 annotated transcripts with expression > 5

TPM in either wild-type CB or AM), while genes with significantly different expression and greater than 1.5-fold downregulation assigned as AM-specific (1204 out of 12067) (Figure 6-3Bi). Changes in mRNA expression were then assessed in *Phd2*KO *vs* wild-type AMs. In this comparison, fewer genes were found to be 1.5-fold or more upregulated (98 out of 10738 annotated transcripts with expression > 5 TPM in either wild-type or *Phd2*KO AM) and 1.5-fold or more downregulated (67 out of 10738) in the *Phd2*KO relative to wild-type AM (Figure 6-3Bii), in line with the small separation in the PCA plot (Figure 6-3A, PC2). Among the *Phd2*KO-induced genes were those found to be up-regulated in RT-qPCR and spatial analysis, including *Rgs5, Cox4i2, Rgs4* and *Ldha* (Table 6-2), *Adora2a* and *Epas1* (not shown in Table 6-2, but significantly up-regulated, see Figure 6-3Ciii); increased expression of *Ndufa4l2* was also found, as described in pseudohypoxic PPGL patients (Table 6-1), although this was not evident in the RT-qPCR data (Figure 6-1A), while *Pnmt* was one of the down-regulated genes (log2fold change -2.55, adjusted $P < 0.0001$), providing internal validation of the results. No significant differences in the expression of previously tested HIF-target genes: *Vegfa* and *Ccnd1*, were found between wild-type and *Phd2*KO AMs, possibly due to smaller changes in the expression of these genes and low sensitivity due to exclusion of one set of AMs in the analysis. *Phd2* recombination efficiency could not be assessed using RNA Sequencing data, as only the exon 2 of *Phd2* gene is excised in *Phd2$^{f/f}$;THCre* mice and residual mRNA may still be recognised in the sequencing process. Testing *Phd2* expression using an RT-qPCR probe designed specifically against the exon 2, however, showed ~50% loss in *Phd2* mRNA (data not shown), in line with recombination observed in other Cre-loxP animal models (see Chapters 4 and 5 in this thesis).

Tissue specific genes (Figure 6-3Bi) were then mapped to the *Phd2*KO *vs* wild-type AM gene expression comparison and CB-specific genes were found to be significantly more common in the *Phd2*KO upregulated set, while AM-specific genes were significantly more common in the *Phd2*KO downregulated set (Figure 6-3Ci), suggesting that *Phd2* inactivation in the AM is more likely to induce CB-specific, than AM-specific genes. Similarly, genes up- and downregulated in the *Phd2*KO AM (Figure 6-3Bii) were mapped to the CB *vs* AM mRNA expression comparison, and *Phd2*KO induced genes appeared to map to the CB-enriched gene set, while *Phd2*KO supressed genes to the AM-enriched (CB-downregulated) gene set (Figure 6-3Cii), suggesting genes induced by *Phd2* inactivation in the AM are significantly upregulated in the wild-type CB relative to AM.

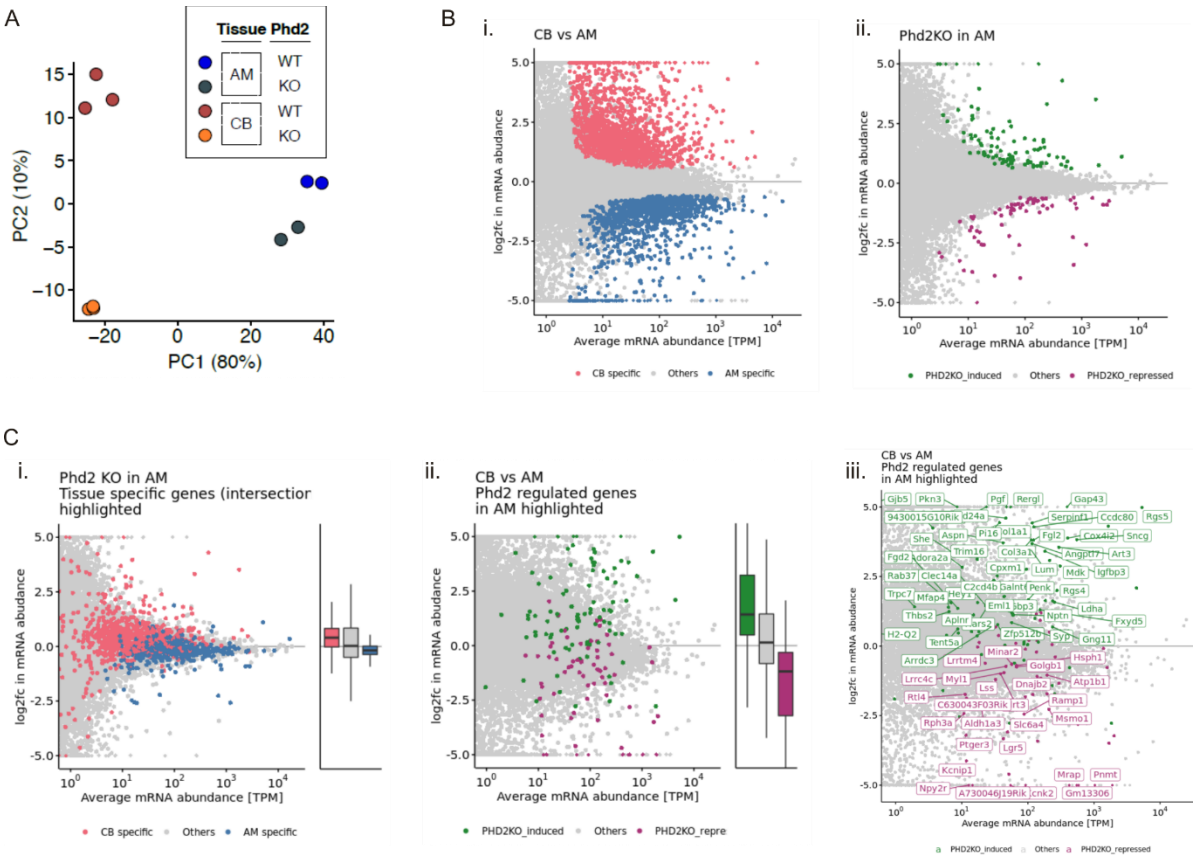


Figure 6-3. RNA Sequencing of *Phd2*$^{f/f}$*;THCre* vs *Phd2*$^{f/f}$ AM and CB. [14]

[14] Data were processed and analysed by Dr Yoichiro Sugimoto.

(**A**) PCA component analysis of *Phd2*KO *vs* wild-type CBs and AMs; RNA extracted from 5 pairs of animals per biological replicate; $n = 3$ biological replicates with $n = 1$ pair of AMs excluded due to poor RNA quality (not shown). (**B**) Identification of **i**. genes enriched in the CB *vs* AM (CB-specific, FDR < 0.1 and fold change ≥ 1.5) and downregulated in the CB *vs* AM (AM-specific, FDR < 0.1 and fold change ≤ -1.5); **ii**. genes up- and down-regulated in the *Phd2*KO *vs* wild-type AM. (**C**) **i**. CB-specific genes (as identified in B) are upregulated and AM-specific genes downregulated, in *Phd2*KO AM; **ii.** Genes induced in *Phd2*KO *vs* wild-type AM map to CB-specific, and genes repressed to AM-specific sets (compare with B.i); individual genes are annotated in the rightmost graph.

Table 6-2. Top 20 genes upregulated in the *Phd2$^{f/f}$;THCre*, relative to wild-type AM.
Top 20 significantly upregulated genes, with genes < 5 TPM expression in the wild-type AM excluded from analysis.

Gene	Description	log2 fold change
C2cd4b	C2 Calcium Dependent Domain Containing 4B	5.24
Penk	Proenkephalin	4.30
Rgs5	Regulator of G-protein Signalling 5	3.51
Cox4i2	Cytochrome C Oxidase Subunit 4i2	3.32
Cd164l2	CD164 Molecule Like 2	2.59
Galnt6	Polypeptide N-Acetylgalactosaminyltransferase 6	2.39
Angptl7	Angiopoietin-like Protein 7	2.17
Serpinf1	Serpin Family F Member 1	2.29
Esm1	Endothelial Cell Specific Molecule 1	2.18
Cpxm1	Carboxypeptidase X, M14 Family Member 1	2.10
Rnf128	Ring Finger Protein 128	1.88
Fgl2	Fibrinogen Like 2	1.87
Cartpt	CART Prepropeptide	1.83
Rgs4	Regulator of G-protein Signalling 4	1.73
Aspn	Asporin	1.97
Igfbp3	Insulin Like Growth Factor Binding Protein 3	1.76
Mdk	Midkine	1.81
Gap43	Growth Associated Protein 43	1.90
Col3a1	Collagen Type III Alpha 1 Chain	1.56
Ldha	Lactate Dehydrogenase A	1.51

6.2.3 *Testing acute oxygen sensitivity in Phd2$^{f/f}$;THCre adrenal medulla*

Neonatal chromaffin cells are acutely oxygen sensitive, like the CB type I cells in the adult (see section 1.2.2.3). Given that developmental *Phd2* inactivation in chromaffin cells altered the AM morphology in a way suggesting arrested/incomplete migration into the cortex, as well as altering the chromaffin cell population composition to a dominating 'immature' noradrenergic state, and that *Phd2*KO AM transcriptome is more CB-like than in wild-type mice, we sought to test whether this may also be true at the functional level. Responses of adult *Phd2*KO AM to acute hypoxia were therefore tested.

Acute oxygen sensitivity can be tested *ex vivo* using multiple different readouts (see section 1.2.2). Here, changes in $[Ca^{2+}]_i$ during hypoxia were measured to monitor the electrical activity, as well as secretory potential of the cells.

Initial experiments tested changes in Ca^{2+} fluorescence using reporter dye, indo-1, loaded into dispersed AM cells, as described previously in CB type I cells (Buckler and Turner, 2013, Buckler and Vaughan-Jones, 1994). However, responses to both hypoxia and GPCR agonist (acetylcholine) were variable with no clear biological effect of *Phd2* inactivation, suggesting dissociation of the AM might disrupt physiological properties of adult chromaffin cells. Subsequent experiments were therefore performed in whole-mount tissues, which additionally provides spatial information about chromaffin cell depolarization and secretion under hypoxia.

Loading Ca^{2+} indicator dyes into whole-tissues is limited by rate of diffusion, therefore, to record changes in the intracellular Ca^{2+} concentration ($[Ca^{2+}]_i$) in whole tissues, transgenic mice expressing the GCaMP6f Ca^{2+} sensor (Chen et al., 2013) were used. The GCaMP6f expression is restricted with a STOP sequence under a CAG promoter

flanked by LoxP sites, therefore requiring Cre-dependent excision to activate expression (Ai95 line, Madisen et al., 2015). *Ai95*$^{f/+}$ mice were therefore intercrossed with *THCre* or *Phd2*$^{f/f}$*;THCre* animals to produce *Ai95*$^{f/+}$*;THCre* control (subsequently referred to as 'wild-type' with respect to *Phd2*) and *Phd2*$^{f/f}$*;Ai95*$^{f/+}$*;THCre* (*Phd2*KO) mice. These animals only express the GCaMP6f sensor in catecholaminergic, TH^+ cells, reducing background fluorescence in whole-mount preparations.

To validate this technique in the Oxford laboratory, carotid artery bifurcations were dissected from control animals and kept in ice-cold phosphate-buffered saline, then further sub-dissected to remove fat and connective tissue, but leaving the CB attached to the internal carotid artery (Figure 6-4A). Tissues were acclimatised in normoxic media at 37˚C and then exposed to a range of hypoxic oxygen tensions using a gravity-based perfusion system, with GFP fluorescence measured under a x40 oil-immersion objective (Figure 6-4, see section 8.15.2). High level of autofluorescence was found in the arteries (Figure 6-4A) and the intensity of the GFP signal coming from the CB type I cells varied between samples, in part depending on how well the tissue was sub-dissected. For easier comparisons between samples, fluorescence (F) was therefore normalised to the level at the beginning of the experiment (F0), and F/F_0 data plotted against time to observe changes in $[Ca^{2+}]_i$ over the course of the experiment (Figure 6-4C-D).

As described previously in single-cell recordings (Buckler and Turner, 2013) and in CB slices (using catecholamine secretion as a readout, Pardal and Lopez-Barneo, 2002), stimulation with a solution at high $[K^+]$ caused a rapid and reversible increase in GCaMP6f fluorescence in the TH^+ CB cells (Figure 6-4C), due to membrane depolarisation resulting in opening of voltage-gated Ca^{2+} channels allowing extracellular Ca^{2+} uptake (see section 1.2.2). Exposure to solutions bubbled with

decreasing levels of oxygen showed graded increase in GCaMP6f fluorescence, with rapid onset and offset, similar to the response to high [K^+] (Figure 6-4C). A secondary increase in fluorescence following exposure to chemical anoxia (solution bubbled with 93% N_2, 2% air, 5% CO_2 and supplemented with an oxygen scavenger, sodium sulphite) was observed, which could be due to the secondary release of Ca^{2+} ions from internal stores or delayed excitation of cells buried deeper within the tissue and thus with delayed O_2 deprivation relative to the surface cells. A 'sham' line switch with both control and test lines inserted into the control (normoxic) solution was performed to ensure that increased fluorescence was not an artefact caused by alternating between the control and test lines supplying the different solutions; no changes in fluorescence were observed under this stimulus (Figure 6-4C).

Over the course of the experiment, there was a gradual decrease in relative fluorescence under basal conditions, probably due to the bleaching of the sensor due to frequent excitation with light, as well as changes in focus as the tissue shifts and thermal changes alter the distance of surface cells from the objective. To accurately compare changes in fluorescence under progressive hypoxia, area under curve (AUC) was therefore calculated using trapeziums method, with baseline level calculated by averaging fluorescence during the 10s immediately prior to application of the stimulus, and during the 10s starting 20s after reversal back to control perfusion, to allow time for recovery of the basal signal (see section 8.15.3). Due to the longer offset period following anoxia and K^+ stimulation, baseline was only calculated using the 10s before the stimulus for these two tests. Area under curve was averaged per time unit and normalised to the maximum response achieved with 45 mM K^+ ion stimulation (Figure 6-4B). As observed in the representative F/F_0 trace, there was a graded, inverse exponential relationship between the oxygen tension and AUC under hypoxia as % of response to

K^+, with response to anoxia on average the same magnitude as that to K^+ (100.1%), and a 50% K^+ response (P_{50}) estimated at 2.3% O_2 (Figure 6-4B). This is similar to the P_{50} reported in dissociated rat type I cells (12.5 mmHg ≈ 1.6% O_2, Buckler and Turner, 2013).

To negatively control for Ca^{2+} fluctuations observed in the CB under acute exposure to hypoxia, SCG, a non-oxygen-sensitive (Buckler and Turner, 2013) sympathetic ganglion was subjected to the same protocol as the CB. Like the CB type I cells, the SCG cells are TH^+ and therefore express the GCaMP6f reporter in *Ai95$^{f/+}$;THCre* mice. The SCG is much larger than the CB and with clean boundary discernible under a dissection microscope, ganglia were therefore removed from the carotid bifurcations and cleaned from fat and connective tissue, then imaged under a x40 oil-immersive objective, same as the CB (Figure 6-4A). SCG cells are large and easily discernible at x40 magnification (Figure 6-4A), fluorescence levels in individual cells (rather than whole area, like in the CB) was therefore plotted over time and the signal averaged across all visible cells in each preparation (Figure 6-4D). All of the SCG cells showed high increase in GCaMP6f fluorescence in response to high K^+ ion concentration, in a rapid and reversible manner, as in the CB (Figure 6-4C). In contrast to the CB, however, no responses to hypoxia were observed in any of the cells, with only a small response to anoxia observed in a subset of cells (Figure 6-4C). On average, no response to anoxia or hypoxia could be detected in the SCG, with both CBs tested responding to a range of 0-10% O_2 in a similar way (Figure 6-4D). This is in line with previously published data showing isolated rat SCG neuron cells responding only to anoxia, but not to 0.5 or 1% O_2 hypoxia (Buckler and Turner, 2013).

Together, these results demonstrate high sensitivity of mouse CB, but not SCG, to graded hypoxia, in line with published work in this and other species (Buckler and Turner, 2013, Duchen and Biscoe, 1992b, Perez-Garcia et al., 2004), and confirm GCaMP6f fluorescence recordings in whole-mount tissue can be used to assay oxygen sensitivity in neuroendocrine tissues.

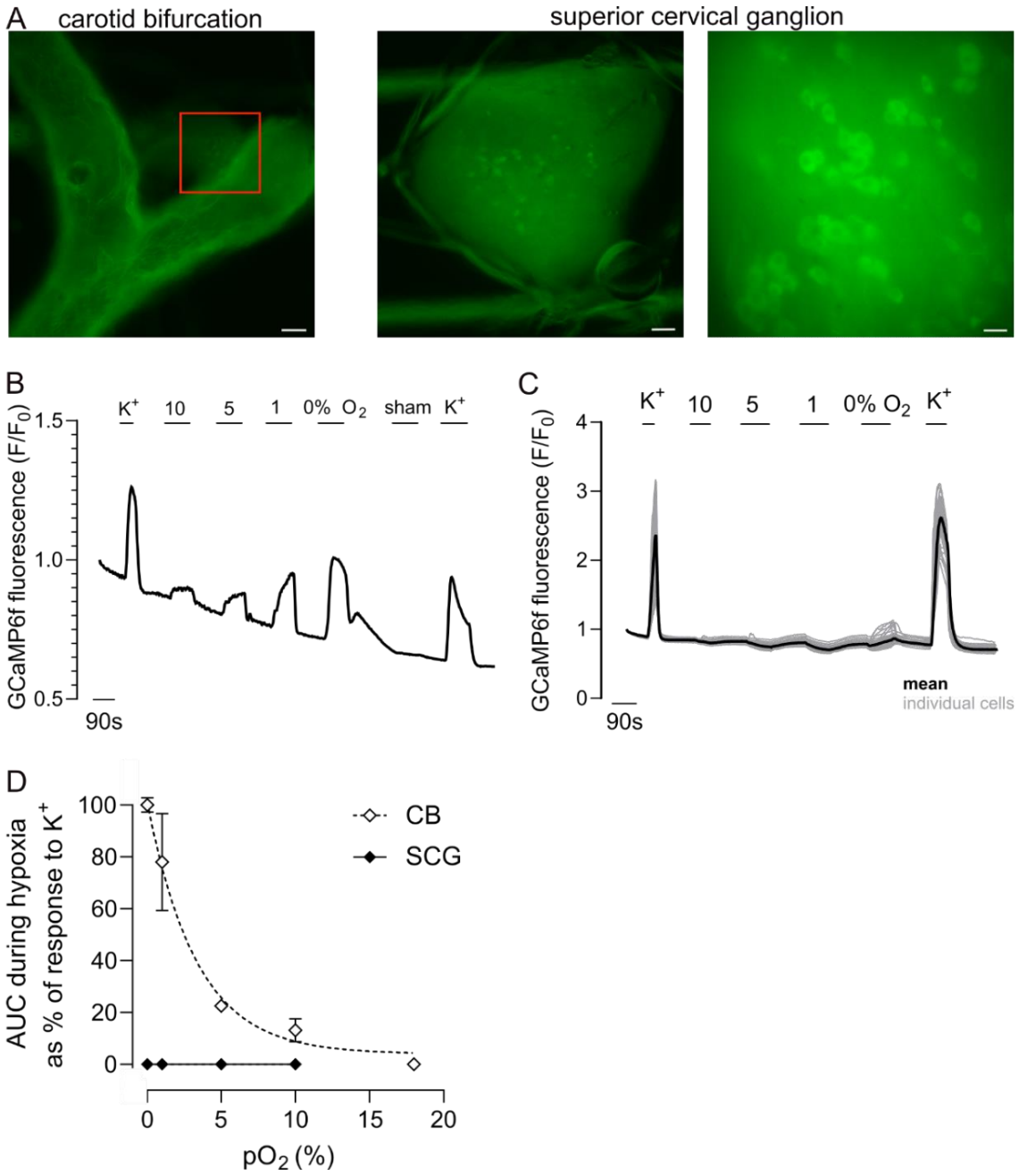


Figure 6-4. Acute hypoxia causes graded Ca^{2+} influx into the CB and SCG.

(**A**) Carotid bifurcation and SCG in an *Ai95*$^{f/+}$*;THCre* mouse, with region containing the CB, from which recordings were subsequently taken using a different objective, shown in the red

frame and low- and high-magnification images of the SCG shown in the right panels. Scale bars show 0.1 mm in the first two panels and 0.025 mm in the rightmost panel. (**B-C**) Representative traces of GCaMP6f fluorescence (F), normalized to the fluorescence at the start of the recording (F_0), recorded from the region containing (**B**) CB type I cells and (**C**) SCG cells, with individual cells shown in grey and average signal in black in the SCG; tissues were perfused with 45 mM K^+ to induce membrane depolarisation, as well as with solutions bubbled with 10, 5 or 1% O_2 and with an anoxic solution (supplemented with an oxygen scavenger) to test acute oxygen sensitivity. Sham is the same as control solution but supplied via the test line. (**D**) Responses to hypoxia are quantified as the average area under curve during 2s hypoxia, presented as % of the response to high K^+. Data plotted are mean ± range, $n = 2$. One phase decay curve was fitted to the data with P_{50} = 2.3% O_2 in the CB.

The AM is much larger than the CB or SCG and is encapsulated with a thick, dense cortex. To test AM acute oxygen sensitivity, 150 μm adrenal gland slices were therefore prepared from *Phd2*KO and control animals expressing the GCaMP6f reporter in TH^+ cells, to allow uniform exposure to stimuli, while preserving the anatomy of the gland (De Nardi et al., 2017, Garcia-Fernandez et al., 2007). Following the same protocol as for the CBs/SCGs, slices were perfused with 10, 5, 1 and 0% O_2, as well as 45 mM K^+ solutions, and GFP fluorescence was imaged under a 10x objective to capture the entire AM area (Figure 6-5).

For quantitative analysis, regions of interest were selected primarily based on bright-field images to distinguish the AM and adrenal cortex, and further refined by consulting images from AM slices exposed to 45 mM K^+ to accurately select chromaffin cells and exclude the zona reticularis (Figure 6-5A, red outlines indicate regions of interest used to quantify fluorescence), since cells within the zona reticularis (between the cortex and medulla) are much less densely packed than in the cortex, but unlike the chromaffin cells do not express TH. In contrast to the CBs, basal fluorescence in the AM was relatively stable throughout the recording, with only small changes caused by tissue

shifting within the perfusion chamber or subtle changes to the level of the solution within the chamber (Figure 6-5B).

Cell viability and the ability of the tissue to increase $[Ca^{2+}]_i$ in a voltage-dependent manner was confirmed by stimulation with 45 mM K^+, which resulted in a rapid and reversible increase in GCaMP6f fluorescence (Figure 6-5A-B). Notably, increased fluorescence during K^+ stimulation was not uniform across the AM, with some regions in the centre of the medulla showing no change in fluorescence relative to the basal levels (Figure 6-5A, note dark patches with no green fluorescence signal under 45 mM K^+ stimulus). This could be explained by differences in slice thickness/cell density as the slicing process can cause some chromaffin cell detachment resulting in apparently 'empty' patches across the medulla, as well as the AM anatomy in itself, with large medullary veins creating hollow spaces across the gland.

In contrast to the response to high K^+, no changes in GCaMP6f fluorescence were detected under 1-10% O_2 hypoxia in wild-type adrenal slices, with only a small and slow increase in fluorescence under anoxia in some, but not all slices (Figure 6-5). This contrasts to the acute oxygen sensitivity reported in the CB above but is in line with previous studies showing minimal acute oxygen sensitivity in adult AMs (reviewed in Nurse et al., 2009).

In stark contrast to the apparently hypoxia insensitive wild-type AM, *Phd2*KO AMs showed marked increase in GCaMP6f fluorescence upon exposure to 5, 1 and 0% O_2 (Figure 6-5A-B), with a minor increase in fluorescence observed under 10% O_2 in some, but not all preparations (Figure 6-5B-C). The magnitude of the response to anoxia in *Phd2*$^{f/f}$*;THCre* adrenal was less than that to K^+, with average area under the curve

during 2s anoxia reaching 35.5 ± 9.8% of AUC during 2s 45 mM K^+, *vs* 100.1% in the CB (compare Figure 6-5C with Figure 6-4D).

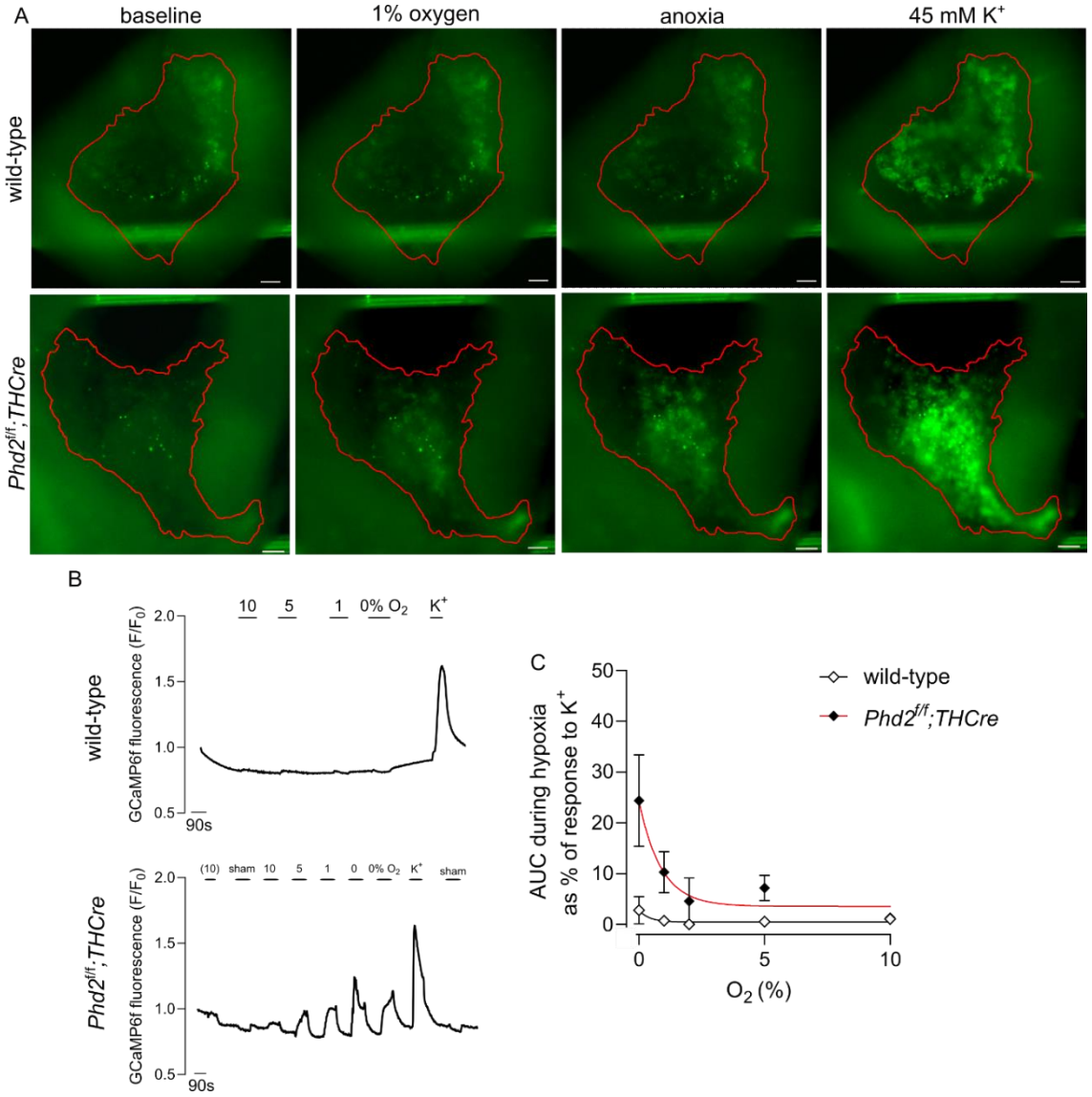


Figure 6-5. Ca^{2+} fluorescence imaging showing acute oxygen sensitivity in the *Phd2$^{f/f}$;THCre* AM.

(**A**) Images showing GFP fluorescence in wild-type (*Ai95$^{f/+}$;THCre*, top row) and *Phd2*KO (bottom row) AM slices perfused with control (baseline), 1% O_2 hypoxic, anoxic or 45 mM K^+ Tyrode's buffer. Red outline shows region of interest from which GCaMP6f fluorescence is quantified. Scale bars are 0.1 mm. (**B**) Representative traces showing GCaMP6f fluorescence (F) in the AM, normalized to the fluorescence at the beginning of the recording (F_0) as the tissue is exposed to periods of progressive hypoxia (10-0% O_2) and high K^+, as well as a sham solution switch. (**C**) Average area under curve per 2s hypoxia, normalised as % of AUC under 45 mM K^+, quantified in wild-type and *Phd2$^{f/f}$;THCre* AM slices. Data show mean ± SEM, $n =$

3 at 10% O_2; $n = 4$ at 2% O_2 in WT and $n = 2$ at 2% O_2 in *Phd2*KO; $n = 8$ at 5, 1, 0% O_2 in WT and $n = 5$ at 5, 1, 0% O_2 in *Phd2*KO samples. Data were fitted with a one-phase decay exponential curve with wild-type P_{50} = 0.3% and *Phd2*$^{f/f}$*;THCre* P_{50} = 0.6% O_2.

6.2.4 *Spatial heterogeneity in adrenal medulla acute oxygen sensitivity*

Testing acute oxygen sensitivity in adrenal slices, rather than isolated cells, provides an opportunity to investigate potential heterogeneity and spatial localisation in the acute oxygen sensitivity of different chromaffin cell populations, as both adrenergic and noradrenergic cells are exposed to the same conditions concurrently and changes in intracellular Ca^{2+} levels can be compared across the slice. To test whether a small population of hypoxia-responsive cells might exist in the wild-type AM, AM area previously selected for analysis (Figure 6-5) was sub-divided into small square regions of interest (ROIs) by applying a grid of 961 ROIs to a 600×600 pixel image cropped just outside the AM area (Figure 6-6, top row GFP images). GCaMP6f fluorescence (normalised to starting fluorescence, F_0, as before) was then quantified within each ROI over the course of the experiment and responses to hypoxia and hyperkalaemia calculated as before (Figure 6-5). K^+-responsive ROIs were selected based on the absolute change in F/F_0 during 45mM K^+ exposure greater than 0.3 and Hpx-responsive ROIs were selected by additionally testing if AUC during 90s anoxia exposure is greater than 3 and AUC during 90s of 1% O_2 is greater than 2 (see section 8.15.3). These criteria were tested on a set of preliminary recordings with clear differences in fluorescence changes under hypoxia (*Phd2*KO samples) and evaluated by comparing time-course graphs of F/F_0 in 'Hpx-responsive' and 'Hpx non-responsive' ROIs in each sample to make sure no Hpx-induced peaks in GCaMP6f fluorescence were missed (Figure 6-6, blue and green plots in bottom panels).

Majority of AM areas previously selected for bulk analysis responded to high [K^+], with small subsets of ROIs excluded at this stage possibly due to lower cell density or

GCaMP6f expression (Figure 6-6, grey/blue overlaid images in the second row from the top – uncoloured ROIs are excluded from analysis). Within the Hpx non-responsive ROIs group, a few ROIs responsive to anoxia and 1% O_2 were identified in some, but not all, wild-type AMs (Figure 6-6, compare number of green ROIs in the first two columns). These Hpx-responsive ROIs in wild-type AMs did not show changes in GCaMP6f fluorescence under milder hypoxia, as evident by no changes in F/F_0 in the individual traces from Hpx-responsive ROIs under 2 or 5% O_2 (Figure 6-6, second column from the left, bottom graph).

In contrast to wild-type AM, where only $2 \pm 1\%$ of the AM was Hpx-responsive, the majority ($64 \pm 12\%$) of the *Phd2*$^{f/f}$*;THCre* AM ROIs were Hpx-responsive (Figure 6-6, two columns on the right; Figure 6-7A; $P = 0.0001$, $n = 7$ wild-type and $n = 5$ *Phd2*KO AMs). Hpx non-responsive regions generally clustered around the edges of the AM (Figure 6-6, two rightmost columns, blue regions in the AM images second row from the top). However, some Hpx-responsive ROIs were also noted at the edge of one sample with 'ectopic' K^+-responding cells (Figure 6-6, second column from the right, note the green ROIs in the bottom-right corner of the image), corresponding to the morphological abnormalities resembling of incomplete chromaffin cell migration through the cortex (which are *Pnmt*$^-$*/Epas1*$^+$*/Rgs5*$^+$, Eckardt et al., 2021), described earlier (Figure 6-1C).

To confirm 'Hpx-responsive' regions have been assigned correctly, GCaMP6f fluorescence from each ROI was plotted against time and compared between the Hpx-responsive and non-responsive sets (Figure 6-6, blue and green time-plots at the bottom). Within the *Phd2*KO Hpx-responsive ROIs, there was a graded increase in GCaMP6f fluorescence under progressive hypoxia, with all ROIs responding to each hypoxic stimulus. In contrast, very small changes in fluorescence under hypoxic stimuli

(1-10% O_2) were observed in Hpx non-responsive ROIs, possibly caused by small shifts in tissue rather than a biological effect. Notably, however, Hpx non-responsive regions in *Phd2*KO AMs still showed a robust increase in GCaMP6f fluorescence under anoxia, in contrast to the Hpx non-responsive regions in the wild-type AM (Figure 6-6A).

It should be noted that the average magnitude of the response to high [K^+] was lower in the Hpx non-responsive than in Hpx responsive regions in the *Phd2$^{f/f}$;THCre* AM, which could suggest lower reporter levels in these regions mean the response to hypoxia is below the threshold for detection under the imaging conditions used. However, there was a large range of magnitudes of K^+ response in the Hpx-responsive ROIs (see Figure 6-6, light-grey traces in bottom panels representing individual ROIs), suggesting some regions with low response to [K^+] increase are still able to respond to hypoxia and so 'Hpx non-responsive' regions are likely correctly assigned as such. Further, the response to anoxia appears to be less diminished than that to 45 mM K^+ in the Hpx non-responsive ROIs compared with the Hpx-responsive regions, again suggesting the reduced sensitivity to hypoxia is not due to overall reduction in the GCaMP6f fluorescence intensity.

Comparison of the AUC during hypoxic stimulus as % of the response to high [K^+] across a range of oxygen tensions in Hpx-responsive and Hpx non-responsive ROIs in wild-type *vs Phd2*KO adrenals showed exponential decay curves can be fitted to data in both K^+ and Hpx-responsive ROIs in the *Phd2*KO and in the Hpx-responsive, but not in the Hpx non-responsive ROIs in the wild-type AM (Figure 6-7B). There was a marked increase in the maximum (anoxic) response in *Phd2*KO AMs, from 7.7% in wild-type to 32.8% of response to K^+ in the *Phd2*KO AM (Figure 6-7B, Student's *t*-test $P < 0.0001$). Comparison of the $\%O_2$ resulting in stimulation to 50% of the response to anoxia (P_{50}) across the groups showed a rightward shift from 0.8% O_2 in the wild-type

to 1.3% O_2 in the *Phd2*KO Hpx-responsive ROIs (Figure 6-7B)(although the one-phase decay curve does not provide a good enough fit to this data to run a statistical comparison between the P_{50} values).

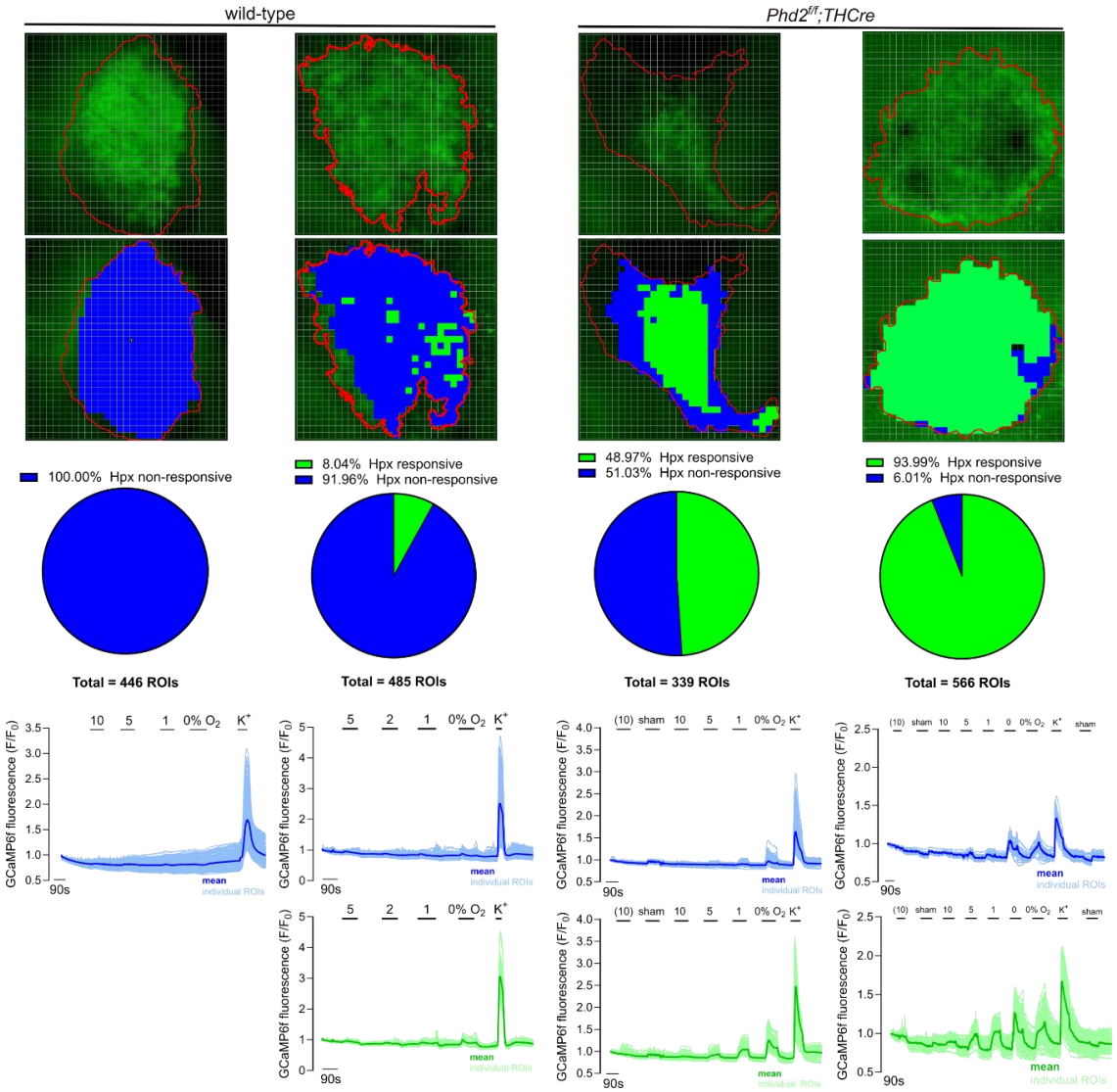


Figure 6-6. Spatial distribution of chromaffin cells responsive to hypoxia and hyperkalaemia in wild-type and *Phd2*KO AM.

Examples of spatial analysis in wild-type (two left columns) and *Phd2*$^{f/f}$*;THCre* (two right columns) AMs. AM area previously selected for bulk analysis was sub-divided into square regions of interest as shown in the top row and individual squares are assigned as hypoxia (Hpx) responsive (AUC under anoxia > 3 and AUC under 1% O_2 > 2) or Hpx-non-responsive ($\Delta F/F_0$ at 45 mM K^+ > 0.3 but Hpx-responsive condition not met) and coloured green for Hpx-responsive and blue for Hpx non-responsive (second row panels). Pie chart shows proportion of all the K^+-responsive regions in the AM that are Hpx-responsive. Individual traces from Hpx-non-responsive (blue) and Hpx-responsive (green) regions are plotted in the bottom two rows.

Together, wild-type AM in adult mice is almost completely oxygen insensitive, whilst *Phd2* inactivation induces graded sensitivity to progressive hypoxia with respect to changes in $[Ca^{2+}]_i$. Spatial analysis of changes in GCaMP6f fluorescence under hypoxia across the AM further revealed a few mildly hypoxia-responsive regions in a portion of the wild-type AMs and showed potential heterogeneity of hypoxia-sensitivity in the *Phd2$^{f/f}$;THCre* adrenal, with majority of the AM (including ectopic chromaffin cells) responding to 0-10% O_2 and a small proportion of the medulla responding to anoxic, but not hypoxic exposure.

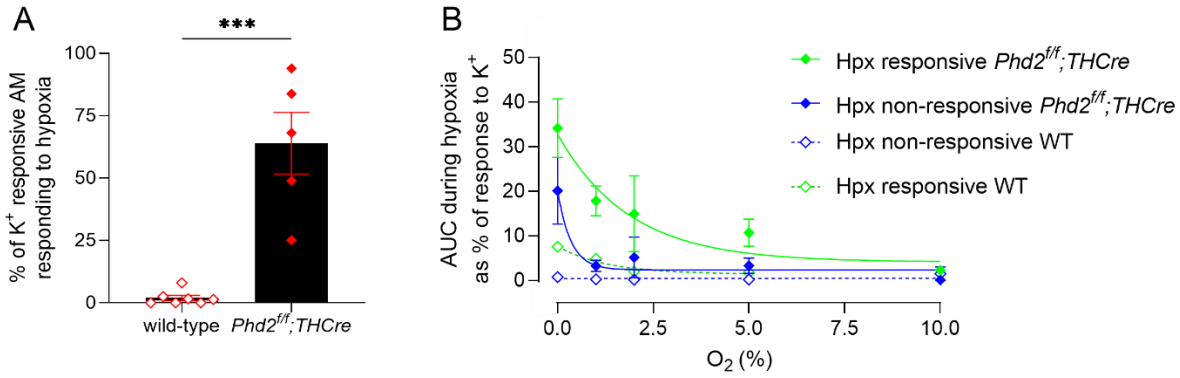


Figure 6-7. Heterogeneity of acute responses to hypoxia in *Phd2$^{f/f}$;THCre* *vs* wild-type AM. (**A**) % AM area responsive to 45 mM K^+ which also responded to 1% O_2 and anoxia ('hypoxia'). Data are plotted as mean ± SEM with individual values shown. (**B**) Area under curve during hypoxic perfusion, as a % of response to 45 mM K^+, in Hpx-responsive and Hpx-non-responsive AM regions of WT and *Phd2$^{f/f}$;THCre* AMs. Data are plotted as mean ± SEM and fitted with exponential one phase decay curves; $n = 3$ for 10% O_2; $n = 5$ for 5% O_2, 1% O_2 and 0% O_2 in *Phd2$^{f/f}$;THCre* mice; $n = 7$ for 5% O_2, 1% O_2 and 0% O_2 in wild-type mice; $n = 2$ for 2% O_2 in *Phd2$^{f/f}$;THCre* mice, $n = 4$ for 2% O_2 in wild-type mice.

6.2.5 *Abdominal Organ of Zuckerkandl paragangliomas in mice with developmental Phd2 inactivation*

One of the morphological abnormalities noted in *Phd2$^{f/f}$;THCre* adrenal glands were clusters of ectopic TH^+ cells, either with chromaffin cell morphology or in the form of small extra-adrenal ganglia (Figure 6-1). To further investigate chromaffin cell distribution in *Phd2*KO animals, posterior contents of the abdominal cavity: aortas,

inferior vena cavas, renal arteries, ureters and kidneys from 2-3-month-old *Phd2$^{f/f}$;THCre* and *Phd2$^{f/f}$* mice were fixed and sectioned transversely. 4 in every 16 4μm sections were immunostained with Chromogranin A and TH antibodies to identify chromaffin cells (CGA^{+}, TH^{+}) and distinguish them from sympathoadrenal ganglia (CGA^{-}, TH^{+}) in the abdominal cavity (Figure 6-8). A large CGA and TH^{+} structure was discovered at the midline, along the aorta of *Phd2$^{f/f}$;THCre* mice, with cells clustered into glomeruli, similar to the CB. Within this structure, there was evidence of cell 'clearing' (Figure 6-8, red frame insert), characteristic of human Organ of Zuckerkandl (OZ) paragangliomas (Subramanian and Maker, 2006, Dossett et al., 2007) and previously reported in the *Phd2$^{f/f}$;THCre* CB PGLs (Fielding et al., 2018). OZ paragangliomas were identified in all 19/19 *Phd2$^{f/f}$;THCre* mice studied. These were absent from 4/4 *Phd2$^{f/f}$* animals checked, with only TH^{+}/CGA^{-} sympathetic ganglia, characterized by large cells interspaced with neurons, observed in the abdominal cavities (Figure 6-8).

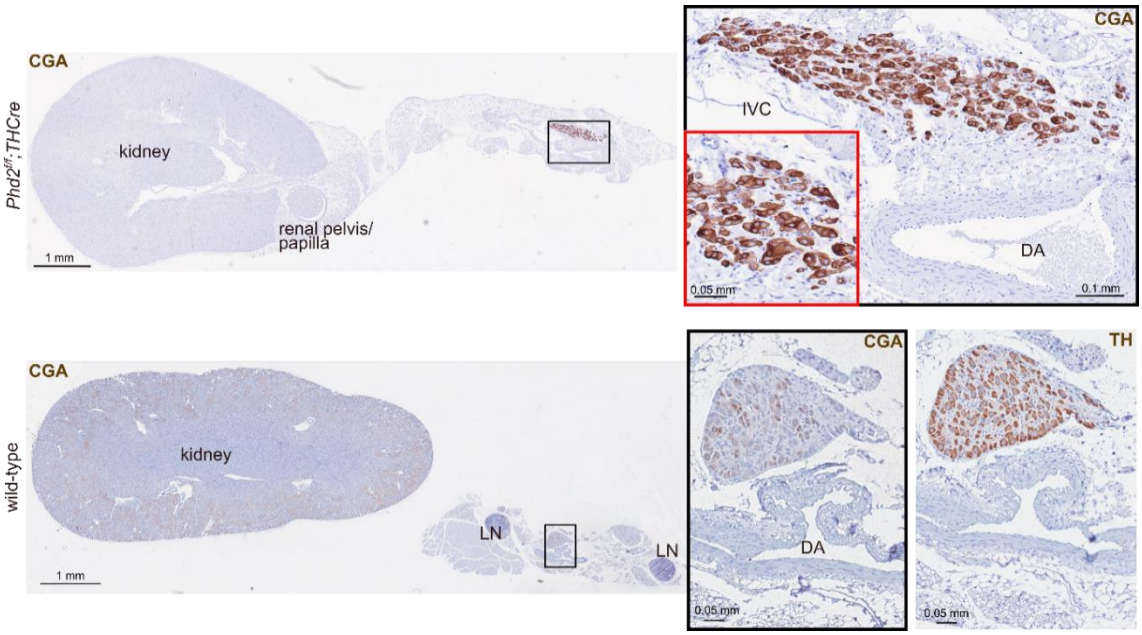


Figure 6-8. Abdominal paraganglioma in *Phd2$^{f/f}$;THCre* mice.

Chromogranin A (CGA) and tyrosine hydroxylase (TH) immunohistochemistry in transverse sections of aorta and kidneys in *Phd2$^{f/f}$;THCre* compared to *Phd2$^{f/f}$* adults. Low magnification

images show a transverse section of abdominal cavity, with the aorta-adjacent paraganglioma (PGL) shown at higher magnification (see red insert for detailed cellular morphology showing 'clear' CGA^+ cells within the PGL). Comparable region in the wild-type mouse only shows presence of a sympathetic ganglion (TH^+/CGA^-). DA – dorsal aorta, IVC – inferior vena cava, LN – lymph node.

To check if abdominal paragangliomas identified in the *Phd2*KO mice are Organs of Zuckerkandl – embryonic catecholaminergic organs which normally reach their maximum size at ~3 years of age in humans and then undergo involution in adolescence (Subramanian and Maker, 2006), aortas were dissected from wild-type and *Phd2$^{f/f}$;THCre* neonates (Figure 6-9). At post-natal day 0.5 (P0.5), wild-type Organs of Zuckerkandl were characterized by high density of CGA^+ cells organized into distinct clusters (glomeruli), similar to the adult CB structure (Figure 6-9A, compare with TH IHC in Chapters 4-5). OZ was also present in *Phd2$^{f/f}$;THCre* neonates, with no differences in morphology compared to the wild-type tissue. There was no evidence of cell clearing in either genotype at this age, in contrast to the adult *Phd2$^{f/f}$;THCre* abdominal PGLs (compare Figure 6-9 with Figure 6-8).

Interestingly, in addition to the OZ, CGA^+ cells were also observed in a portion of renal tubules in majority of the *Phd2$^{f/f}$;THCre,* but none of the wild-type, neonates (Figure 6-9). Catecholamine synthesis along the nephron has previously been described in rats and human cells (Hayashi et al., 1990, Di Marco et al., 2007) and neural crest cells have been proposed to contribute to kidney organogenesis (Itaranta et al., 2009). It is possible that *Phd2* inactivation in the TH^+ cells may lead to functional abnormalities in the kidney (in addition to sympathoadrenal tissues). For example, we have previously noted that a portion of *Phd2$^{f/f}$;THCre* mice are polycythaemic (unpublished observations, MBP, EJH and TB), which may be due to abnormal renal EPO production.

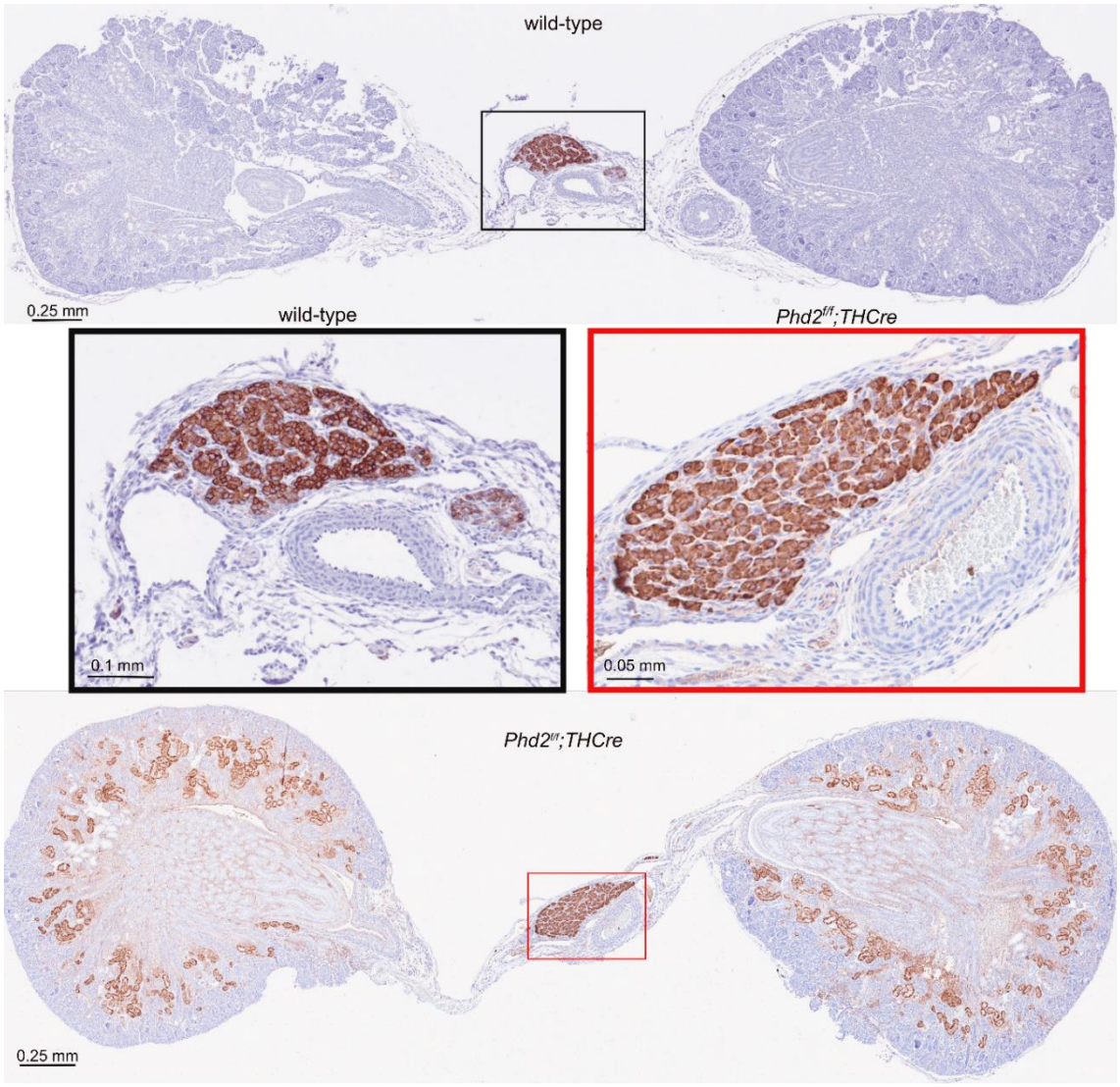


Figure 6-9. Organ of Zuckerkandl in neonatal wild-type *vs* *Phd2*$^{f/f}$*;THCre* mice.
Chromogranin A immunohistochemistry in wild-type (top) and *Phd2*$^{f/f}$*;THCre* (bottom) transverse sections from abdominal cavity collected at post-natal day 0.5. Middle panel shows high magnification inserts from the top and bottom images.

To test whether the OZ PGL is a remnant neonatal OZ, or a proliferating tumour, OZ volume was modelled based on the CGA^{+} area of the structure in neonates and *Phd2*KO adults (Figure 6-10). Quantification of neonatal OZ volume showed these to be an order of magnitude larger than wild-type CB (~0.002 mm^3, see Chapters 2-5 and Cheng et al., 2020, Fielding et al., 2018). *Phd2*$^{f/f}$*;THCre* neonatal OZs were similar in size to the wild-type ones, with no significant difference detected (Figure 6-10, Sidak's multiple comparison's test $P > 0.999$). Marked increase in size was however observed in adult

OZ PGLs compared to the neonatal *Phd2*KO OZs (Figure 6-10, 2.8-fold increase, Sidak's multiple comparison's test $P = 0.002$), and significant interaction between the age and the *Phd2* status of mice was detected with a two-way ANOVA (Figure 6-10, $P = 0.0002$). This shows that not only does the *Phd2*$^{f/f}$*;THCre* OZ escape post-natal involution, but it also proliferates to form a PGL in adulthood.

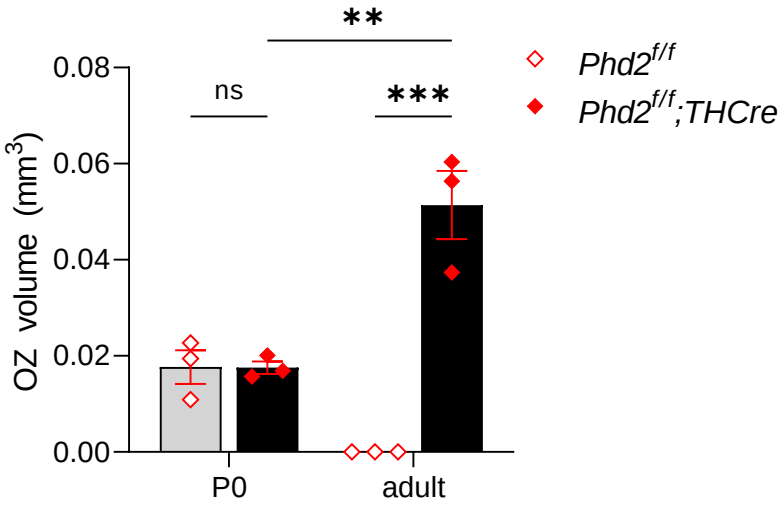


Figure 6-10. Neonatal Organ of Zuckerkandl and abdominal PGL volume in wild-type and *Phd2*KO mice.

OZ abdominal PGL volume modelled based on the area of CGA^+ structures in sequential sections in abdominal cavities in neonatal and adult *Phd2*$^{f/f}$ and *Phd2*$^{f/f}$*;THCre.* Bars show mean ± SEM with individual values displayed. Data were analysed by a two-way ANOVA, age $P = 0.0677$, *Phd2*KO $P = 0.0004$, interaction $P = 0.0008$; followed by a Sidak's multiple comparisons test with significance shown in the graph; $^{**}P < 0.01$, $^{****}P < 0.001$.

Next, expression of a selected panel of genes that are highly expressed in the CB (as well as upregulated in the *Phd2*$^{f/f}$*;THCre* AM) was tested in paraffin sections of the OZ PGL by ISH (Figure 6-11). *Hif-2α,* atypical mitochondrial subunits *Cox4i2*, *Ndufa4l2*, *Higd1c*, as well as components of the G-protein signalling pathway *Adora2* and *Rgs5*, were all highly expressed in the OZ compared to adjacent vasculature (with the exception of *Rgs5*, which is also highly expressed in the aorta) and at levels similar to

the expression in the normoxic CB. Expression in both the OZ and CB was generally higher than in the *Phd2*$^{f/f}$*;THCre* AM (Figure 6-11).

To determine the catecholaminergic status of the PGL chromaffin cells, expression of *Dbh*¸ encoding the dopamine beta-hydroxylase, catalysing conversion of dopamine into noradrenaline, and *Pnmt*, encoding the enzyme converting noradrenaline to adrenaline, was tested by ISH in the OZ PGL sections and compared with the *Phd2*$^{f/f}$*;THCre* AM (Figure 6-12). The OZ PGL expressed high levels of *Dbh* mRNA, suggesting this tissue produces noradrenaline similar to the medullary chromaffin cells (Figure 6-12). By contrast, no *Pnmt* expression was observed in the *Phd2*KO OZ PGL, indicating only noradrenaline, and not adrenaline, is produced by this tissue. This is similar to the *Phd2*KO AM, where cells are predominantly noradrenergic, though a small portion of *Pnmt*$^{+}$ (adrenergic) cells was found in *Phd2*KO AM, whereas no *Pnmt*$^{+}$ cells were detected in the OZ PGL.

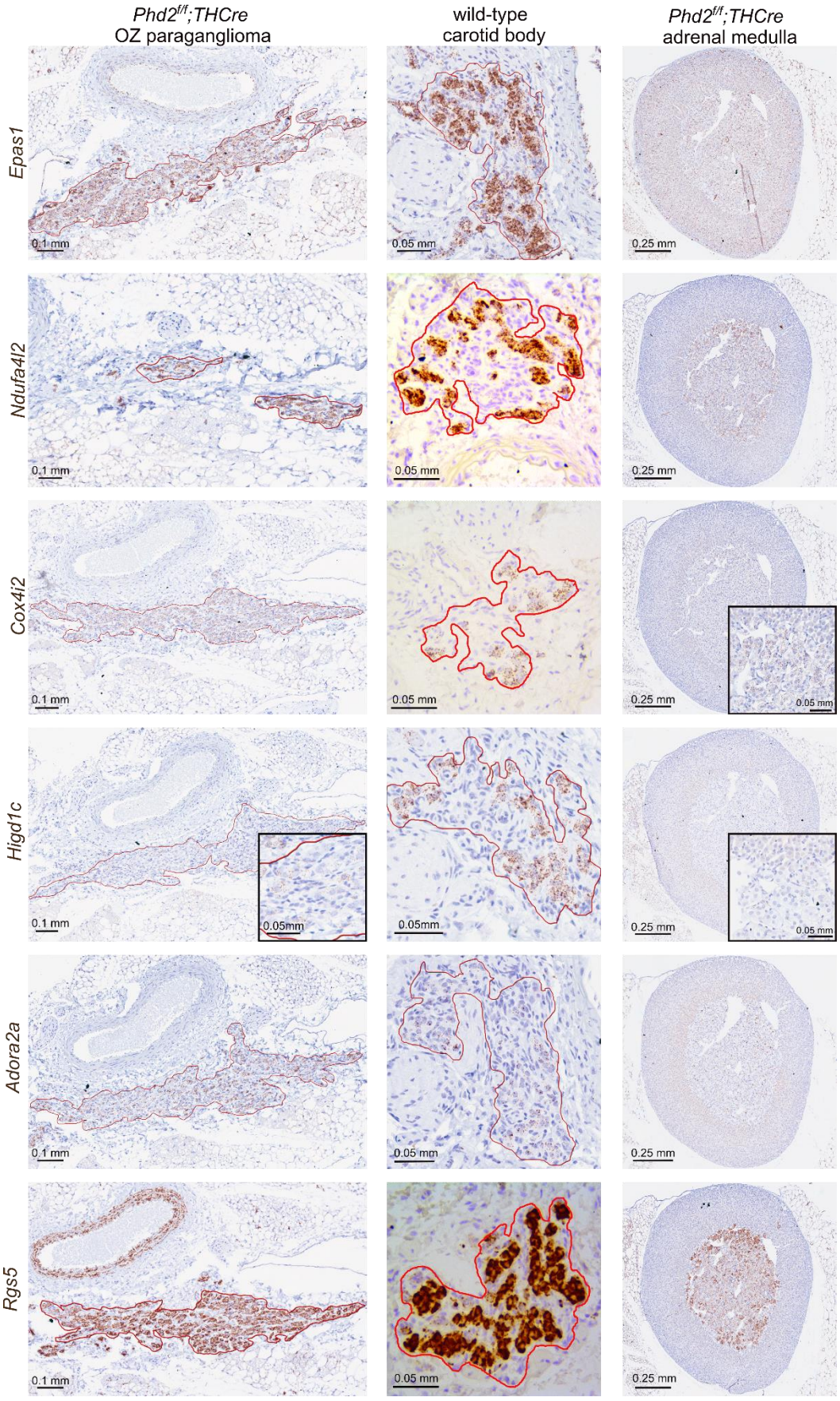


Figure 6-11. Gene expression in the OZ paraganglioma, compared with wild-type CB and *Phd2*KO AM.

ISH against mRNA of selected genes highly differentially expressed in the CB and *Phd2*KO AM (brown signal/ blue Harris haematoxylin counterstain).

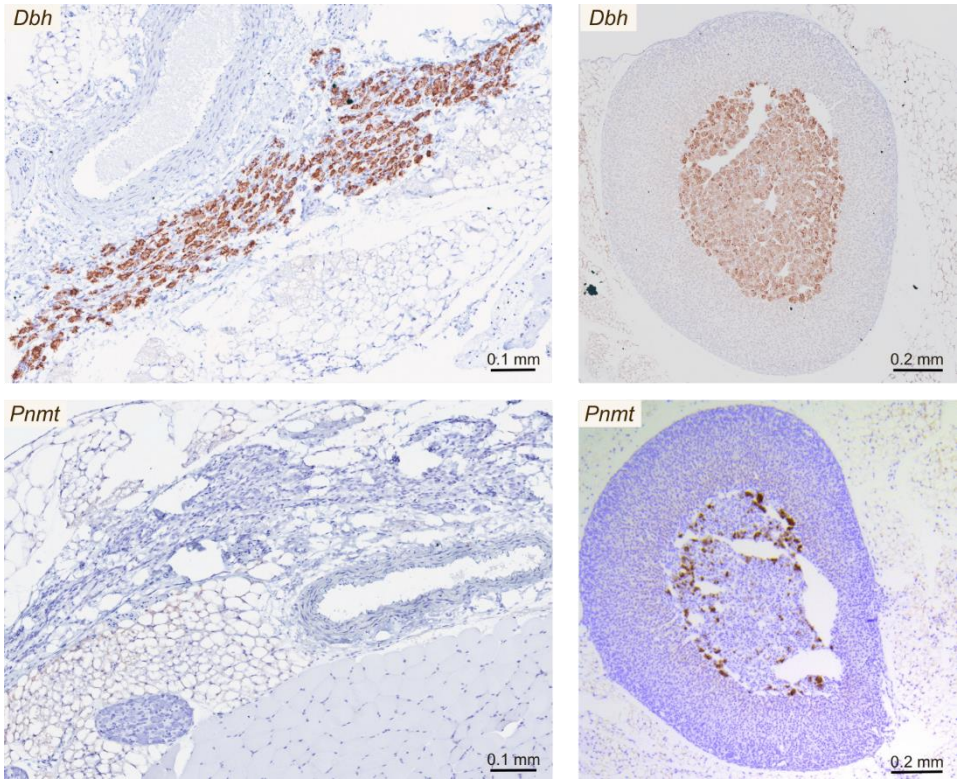


Figure 6-12. Expression of catecholamine-synthesising enzymes in the *Phd2*KO OZ paraganglioma.

ISH against *Dbh* (top) and *Pnmt* (bottom) mRNA (brown signal on blue/grey Harris haematoxylin counterstain) in the OZ abdominal praganglioma (left) and adrenal gland (right) of adult *Phd2$^{f/f}$;THCre* mice.

Phd2 inactivation in the AM results in gene expression changes suggestive of arrested development and a CB-like phenotype, and this results in preserved acute oxygen sensitivity in the AM. Given that similar changes were observed in the OZ, with the tissue escaping postnatal involution and showing high mRNA expression of CB specific genes, we hypothesized that the *Phd2$^{f/f}$;THCre* OZ PGL may also be acutely oxygen-sensitive. Ca^{2+} fluctuations in response to graded hypoxia were tested in the whole-mount OZ PGLs from *Phd2$^{f/f}$;Ai95$^{f/+}$;THCre* mice, as described above (section 6.2.3).

Within the region dissected from along the aorta, large populations of electrically active cells responding to increased [K^+] were found (Figure 6-13A). Quantitative analysis of GCaMP6f fluorescence in the K^+-responsive regions (selected by applying a fluorescence threshold cut-off defined in images taken during 45 mM K^+ exposure, Figure 6-13A, red outlines) showed a rapid and graded increase in $[Ca^{2+}]_i$, proportional to progressive hypoxia (Figure 6-13B-C), similar to the responses observed in the *Phd2*KO AM, but with higher sensitivity to hypoxia, as defined by P_{50} = 2.4% O_2 (Figure 6-13C) *vs* 0.6% O_2 in the AM (Figure 6-5C). Nevertheless, the magnitude of fluorescence changes in response to hypoxia was still different than in the CB, with the AUC during anoxia only reaching ~40% of the response to high [K^+], in contrast to the response to anoxia being the same as that to high [K^+] in the CB (Figure 6-4).

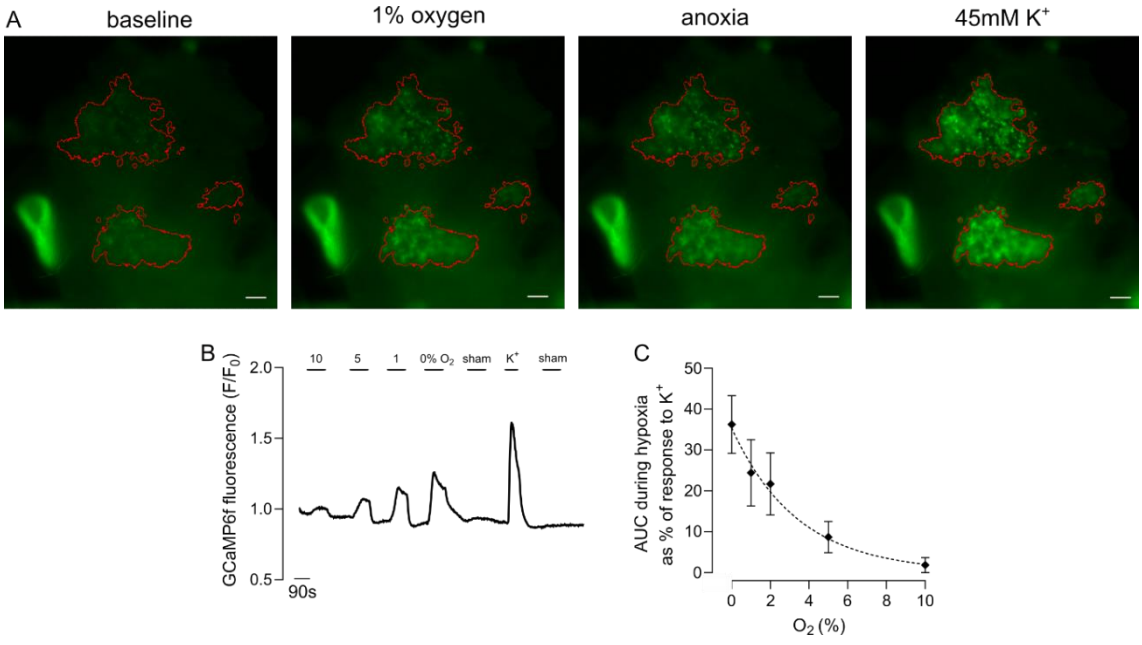


Figure 6-13. Acute oxygen sensitivity in the OZ paraganglioma.
(**A**) Images showing GFP fluorescence in whole-mount OZ PGL perfused with control (baseline), 1% O_2 hypoxic, anoxic or 45 mM K^+ Tyrode's buffer. Red outline shows region of interest from which GCaMP6f fluorescence is quantified (based on fluorescence threshold under K^+ exposure). Scale bars are 0.2 mm. Large bright-green structure visible in the bottom left corner is an adjacent vessel. (**B**) GCaMP6f fluorescence (F) in the K^+-responsive regions, normalized to the fluorescence at the beginning of recording (F_0), as the tissue is exposed to

periods of progressive hypoxia (10-0% O_2) and high K^+, as well as to a sham solution switch. (**C**) Average area under curve per 2s hypoxia, normalised as % of AUC under 45 mM K^+, quantified in the *Phd2$^{f/f}$;THCre* OZ PGL, plotted as mean ± SEM; $n = 4$ at 5, 1, 0% O_2; $n = 2$ at 10% O_2 and 2% O_2. Data were fitted with a one-phase decay curve with $P_{50} = 2.4\%$ O_2.

In summary, *Phd2$^{f/f}$;THCre* mice develop abdominal paragangliomas with high morphological and anatomical similarity to the OZ, and with transcriptomic profile as well as oxygen sensitivity similar to that of the 'immature' *Phd2$^{f/f}$;THCre* AM, suggesting gross abnormalities in sympathoadrenal development caused by HIF-α stabilisation in these mice.

6.2.6 *Investigating the molecular mechanisms behind increased oxygen sensitivity in Phd2$^{f/f}$;THCre chromaffin cells.*

Oxygen (and acid) sensitivity of CB type I cells has previously been proposed to be due to their high expression of the acid-sensitive TASK channels and Na^+-H^+/HCO_3^- exchangers (Turner and Buckler, 2013, Buckler et al., 2000, Yamamoto et al., 2002, Prabhakar, 2016). To test if the gain of hypoxia sensitivity in the chromaffin cells is associated with changes in the sensitivity to K^+ channel inhibitors or acidosis, responses to increased P_{CO2} and Doxapram, a respiratory stimulant previously described as a potent TASK channel inhibitor (O'Donohoe et al., 2018, Yost, 2006), were tested in the AM slices of wild-type and *Phd2*KO GCaMP6f expressing mice (Figure 6-14). 1% oxygen hypoxia was chosen as a positive control to define the Hpx-responsive *Phd2*KO adrenals and AM slices were exposed to 45 mM K^+ at the end of each experiment to confirm intact electrophysiological activity of the tissue. The test stimuli consisted of 10% CO_2 (5% above the P_{CO2} in the control solution), since 10% CO_2 elicits increased $[Ca^{2+}]_i$ in the CB (Dasso et al., 2000), as well as neonatal AM (Rico et al., 2005, Munoz-Cabello et al., 2005); or 50 μM Doxapram which elicits $[Ca^{2+}]_i$ increase in rat

type I cells (O'Donohoe et al., 2018). Responses to a sham solution perfused with 90% air, 5% CO_2 and 5% N_2 to match the P_{O2} of the 10% CO_2 stimulus were also tested.

Preliminary data on three sets of preparations (with one excluded from quantitative analysis due to issues with perfusion system on the day, confounding interpretation of the results), showed no responses to hypoxia, 10% CO_2 or Doxapram in the wild-type AM (Figure 6-14A, top row), in line with previous studies showing hypoxia and acid sensitivity is lost in mature chromaffin cells (Rico et al., 2005).

In contrast to the wild-type AM, there was a clear increase in GCaMP6f fluorescence in the *Phd2*KO AM in response to hypoxia, hypercapnia and doxapram (Figure 6-14A). Quantification of the average GCaMP6f fluorescence across the AM showed a mild increase in Ca^{2+} fluorescence under hypercapnic acidosis, with the magnitude smaller than in response to 1% O_2 (Figure 6-14C). No change in GCaMP6f fluorescence was observed under the sham test, confirming the response to 10% CO_2 is due to changes in the pH, rather than the mild reduction in oxygen tension (Figure 6-14B). A high increase in Ca^{2+} fluorescence was observed in response to 50 μM Doxapram, although the kinetics of this response differed to those of responses to hypoxia and acidosis, with the slower increase in signal intensity so that a plateau could not be reached before returning to the control solution 90s after the start of Doxapram perfusion, and a very slow (more than six minutes) return to baseline fluorescence following application of the inhibitor (Figure 6-14B). Although Doxapram is thought to act by inhibiting K^+ ion channels, the magnitude of the response achieved with 50 μM Doxapram was only ~40% of the response to high [K^+] in one sample and 10% in the other (Figure 6-14B-C, K^+ response was weaker in the sample with 40% response to Doxapram), suggesting either incomplete TASK channel inhibition, or K^+ escape through other, Doxapram-insensitive channels, limiting the extent of membrane depolarisation.

In line with previous results showing hypoxia-sensitivity in the 'immature' ectopic *Phd2*$^{f/f}$*;THCre* AM regions (Figure 6-6), the cortex-protruding K^+-responsive region in one of the *Phd2*KO samples also responded to Doxapram (Figure 6-14A), suggesting the same AM regions respond to hypoxia and TASK channel inhibition.

Together, these preliminary results suggest that, in parallel with gain of acute oxygen sensitivity, *Phd2* inactivation sensitises chromaffin cells to acidosis and TASK channel inhibitors, such that adult *Phd2*KO AM preserves the chemosensory properties normally only observed in neonatal chromaffin cells and adult CB.

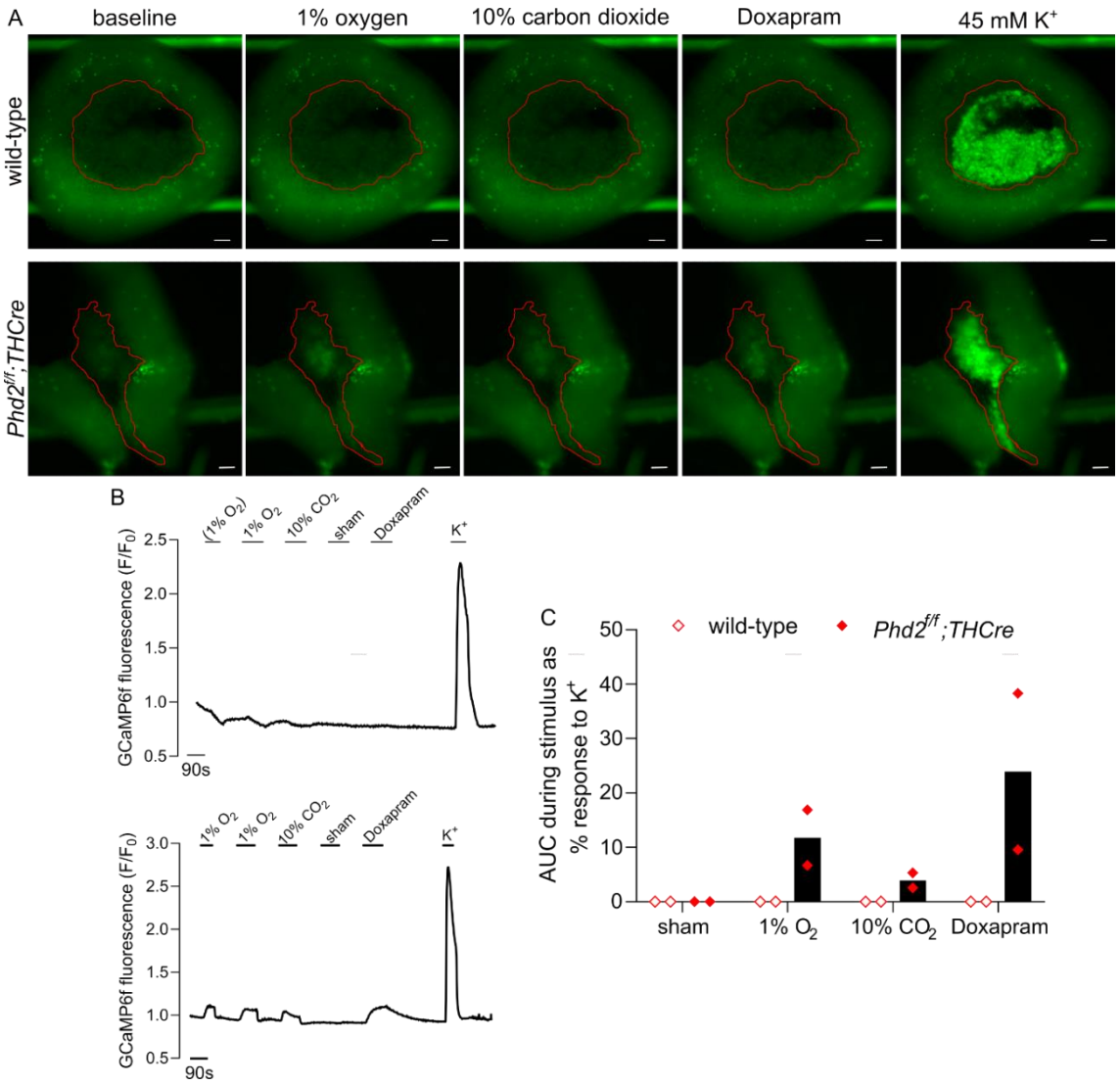


Figure 6-14. *Phd2* inactivation induces Ca^{2+} influx into chromaffin cells in response to hypercapnic acidosis and K^+ ion channel inhibition.

(**A**) Images showing wild-type (*Ai95*$^{f/+}$*;THCre*, top row) and *Phd2*KO (bottom row) AM slice GFP fluorescence images with the slice perfused with control (baseline), 1% O_2 hypoxic, 10% CO_2 acidic, 50 μM Doxapram or 45 mM K^+ Tyrode's buffer. Red outline shows region of interest from which GCaMP6f fluorescence is quantified. Scale bars are 0.1 mm. (**B**) GCaMP6f fluorescence (F) in the region of interest shown in A, normalized to the fluorescence at the beginning of recording (F_0) as the tissue is exposed to subsequent stimuli shown in A, as well as a sham test solution switch. (**C**) Average area under curve per 2s stimulus, normalised as % of AUC under 45 mM K^+, quantified in wild-type and *Phd2*$^{f/f}$*;THCre* AM slices; $n = 2$.

6.3 **Discussion**

Constitutive *Phd2* inactivation in TH^+ cells causes CB paragangliomas, similar to those seen in pseudohypoxic PPGL patients (Fielding et al., 2018). Here, a further PPGL-like phenotype in *Phd2*$^{f/f}$*;THCre* mice is described, showing morphological and transcriptomic abnormalities in the AM, including upregulation of genes typically found in pseudohypoxic PPGLs, as well as a marked loss in *Pnmt* expression associated with altered catecholaminergic profile, again in line with changes in plasma catecholamine levels typical for pseudohypoxic pheochromocytoma patients (Eisenhofer et al., 2011).

The PCC-like characteristics of *Phd2*$^{f/f}$*;THCre* AMs contrast with other animal models modifying components of the HIF pathway: a similar model with *Vhl* inactivation in TH^+ cells previously showed a drastic reduction in the number of TH^+ cells in adult AMs, with no signs of tumorigenesis (Macias et al., 2014). Interestingly, mice with constitutive overactivation of HIF-2α by a genetic proline-to-alanine substitution, restricted to the TH^+ cells, were also studied in the same publication, and showed seemingly normal AMs, although these results were not discussed in text and no further biochemical analysis was conducted to compare with the findings presented here (Macias et al., 2014). *Pnmt* downregulation was however reported in *Epas1*^{A529V} mutant mice, modelling the effects of mutations found in Pacak-Zhuang syndrome patients

(Wang et al., 2019). Together, the effects of HIF-stabilisation in mouse sympathoadrenal system are likely dose-dependent, with full activation (caused by VHL loss) resulting in vestigial AMs, while milder interventions (*Phd2* inactivation and point mutations activating HIF-2α) leading to development of PCC-like features. This is in line with the variety of phenotypes in human VHL mutations, with mutations causing complete protein misfolding rarely resulting in PPGLs (see section 1.5).

Although *Phd2* inactivation prevents post-translational degradation of both the HIF-1 and HIF-2α isoforms, HIF-2α has received more interest as a potential mediator of tumorigenesis in pseudohypoxic PPGLs. This is because preferential HIF-2α protein stabilisation has been described in human pseudohypoxic paragangliomas and pheochromocytomas (Pollard et al., 2006, Celada et al., 2022) and HIF-2α expression in pheochromocytoma is positively correlated with metastatic disease (Favier et al., 2002, Bechmann and Eisenhofer, 2022). Indeed, mutations directly in the *EPAS1*, but not in the *HIF1A*, gene have been described in paragangliomas (Zhuang et al., 2012, Favier et al., 2015). In line with these observations, the role of HIF-2α in the development of PCC-like morphological abnormalities and cell lineage shift observed in *Phd2$^{f/f}$;THCre* mice was confirmed by demonstrating normal AM morphology and adrenergic:noradrenergic cell ratios in *Phd2$^{f/f}$;Hif-2α$^{f/f}$;THCre* mice, with *Phd2$^{f/f}$;Hif-1α$^{f/f}$;THCre* animals displaying the same arrested chromaffin cell migration and lineage shift as *Phd2*KOs (Eckardt et al., 2021). These findings suggest that pharmacological HIF-2α inhibitors may be useful in the treatment of pseudohypoxic PPGLs. Indeed, Belzutifan, which has already been licenced for treatment of VHL-disease-associated ccRCCs, hemangioblastomas and pancreatic neuroendocrine tumours, is currently in clinical trials for PPGLs with patient recruitment independent of genetic status of the tumour (NIH ID: NCT04924075).

However, evidence presented in this thesis and in PPGL patients suggests that HIF-2 might exert its tumorigenic effects during early development (as outlined below), therefore, administration of pharmacological HIF-2α inhibitors in adulthood may not be sufficient to reverse the immature, pro-tumorigenic changes in chromaffin cells in patients with hereditary PPGLs. First, germline or early-somatic mutations are highly prevalent in PPGLs (Dahia, 2014). Second, loss of *Pnmt* expression and arrest in chromaffin cell migration have been demonstrated to be dependent on developmental *Phd2* inactivation by showing normal AM maturation in mice with acute *Phd2* inactivation in adulthood, using ubiquitously expressed and TH^+-cell-restricted, tamoxifen-inducible Cre drivers (Eckardt et al., 2021). Third, *Hif-2α* expression throughout the sympathoadrenal system has previously been noted in mouse embryos (Tian et al., 1998), but low *Hif-2α* mRNA was found in adult wild-type adrenals here. Chromaffin cell lineage shift to retain the immature features due to the persistent HIF-2α stabilisation beyond embryonic development, rather than continuous HIF-2 signalling in adulthood, may therefore predispose to PCC-development eventually causing tumorigenesis in pseudohypoxic PPGL patients.

In further support of arrested sympathoadrenal development in *Phd2$^{f/f}$;THCre* mice, retention (and proliferation) of the OZ has been noted in adult *Phd2*KOs, to form PGLs with similar 'clear cell' morphology to human abdominal paragangliomas. The OZ is a transient, embryonic organ, secreting catecholamines while the AMs develop, and undergoes involution after birth (Schober et al., 2013, Coupland, 1965). Given their common developmental origin, and similarities in morphology and gene expression, as well as the close anatomical association, the OZ could be formed temporarily by migrating chromaffin cells, which later progress to complete AM formation. However, at the time when the OZ reaches its maximum size (just before birth in rodents), the

AMs are already mostly formed, with migrating chromaffin cells extending beyond the adrenal cortex forming clusters separate to the OZ in the abdominal cavity (Kastriti et al., 2019 and the author's histological observations not shown in this Chapter). Further, *Phd2$^{f/f}$;THCre* AM volume was similar to their wild-type littermates, despite marked postnatal overgrowth of OZ PGLs, suggesting AM and OZ chromaffin cells proliferate separately. Finally, although the genes typically upregulated in the CB: *Epas1, Rgs5, Adora2a, Cox4i2, Ndufa4l2* and *Higd1c*, were expressed in both the OZ PGL and the AM in *Phd2*KO mice, expression was stronger in the OZ (and more similar to that in the CB) than in the 'immature', noradrenergic AM cells, suggesting independent functions of these two organs.

In addition to the arrested chromaffin migration and altered transcriptomic profile, *Phd2*KO AM (and OZ PGL) cells were found to acutely respond to hypoxia by elevating intracellular [Ca^{2+}]. This feature is typically restricted to adult CB type I cells and neonatal AM, with the latter allowing responses to stress prior to the development of splanchnic innervation (Buckler and Turner, 2013, Seidler and Slotkin, 1985, Mojet et al., 1997, Rico et al., 2005, Adams et al., 1996). Indeed, previous studies showed that hypoxic catecholamine release is preserved in denervated juvenile adrenals (Seidler and Slotkin, 1986), while stimulation of adrenals with nicotine *in utero* reduces hypoxia-sensitivity of subsequently dispersed chromaffin cells at P0, suggesting an involvement of post-synatpic nicotinic acetylcholine receptors in dampening of hypoxia-sensitivity upon AG innervation (Nurse et al., 2009). The current study did not investigate changes in innervation between wild-type and *Phd2$^{f/f}$;THCre* adrenals, however, upregulation of many genes typically highly differentially expressed in the O_2-sensitive CB, in *Phd2*KO AMs, is more likely responsible for the morphological changes allowing these chromaffin cells to respond to hypoxia. If, like the other changes, acute oxygen

sensitivity in the *Phd2*KO AM is HIF-2α-dependent, this would further support the importance of HIF-2α in chromaffin cell development.

While the role of HIF-2α in cell differentiation likely depends on regulation of gene expression and the altered transcriptomic profile of chromaffin cells with germline pseudohypoxic mutations might predispose to subsequent tumorigenesis, altered catecholamine secretion in human PGLs and hypoxia-sensitivity of *Phd2*KO AMs could still be mediated by a non-transcriptional HIF-2α action (discussed in Chapters 3 and 4). Future studies should therefore test whether acute oxygen sensitivity in the *Phd2*KO AMs and OZ PGLs can be blocked with HIF-2α inhibitors administered in adulthood. This is of clinical relevance, as cardiac complications are common in pheochromocytoma patients (Lenders et al., 2005, Galetta et al., 2010) due to the continued elevation, or episodic release of large amounts of catecholamines (Eisenhofer et al., 2011). Recently, dramatic suppression of plasma normetanephrine (noradrenaline metabolite) levels with HIF-2α inhibitor, Belzutifan, treatment has been reported in a paediatric case of Pacak-Zhuang syndrome (Kamihara et al., 2021). Coupling of continuous HIF-2α signalling in pseudohypoxic PPGLs to elevated chromaffin cell basal activity and sensitivity to hypoxic or hypercapnic stimulation could explain the rapid reduction in plasma catecholamines in this patient.

Beyond the clinical implications, the finding that developmental HIF-2α stabilisation is sufficient to preserve acute oxygen sensitivity in the AM allows in-depth analysis of the molecular mechanism behind hypoxic chemostransduction in oxygen-sensitive cells. Transcriptomic analysis of gene expression in the *Phd2*KO *vs* wild-type AMs revealed induction of many genes typically upregulated in the CB, in line with the common ontogeny of these two tissues and supporting the hypothesis that a common mechanism of acute oxygen sensing is shared between the adult CB type I and the neonatal

chromaffin cells. Further in-depth analysis of the generated transcriptomic data should therefore focus on the groups of genes previously implicated in the type I cell oxygen sensitivity: atypical mitochondrial subunits, G-protein signalling pathway components and ion channels (Zhou et al., 2016, Gao et al., 2017, Moreno-Dominguez et al., 2019, Chang et al., 2015).

Potential changes in the expression of specific types of K^+ ion channels in the 'immature' *Phd2*$^{f/f}$*;THCre* chromaffin cells are suggested by the discovery of *Phd2*KO AM sensitivity to Doxapram (a TASK channel inhibitor), which is absent in the wild-type adrenals. Previous work suggested a role of small conductance K^+ (SK) channels in mediating oxygen sensitivity of neonatal chromaffin cells in the sheep, by demonstrating suppression of K^+ currents with SK channel inhibitors: apamine and tetraethylammonium (Keating et al., 2001). Others suggested a role of T-Type voltage-gated Ca^{2+} channels in the neonatal rat AM oxygen sensitivity, by showing suppression of hypoxia-stimulated catecholamine secretion with T-type Ca^{2+} channel inhibitors: nickel and Pimozide, and re-expression of T-type channels in adult, denervated adrenal glands (Levitsky and Lopez-Barneo, 2009). Detailed analysis of ion channel expression using the bulk RNA Sequencing data is difficult, as these genes are typically lowly expressed and RNA signal from the chromaffin cells is diluted by material from vasculature, immune cells and others in a bulk preparation. Electrophysiological studies in isolated chromaffin cells from *Phd2*KO mice might therefore be more helpful in determining potential differences in K^+ (or Ca^{2+}) currents in these animals.

While the comprehensive analysis of gene expression by RNA sequencing was performed on bulk material from across the AM in this study, it is important to consider the potential relationship between spatial distribution of different transcripts and the heterogeneity in hypoxia-sensitivity across AM slices observed. The negative

correlation between *Pnmt* and *Epas1* (as well as *Rgs5* and *Cox4i2*) expression in the chromaffin cells suggests differential cell maturation across the AM, as the late embryonic adrenals are entirely noradrenergic (thus $PNMT^-$), with a transient state, in which both noradrenaline and adrenaline are produced by the same cell occurring around birth, before the development of dominant adrenergic chromaffin cell population (Verhofstad et al., 1989). Since changes in AM oxygen-sensitivity occur at around the same time as the alteration of catecholaminergic status and spatial analysis revealed expression of the CB-marker genes (*Epas1, Rgs5, Cox4i2*, etc.) specifically in the $Pnmt^-$ cells, there may be a correlation between acute oxygen sensitivity and catecholaminergic status of the cell. Despite clear existence of a noradrenergic, $Pnmt^+$ cell population in the adult wild-type AM, hypoxia-induced changes in Ca^{2+} fluorescence in these adrenals were very scarce and mild compared with the responses to 45 mM K^+, with the distribution pattern of Hpx-responsive *vs* non-responsive cells not resembling that of *Pnmt* expression. By contrast, there was greater heterogeneity in *Phd2*KO AM, with the Hpx-insensitive regions generally clustering around the edges of the medulla, where the $Pnmt^+$ cells are typically found by ISH. Acute oxygen sensitivity in the AM might therefore be restricted to the 'immature', noradrenergic cells, with HIF-2α protein stabilisation required for hypoxia chemotransduction. Future studies could test this by acutely stabilising HIF-2α in otherwise normally developed AMs, for example by chronic exposure to hypoxia or administration of prolyl hydroxylase inhibitors.

This points to one caveat of using GCaMP6f fluorescence in adrenal slices to assay acute oxygen sensitivity. While this technique allowed comprehensive observation of responses in different (adrenergic and noradrenergic) cells across the medulla and provides a more physiological assay than that in dispersed cells, averaging the signal

across large patches of cells may result in missed information about the behaviour of individual cells and the potential paracrine relationships between them. Indeed, continuous, small fluctuations in GCaMP6f fluorescence were observed in majority of the adrenal slices (both wild-type and *Phd2*KO), but these are not apparent in traces from across the medulla, or even in the more detailed spatial analysis, possibly due to different discharge frequency even in neighbouring cells.

Together, there is strong evidence for the specific role of HIF-2α in preservation of the immature phenotype of chromaffin cells in pseudohypoxia. This informs on the potential mechanisms of acute oxygen sensitivity in this and other tissues, as well as providing a better understanding of the mechanism underlying development of pseudohypoxic PCCs. Future studies should focus on detailed molecular analysis of oxygen sensitivity in *Phd2*KO AM, to understand how HIF-2α stabilisation supports hypoxic chemotransduction and what are the physiological implications of such signalling in PPGL patients.

7
Concluding remarks

Experiments carried out in this thesis investigated the role and mechanism of HIF-2α action in the CB-mediated adaptations to hypoxia. Using pharmacological and genetic interventions, HIF-2α was demonstrated to be necessary for CB function in adaptations to hypoxia, and sufficient to induce acute oxygen sensitivity in the related AM. Importantly, demonstration of complete VAH and hypoxia-induced CB proliferation inhibition with a specific HIF-2α inhibitor resolved the previous controversy on the role of HIF-1 *vs* HIF-2α in carotid body function.

Many different mechanisms behind CB-mediated HVR and VAH have been described, with changes in electrophysiological properties of the cells, G-protein signalling, cell proliferation and hypoxia-induced changes in gene expression all proposed to play a role in modulation of hypoxic chemotransduction in this tissue. In this thesis, potential mechanisms of HIF-2α action in the CB have been explored.

HIF-2 is classically considered to act as a transcription factor, however, although hypoxic induction of HIF-target genes is well established and hundreds of target genes have been described, HIF-2 specific target genes known to be induced by hypoxia *in vivo* are scarce. Previous studies suggested a role of *Vegfa* in mediating the effects of HIF-2α in CB responses to hypoxia through neovascularisation, which might increase

the sensitivity of the type I cells to changes in arterial P_{O2} (Fielding et al., 2018). Demonstration of mild VAH and CB proliferation loss in acclimatised *Arnt1/2*dKO mice supports the canonical HIF-2 transcriptional function in the CB (Chapter 4), however, since inactivation of *Arnt* does not phenocopy the effects of genetic *Hif-2α* loss (or pharmacological HIF-2α inactivation), some HIF-2 functions may be HIF-β-independent. Indeed, a non-transcriptional HIF-2α function has been suggested based on the rapid (within 1h of first oral dose) PT2385 effect on HVR (Chapter 2) and the hypomorphic VAH phenotype in S305M mutant mice, with obstructed ligand-binding cavity in HIF-2α PAS-B domain, but with intact HIF-β-heterodimerisation and HIF-target induction (Chapter 3).

One aspect of type I cell signalling that could be modulated by both the HIF-β-dependent and non-transcriptional HIF-2α is G-protein signalling. Genes encoding components of the G-protein signalling pathway are highly expressed in the CB and upregulated in the CB relative to the non-oxygen-sensitive SCG (Gao et al., 2017, Zhou et al., 2016). Among these is *Rgs5,* genetic inactivation of which significantly diminished VAH, although no effects on acute HVR were found (Chapter 5). This supports previous studies, which have proposed a role of G-protein signalling in CB responses to hypoxia (reviewed in Chapter 1). Given that G-proteins act via a complex signalling pathway with multiple second messengers, it is possible that HIF-2α might modulate RGS5 signalling in hypoxia not just by upregulating *Rgs5* mRNA, but also by interacting with G-protein second messengers, via the ligand-binding pocket in the HIF-2α PAS-B domain, proposed to play a HIF-β heterodimerisation-independent role in VAH here (Chapters 3 and 4).

These systemic analyses of adaptations to hypoxia, as measured by plethysmography, may be confounded by many compensatory mechanisms. While the role of the CB in

VAH is beyond doubt, several other sensors and mechanisms have been described to modulate VAH, including central, acid-sensitive chemoreceptors (although the role of P_{CO2} on VAH is more likely due to direct effects on the CB, Khamnei and Robbins, 1990, Robbins, 2007), and aortic paraganglia, which have been demonstrated to take over the role of destroyed CBs in some species (Sapru and Krieger, 1977). Further, adaptive stimuli independent of ventilatory acclimatisation, including pulmonary ventilation-perfusion matching and erythropoiesis, might cause differences in hypoxaemia experienced by the experimental animals, despite equal environmental conditions applied. The possibility to exclude these confounding factors has been explored in the final chapter of this thesis, by performing *ex vivo* studies on CBs from mice expressing the GCaMP6f Ca^{2+} reporter. Monitoring real-time changes in intracellular [Ca^{2+}] demonstrated quantitative changes in oxygen sensitivity, providing a platform to directly measure changes in chromaffin (and CB type I cell) oxygen sensitivity in genetically modified animals. Going forward, it will be interesting to test the CB hypoxia-sensitivity in mice with *Epas1* S305M mutation, *Arnt1/2* loss and *Rgs4/5* loss, and use pharmacological HIF-2α inhibitors to define the time-course of the effects of HIF-2α inhibition on CB function independent of systemic bioavailability.

In addition to studies on HIF-2α mechanism in CB oxygen sensitivity, acute sensitivity to hypoxia has been demonstrated in the AM with HIF-2α stabilisation via inactivation of PHD2 (Chapter 6). Demonstration of parallel changes in gene expression and neurosecretory function in *Phd2*KO AM opens a new avenue for mechanistic dissection of acute oxygen sensing. In the first step towards this, we demonstrated sensitivity of the O_2-sensitive *Phd2*KO AM to Doxapram, a TASK channels inhibitor typically considered to exert its function via actions on the carotid body (Yost, 2006). Subsequent

analysis of changes in expression of TASK channels in the *Phd2*KO AM is therefore of interest.

Given this parallel between changes in gene expression and gain of acute oxygen sensitivity in *Phd2*KO AMs, transcriptomic data collected in Chapter 6 could be used to construct a subset of genes comprising the oxygen sensing system in the sympathoadrenal cells. With HIF-2α stabilisation found to be sufficient to induce acute oxygen sensitivity in the AM, similar genetic interventions could be tested in existing neural-crest derived, excitable cell lines, such as the neuroblastoma SH-SY5Y cells, which are known to highly express *Rgs4* and *Rgs5*, and respond to GPCR agonists by increasing their intracellular [Ca^{2+}] (Masson et al., 2019).

In an alternative approach, an immortalised, acutely oxygen sensitive cell line could be generated from the PPGL-like tissues described here (Chapter 6). The use of genetically modified animals expressing the GCaMP reporters provides an excellent opportunity to dissect CB responses to hypoxia in already existing models, however, generation of new transgenic mouse lines is costly and time-consuming. In the past, a similar problem in the research on HIF signalling has been resolved by the demonstration of pO_2-sensitive production of erythropoietin in two hepatoma cell lines: HepG2 and HepG3 (Goldberg et al., 1987). *In vitro* studies on the CB type I cells are technically challenging due to the small size of the tissue, particularly in rodents, and the inability to culture the oxygen-sensitive cells long-term, with most studies recording O_2 sensitivity within 24h of dispersion (Fishman et al., 1985, Wyatt and Buckler, 2004, Lopez-Barneo et al., 1988), thus not permitting transfection and other long-term studies. The discovery of large, chromaffin-cell structures sensitive to changes in oxygen tension, which proliferate during post-natal development in the *Phd2$^{f/f}$;THCre* mice (Chapter 6), might provide an opportunity to generate an acutely oxygen-sensitive cell culture system. The

size of the OZ PGLs permits much higher cell yield than that of the CB, and the proliferative potential of both the abdominal PGLs and *Phd2*KO AM, as demonstrated by expression of proliferative marker Ki67 in the OZ (data not shown) and increased expression of oncogenes, including *Stc1* and *Igf2*, in the *Phd2*KO AM, could be exploited to stimulate cell proliferation *in vitro*.

Overall, studies presented in this thesis demonstrate the crucial role of HIF-2α in CB-mediated adaptations to hypoxia and, perhaps unexpectedly, given its canonical role as a transcription factor, provide evidence that HIF-2α activity underlies the acute oxygen sensitivity of peripheral chemoreceptors. While historically, chronic and acute adaptations to hypoxia have been considered to be mediated by independent mechanisms, evidence presented here suggests that HIF-2α might be a 'bridge' molecule between the long-term HIF signalling and rapid acute oxygen sensitivity. HIF-2α involvement in two responses acting on such different time-scales may be explained by the multiple mechanisms of action: either by mediating gene expression or in a rapid, non-transcriptional way. These findings provide an opening for further research into understanding the molecular basis of acute oxygen sensing in the CB and other tissues, with potential clinical implications in ventilatory disease and cancer.

8
Materials and methods

8.1 Materials and chemicals

All chemical substances were purchased from Merck (formerly Sigma), unless otherwise stated. Phosphate Buffered Saline (PBS) was prepared in-house as 1.37 M NaCl, 26.8 mM KCl, 46.7 mM $Na_2HPO_4 \cdot 7H_2O$, 14.7 mM KH_2PO_4 in distilled water. PBS-T is 1% v/v Tween20 in PBS.

8.2 Ethical approval

All procedures carried out on animals were compliant with the UK Home Office Animals (Scientific Procedures) Act 1986 and local ethical review. Procedures were authorised by project and personal licences and approved by the University of Oxford Medical Sciences Division Ethical Review Committee.

8.3 Animals

Animals were housed in individually ventilated cages in a 12/12 or 13/11 hours light/dark cycle, with unlimited access to food and water. Both male and female mice have been used in experiments (with ventilatory assessments carried out exclusively in males) and control animals were always age and sex matched (usually from the same litter). Adult, 2-3 months old mice were used for all experiments, unless otherwise stated. Wild-type mice were C57BL/6 mice purchased from the Charles River facility,

UK. All genetically modified mouse lines were on the C57BL/6 genetic background. Details of externally-sourced mouse lines used and the sources they were obtained from are provided in Table 8-1. *Arnt2*$^{f/f}$ mice have been generated from the KOMP ES cell line *Arnt2*$^{tm1a(KOMP)Wtsi}$ by Prof Ben Davis's group at the Wellcome Centre for Human Genetics, University of Oxford, UK.

8.4 Genotyping

Ear biopsies were obtained from around 2 weeks-old pups to establish inherited genotype. Samples were digested in Proteinase K buffer (10% SDS, Sigma, 0.02 EDTA pH 8.0, Invitrogen, 0.05M Tris pH 8.0, Invitrogen, 488 μg·ml^{-1} Proteinase K, Meridian Bioscience) at 55°C overnight. Digests were then cooled at 4°C for 30 min, followed by addition of saturated NaCl in water and further 10 min incubation at 4°C to remove protein contaminates. Resulting mixture was centrifuged at 10 000 rpm for 10 min and the supernatant removed and mixed with isopropanol in a 1:1 ratio, followed by a 30 min incubation at 4°C. DNA was precipitated by centrifugation at 13 000 rpm for 30-60 min (4°C). Isopropanol was removed and DNA pellets dried at 45°C, followed by resuspension in 50 μl nuclease free water (Invitrogen).

Genotypes were established by PCR amplification of target regions within the alleles of interest, using primers described in Table 8-1 and with either a Taq DNA Polymerase (Qiagen) or a BioTaq DNA Polymerase (Meridian Bioscience), as per manufacturer's instructions.

Table 8-1. Primer sequences used for PCR genotyping of mice.

Genotype	Source/Reference	Primers (5' to 3')
Phd2$^{+/-}$ *Phd2*$^{f/f}$	Takeda et al., 2006	P2MPLEXwtrv1: CACGGGGAACTCTGATTCAT

		P2MPLEXkorv1: CCAAAATCACCAATCTAGAATAA
Epas1$^{S305M/S305M}$	Feng et al., 2018	S305M Oligo F: TACAAAGGGGCAGGTGGTAATG S305M Oligo R: GCCGCTCATAGTCTTTCCAG WT Oligo F: AGGAGGTGAAGTCAGTAGGGTG WT Oligo R: TAGCATCCGGTACTGGCCAGA
Arnt$^{f/f}$	Tomita et al., 2000	ARNTYPE-F2: TGCAAACATGTGCCACCATGT ARNTYPE – R2: GTGAGGCAGATTTCTTCCATGCTC
Arnt2$^{f/f}$	UCDavis KOMP Repository Strain Arnt2$^{tm1a(KOMP)Wtsi}$_A12 ; generated by Dr Ben Davies, Wellcome Centre for Human Genetics Transgenics Core	CSD-loxF: GAGATGGCGCAACGCAATTAATG CSD-Arnt2-F: ACTGGTAAGCCTGGTAAGAAGAG GC CSD-Arnt2-R: GTCTCGCTAATGTGGAAAGAGCA CC CSD-Arnt2-ttR: AGGAGTTGCTGACTTGCCATTTTC C
Rgs4$^{f/f}$	The Jackson Laboratory Stock No 026695	22719 GCTCACCTTGGGAAGTAGCA 22720 CTGTGTTCGCAGGAATCTGA
Rgs5$^{f/f}$	Rgs5$^{tm1a(EUCOMM)Wtsi}$/H strain MRC Harwell	5mut-R1 GAACTTCGGAATAGGAACTTCG Rgs5-5arm-WTF CCAGAATGGGGTAATATCAAGC

		Rgs5-Crit-WTR CATTTGTCCCGAGGCTATGT
Ai95$^{f/f}$	The Jackson Laboratory Stock No: 024105	oIMR902 CCGAAAATCTGTGGGAAGTC Oimr9020 AAGGGAGCTGCAGTGGAGTA 19908 ACGAGTCGGATCTCCCTTTG
THCre *RosaCreER*	Lindeberg et al., 2004, Vooijs et al., 2001	creJun-fw CGGTCGATGCAACGAGTGATGAG G creJuj-rv CCAGAGACGGAAATCCATCGCTC G CreJUNfw CTCATACCAGTTCGCACAGGCGG C CreJUNrv CCGCTAGCACTCACGTTGGTAGG C

8.5 **Substance administration**

8.5.1 *Tamoxifen*

Mice expressing the inducible RosaCre^{ERT2} were dosed with 2 mg tamoxifen (20 mg·ml^{-1} in corn oil with 10% Ethanol) by oral gavage, once daily for 5 consecutive days, as described previously (Arsenault et al., 2013).

8.5.2 *BrdU*

To measure cellular proliferation in the hypoxic CBs, a single dose of 50 mg·kg^{-1} 5-Bromo-2'-deoxyuridine (10 mg·ml^{-1} in pH 7 Buffer, J/2850/15, Fisher Scientific) was administered immediately prior to the start of CH, and drinking water was

supplemented with 1 mg·ml^{-1} BrdU and 1% sucrose for the duration of experiment (Bishop et al., 2013, Hodson et al., 2016).

8.5.3 *HIF-2α inhibitors*

PT2385, PT2399 and PT2977 were purchased from MedChemExpress and dosing suspension was prepared at 1.25 or 2.5 mg·ml^{-1} in vehicle (5 mg·ml^{-1} methyl cellulose, 0.5% Tween80 in water)(Wallace et al., 2016). Animals were dosed with 10 or 60 mg·kg^{-1} PT2385, 30 mg·kg^{-1} PT2399 or 10 mg·kg^{-1} PT2977 by oral gavage, once or twice daily (with ~6-7h interval between the two doses), with control animals dosed with equivalent volume of vehicle.

8.6 **Plethysmography**

Hypoxic and hypercapnic AVRs were assessed by whole-body plethysmography in awake animals (Bishop et al., 2013, Cheng et al., 2020): Mice were placed in Buxco whole-body plethysmographs (PLY4211, 600 ml, DSI) and allowed to acclimatise to the new environment for 30 min with plethysmographs unsealed and filled with room air. 1.5 L·min^{-1} medical air flow was initiated ~3 min prior to the start of the recording and TVb and RR were measured for 5 min in air, followed by 5 min at 10% O_2/balance N_2, 10% O_2/3% CO_2/balance N_2 or 21% O_2/3% CO_2/balance N_2 (all gases supplied from pressured gas cylinders, BOC) and another 5 min at medical air. Following each 15 min recording, a 15 min break was allowed with open plethysmographs. MVb and TVb values averaged every 30s were exported from DSI software and RR was calculated as $\frac{MVb}{TVb}$. Data were normalised to animal's body weight on the day of the recording (usually recorded immediately prior to placing the animal in the plethysmograph) and plotted against time. AVRs were quantified as:

$$AVR = \overline{MVb_H} - \overline{MVb_B}$$

$\overline{MVb_H}$ – average MVb during first minute of stable hypoxia (excluding the first 30s after switching the gas supply)

$\overline{MVb_B}$ – average MVb during last minute of normoxia.

For more detailed analysis of AVRs in unacclimatised mice, average MVb/TVb/RR during the hypoxic stimulus was also quantified (with exclusion of first 30s after gas switch, as before) and compared with average MVb during normoxia across the 5 min resting periods prior to all 3 stimuli (10% O_2, 10% O_2/3% CO_2 and 3% CO_2).

8.7 **Chronic hypoxia**

CH was induced by placing animals in a normobaric altitude chamber with gas composition altered using Everest Summit II hypoxicators (Hypoxico)(Bishop et al., 2013). Animals were placed in the chamber in their standard housing cages with unlimited access to food and water and the oxygen levels were steadily reduced from ~21% to ~11% O_2 during the first 20h. Final 10% O_2 was then applied and maintained for further 6 days, after which animals were culled by overdose of isoflurane (Piramal Critical Care) inside the altitude chamber and tissues collected for immunohistochemistry and RNA isolation. For experiments involving plethysmography, ventilation was measured prior to the start of hypoxic acclimatisation, after which animals were removed from the chamber on days 2, (5) and 7, and returned to normoxic conditions for 30 min prior to the start of plethysmography.

8.8 **Blood measurements**

Following death by terminal anaesthesia, animals were exsanguinated from the inferior vena cava using needles and syringes treated with heparin sodium (1000IU/ml, Wockhardt) and blood was stored on ice in EDTA-coated Microvette tubes (Sarstedt). Tissues were removed and immersion-fixed in 4% paraformaldehyde (w/v in PBS) or

snap-frozen in liquid N_2. Some of the animals with constitutive gene inactivation using TH-IRES-Cre were perfused-fixed with 5 ml PBS and 5 ml paraformaldehyde prior to tissue dissection.

8.8.1 *Haematocrit measurement*

Haematocrits were measured by placing a small volume of blood in capillary tubes and spinning in haematocrit centrifuge (C-MH30, Unico), then measuring the volume of blood occupied by the red blood cells. Remaining blood was centrifuged at 4°C, 3000 rpm for 5 min and plasma supernatant was removed and frozen at -80°C.

8.8.2 *Plasma catecholamine measurement*

Adrenaline and noradrenaline concentrations were measured in diluted plasma samples using the Epinephrine/Norepinephrine ELISA Kit (KA1877, Abnova) according to manufacturer's instructions. Signal absorbance was read at 450 nm using a FLUOstar Omega microplate reader (BMG Labtech). Catecholamine concentration was calculated using a linear standard curve.

8.9 **Immunohistochemistry**

Tissue processing and immunohistochemistry procedures were as described previously (Fielding et al., 2018): following dissection, tissues were placed in 4% paraformaldehyde (w/v in PBS) and left to fix at room temperature overnight. The following day, tissues were transferred into 70% ethanol and stored at 4°C until processing. Tissues were processed by gradual dehydration in 70%, 90% and 100% ethanol, then Histo-Clear II (National Diagnostics) and finally wax at 60°C in an automated tissue processor (Excelsior AS, Thermo Scientific). Tissues were embedded in paraffin and sectioned with a Microm HM 355S Microtome (Thermo Scientific)

using MB35 Premier Blades (Thermo Scientific) to 4 μm thickness, then placed on polysine-coated slides (VWR) and allowed to dry at 37°C overnight.

To identify CBs or OZ PGLs in dissected regions, 1/6 or 1/8, respectively, slides were stained with Harris Hematoxylin. Briefly, paraffin was removed by two washes in xylene (MP Biomedicals) and tissues rehydrated in 100%, 90% and 70% ethanol, followed by a brief immersion in modified Harris Hematoxylin (Epredia) and multiple washes in tap water. Tissues were then dehydrated in the reverse ethanol/xylene series and mounted with coverslips using DPX Mountant.

8.9.1 *Tyrosine Hydroxylase and Chromogranin A IHC*

To detect catecholaminergic cells, paraffin sections were rehydrated in xylene/ethanol series as above, then placed in hot antigen retrieval solution, pH 6.8 (Dako) in a pressure cooker for 10 min. Slides were allowed to cool for 30-60 min then transferred to PBS and blocked with Peroxidase Block (Dako) for 5 min. 1:5000 Rabbit anti-TH antibody (NB300-109, Novus Biologicals) or 1:500 Rabbit anti-CGA antibody (ab68271, Abcam) in Dako Antibody diluent was applied overnight at 4°C, followed by washes in PBS-T and application of secondary HRP-conjugated anti-rabbit antibody (Dako) for 30 min at room temperature. Signal was detected with DAB chromogen (Dako) prepared according to manufacturer's instructions, incubated for 10 min and removed with tap water. Tissues were counterstained with modified Harris Hematoxylin (Epredia) differentiated with 1% acetic acid for optimal stain intensity and dehydrated and mounted as above.

8.9.2 *BrdU immunohistochemistry*

BrdU was detected in paraffin sections using the BrdU In-Situ Detection Kit II (BD Pharmingen), according to manufacturer's instructions and as described previously

(Hodson et al., 2016, Fielding et al., 2018). Briefly, tissues were rehydrated in a xylene/ethanol series then placed in 3% hydrogen peroxide (v/v in PBS) for 10 min and washed in PBS. Antigen retrieval solution was boiled in a pressure cooker for 10 min and sections allowed to cool for 30-60 min. Tissues were blocked with 5 min avidin, 5 min biotin (Abcam), and 5 min protein block (Dako) with PBS-T washes in between. BrdU antibody was diluted as per instructions and applied overnight at 4°C. Antibody detection steps were as per manufacturer's instructions.

8.10 *In situ* hybridisation

RNA was detected in formalin-fixed paraffin-embedded tissues (as prepared in section 8.9) using the RNAScope or Basescope manual assays (ACDBio) as per manufacturer's instructions. Probes used to detect specific target genes are listed in Table 8-2. Harris Hematoxylin (Epredia), differentiated with 1% acetic acid for optimal intensity, was used as a counterstain in RNAScope and 2 min incubation with 50% Gill Hematoxylin (v/v in distilled water, ThermoScientific) counterstain was used in the Basescope assay.

Table 8-2. RNAScope and BaseScope probes.

Target gene	Probe name	Catalogue number
Epas1	Mm-Epas1	314371
Vegfa	Mm-Vegfa-O1	43961
Arnt	Mm-Arnt-CDS	457301
Arnt2	Mm-Arnt2	463371
Rgs4	Mm-Rgs4	467461
Rgs5	Mm-Rgs5 BA-Mm-Rgs5-1zz-st-C1	430181 901541-C1
Hif1a	Mm-Hif1a	313821
Ado	Mm-Ado	570001
Cox4i2	Mm-Cox4i2	497901
Ndufa4l2	Mm-Ndufa4l2	816431
Higd1c	Mm-Higd1c-O1	527761
Dbh	Mm-Dbh	407851
Pnmt	Mm-Pnmt	426421
Adora2a	Mm-Adora2a	409431

8.11 **IHC/ISH imaging and quantification**

Stained slides were imaged under a DM1000 LED microscope (Leica Biosystems) or with the NanoZoomer S210 slide scanner (Hamamatsu).

To estimate the volume of the CB and OZ, tissue area was calculated using Fiji (NIH) or NDP.View2 software (Hamamatsu) in 4 sections on every 4th slide and area for intermediate (non-stained) slides was estimated by averaging the CB/OZ area on the bordering slides (e.g. stain slides 8 and 12, for slides 9, 10 and 11 CB area = average area in slides 8 and 12). Sum of CB/OZ areas across all CB/OZ^{+} sections was then multiplied by the section thickness to calculate the volume.

BrdU^{+} cell density was quantified by measuring the CB area using Fiji (NIH) software and counting the number of BrdU^{+} nuclei per CB section. At least 3 sections from 2 different slides were used to calculate average BrdU^{+} density for each sample.

8.12 **RNA extraction**

8.12.1 *Small tissues: CBs, SCGs, AMs*

CBs, SCGs and AMs, were pooled from multiple animals per genotype to obtain sufficient material and RNA was extracted using RNEasy Micro Plus kit (Qiagen) according to manufacturer's instructions and as described previously (Gao et al., 2017): Tissues were sub-dissected into RNAProtect Tissue Reagent (Qiagen) and placed on ice for 2-5h until all tissues were collected. 1 volume of PBS in Diethyl Pyrocarbonate-treated H_2O was then added to Tissue Protect and tissues centrifuged at full speed for 1 min to collect at the bottom of the tube, allowing to remove the Tissue Protect and PBS mix. Subsequently, 300 µl of ice-cold RLT Plus buffer with 20 µl of 2M DTT per 1 ml was added and tissues homogenized using the Pro200 homogenizer (ProScientific) in: 5x6s pulses for CBs, 3x10s pulses for SCGs, 4x5s pulses for AMs. Lysate was then

centrifuged for 3 min at 1500 rpm, 4°C and supernatant transferred into a clean, RNAse-free tube then immediately frozen on dry ice. Lysates were stored at -80°C for 24h-7 days before continuing with RNA extraction. Lysates were thawed on ice and the remaining steps from Qiagen kit were carried out at room temperature. RNA was eluted with 14 µl RNAse-free H_2O and quality assessed using the High Sensitivity RNA ScreenTape (Agilent), as per manufacturer's instructions. Remaining RNA was used immediately or stored at -80°C.

8.12.2 *Large tissues (kidneys)*

½ of each kidney was snap-frozen in liquid nitrogen upon dissection from animals under terminal anaesthesia and stored at -80°C. Frozen kidneys were pulverized on dry ice and 20-30 mg of powder was collected for RNA extraction using the RNEasy Plus Mini kit (Qiagen). RLT Plus buffer was supplemented with 20 µl 2M DTT per 1 ml. Tissues were homogenized with 3x10s pulses with Pro200 homogenizer (ProScientific) on ice and lysates centrifuged for 3 min at 1500 rpm, 4°C then supernatant transferred to a new RNAse-free tube before proceeding with gDNA wipe-out as per manufacturer's instructions (Qiagen RNEasy Plus Mini). RNA was eluted with 30 µl RNAse-free water and concentration measured with NanoDrop 8000 (Thermo Scientific). Eluted RNA was stored on ice until RT-PCR or at -80°C long-term.

8.13 **Quantitative Real-Time RT-PCR**

To quantify gene expression, cDNA was prepared using the QuantiTect Reverse Transcription Kit (Qiagen) according to manufacturer's instructions. Gene expression was quantified in triplicates in a duplex quantitative Real-Time PCR with TaqMan Fast Advanced master mix and target gene FAM and *Actb* VIC expression assays (Mm01205647_g1, ThermoFisher Scientific). Details of FAM gene expression assays used to detect target genes are listed in Table 8-3. The reaction was carried out in the

StepOnePlus Real-Time PCR System (Applied Biosystems). Relative gene expression was expressed as $2^{-\Delta\Delta CT}$, with

$$\Delta\Delta C_T = \Delta C_T(mutant) - \Delta C_T(wildtype),$$

where $\Delta C_T = C_T(target\ gene) - C_T(Actb)$ (Livak and Schmittgen, 2001). For pooled tissues, C_T values were averaged across technical triplicates before analysis. For kidneys, C_T values were averaged across technical triplicates within each sample and ΔC_T were averaged across biological replicates before calculating $2^{-\Delta\Delta CT}$. Standard deviation of $2^{-\Delta\Delta CT}$ was extrapolated from the standard deviation of the ΔC_Ts.

Table 8-3. TaqMan gene expression assays used for RT-qPCR

Gene name	TaqMan assay	Exon boundary targeted
Hif-2α	Mm00438712_m1	2-3
Vegfa	Mm00437306_m1	3-4
Arnt	Mm00507824_m1	6-7
Arnt2	Mm00476009_m1 Mm01312837_m1 Custom; LOT:2070811 A7	17-18 5-6 5
Rgs4	Mm00501389_m1 Mm01294334_g1	1-2 3-4
Rgs5	Mm00501393_m1	3-4
Pnmt	Mm00476993_m1	1-2
Adora2a	Mm00802075_m1	2-3
Cox4i2	Mm00446387_m1	2-3
Ndufa4l2	Mm01160374_g1	1-2
Slc2a1	Mm00441480_m1	8-9
Ccnd1	Mm00432359_m1	3-4
Ldha	Mm01612132_g1	6-7
Hif1a	Mm00468869_m1	4-5
Stc1	Mm01322191_m1	3-4
Igf2	Mm00439564_m1	2-3
Ret	Mm00436304_m1	2-3
Actb	Mm01205647_g1	2-3

8.14 RNA Sequencing

RNA was prepared from *Phd2$^{f/f}$;THCre* and *Phd2$^{f/f}$* CBs and AMs as described (8.12.1), from tissues isolated from 5 animals per genotype group, 3 biological repeats. Ultra-low library preparation and RNA sequencing using the NovaSeq6000 platform were performed by the Wellcome Centre for Human Genetics Genomics Facility. Data were processed and analysed by Dr Yoichiro Sugimoto.

8.15 Ca^{2+} imaging in live tissues

8.15.1 *Tissue preparation*

To image Ca^{2+} fluctuations in live tissues, transgenic animals expressing GCaMP6f in TH^{+} expressing cells were used (Madisen et al., 2015). 2-6 months-old animals were culled by terminal anaesthesia (or cervical dislocation if CBs/SCGs not used) and exsanguination and carotid bifurcations, aortas and adrenal glands were collected into ice-cold PBS. CBs, SCGs and OZ PGLs were then sub-dissected under an S9i stereo microscope (Leica) in ice-cold PBS and placed on a nylon mash (Warner Instruments) in F12 media (Gibco) with Foetal Bovine Serum (Gibco), Penicilin/Streptavidin and L-Glutamine, then kept at 37°C, 21% O_2/5% CO_2 until imagining (up to 4h). Adrenal glands were embedded in 5% low-melting-point agarose (BP1360, Fisher Scientific) in modified Tyrode's buffer (25 mM $NaHCO_3$, 117 mM NaCl, 1 mM NaH_2PO_4, 11 mM D-Glucose, 4.5 mM KCl, 1 mM $MgCl_2$, 25 mM HEPES) at 39°C and allowed to cool on ice for ~5 min. 150 μm slices were obtained with a VT100S Vibratome (Leica) using Feather FA-10 carbon blades (Labtech) vibrating at 80 Hz, 0.2 mm/s. Slices were placed in DMEM media (Gibco) then kept at 37°C, 21% O_2/5% CO_2 until imagining (up to 4h).

8.15.2 *Fluorescent imaging*

Tissues were imaged in a custom-built gravity-based perfusion system, with an epifluorescence Leica DMi8 microscope (Leica Microsystems CMS), rigged with the pE340^{fura} light source (CoolLED), a GFP filter cube: excitation filter 470 ± 40 nm, dichroic mirror 495 nm, emission filter 525 ± 50 nm and a monochrome Prime 95B camera (Photometrics). Tyrode's buffer (25 mM $NaHCO_3$, 117 mM NaCl, 1 mM NaH_2PO_4, 11 mM D-Glucose, 4.5 mM KCl, 1 mM $MgCl_2$)-based test solutions were bubbled with gases using the 3-channel Gas Blender 100 Series mixers (MCQ Instruments) for 1.5h+ prior to the start of the experiment; $CaCl_2$ was added after ~2h of bubbling with 5% CO_2 to a final concentration of 1 mM to prevent bicarbonate precipitation. For gas composition see Table 8-4. Solutions were heated to 41°C upstream of the tissue chamber resulting in 36-37°C in the chamber. Tissues were placed in the perfusion chamber and immobilised with a SHD-22L/15 or SHD-22L/10 slice anchor (Warner Instruments) and control solution was supplied until experiment start. GFP images were obtained every 2s with a x40 oil-immersive objective (HC PL FLUOTAR 40x/1.30 OIL 340nm, Leica Microsystems CMS) used for CBs and SCGs and a x10 objective (N PLAN 10x/0.25 achromatic corrected objective, Leica Microsystems CMS) used for OZ and AM. Bright-field images of the AM were taken prior to the start of GFP recording to select the AM area for analysis. Baseline fluorescence was measured for at least 60s prior to the application of the first test. Test solutions were applied for 90s (or up to 60s for K^+), with at least 120s rest in control solution between tests.

Table 8-4. Composition of gases used to bubble test solutions for Ca^{2+} imaging of fresh tissues.

50 μM Doxapram solution was prepared by adding 250 μl of 1000x Doxapram hydrochloride (USP) stock in DMSO to the Tyrode's control buffer (O'Donohoe et al., 2018). Anoxic solution was supplemented with 4 $mg \cdot ml^{-1}$ sodium sulphite.

Test solution	Compressed air	N_2	CO_2
Control, 50 μM Doxapram, 45 mM K^+	95%	0%	5%
10% O_2	48%	47%	5%
5% O_2	23%	72%	5%
2% O_2	9%	86%	5%
1% O_2 Anoxia	2%	93%	5%
10% CO_2	90%	0%	10%

8.15.3 *Ca^{2+} imaging data analysis*

GFP images were exported from the Leica Application Suite X version 3 software (Leica Microsystems CMS) and analysed in Fiji (ImageJ, NIH). For single area analysis, a region of interest (ROI) was selected based on the peak fluorescence image under 45 mM K^+, using threshold adjustment to isolate the region with high GCaMP6f fluorescence where possible. For AM slices, ROI selection was also based on the bright-field images to delineate the AM from the densely packed cortex. Regions of interest were never selected based on images from hypoxic or other test exposures. Average fluorescence across the ROI was calculated in all images within one experimental Z-stack and subsequent quantitative analysis was carried out with the Microsoft Office 2019 Excel package.

For each time-point, average fluorescence was normalised to the starting fluorescence in that sample (F/F_0) and data were plotted against time to confirm responses to K^+ are detected and no unexpected shifts in the baseline fluorescence occurred.

Responses to test stimuli were quantified by calculating the area under curve (AUC) during the test and normalising to the AUC during 45 mM K^+ exposure.

$$AUC = 2 \times \sum_{i=t1}^{tn-1} F/F_{0_i} + F/F_{0_{t0}} + F/F_{0_{tn}} - \frac{\sum_{i=t-5}^{t-1} F/F_{0_i} + \sum_{i=tn+10}^{tn+14} F/F_{0_i}}{10} \times 2 \times n$$

t_0 - first time-point when the stimulus is applied

t_n - last time-point before the stimulus is removed

n - number of time-points (2s intervals) during the stimulus

Both the test and K^+ AUC were divided by *n* (duration of the stimulus) before normalisation to account for varying stimuli duration.

As the AUC < 0 results from noise in the baseline and/or progressive reduction in the baseline fluorescence intensity, rather than a biological phenomenon, all AUC < 0 values were assigned a value of 0 instead.

For spatial analysis of GCaMP6f fluorescence changes in the AM, 600x600 pixel raw images were cropped to just outside the border of the AM ROI and resized to 600x600 pixels, prior to applying a grid of 31x31 (961) ROIs to the Z-stack. Average fluorescence was calculated for each ROI in each time-frame using the Multi Measure function and data exported to Excel. F/F_0 was calculated as before. Hpx-responsive and non-responsive ROIs were detected as follows:

1. Absolute change in F/F_0 during exposure to 45 mM K^+ was calculated as

$$\Delta K^+ = F/F_{0_{\max(t0-tn)}} - F/F_{0_{t-1}}$$

t_0 - first time-point when 45 mM K^+ is applied

t_n - last time-point before 45 mM K^+ is removed

2. AUC for 1% O_2 and anoxia stimuli were calculated as above.

The ROIs were then classified as Hpx-responsive, Hpx non-responsive or excluded, based on criteria outlined in Table 8-5.

Table 8-5. Criteria used to classify AM ROIs as Hpx-responsive or non-responsive.

Criterium	Hpx non-responsive	Hpx-responsive
ΔK^+	≥ 0.3	≥ 0.3
AUC anoxia (non-normalised)	< 3	≥ 3
AUC 1% O_2 (non-normalised)	no criteria	≥ 2

Using the *roiManager("select",newarray(list of ROI numbers))* command in Fiji, K^+ and Hpx-responsive ROIs were coloured with blue and green respectively within a 45 mM K^+ frame from the analysed Z-stack. ROIs falling outside of the AM area defined for bulk analysis were excluded, as the changes in intensity within those likely result from 'bleed-through' of light from adjacent regions.

GCaMP6f F/F_0 from individual Hpx-responsive and non-responsive ROIs was plotted against time and AUC during hypoxic stimuli as % of the K^+ response plotted against the $\%O_2$ and fitted with an exponential One Phase Decay curve in Prism 9 software (GraphPad). Any AUC < 0 values were assigned as 0 as above.

8.16 Statistical analysis

All quantitative data were plotted and statistical analysis carried out in Prism 9 software (GraphPad), except for RNA Sequencing data, which were processed, analysed and plotted by Dr Yoichiro Sugimoto using R version 4.0.0.

Data are shown as mean ± SEM, with individual values displayed were possible, unless otherwise stated. Pairwise comparisons between animal groups of different conditions/genotypes were done with an unpaired Student's *t*-test, with $P < 0.05$ considered statistically significant. For multi-group comparisons (e.g. hypoxia time-

course in control *vs* mutant animals), multi-measure two-way ANOVA tests were used with Sidak's multiple comparisons *t*-tests used to compare genotypes at individual time-points. Details of all statistical analyses are included with each dataset.

Bibliography

AARON, E. A. & POWELL, F. L. 1993. Effect of chronic hypoxia on hypoxic ventilatory response in awake rats. *J Appl Physiol (1985),* 74**,** 1635-40.

ADAMS, M. B., SIMONETTA, G. & MCMILLEN, I. C. 1996. The non-neurogenic catecholamine response of the fetal adrenal to hypoxia is dependent on activation of voltage sensitive Ca2+ channels. *Brain Res Dev Brain Res,* 94**,** 182-9.

ADMINISTRATION, U. S. F. A. D. 2021. Merck Sharp & Dohme Corp: Welireg [package insert]; Reference ID: 4840574

AITOLA, M. H. & PELTO-HUIKKO, M. T. 2003. Expression of Arnt and Arnt2 mRNA in developing murine tissues. *J Histochem Cytochem,* 51**,** 41-54.

ALDOSSARY, H. S., ALZAHRANI, A. A., NATHANAEL, D., ALHUTHAIL, E. A., RAY, C. J., BATIS, N., KUMAR, P., CONEY, A. M. & HOLMES, A. P. 2020. G-Protein-Coupled Receptor (GPCR) Signaling in the Carotid Body: Roles in Hypoxia and Cardiovascular and Respiratory Disease. *Int J Mol Sci,* 21.

APPELHOFF, R. J., TIAN, Y. M., RAVAL, R. R., TURLEY, H., HARRIS, A. L., PUGH, C. W., RATCLIFFE, P. J. & GLEADLE, J. M. 2004. Differential function of the prolyl hydroxylases PHD1, PHD2, and PHD3 in the regulation of hypoxia-inducible factor. *J Biol Chem,* 279**,** 38458-65.

ARAGONES, J., SCHNEIDER, M., VAN GEYTE, K., FRAISL, P., DRESSELAERS, T., MAZZONE, M., DIRKX, R., ZACCHIGNA, S., LEMIEUX, H., JEOUNG, N. H., LAMBRECHTS, D., BISHOP, T., LAFUSTE, P., DIEZ-JUAN, A., HARTEN, S. K., VAN NOTEN, P., DE BOCK, K., WILLAM, C., TJWA, M., GROSFELD, A., NAVET, R., MOONS, L., VANDENDRIESSCHE, T., DEROOSE, C., WIJEYEKOON, B., NUYTS, J., JORDAN, B., SILASI-MANSAT, R., LUPU, F., DEWERCHIN, M., PUGH, C., SALMON, P., MORTELMANS, L., GALLEZ, B., GORUS, F., BUYSE, J., SLUSE, F., HARRIS, R. A., GNAIGER, E., HESPEL, P., VAN HECKE, P., SCHUIT, F., VAN VELDHOVEN, P., RATCLIFFE, P., BAES, M., MAXWELL, P. & CARMELIET, P. 2008. Deficiency or inhibition of oxygen sensor Phd1 induces hypoxia tolerance by reprogramming basal metabolism. *Nat Genet,* 40**,** 170-80.

ARSENAULT, P. R., PEI, F., LEE, R., KERESTES, H., PERCY, M. J., KEITH, B., SIMON, M. C., LAPPIN, T. R. J., KHURANA, T. S. & LEE, F. S. 2013. A knock-in mouse model of human PHD2 gene-associated erythrocytosis establishes a haploinsufficiency mechanism. *J Biol Chem,* 288**,** 33571-33584.

BEALL, C. M., CAVALLERI, G. L., DENG, L., ELSTON, R. C., GAO, Y., KNIGHT, J., LI, C., LI, J. C., LIANG, Y., MCCORMACK, M., MONTGOMERY, H. E., PAN, H., ROBBINS, P. A., SHIANNA, K. V., TAM, S. C., TSERING, N., VEERAMAH, K. R., WANG, W., WANGDUI, P., WEALE, M. E., XU, Y., XU, Z., YANG, L., ZAMAN, M. J., ZENG, C., ZHANG, L., ZHANG, X., ZHAXI, P. & ZHENG, Y. T. 2010. Natural selection on EPAS1 (HIF2alpha) associated with low hemoglobin concentration in Tibetan highlanders. *Proc Natl Acad Sci U S A,* 107**,** 11459-64.

BECHMANN, N. & EISENHOFER, G. 2022. Hypoxia-inducible Factor 2alpha: A Key Player in Tumorigenesis and Metastasis of Pheochromocytoma and Paraganglioma? *Exp Clin Endocrinol Diabetes,* 130**,** 282-289.

BERNARDINI, A., BROCKMEIER, U., METZEN, E., BERCHNER-PFANNSCHMIDT, U., HARDE, E., ACKER-PALMER, A., PAPKOVSKY, D., ACKER, H. & FANDREY, J. 2015. Measurement of ROS Levels and Membrane Potential Dynamics in the Intact Carotid Body Ex Vivo. *Adv Exp Med Biol,* 860**,** 55-9.

BERRA, E., BENIZRI, E., GINOUVES, A., VOLMAT, V., ROUX, D. & POUYSSEGUR, J. 2003. HIF prolyl-hydroxylase 2 is the key oxygen sensor setting low steady-state levels of HIF-1alpha in normoxia. *EMBO J,* 22**,** 4082-90.

BERT, P. 1878. *La pression barométrique : recherches de physiologie expérimentale,* Paris, Masson.

BIGHAM, A. W. & LEE, F. S. 2014. Human high-altitude adaptation: forward genetics meets the HIF pathway. *Genes Dev,* 28**,** 2189-204.

BISGARD, G. E. 2000. Carotid body mechanisms in acclimatization to hypoxia. *Respir Physiol,* 121**,** 237-46.

BISHOP, T., GALLAGHER, D., PASCUAL, A., LYGATE, C. A., DE BONO, J. P., NICHOLLS, L. G., ORTEGA-SAENZ, P., OSTER, H., WIJEYEKOON, B., SUTHERLAND, A. I., GROSFELD, A., ARAGONES, J., SCHNEIDER, M., VAN GEYTE, K., TEIXEIRA, D., DIEZ-JUAN, A., LOPEZ-BARNEO, J., CHANNON, K. M., MAXWELL, P. H., PUGH, C. W., DAVIES, A. M., CARMELIET, P. & RATCLIFFE, P. J. 2008. Abnormal sympathoadrenal development and systemic hypotension in PHD3-/- mice. *Mol Cell Biol,* 28**,** 3386-400.

BISHOP, T. & RATCLIFFE, P. J. 2014. Signaling hypoxia by hypoxia-inducible factor protein hydroxylases: a historical overview and future perspectives. *Hypoxia (Auckl),* 2**,** 197-213.

BISHOP, T. & RATCLIFFE, P. J. 2020. Genetic basis of oxygen sensing in the carotid body: HIF2alpha and an isoform switch in cytochrome c oxidase subunit 4. *Sci Signal,* 13.

BISHOP, T., TALBOT, N. P., TURNER, P. J., NICHOLLS, L. G., PASCUAL, A., HODSON, E. J., DOUGLAS, G., FIELDING, J. W., SMITH, T. G., DEMETRIADES, M., SCHOFIELD, C. J., ROBBINS, P. A., PUGH, C. W., BUCKLER, K. J. & RATCLIFFE, P. J. 2013. Carotid body hyperplasia and enhanced ventilatory responses to hypoxia in mice with heterozygous deficiency of PHD2. *J Physiol,* 591**,** 3565-77.

BUCKLER, K. J. 1997. A novel oxygen-sensitive potassium current in rat carotid body type I cells. *J Physiol,* 498 (Pt 3)**,** 649-62.

BUCKLER, K. J. & TURNER, P. J. 2013. Oxygen sensitivity of mitochondrial function in rat arterial chemoreceptor cells. *J Physiol,* 591**,** 3549-63.

BUCKLER, K. J. & VAUGHAN-JONES, R. D. 1994. Effects of hypoxia on membrane potential and intracellular calcium in rat neonatal carotid body type I cells. *J Physiol,* 476**,** 423-8.

BUCKLER, K. J., WILLIAMS, B. A. & HONORE, E. 2000. An oxygen-, acid- and anaesthetic-sensitive TASK-like background potassium channel in rat arterial chemoreceptor cells. *J Physiol,* 525 Pt 1**,** 135-42.

BUFFET, A., BURNICHON, N., FAVIER, J. & GIMENEZ-ROQUEPLO, A. P. 2020. An overview of 20 years of genetic studies in pheochromocytoma and paraganglioma. *Best Pract Res Clin Endocrinol Metab,* 34**,** 101416.

BURNICHON, N., VESCOVO, L., AMAR, L., LIBE, R., DE REYNIES, A., VENISSE, A., JOUANNO, E., LAURENDEAU, I., PARFAIT, B.,

BERTHERAT, J., PLOUIN, P. F., JEUNEMAITRE, X., FAVIER, J. & GIMENEZ-ROQUEPLO, A. P. 2011. Integrative genomic analysis reveals somatic mutations in pheochromocytoma and paraganglioma. *Hum Mol Genet,* 20**,** 3974-85.

BURSLEM, G. M., KYLE, H. F., NELSON, A., EDWARDS, T. A. & WILSON, A. J. 2017. Hypoxia inducible factor (HIF) as a model for studying inhibition of protein-protein interactions. *Chem Sci,* 8**,** 4188-4202.

CACERES, A. I., GONZALEZ-OBESO, E., GONZALEZ, C. & ROCHER, A. 2009. RT-PCR and pharmacological analysis of L-and T-type calcium channels in rat carotid body. *Adv Exp Med Biol,* 648**,** 105-12.

CAMPANUCCI, V. A. & NURSE, C. A. 2007. Autonomic innervation of the carotid body: role in efferent inhibition. *Respir Physiol Neurobiol,* 157**,** 83-92.

CARD, P. B., ERBEL, P. J. & GARDNER, K. H. 2005. Structural basis of ARNT PAS-B dimerization: use of a common beta-sheet interface for hetero- and homodimerization. *J Mol Biol,* 353**,** 664-77.

CASSOL, C. A., WINER, D., LIU, W., GUO, M., EZZAT, S. & ASA, S. L. 2014. Tyrosine kinase receptors as molecular targets in pheochromocytomas and paragangliomas. *Mod Pathol,* 27**,** 1050-62.

CELADA, L., CUBIELLA, T., SAN-JUAN-GUARDADO, J., SAN JOSE MARTINEZ, A., VALDES, N., JIMENEZ-FONSECA, P., DIAZ, I., ENGUITA, J. M., ASTUDILLO, A., ALVAREZ-GONZALEZ, E., SIERRA, L. M. & CHIARA, M. D. 2022. Differential HIF2alpha Protein Expression in Human Carotid Body and Adrenal Medulla under Physiologic and Tumorigenic Conditions. *Cancers (Basel),* 14.

CHAN, W. H., KOMADA, M., FUKUSHIMA, T., SOUTHARD-SMITH, E. M., ANDERSON, C. R. & WAKEFIELD, M. J. 2019. RNA-seq of Isolated Chromaffin Cells Highlights the Role of Sex-Linked and Imprinted Genes in Adrenal Medulla Development. *Sci Rep,* 9**,** 3929.

CHANG, A. J., ORTEGA, F. E., RIEGLER, J., MADISON, D. V. & KRASNOW, M. A. 2015. Oxygen regulation of breathing through an olfactory receptor activated by lactate. *Nature,* 527**,** 240-4.

CHANG, Y. T., YANG, C. C., PAN, S. Y., CHOU, Y. H., CHANG, F. C., LAI, C. F., TSAI, M. H., HSU, H. L., LIN, C. H., CHIANG, W. C., WU, M. S., CHU, T. S., CHEN, Y. M. & LIN, S. L. 2016. DNA methyltransferase inhibition restores erythropoietin production in fibrotic murine kidneys. *J Clin Invest,* 126**,** 721-31.

CHEN, J., HE, L., LIU, X., DINGER, B., STENSAAS, L. & FIDONE, S. 2007. Effect of the endothelin receptor antagonist bosentan on chronic hypoxia-induced morphological and physiological changes in rat carotid body. *Am J Physiol Lung Cell Mol Physiol,* 292**,** L1257-62.

CHEN, T. W., WARDILL, T. J., SUN, Y., PULVER, S. R., RENNINGER, S. L., BAOHAN, A., SCHREITER, E. R., KERR, R. A., ORGER, M. B., JAYARAMAN, V., LOOGER, L. L., SVOBODA, K. & KIM, D. S. 2013. Ultrasensitive fluorescent proteins for imaging neuronal activity. *Nature,* 499**,** 295-300.

CHEN, W., HILL, H., CHRISTIE, A., KIM, M. S., HOLLOMAN, E., PAVIA-JIMENEZ, A., HOMAYOUN, F., MA, Y., PATEL, N., YELL, P., HAO, G., YOUSUF, Q., JOYCE, A., PEDROSA, I., GEIGER, H., ZHANG, H., CHANG, J., GARDNER, K. H., BRUICK, R. K., REEVES, C., HWANG, T. H., COURTNEY, K., FRENKEL, E., SUN, X., ZOJWALLA, N., WONG, T., RIZZI, J. P., WALLACE, E. M., JOSEY, J. A., XIE, Y., XIE, X. J., KAPUR, P.,

MCKAY, R. M. & BRUGAROLAS, J. 2016. Targeting renal cell carcinoma with a HIF-2 antagonist. *Nature,* 539**,** 112-117.

CHEN, Y., TIPOE, G. L., LIONG, E., LEUNG, S., LAM, S. Y., IWASE, R., TJONG, Y. W. & FUNG, M. L. 2002. Chronic hypoxia enhances endothelin-1-induced intracellular calcium elevation in rat carotid body chemoreceptors and up-regulates ETA receptor expression. *Pflugers Arch,* 443**,** 565-73.

CHENG, X., PRANGE-BARCZYNSKA, M., FIELDING, J. W., ZHANG, M., BURRELL, A. L., LIMA, J. D., ECKARDT, L., ARGLES, I., PUGH, C. W., BUCKLER, K. J., ROBBINS, P. A., HODSON, E. J., BRUICK, R. K., COLLINSON, L. M., RASTINEJAD, F., BISHOP, T. & RATCLIFFE, P. J. 2020. Marked and rapid effects of pharmacological HIF-2alpha antagonism on hypoxic ventilatory control. *J Clin Invest*.

CHO, H., DU, X., RIZZI, J. P., LIBERZON, E., CHAKRABORTY, A. A., GAO, W., CARVO, I., SIGNORETTI, S., BRUICK, R. K., JOSEY, J. A., WALLACE, E. M. & KAELIN, W. G. 2016. On-target efficacy of a HIF-2alpha antagonist in preclinical kidney cancer models. *Nature,* 539**,** 107-111.

CHO, H., KOZASA, T., BONDJERS, C., BETSHOLTZ, C. & KEHRL, J. H. 2003. Pericyte-specific expression of Rgs5: implications for PDGF and EDG receptor signaling during vascular maturation. *FASEB J,* 17**,** 440-2.

CHOU, C. L., SHAM, J. S., SCHOFIELD, B. & SHIRAHATA, M. 1998. Electrophysiological and immunocytological demonstration of cell-type specific responses to hypoxia in the adult cat carotid body. *Brain Res,* 789**,** 229-38.

COMPERNOLLE, V., BRUSSELMANS, K., ACKER, T., HOET, P., TJWA, M., BECK, H., PLAISANCE, S., DOR, Y., KESHET, E., LUPU, F., NEMERY, B., DEWERCHIN, M., VAN VELDHOVEN, P., PLATE, K., MOONS, L., COLLEN, D. & CARMELIET, P. 2002. Loss of HIF-2alpha and inhibition of VEGF impair fetal lung maturation, whereas treatment with VEGF prevents fatal respiratory distress in premature mice. *Nat Med,* 8**,** 702-10.

CONDE, S. V., OBESO, A., VICARIO, I., RIGUAL, R., ROCHER, A. & GONZALEZ, C. 2006. Caffeine inhibition of rat carotid body chemoreceptors is mediated by A2A and A2B adenosine receptors. *J Neurochem,* 98**,** 616-28.

CORNFIELD, D. N., STEVENS, T., MCMURTRY, I. F., ABMAN, S. H. & RODMAN, D. M. 1994. Acute hypoxia causes membrane depolarization and calcium influx in fetal pulmonary artery smooth muscle cells. *Am J Physiol,* 266**,** L469-75.

COUPLAND, R. The natural history of the chromaffin cell. 1965.

COUPLAND, R. E. & HOPWOOD, D. 1966. Mechanism of a histochemical reaction differentiating between adrenaline- and noradrenaline-storing cells in the electron microscope. *Nature,* 209**,** 590-1.

COURTNEY, K. D., INFANTE, J. R., LAM, E. T., FIGLIN, R. A., RINI, B. I., BRUGAROLAS, J., ZOJWALLA, N. J., LOWE, A. M., WANG, K., WALLACE, E. M., JOSEY, J. A. & CHOUEIRI, T. K. 2018. Phase I Dose-Escalation Trial of PT2385, a First-in-Class Hypoxia-Inducible Factor-2alpha Antagonist in Patients With Previously Treated Advanced Clear Cell Renal Cell Carcinoma. *J Clin Oncol,* 36**,** 867-874.

COWBURN, A. S., CROSBY, A., MACIAS, D., BRANCO, C., COLACO, R. D., SOUTHWOOD, M., TOSHNER, M., CROTTY ALEXANDER, L. E., MORRELL, N. W., CHILVERS, E. R. & JOHNSON, R. S. 2016. HIF2alpha-arginase axis is essential for the development of pulmonary hypertension. *Proc Natl Acad Sci U S A,* 113**,** 8801-6.

CRONA, J., TAIEB, D. & PACAK, K. 2017. New Perspectives on Pheochromocytoma and Paraganglioma: Toward a Molecular Classification. *Endocr Rev,* 38**,** 489-515.

CZYZYK-KRZESKA, M. F., BAYLISS, D. A., LAWSON, E. E. & MILLHORN, D. E. 1992. Regulation of tyrosine hydroxylase gene expression in the rat carotid body by hypoxia. *J Neurochem,* 58**,** 1538-46.

DAHAN, A., NIEUWENHUIJS, D. & TEPPEMA, L. 2007. Plasticity of central chemoreceptors: effect of bilateral carotid body resection on central CO2 sensitivity. *PLoS Med,* 4**,** e239.

DAHIA, P. L. 2014. Pheochromocytoma and paraganglioma pathogenesis: learning from genetic heterogeneity. *Nat Rev Cancer,* 14**,** 108-19.

DAHIA, P. L., ROSS, K. N., WRIGHT, M. E., HAYASHIDA, C. Y., SANTAGATA, S., BARONTINI, M., KUNG, A. L., SANSO, G., POWERS, J. F., TISCHLER, A. S., HODIN, R., HEITRITTER, S., MOORE, F., DLUHY, R., SOSA, J. A., OCAL, I. T., BENN, D. E., MARSH, D. J., ROBINSON, B. G., SCHNEIDER, K., GARBER, J., ARUM, S. M., KORBONITS, M., GROSSMAN, A., PIGNY, P., TOLEDO, S. P., NOSE, V., LI, C. & STILES, C. D. 2005. A HIF1alpha regulatory loop links hypoxia and mitochondrial signals in pheochromocytomas. *PLoS Genet,* 1**,** 72-80.

DAMES, S. A., MARTINEZ-YAMOUT, M., DE GUZMAN, R. N., DYSON, H. J. & WRIGHT, P. E. 2002. Structural basis for Hif-1 alpha /CBP recognition in the cellular hypoxic response. *Proc Natl Acad Sci U S A,* 99**,** 5271-6.

DASSO, L. L., BUCKLER, K. J. & VAUGHAN-JONES, R. D. 2000. Interactions between hypoxia and hypercapnic acidosis on calcium signaling in carotid body type I cells. *Am J Physiol Lung Cell Mol Physiol,* 279**,** L36-42.

DE CASTRO, F. 2009a. The discovery of sensory nature of the carotid bodies--invited article. *Adv Exp Med Biol,* 648**,** 1-18.

DE CASTRO, F. 2009b. Towards the sensory nature of the carotid body: hering, de castro and heymansdagger. *Front Neuroanat,* 3**,** 23.

DE KOCK, L. L. 1951. Histology of the carotid body. *Nature,* 167**,** 611-2.

DE KOCK, L. L. 1954. The intra-glomerular tissues of the carotid body. *Acta Anat (Basel),* 21**,** 101-16.

DE NARDI, F., LEFORT, C., BREARD, D., RICHOMME, P., LEGROS, C. & GUERINEAU, N. C. 2017. Monitoring the Secretory Behavior of the Rat Adrenal Medulla by High-Performance Liquid Chromatography-Based Catecholamine Assay from Slice Supernatants. *Front Endocrinol (Lausanne),* 8**,** 248.

DEMIREL, E., ARNOLD, C., GARG, J., JAGER, M. A., STICHT, C., LI, R., KUK, H., WETTSCHURECK, N., HECKER, M. & KORFF, T. 2021. RGS5 Attenuates Baseline Activity of ERK1/2 and Promotes Growth Arrest of Vascular Smooth Muscle Cells. *Cells,* 10.

DEMPSEY, J. A. & FORSTER, H. V. 1982. Mediation of Ventilatory Adaptations. *Physiol Rev,* 62**,** 262-346.

DHILLON, D. P., BARER, G. R. & WALSH, M. 1984. The enlarged carotid body of the chronically hypoxic and chronically hypoxic and hypercapnic rat: a morphometric analysis. *Q J Exp Physiol,* 69**,** 301-17.

DI MARCO, G. S., VIO, C. P., DOS SANTOS, O. F., SCHOR, N. & CASARINI, D. E. 2007. Catecholamine production along the nephron. *Cell Physiol Biochem,* 20**,** 919-24.

DOSSETT, L. A., RUDZINSKI, E. R., BLEVINS, L. S. & CHAMBERS, E. P., JR. 2007. Malignant pheochromocytoma of the organ of Zuckerkandl requiring aortic and vena caval reconstruction. *Endocr Pract,* 13**,** 493-7.

DOUGLAS, C. G., HALDANE, J. S., HENDERSON, Y., SCHNEIDER, E. C., WEBB, G. B. & RICHARDS, J. 1913. Physiological Observations Made on Pike's Peak, Colorado, with Special Reference to Adaptation to Low Barometric Pressures. *Philosophical Transactions of the Royal Society of London. Series B, Containing Papers of a Biological Character,* 203**,** 185-318.

DRUTEL, G., KATHMANN, M., HERON, A., SCHWARTZ, J. C. & ARRANG, J. M. 1996. Cloning and selective expression in brain and kidney of ARNT2 homologous to the Ah receptor nuclear translocator (ARNT). *Biochem Biophys Res Commun,* 225**,** 333-9.

DUCHEN, M. R. & BISCOE, T. J. 1992a. Mitochondrial function in type I cells isolated from rabbit arterial chemoreceptors. *J Physiol,* 450**,** 13-31.

DUCHEN, M. R. & BISCOE, T. J. 1992b. Relative mitochondrial membrane potential and [Ca2+]i in type I cells isolated from the rabbit carotid body. *J Physiol,* 450**,** 33-61.

DUCHEN, M. R., CADDY, K. W., KIRBY, G. C., PATTERSON, D. L., PONTE, J. & BISCOE, T. J. 1988. Biophysical studies of the cellular elements of the rabbit carotid body. *Neuroscience,* 26**,** 291-311.

DUFFIN, J. 2007. Measuring the ventilatory response to hypoxia. *J Physiol,* 584**,** 285-93.

ECKARDT, L., PRANGE-BARCZYNSKA, M., HODSON, E. J., FIELDING, J. W., CHENG, X., LIMA, J., KURLEKAR, S., DOUGLAS, G., RATCLIFFE, P. J. & BISHOP, T. 2021. Developmental role of PHD2 in the pathogenesis of pseudohypoxic pheochromocytoma. *Endocr Relat Cancer,* 28**,** 757-772.

EISENHOFER, G., PACAK, K., HUYNH, T. T., QIN, N., BRATSLAVSKY, G., LINEHAN, W. M., MANNELLI, M., FRIBERG, P., GREBE, S. K., TIMMERS, H. J., BORNSTEIN, S. R. & LENDERS, J. W. 2011. Catecholamine metabolomic and secretory phenotypes in phaeochromocytoma. *Endocr Relat Cancer,* 18**,** 97-111.

ENDO, Y., BALDINO, K., LI, B., ZHANG, Y., SAKTHIVEL, D., MACARTHUR, M., PANAYI, A. C., KIP, P., SPENCER, D. J., JASUJA, R., BAGCHI, D., BHASIN, S., NUUTILA, K., NEPPL, R. L., WAGERS, A. J. & SINHA, I. 2020. Loss of ARNT in skeletal muscle limits muscle regeneration in aging. *FASEB J,* 34**,** 16086-16104.

ENGWALL, M. J. & BISGARD, G. E. 1990. Ventilatory responses to chemoreceptor stimulation after hypoxic acclimatization in awake goats. *J Appl Physiol (1985),* 69**,** 1236-43.

ENSERINK, M. 2019. Hypoxia City. *Science.* https://vis.sciencemag.org/hypoxia-city/.

EPSTEIN, A. C., GLEADLE, J. M., MCNEILL, L. A., HEWITSON, K. S., O'ROURKE, J., MOLE, D. R., MUKHERJI, M., METZEN, E., WILSON, M. I., DHANDA, A., TIAN, Y. M., MASSON, N., HAMILTON, D. L., JAAKKOLA, P., BARSTEAD, R., HODGKIN, J., MAXWELL, P. H., PUGH, C. W., SCHOFIELD, C. J. & RATCLIFFE, P. J. 2001. C. elegans EGL-9 and mammalian homologs define a family of dioxygenases that regulate HIF by prolyl hydroxylation. *Cell,* 107**,** 43-54.

ERBEL, P. J., CARD, P. B., KARAKUZU, O., BRUICK, R. K. & GARDNER, K. H. 2003. Structural basis for PAS domain heterodimerization in the basic helix--

loop--helix-PAS transcription factor hypoxia-inducible factor. *Proc Natl Acad Sci U S A,* 100**,** 15504-9.

EVANS, A. M., MUSTARD, K. J., WYATT, C. N., PEERS, C., DIPP, M., KUMAR, P., KINNEAR, N. P. & HARDIE, D. G. 2005. Does AMP-activated protein kinase couple inhibition of mitochondrial oxidative phosphorylation by hypoxia to calcium signaling in O2-sensing cells? *J Biol Chem,* 280**,** 41504-11.

EYZAGUIRRE, C. & ABUDARA, V. 1999. Carotid body glomus cells: chemical secretion and transmission (modulation?) across cell-nerve ending junctions. *Respir Physiol,* 115**,** 135-49.

FATEMIAN, M. & ROBBINS, P. A. 1998. Effect of 8 hours of isocapnic/poikilocapnic hypoxia on the ventilatory response to CO2. *Adv Exp Med Biol,* 450**,** 17-9.

FAVIER, J., AMAR, L. & GIMENEZ-ROQUEPLO, A. P. 2015. Paraganglioma and phaeochromocytoma: from genetics to personalized medicine. *Nat Rev Endocrinol,* 11**,** 101-11.

FAVIER, J., BRIÈRE, J. J., BURNICHON, N., RIVIÈRE, J., VESCOVO, L., BENIT, P., GISCOS-DOURIEZ, I., DE REYNIÈS, A., BERTHERAT, J., BADOUAL, C., TISSIER, F., AMAR, L., LIBÉ, R., PLOUIN, P. F., JEUNEMAITRE, X., RUSTIN, P. & GIMENEZ-ROQUEPLO, A. P. 2009. The Warburg effect is genetically determined in inherited pheochromocytomas. *PLoS One,* 4**,** e7094.

FAVIER, J., BUFFET, A. & GIMENEZ-ROQUEPLO, A. P. 2012. HIF2A mutations in paraganglioma with polycythemia. *N Engl J Med,* 367**,** 2161; author reply 2161-2.

FAVIER, J., KEMPF, H., CORVOL, P. & GASC, J. M. 1999. Cloning and expression pattern of EPAS1 in the chicken embryo. Colocalization with tyrosine hydroxylase. *FEBS Lett,* 462**,** 19-24.

FAVIER, J., KEMPF, H., CORVOL, P. & GASC, J. M. 2001. Coexpression of endothelial PAS protein 1 with essential angiogenic factors suggests its involvement in human vascular development. *Dev Dyn,* 222**,** 377-88.

FAVIER, J., PLOUIN, P. F., CORVOL, P. & GASC, J. M. 2002. Angiogenesis and vascular architecture in pheochromocytomas: distinctive traits in malignant tumors. *Am J Pathol,* 161**,** 1235-46.

FENG, Z., ZOU, X., CHEN, Y., WANG, H., DUAN, Y. & BRUICK, R. K. 2018. Modulation of HIF-2alpha PAS-B domain contributes to physiological responses. *Proc Natl Acad Sci U S A.*

FIELDING, J. W., HODSON, E. J., CHENG, X., FERGUSON, D. J. P., ECKARDT, L., ADAM, J., LIP, P., MATON-HOWARTH, M., RATNAYAKA, I., PUGH, C. W., BUCKLER, K. J., RATCLIFFE, P. J. & BISHOP, T. 2018. PHD2 inactivation in Type I cells drives HIF-2alpha-dependent multilineage hyperplasia and the formation of paraganglioma-like carotid bodies. *J Physiol*.

FISHBEIN, L., LESHCHINER, I., WALTER, V., DANILOVA, L., ROBERTSON, A. G., JOHNSON, A. R., LICHTENBERG, T. M., MURRAY, B. A., GHAYEE, H. K., ELSE, T., LING, S., JEFFERYS, S. R., DE CUBAS, A. A., WENZ, B., KORPERSHOEK, E., AMELIO, A. L., MAKOWSKI, L., RATHMELL, W. K., GIMENEZ-ROQUEPLO, A. P., GIORDANO, T. J., ASA, S. L., TISCHLER, A. S., CANCER GENOME ATLAS RESEARCH, N., PACAK, K., NATHANSON, K. L. & WILKERSON, M. D. 2017. Comprehensive Molecular Characterization of Pheochromocytoma and Paraganglioma. *Cancer Cell,* 31**,** 181-193.

FISHBEIN, L. & NATHANSON, K. L. 2017. Pheochromocytoma and Paraganglioma Susceptibility Genes: Estimating the Associated Risk of Disease. *JAMA Oncol,* 3**,** 1212-1213.

FISHMAN, M. C., GREENE, W. L. & PLATIKA, D. 1985. Oxygen chemoreception by carotid body cells in culture. *Proc Natl Acad Sci U S A,* 82**,** 1448-50.

FITZGERALD, R. S., EYZAGUIRRE, C. & ZAPATA, P. 2016. Fifty Years of Progress in Carotid Body Physiology – Invited Article. *In:* GONZALEZ, C. (ed.) *Arterial Chemoreceptors.*

FORSTER, H. V., BISGARD, G. E. & KLEIN, J. P. 1981. Effect of peripheral chemoreceptor denervation on acclimatization of goats during hypoxia. *J Appl Physiol Respir Environ Exerc Physiol,* 50**,** 392-8.

FORSTER, H. V., DEMPSEY, J. A., VIDRUK, E. & DO PICO, G. 1974. Evidence of altered regulation of ventilation during exposure to hypoxia. *Respir Physiol,* 20**,** 379-92.

FREEBURG, P. B. & ABRAHAMSON, D. R. 2004. Divergent expression patterns for hypoxia-inducible factor-1beta and aryl hydrocarbon receptor nuclear transporter-2 in developing kidney. *J Am Soc Nephrol,* 15**,** 2569-78.

GALETTA, F., FRANZONI, F., BERNINI, G., POUPAK, F., CARPI, A., CINI, G., TOCCHINI, L., ANTONELLI, A. & SANTORO, G. 2010. Cardiovascular complications in patients with pheochromocytoma: a mini-review. *Biomed Pharmacother,* 64**,** 505-9.

GAO, L., BONILLA-HENAO, V., GARCÍA-FLORES, P., ARIAS-MAYENCO, I., ORTEGA-SÁENZ, P. & LÓPEZ-BARNEO, J. 2017. Gene expression analyses reveal metabolic specifications in acute O2 -sensing chemoreceptor cells. *The Journal of physiology,* 595**,** 6091-6120.

GARCIA-FERNANDEZ, M., MEJIAS, R. & LOPEZ-BARNEO, J. 2007. Developmental changes of chromaffin cell secretory response to hypoxia studied in thin adrenal slices. *Pflugers Arch,* 454**,** 93-100.

GOLDBERG, M. A., GLASS, G. A., CUNNINGHAM, J. M. & BUNN, H. F. 1987. The regulated expression of erythropoietin by two human hepatoma cell lines. *Proc Natl Acad Sci U S A,* 84**,** 7972-6.

GONZALEZ, C., ALMARAZ, L., OBESO, A. & RIGUAL, R. 1994. Carotid body chemoreceptors: from natural stimuli to sensory discharges. *Physiol Rev,* 74**,** 829-98.

GUNAWARDANA, D. M., HEATHCOTE, K. C. & FLASHMAN, E. 2021. Emerging roles for thiol dioxygenases as oxygen sensors. *FEBS J.*

HAASE, V. H. 2010. Hypoxic regulation of erythropoiesis and iron metabolism. *Am J Physiol Renal Physiol,* 299**,** F1-13.

HANEMAAIJER, E. S., MARGARITIS, T., SANDERS, K., BOS, F. L., CANDELLI, T., AL-SAATI, H., VAN NOESEL, M. M., MEYER-WENTRUP, F. A. G., VAN DE WETERING, M., HOLSTEGE, F. C. P. & CLEVERS, H. 2021. Single-cell atlas of developing murine adrenal gland reveals relation of Schwann cell precursor signature to neuroblastoma phenotype. *Proc Natl Acad Sci U S A,* 118.

HAYASHI, M., YAMAJI, Y., KITAJIMA, W. & SARUTA, T. 1990. Aromatic L-amino acid decarboxylase activity along the rat nephron. *Am J Physiol,* 258**,** F28-33.

HEMPLEMAN, S. C. 1996. Increased calcium current in carotid body glomus cells following in vivo acclimatization to chronic hypoxia. *J Neurophysiol,* 76**,** 1880-6.

HEYMANS, C. 1945. *The part played by vascular presso- and chemo-receptors in respiratory control. Nobel Lecture* [Online]. Nobel Prize Outreach AB. Available: https://www.nobelprize.org/prizes/medicine/1938/heymans/lecture/ [Accessed 18th August 2022].

HEYMANS, C. & BOUCKAERT, J. J. 1930. Sinus caroticus and respiratory reflexes: I. Cerebral blood flow and respiration. Adrenaline apnoea. *J Physiol,* 69**,** 254-66.

HICKEY, M. M., LAM, J. C., BEZMAN, N. A., RATHMELL, W. K. & SIMON, M. C. 2007. von Hippel-Lindau mutation in mice recapitulates Chuvash polycythemia via hypoxia-inducible factor-2alpha signaling and splenic erythropoiesis. *J Clin Invest,* 117**,** 3879-89.

HIROSE, K., MORITA, M., EMA, M., MIMURA, J., HAMADA, H., FUJII, H., SAIJO, Y., GOTOH, O., SOGAWA, K. & FUJII-KURIYAMA, Y. 1996. cDNA cloning and tissue-specific expression of a novel basic helix-loop-helix/PAS factor (Arnt2) with close sequence similarity to the aryl hydrocarbon receptor nuclear translocator (Arnt). *Molecular and cellular biology,* 16**,** 1706-13.

HODSON, E. J., NICHOLLS, L. G., TURNER, P. J., LLYR, R., FIELDING, J. W., DOUGLAS, G., RATNAYAKA, I., ROBBINS, P. A., PUGH, C. W., BUCKLER, K. J., RATCLIFFE, P. J. & BISHOP, T. 2016. Regulation of ventilatory sensitivity and carotid body proliferation in hypoxia by the PHD2/HIF-2 pathway. *J Physiol,* 594**,** 1179-95.

HOLMES, A. P., RAY, C. J., CONEY, A. M. & KUMAR, P. 2018. Is Carotid Body Physiological O2 Sensitivity Determined by a Unique Mitochondrial Phenotype? *Front Physiol,* 9**,** 562.

HOWARD, L. S. & ROBBINS, P. A. 1995a. Alterations in respiratory control during 8 h of isocapnic and poikilocapnic hypoxia in humans. *J Appl Physiol (1985),* 78**,** 1098-107.

HOWARD, L. S. & ROBBINS, P. A. 1995b. Ventilatory response to 8 h of isocapnic and poikilocapnic hypoxia in humans. *J Appl Physiol (1985),* 78**,** 1092-7.

HU, C. J., WANG, L. Y., CHODOSH, L. A., KEITH, B. & SIMON, M. C. 2003. Differential Roles of Hypoxia-Inducible Factor 1α (HIF-1α) and HIF-2α in Hypoxic Gene Regulation. *Mol Cell Biol.*

HUTTEMANN, M., KADENBACH, B. & GROSSMAN, L. I. 2001. Mammalian subunit IV isoforms of cytochrome c oxidase. *Gene,* 267**,** 111-23.

ITARANTA, P., VIIRI, K., KAARTINEN, V. & VAINIO, S. 2009. Lumbo-sacral neural crest derivatives fate mapped with the aid of Wnt-1 promoter integrate but are not essential to kidney development. *Differentiation,* 77**,** 199-208.

IYER, N. V., KOTCH, L. E., AGANI, F., LEUNG, S. W., LAUGHNER, E., WENGER, R. H., GASSMANN, M., GEARHART, J. D., LAWLER, A. M., YU, A. Y. & SEMENZA, G. L. 1998. Cellular and developmental control of O2 homeostasis by hypoxia-inducible factor 1 alpha. *Genes Dev,* 12**,** 149-62.

JAIN, S., MALTEPE, E., LU, M. M., SIMON, C. & BRADFIELD, C. A. 1998. Expression of ARNT, ARNT2, HIF1 alpha, HIF2 alpha and Ah receptor mRNAs in the developing mouse. *Mech Dev,* 73**,** 117-23.

JIN, Y., AN, X., YE, Z., CULLY, B., WU, J. & LI, J. 2009. RGS5, a hypoxia-inducible apoptotic stimulator in endothelial cells. *J Biol Chem,* 284**,** 23436-43.

JOCHMANOVA, I. & PACAK, K. 2018. Genomic Landscape of Pheochromocytoma and Paraganglioma. *Trends Cancer,* 4**,** 6-9.

JOSHUA, A. M., EZZAT, S., ASA, S. L., EVANS, A., BROOM, R., FREEMAN, M. & KNOX, J. J. 2009. Rationale and evidence for sunitinib in the treatment of

malignant paraganglioma/pheochromocytoma. *J Clin Endocrinol Metab,* 94**,** 5-9.

KAELIN, W. G., JR. 2008. The von Hippel-Lindau tumour suppressor protein: O2 sensing and cancer. *Nat Rev Cancer,* 8**,** 865-73.

KAMIHARA, J., HAMILTON, K. V., POLLARD, J. A., CLINTON, C. M., MADDEN, J. A., LIN, J., IMAMOVIC, A., WALL, C. B., WASSNER, A. J., WEIL, B. R., HEENEY, M. M., VARGAS, S. O., KAELIN, W. G., JR., JANEWAY, K. A., PERINI, R. F., ZOJWALLA, N. J., VOSS, S. D. & DUBOIS, S. G. 2021. Belzutifan, a Potent HIF2alpha Inhibitor, in the Pacak-Zhuang Syndrome. *N Engl J Med,* 385**,** 2059-2065.

KAPITSINOU, P. P., LIU, Q., UNGER, T. L., RHA, J., DAVIDOFF, O., KEITH, B., EPSTEIN, J. A., MOORES, S. L., ERICKSON-MILLER, C. L. & HAASE, V. H. 2010. Hepatic HIF-2 regulates erythropoietic responses to hypoxia in renal anemia. *Blood,* 116**,** 3039-48.

KARASAWA, N., KONDO, Y. & NAGATSU, I. 1982. Immunohistocytochemical and immunofluorescent localization of catecholamine-synthesizing enzymes in the carotid body of the bat and dog. *Arch Histol Jpn,* 45**,** 429-35.

KASTRITI, M. E., KAMENEVA, P., KAMENEV, D., DYACHUK, V., FURLAN, A., HAMPL, M., MEMIC, F., MARKLUND, U., LALLEMEND, F., HADJAB, S., CALVO-ENRIQUE, L., ERNFORS, P., FRIED, K. & ADAMEYKO, I. 2019. Schwann Cell Precursors Generate the Majority of Chromaffin Cells in Zuckerkandl Organ and Some Sympathetic Neurons in Paraganglia. *Front Mol Neurosci,* 12**,** 6.

KEATING, D. J., RYCHKOV, G. Y. & ROBERTS, M. L. 2001. Oxygen sensitivity in the sheep adrenal medulla: role of SK channels. *Am J Physiol Cell Physiol,* 281**,** C1434-41.

KEITH, B., ADELMAN, D. M. & SIMON, M. C. 2001. Targeted mutation of the murine arylhydrocarbon receptor nuclear translocator 2 (Arnt2) gene reveals partial redundancy with Arnt. *Proceedings of the National Academy of Sciences of the United States of America,* 98**,** 6692-7.

KEITH, B., JOHNSON, R. S. & SIMON, M. C. 2011. HIF1alpha and HIF2alpha: sibling rivalry in hypoxic tumour growth and progression. *Nat Rev Cancer,* 12**,** 9-22.

KEITH, B. & SIMON, M. C. 2007. Hypoxia-inducible factors, stem cells, and cancer. *Cell,* 129**,** 465-72.

KEWLEY, R. J., WHITELAW, M. L. & CHAPMAN-SMITH, A. 2004. The mammalian basic helix–loop–helix/PAS family of transcriptional regulators. *The International Journal of Biochemistry & Cell Biology,* 36**,** 189-204.

KHAMNEI, S. & ROBBINS, P. A. 1990. Hypoxic depression of ventilation in humans: alternative models for the chemoreflexes. *Respir Physiol,* 81**,** 117-34.

KIMPLE, A. J., BOSCH, D. E., GIGUERE, P. M. & SIDEROVSKI, D. P. 2011. Regulators of G-protein signaling and their Galpha substrates: promises and challenges in their use as drug discovery targets. *Pharmacol Rev,* 63**,** 728-49.

KLINE, D. D., PENG, Y. J., MANALO, D. J., SEMENZA, G. L. & PRABHAKAR, N. R. 2002. Defective carotid body function and impaired ventilatory responses to chronic hypoxia in mice partially deficient for hypoxia-inducible factor 1 alpha. *Proc Natl Acad Sci U S A,* 99**,** 821-6.

KLUCKOVA, K. & TENNANT, D. A. 2018. Metabolic implications of hypoxia and pseudohypoxia in pheochromocytoma and paraganglioma. *Cell Tissue Res,* 372**,** 367-378.

KOBAYASHI, S. 1968. Fine structure of the carotid body of the dog. *Arch Histol Jpn,* 30**,** 95-120.

KOBAYASHI, S. & UEHARA, M. 1970. Occurrence of afferent synaptic complexes in the carotid body of the mouse. *Arch Histol Jpn,* 32**,** 193-201.

KOIVUNEN, P., HIRSILA, M., GUNZLER, V., KIVIRIKKO, K. I. & MYLLYHARJU, J. 2004. Catalytic properties of the asparaginyl hydroxylase (FIH) in the oxygen sensing pathway are distinct from those of its prolyl 4-hydroxylases. *J Biol Chem,* 279**,** 9899-904.

KONDO, H., IWANAGA, T. & NAKAJIMA, T. 1982. Immunocytochemical study on the localization of neuron-specific enolase and S-100 protein in the carotid body of rats. *Cell Tissue Res,* 227**,** 291-5.

KOZAK, K. R., ABBOTT, B. & HANKINSON, O. 1997. ARNT-deficient mice and placental differentiation. *Dev Biol,* 191**,** 297-305.

KUMAR, P. & PRABHAKAR, N. R. 2012. Peripheral chemoreceptors: function and plasticity of the carotid body. *Compr Physiol,* 2**,** 141-219.

LAHIRI, S., RUMSEY, W. L., WILSON, D. F. & ITURRIAGA, R. 1993. Contribution of in vivo microvascular PO2 in the cat carotid body chemotransduction. *J Appl Physiol (1985),* 75**,** 1035-43.

LAIDLER, P. & KAY, J. M. 1975. A quantitative morphological study of the carotid bodies of rats living at a simulated altitude of 4300 metres. *J Pathol,* 117**,** 183-91.

LANDO, D., PEET, D. J., GORMAN, J. J., WHELAN, D. A., WHITELAW, M. L. & BRUICK, R. K. 2002. FIH-1 is an asparaginyl hydroxylase enzyme that regulates the transcriptional activity of hypoxia-inducible factor. *Genes Dev,* 16**,** 1466-71.

LAU, S. M., CHA, K. M., KARUNATILLAKE, A., STOKES, R. A., CHENG, K., MCLEAN, M., CHEUNG, N. W., GONZALEZ, F. J. & GUNTON, J. E. 2013. Beta-cell ARNT is required for normal glucose tolerance in murine pregnancy. *PLoS One,* 8**,** e77419.

LAUWERYNS, J. M., COKELAERE, J. & THEUNYNCK, P. 1973. Serotonin producing neuroepithelial bodies in rabbit respiratory mucosa. *Science,* 180**,** 410-3.

LEE, C. K., SUNKIN, S. M., KUAN, C., THOMPSON, C. L., PATHAK, S., NG, L., LAU, C., FISCHER, S., MORTRUD, M., SLAUGHTERBECK, C., JONES, A., LEIN, E. & HAWRYLYCZ, M. 2008. Quantitative methods for genome-scale analysis of in situ hybridization and correlation with microarray data. *Genome Biol,* 9**,** R23.

LEE, M. J., TASAKI, T., MOROI, K., AN, J. Y., KIMURA, S., DAVYDOV, I. V. & KWON, Y. T. 2005. RGS4 and RGS5 are in vivo substrates of the N-end rule pathway. *Proc Natl Acad Sci U S A,* 102**,** 15030-5.

LENDAHL, U., LEE, K. L., YANG, H. & POELLINGER, L. 2009. Generating specificity and diversity in the transcriptional response to hypoxia. *Nat Rev Genet,* 10**,** 821-32.

LENDERS, J. W., EISENHOFER, G., MANNELLI, M. & PACAK, K. 2005. Phaeochromocytoma. *Lancet,* 366**,** 665-75.

LEPOUTRE-LUSSEY, C., THIBAULT, C., BUFFET, A., MORIN, A., BADOUAL, C., BENIT, P., RUSTIN, P., OTTOLENGHI, C., JANIN, M., CASTRO-VEGA, L. J., TRAPMAN, J., GIMENEZ-ROQUEPLO, A. P. & FAVIER, J. 2016. From Nf1 to Sdhb knockout: Successes and failures in the quest for animal models of pheochromocytoma. *Mol Cell Endocrinol,* 421**,** 40-8.

LETOUZE, E., MARTINELLI, C., LORIOT, C., BURNICHON, N., ABERMIL, N., OTTOLENGHI, C., JANIN, M., MENARA, M., NGUYEN, A. T., BENIT, P., BUFFET, A., MARCAILLOU, C., BERTHERAT, J., AMAR, L., RUSTIN, P., DE REYNIES, A., GIMENEZ-ROQUEPLO, A. P. & FAVIER, J. 2013. SDH mutations establish a hypermethylator phenotype in paraganglioma. *Cancer Cell,* 23**,** 739-52.

LEVER, J. D. & BOYD, J. D. 1957. Osmiophile granules in the glomus cells of the rabbit carotid body. *Nature,* 179**,** 1082-3.

LEVITSKY, K. L. & LOPEZ-BARNEO, J. 2009. Developmental change of T-type Ca2+ channel expression and its role in rat chromaffin cell responsiveness to acute hypoxia. *J Physiol,* 587**,** 1917-29.

LEWIS, A., HARTNESS, M. E., CHAPMAN, C. G., FEARON, I. M., MEADOWS, H. J., PEERS, C. & KEMP, P. J. 2001. Recombinant hTASK1 is an O(2)-sensitive K(+) channel. *Biochem Biophys Res Commun,* 285**,** 1290-4.

LIM, R., ZAVOU, M. J., MILTON, P. L., CHAN, S. T., TAN, J. L., DICKINSON, H., MURPHY, S. V., JENKIN, G. & WALLACE, E. M. 2014. Measuring Respiratory Function in Mice Using Unrestrained Whole-body Plethysmography. *J Vis Exp*.

LINDEBERG, J., USOSKIN, D., BENGTSSON, H., GUSTAFSSON, A., KYLBERG, A., SODERSTROM, S. & EBENDAL, T. 2004. Transgenic expression of Cre recombinase from the tyrosine hydroxylase locus. *Genesis,* 40**,** 67-73.

LIVAK, K. J. & SCHMITTGEN, T. D. 2001. Analysis of relative gene expression data using real-time quantitative PCR and the 2(-Delta Delta C(T)) Method. *Methods,* 25**,** 402-8.

LOPEZ-BARNEO, J., LOPEZ-LOPEZ, J. R., URENA, J. & GONZALEZ, C. 1988. Chemotransduction in the carotid body: K+ current modulated by PO2 in type I chemoreceptor cells. *Science,* 241**,** 580-2.

LOPEZ-BARNEO, J., PARDAL, R. & ORTEGA-SAENZ, P. 2001. Cellular mechanism of oxygen sensing. *Annu Rev Physiol,* 63**,** 259-87.

LOPEZ-LOPEZ, J., GONZALEZ, C., URENA, J. & LOPEZ-BARNEO, J. 1989. Low pO2 selectively inhibits K channel activity in chemoreceptor cells of the mammalian carotid body. *J Gen Physiol,* 93**,** 1001-15.

LOPEZ-LOPEZ, J. R., PEREZ-GARCIA, M. T., CANET, E. & GONZALEZ, C. 1998. Effects of almitrine bismesylate on the ionic currents of chemoreceptor cells from the carotid body. *Mol Pharmacol,* 53**,** 330-9.

LORENZO, F. R., YANG, C., NG TANG FUI, M., VANKAYALAPATI, H., ZHUANG, Z., HUYNH, T., GROSSMANN, M., PACAK, K. & PRCHAL, J. T. 2013. A novel EPAS1/HIF2A germline mutation in a congenital polycythemia with paraganglioma. *J Mol Med (Berl),* 91**,** 507-12.

LUSSEY-LEPOUTRE, C., BUFFET, A., MORIN, A., GONCALVES, J. & FAVIER, J. 2018. Rodent models of pheochromocytoma, parallels in rodent and human tumorigenesis. *Cell Tissue Res,* 372**,** 379-392.

MACIAS, D., COWBURN, A. S., TORRES-TORRELO, H., ORTEGA-SAENZ, P., LOPEZ-BARNEO, J. & JOHNSON, R. S. 2018. HIF-2alpha is essential for carotid body development and function. *Elife,* 7.

MACIAS, D., FERNANDEZ-AGUERA, M. C., BONILLA-HENAO, V. & LOPEZ-BARNEO, J. 2014. Deletion of the von Hippel-Lindau gene causes sympathoadrenal cell death and impairs chemoreceptor-mediated adaptation to hypoxia. *EMBO Mol Med,* 6**,** 1577-92.

MADISEN, L., GARNER, A. R., SHIMAOKA, D., CHUONG, A. S., KLAPOETKE, N. C., LI, L., VAN DER BOURG, A., NIINO, Y., EGOLF, L., MONETTI, C., GU, H., MILLS, M., CHENG, A., TASIC, B., NGUYEN, T. N., SUNKIN, S. M., BENUCCI, A., NAGY, A., MIYAWAKI, A., HELMCHEN, F., EMPSON, R. M., KNOPFEL, T., BOYDEN, E. S., REID, R. C., CARANDINI, M. & ZENG, H. 2015. Transgenic mice for intersectional targeting of neural sensors and effectors with high specificity and performance. *Neuron,* 85**,** 942-58.

MAHFOUDI, A., ROULET, E., DAUVOIS, S., PARKER, M. G. & WAHLI, W. 1995. Specific mutations in the estrogen receptor change the properties of antiestrogens to full agonists. *Proc Natl Acad Sci U S A,* 92**,** 4206-10.

MALTEPE, E., KEITH, B., ARSHAM, A. M., BRORSON, J. R. & SIMON, M. C. 2000. The role of ARNT2 in tumor angiogenesis and the neural response to hypoxia. *Biochem Biophys Res Commun,* 273**,** 231-8.

MALTEPE, E., SCHMIDT, J. V., BAUNOCH, D., BRADFIELD, C. A. & SIMON, M. C. 1997. Abnormal angiogenesis and responses to glucose and oxygen deprivation in mice lacking the protein ARNT. *Nature,* 386**,** 403-7.

MARTINELLI, S., MAGGI, M. & RAPIZZI, E. 2020. Pheochromocytoma/paraganglioma preclinical models: which to use and why? *Endocr Connect,* 9**,** R251-R260.

MASSON, N., KEELEY, T. P., GIUNTOLI, B., WHITE, M. D., PUERTA, M. L., PERATA, P., HOPKINSON, R. J., FLASHMAN, E., LICAUSI, F. & RATCLIFFE, P. J. 2019. Conserved N-terminal cysteine dioxygenases transduce responses to hypoxia in animals and plants. *Science,* 365**,** 65-69.

MASUHO, I., BALAJI, S., MUNTEAN, B. S., SKAMANGAS, N. K., CHAVALI, S., TESMER, J. J. G., BABU, M. M. & MARTEMYANOV, K. A. 2020. A Global Map of G Protein Signaling Regulation by RGS Proteins. *Cell,* 183**,** 503-521 e19.

MAXWELL, P. H., OSMOND, M. K., PUGH, C. W., HERYET, A., NICHOLLS, L. G., TAN, C. C., DOE, B. G., FERGUSON, D. J., JOHNSON, M. H. & RATCLIFFE, P. J. 1993. Identification of the renal erythropoietin-producing cells using transgenic mice. *Kidney Int,* 44**,** 1149-62.

MAXWELL, P. H., WIESENER, M. S., CHANG, G. W., CLIFFORD, S. C., VAUX, E. C., COCKMAN, M. E., WYKOFF, C. C., PUGH, C. W., MAHER, E. R. & RATCLIFFE, P. J. 1999. The tumour suppressor protein VHL targets hypoxia-inducible factors for oxygen-dependent proteolysis. *Nature,* 399**,** 271-5.

MAZZONE, M., DETTORI, D., DE OLIVEIRA, R. L., LOGES, S., SCHMIDT, T., JONCKX, B., TIAN, Y. M., LANAHAN, A. A., POLLARD, P., DE ALMODOVAR, C. R., DE SMET, F., VINCKIER, S., ARAGONES, J., DEBACKERE, K., LUTTUN, A., WYNS, S., JORDAN, B., PISACANE, A., GALLEZ, B., LAMPUGNANI, M. G., DEJANA, E., SIMONS, M., RATCLIFFE, P., MAXWELL, P. & CARMELIET, P. 2009. Heterozygous deficiency of PHD2 restores tumor oxygenation and inhibits metastasis via endothelial normalization. *Cell,* 136**,** 839-851.

MEDCHEMEXPRESS. 2019. *PT2399* [Online]. Available: https://www.medchemexpress.com/pt2399.html [Accessed 27th May 2020].

MESA-CILLER, C., TURIEL, G., GUAJARDO-GRENCE, A., LOPEZ-RODRIGUEZ, A. B., EGEA, J., DE BOCK, K., ARAGONES, J. & URRUTIA, A. A. 2022. Unique expression of the atypical mitochondrial subunit NDUFA4L2 in cerebral pericytes fine tunes HIF activity in response to hypoxia. *J Cereb Blood Flow Metab***,** 271678X221118236.

MILLS, D. B., FRANCIS, W. R., VARGAS, S., LARSEN, M., ELEMANS, C. P., CANFIELD, D. E. & WORHEIDE, G. 2018. The last common ancestor of animals lacked the HIF pathway and respired in low-oxygen environments. *Elife,* 7.

MILLS, E. & JOBSIS, F. F. 1972. Mitochondrial respiratory chain of carotid body and chemoreceptor response to changes in oxygen tension. *J Neurophysiol,* 35**,** 405-28.

MILSOM, W. K. & BURLESON, M. L. 2007. Peripheral arterial chemoreceptors and the evolution of the carotid body. *Respir Physiol Neurobiol,* 157**,** 4-11.

MOHAWK, J. A., GREEN, C. B. & TAKAHASHI, J. S. 2012. Central and peripheral circadian clocks in mammals. *Annu Rev Neurosci,* 35**,** 445-62.

MOJET, M. H., MILLS, E. & DUCHEN, M. R. 1997. Hypoxia-induced catecholamine secretion in isolated newborn rat adrenal chromaffin cells is mimicked by inhibition of mitochondrial respiration. *J Physiol,* 504 (Pt 1)**,** 175-89.

MOLE, D. R., BLANCHER, C., COPLEY, R. R., POLLARD, P. J., GLEADLE, J. M., RAGOUSSIS, J. & RATCLIFFE, P. J. 2009. Genome-wide association of hypoxia-inducible factor (HIF)-1alpha and HIF-2alpha DNA binding with expression profiling of hypoxia-inducible transcripts. *J Biol Chem,* 284**,** 16767-16775.

MONTEIRO, E. C. & RIBEIRO, J. A. 1987. Ventilatory effects of adenosine mediated by carotid body chemoreceptors in the rat. *Naunyn Schmiedebergs Arch Pharmacol,* 335**,** 143-8.

MONTORO, R. J., URENA, J., FERNANDEZ-CHACON, R., ALVAREZ DE TOLEDO, G. & LOPEZ-BARNEO, J. 1996. Oxygen sensing by ion channels and chemotransduction in single glomus cells. *J Gen Physiol,* 107**,** 133-143.

MOOG, S., LUSSEY-LEPOUTRE, C. & FAVIER, J. 2020. Epigenetic and metabolic reprogramming of SDH-deficient paragangliomas. *Endocr Relat Cancer,* 27**,** R451-R463.

MORENO-DOMINGUEZ, A., ORTEGA-SAENZ, P., GAO, L., COLINAS, O., GARCIA-FLORES, P., BONILLA-HENAO, V., ARAGONES, J., HUTTEMANN, M., GROSSMAN, L. I., WEISSMANN, N., SOMMER, N. & LOPEZ-BARNEO, J. 2019. Acute O2 sensing through HIF2alpha-dependent expression of atypical cytochrome oxidase subunits in arterial chemoreceptors. *Sci Signal*.

MOVERARE-SKRTIC, S., BORJESSON, A. E., FARMAN, H. H., SJOGREN, K., WINDAHL, S. H., LAGERQUIST, M. K., ANDERSSON, A., STUBELIUS, A., CARLSTEN, H., GUSTAFSSON, J. A. & OHLSSON, C. 2014. The estrogen receptor antagonist ICI 182,780 can act both as an agonist and an inverse agonist when estrogen receptor alpha AF-2 is modified. *Proc Natl Acad Sci U S A,* 111**,** 1180-5.

MUNOZ-CABELLO, A. M., TOLEDO-ARAL, J. J., LOPEZ-BARNEO, J. & ECHEVARRIA, M. 2005. Rat adrenal chromaffin cells are neonatal CO2 sensors. *J Neurosci,* 25**,** 6631-40.

MURRAY, T. R., CHEN, L., MARSHALL, B. E. & MACARAK, E. J. 1990. Hypoxic contraction of cultured pulmonary vascular smooth muscle cells. *Am J Respir Cell Mol Biol,* 3**,** 457-65.

NIELSEN, A. M., BISGARD, G. E. & VIDRUK, E. H. 1988. Carotid chemoreceptor activity during acute and sustained hypoxia in goats. *J Appl Physiol (1985),* 65**,** 1796-802.

NISANCIOGLU, M. H., MAHONEY, W. M., JR., KIMMEL, D. D., SCHWARTZ, S. M., BETSHOLTZ, C. & GENOVE, G. 2008. Generation and characterization of rgs5 mutant mice. *Mol Cell Biol,* 28**,** 2324-31.

NOBELPRIZE.ORG, N. P. O. *Corneille Heymans – Facts* [Online]. Available: https://www.nobelprize.org/prizes/medicine/1938/heymans/facts/ [Accessed 18/08/2022 2022].

NURSE, C. A. 2005. Neurotransmission and neuromodulation in the chemosensory carotid body. *Auton Neurosci,* 120**,** 1-9.

NURSE, C. A., BUTTIGIEG, J., BROWN, S. & HOLLOWAY, A. C. 2009. Regulation of oxygen sensitivity in adrenal chromaffin cells. *Ann N Y Acad Sci,* 1177**,** 132-9.

NURSE, C. A. & FEARON, I. M. 2002. Carotid body chemoreceptors in dissociated cell culture. *Microsc Res Tech,* 59**,** 249-55.

O'DONOHOE, P. B., HUSKENS, N., TURNER, P. J., PANDIT, J. J. & BUCKLER, K. J. 2018. A1899, PK-THPP, ML365, and Doxapram inhibit endogenous TASK channels and excite calcium signaling in carotid body type-1 cells. *Physiol Rep,* 6**,** e13876.

O'KANE, G. M., EZZAT, S., JOSHUA, A. M., BOURDEAU, I., LEIBOWITZ-AMIT, R., OLNEY, H. J., KRZYZANOWSKA, M., REUTHER, D., CHIN, S., WANG, L., BROOKS, K., HANSEN, A. R., ASA, S. L. & KNOX, J. J. 2019. A phase 2 trial of sunitinib in patients with progressive paraganglioma or pheochromocytoma: the SNIPP trial. *Br J Cancer,* 120**,** 1113-1119.

OBARA, N., SUZUKI, N., KIM, K., NAGASAWA, T., IMAGAWA, S. & YAMAMOTO, M. 2008. Repression via the GATA box is essential for tissue-specific erythropoietin gene expression. *Blood,* 111**,** 5223-32.

OLECHNOWICZ, S. W., FEDELE, A. O. & PEET, D. J. 2012. Hypoxic induction of the regulator of G-protein signalling 4 gene is mediated by the hypoxia-inducible factor pathway. *PLoS One,* 7**,** e44564.

ORTEGA-SAENZ, P., LEVITSKY, K. L., MARCOS-ALMARAZ, M. T., BONILLA-HENAO, V., PASCUAL, A. & LOPEZ-BARNEO, J. 2010. Carotid body chemosensory responses in mice deficient of TASK channels. *J Gen Physiol,* 135**,** 379-92.

PACAK, K., JOCHMANOVA, I., PRODANOV, T., YANG, C., MERINO, M. J., FOJO, T., PRCHAL, J. T., TISCHLER, A. S., LECHAN, R. M. & ZHUANG, Z. 2013. New syndrome of paraganglioma and somatostatinoma associated with polycythemia. *J Clin Oncol,* 31**,** 1690-8.

PAJUELO REGUERA, D., CUNATOVA, K., VRBACKY, M., PECINOVA, A., HOUSTEK, J., MRACEK, T. & PECINA, P. 2020. Cytochrome c Oxidase Subunit 4 Isoform Exchange Results in Modulation of Oxygen Affinity. *Cells,* 9.

PALIEGE, A., ROSENBERGER, C., BONDKE, A., SCIESIELSKI, L., SHINA, A., HEYMAN, S. N., FLIPPIN, L. A., AREND, M., KLAUS, S. J. & BACHMANN, S. 2010. Hypoxia-inducible factor-2alpha-expressing interstitial fibroblasts are the only renal cells that express erythropoietin under hypoxia-inducible factor stabilization. *Kidney Int,* 77**,** 312-8.

PAMENTER, M. E. & POWELL, F. L. 2016. Time Domains of the Hypoxic Ventilatory Response and Their Molecular Basis. *Compr Physiol,* 6**,** 1345-85.

PAN, W., GODOY, R. S., COOK, D. P., SCOTT, A. L., NURSE, C. A. & JONZ, M. G. 2022. Single-cell transcriptomic analysis of neuroepithelial cells and other cell types of the gills of zebrafish (Danio rerio) exposed to hypoxia. *Sci Rep,* 12**,** 10144.

PANG, P., JIN, X., PROCTOR, B. M., FARLEY, M., ROY, N., CHIN, M. S., VON ANDRIAN, U. H., VOLLMANN, E., PERRO, M., HOFFMAN, R. J., CHUNG, J., CHAUHAN, N., MISTRI, M., MUSLIN, A. J., BONVENTRE, J. V. & SIEDLECKI, A. M. 2015. RGS4 inhibits angiotensin II signaling and macrophage localization during renal reperfusion injury independent of vasospasm. *Kidney Int,* 87**,** 771-83.

PAPADOPOULOS, K. P., JONASCH, E., ZOJWALLA, N. J., WANG, K. & BAUER, T. M. 2018. A first-in-human phase 1 dose-escalation trial of the oral HIF-2a inhibitor PT2977 in patients with advanced solid tumors. *https://doi.org/10.1200/JCO.2018.36.15_suppl.2508*.

PARDAL, R. & LOPEZ-BARNEO, J. 2002. Carotid body thin slices: responses of glomus cells to hypoxia and K(+)-channel blockers. *Respir Physiol Neurobiol,* 132**,** 69-79.

PARDAL, R., ORTEGA-SÁENZ, P., DURÁN, R. & LÓPEZ-BARNEO, J. 2007. Glia-like stem cells sustain physiologic neurogenesis in the adult mammalian carotid body. *Cell,* 131**,** 364-77.

PATEL, S. A. & SIMON, M. C. 2008. Biology of hypoxia-inducible factor-2alpha in development and disease. *Cell Death Differ,* 15**,** 628-34.

PEARSE, A. G., POLAK, J. M., ROST, F. W., FONTAINE, J., LE LIEVRE, C. & LE DOUARIN, N. 1973. Demonstration of the neural crest origin of type I (APUD) cells in the avian carotid body, using a cytochemical marker system. *Histochemie,* 34**,** 191-203.

PEERS, C. 1990. Hypoxic suppression of K+ currents in type I carotid body cells: selective effect on the Ca2(+)-activated K+ current. *Neurosci Lett,* 119**,** 253-6.

PEERS, C. & BUCKLER, K. J. 1995. Transduction of chemostimuli by the type I carotid body cell. *J Membr Biol,* 144**,** 1-9.

PENG, J., ZHANG, L., DRYSDALE, L. & FONG, G. H. 2000. The transcription factor EPAS-1/hypoxia-inducible factor 2alpha plays an important role in vascular remodeling. *Proc Natl Acad Sci U S A,* 97**,** 8386-91.

PENG, Y. J., GRIDINA, A., WANG, B., NANDURI, J., FOX, A. P. & PRABHAKAR, N. R. 2020. Olfactory receptor 78 participates in carotid body response to a wide range of low O2 levels but not severe hypoxia. *J Neurophysiol,* 123**,** 1886-1895.

PENG, Y. J., NANDURI, J., KHAN, S. A., YUAN, G., WANG, N., KINSMAN, B., VADDI, D. R., KUMAR, G. K., GARCIA, J. A., SEMENZA, G. L. & PRABHAKAR, N. R. 2011. Hypoxia-inducible factor 2alpha (HIF-2alpha) heterozygous-null mice exhibit exaggerated carotid body sensitivity to hypoxia, breathing instability, and hypertension. *Proc Natl Acad Sci U S A,* 108**,** 3065-70.

PENG, Y. J., OVERHOLT, J. L., KLINE, D., KUMAR, G. K. & PRABHAKAR, N. R. 2003. Induction of sensory long-term facilitation in the carotid body by intermittent hypoxia: implications for recurrent apneas. *Proc Natl Acad Sci U S A,* 100**,** 10073-8.

PEQUIGNOT, J. M., HELLSTROM, S. & JOHANSSON, C. 1984. Intact and sympathectomized carotid bodies of long-term hypoxic rats: a morphometric ultrastructural study. *J Neurocytol,* 13**,** 481-93.

PEREZ-GARCIA, M. T., COLINAS, O., MIGUEL-VELADO, E., MORENO-DOMINGUEZ, A. & LOPEZ-LOPEZ, J. R. 2004. Characterization of the Kv channels of mouse carotid body chemoreceptor cells and their role in oxygen sensing. *J Physiol,* 557**,** 457-71.

PERSSON, C. U., VON STEDINGK, K., FREDLUND, E., BEXELL, D., PAHLMAN, S., WIGERUP, C. & MOHLIN, S. 2020. ARNT-dependent HIF-2

transcriptional activity is not sufficient to regulate downstream target genes in neuroblastoma. *Exp Cell Res,* 388**,** 111845.

PILLMAN, S. 2018. *Hypoxico Altitude to Oxygen Chart* [Online]. https://hypoxico.com/altitude-to-oxygen-chart/. [Accessed 23/04/2020 2020].

POLLARD, P. J., EL-BAHRAWY, M., POULSOM, R., ELIA, G., KILLICK, P., KELLY, G., HUNT, T., JEFFERY, R., SEEDHAR, P., BARWELL, J., LATIF, F., GLEESON, M. J., HODGSON, S. V., STAMP, G. W., TOMLINSON, I. P. & MAHER, E. R. 2006. Expression of HIF-1alpha, HIF-2alpha (EPAS1), and their target genes in paraganglioma and pheochromocytoma with VHL and SDH mutations. *J Clin Endocrinol Metab,* 91**,** 4593-8.

POWELL, F. L. 2007. The influence of chronic hypoxia upon chemoreception. *Respir Physiol Neurobiol,* 157**,** 154-61.

POWELL, F. L., MILSOM, W. K. & MITCHELL, G. S. 1998. Time domains of the hypoxic ventilatory response. *Respir Physiol,* 112**,** 123-34.

PRABHAKAR, N. R. 2016. Chapter 18 - O2 and CO2 Detection by the Carotid and Aortic Bodies. *In:* FRANK ZUFALL, S. D. M. (ed.) *Chemosensory Transduction.* Academic Press.

PRABHAKAR, N. R., PENG, Y.-J., KUMAR, G., NANDURI, J., DI GIULIO, C. & LAHIRI, S. 2009. Long-Term Regulation of Carotid Body Function: Acclimatization and Adaptation– Invited Article. *In:* GONZALEZ, C. (ed.) *Arterial Chemoreceptors.* Advances in Experimental Medicine and Biology.

RANKIN, E. B., BIJU, M. P., LIU, Q., UNGER, T. L., RHA, J., JOHNSON, R. S., SIMON, M. C., KEITH, B. & HAASE, V. H. 2007. Hypoxia-inducible factor-2 (HIF-2) regulates hepatic erythropoietin in vivo. *J Clin Invest,* 117**,** 1068-77.

RANKIN, E. B., HIGGINS, D. F., WALISSER, J. A., JOHNSON, R. S., BRADFIELD, C. A. & HAASE, V. H. 2005. Inactivation of the arylhydrocarbon receptor nuclear translocator (Arnt) suppresses von Hippel-Lindau disease-associated vascular tumors in mice. *Mol Cell Biol,* 25**,** 3163-72.

RATCLIFFE, P. J. 2007. HIF-1 and HIF-2: working alone or together in hypoxia? *J Clin Invest,* 117**,** 862-5.

RATCLIFFE, P. J. 2013. Oxygen sensing and hypoxia signalling pathways in animals: the implications of physiology for cancer. *J Physiol,* 591**,** 2027-42.

RICO, A. J., PRIETO-LLORET, J., GONZALEZ, C. & RIGUAL, R. 2005. Hypoxia and acidosis increase the secretion of catecholamines in the neonatal rat adrenal medulla: an in vitro study. *Am J Physiol Cell Physiol,* 289**,** C1417-25.

ROBBINS, P. A. 2007. Role of the peripheral chemoreflex in the early stages of ventilatory acclimatization to altitude. *Respir Physiol Neurobiol,* 158**,** 237-42.

ROGERS, J. L., BAYEH, L., SCHEUERMANN, T. H., LONGGOOD, J., KEY, J., NAIDOO, J., MELITO, L., SHOKRI, C., FRANTZ, D. E., BRUICK, R. K., GARDNER, K. H., MACMILLAN, J. B. & TAMBAR, U. K. 2013. Development of inhibitors of the PAS-B domain of the HIF-2alpha transcription factor. *J Med Chem,* 56**,** 1739-47.

ROSENBERGER, C., MANDRIOTA, S., JURGENSEN, J. S., WIESENER, M. S., HORSTRUP, J. H., FREI, U., RATCLIFFE, P. J., MAXWELL, P. H., BACHMANN, S. & ECKARDT, K. U. 2002. Expression of hypoxia-inducible factor-1alpha and -2alpha in hypoxic and ischemic rat kidneys. *J Am Soc Nephrol,* 13**,** 1721-32.

RYTKONEN, K. T., WILLIAMS, T. A., RENSHAW, G. M., PRIMMER, C. R. & NIKINMAA, M. 2011. Molecular evolution of the metazoan PHD-HIF oxygen-sensing system. *Mol Biol Evol,* 28**,** 1913-26.

SAPRU, H. N. & KRIEGER, A. J. 1977. Carotid and aortic chemoreceptor function in the rat. *J Appl Physiol Respir Environ Exerc Physiol,* 42**,** 344-8.

SATO, M., SEVERINGHAUS, J. W., POWELL, F. L., XU, F. D. & SPELLMAN, M. J., JR. 1992. Augmented hypoxic ventilatory response in men at altitude. *J Appl Physiol (1985),* 73**,** 101-7.

SCHEUERMANN, T. H., LI, Q., MA, H. W., KEY, J., ZHANG, L., CHEN, R., GARCIA, J. A., NAIDOO, J., LONGGOOD, J., FRANTZ, D. E., TAMBAR, U. K., GARDNER, K. H. & BRUICK, R. K. 2013. Allosteric inhibition of hypoxia inducible factor-2 with small molecules. *Nat Chem Biol,* 9**,** 271-6.

SCHEUERMANN, T. H., TOMCHICK, D. R., MACHIUS, M., GUO, Y., BRUICK, R. K. & GARDNER, K. H. 2009. Artificial ligand binding within the HIF2α PAS-B domain of the HIF2 transcription factor. *Proc Natl Acad Sci U S A.*

SCHOBER, A., PARLATO, R., HUBER, K., KINSCHERF, R., HARTLEBEN, B., HUBER, T. B., SCHUTZ, G. & UNSICKER, K. 2013. Cell loss and autophagy in the extra-adrenal chromaffin organ of Zuckerkandl are regulated by glucocorticoid signalling. *J Neuroendocrinol,* 25**,** 34-47.

SCHOFIELD, C. J. & RATCLIFFE, P. J. 2004. Oxygen sensing by HIF hydroxylases. *Nat Rev Mol Cell Biol,* 5**,** 343-54.

SCORTEGAGNA, M., DING, K., OKTAY, Y., GAUR, A., THURMOND, F., YAN, L. J., MARCK, B. T., MATSUMOTO, A. M., SHELTON, J. M., RICHARDSON, J. A., BENNETT, M. J. & GARCIA, J. A. 2003. Multiple organ pathology, metabolic abnormalities and impaired homeostasis of reactive oxygen species in Epas1-/- mice. *Nat Genet,* 35**,** 331-40.

SCOTT, C., BONNER, J., MIN, D., BOUGHTON, P., STOKES, R., CHA, K. M., WALTERS, S. N., MASLOWSKI, K., SIERRO, F., GREY, S. T., TWIGG, S., MCLENNAN, S. & GUNTON, J. E. 2014. Reduction of ARNT in myeloid cells causes immune suppression and delayed wound healing. *Am J Physiol Cell Physiol,* 307**,** C349-57.

SCOTT, C., CHA, K., RAO, R., LIDDLE, C., GEORGE, J. & GUNTON, J. E. 2015. Hepatocyte-specific deletion of ARNT (aryl hydrocarbon Receptor Nuclear Translocator) results in altered fibrotic gene expression in the thioacetamide model of liver injury. *PLoS One,* 10**,** e0121650.

SEIDLER, F. J. & SLOTKIN, T. A. 1985. Adrenomedullary function in the neonatal rat: responses to acute hypoxia. *J Physiol,* 358**,** 1-16.

SEIDLER, F. J. & SLOTKIN, T. A. 1986. Ontogeny of adrenomedullary responses to hypoxia and hypoglycemia: role of splanchnic innervation. *Brain Res Bull,* 16**,** 11-4.

SEMENZA, G. L., NEJFELT, M. K., CHI, S. M. & ANTONARAKIS, S. E. 1991. Hypoxia-inducible nuclear factors bind to an enhancer element located 3' to the human erythropoietin gene. *Proc Natl Acad Sci U S A,* 88**,** 5680-4.

SKARNES, W. C., ROSEN, B., WEST, A. P., KOUTSOURAKIS, M., BUSHELL, W., IYER, V., MUJICA, A. O., THOMAS, M., HARROW, J., COX, T., JACKSON, D., SEVERIN, J., BIGGS, P., FU, J., NEFEDOV, M., DE JONG, P. J., STEWART, A. F. & BRADLEY, A. 2011. A conditional knockout resource for the genome-wide study of mouse gene function. *Nature,* 474**,** 337-42.

SLINGO, M. E., TURNER, P. J., CHRISTIAN, H. C., BUCKLER, K. J. & ROBBINS, P. A. 2014. The von Hippel-Lindau Chuvash mutation in mice causes carotid-body hyperplasia and enhanced ventilatory sensitivity to hypoxia. *J Appl Physiol (1985),* 116**,** 885-92.

SMITH, C. A., BISGARD, G. E., NIELSEN, A. M., DARISTOTLE, L., KRESSIN, N. A., FORSTER, H. V. & DEMPSEY, J. A. 1986. Carotid bodies are required for ventilatory acclimatization to chronic hypoxia. *J Appl Physiol (1985),* 60**,** 1003-10.

SMITH, T. G., BROOKS, J. T., BALANOS, G. M., LAPPIN, T. R., LAYTON, D. M., LEEDHAM, D. L., LIU, C., MAXWELL, P. H., MCMULLIN, M. F., MCNAMARA, C. J., PERCY, M. J., PUGH, C. W., RATCLIFFE, P. J., TALBOT, N. P., TREACY, M. & ROBBINS, P. A. 2006. Mutation of von Hippel-Lindau tumour suppressor and human cardiopulmonary physiology. *PLoS Med,* 3**,** e290.

SOMMER, N., HUTTEMANN, M., PAK, O., SCHEIBE, S., KNOEPP, F., SINKLER, C., MALCZYK, M., GIERHARDT, M., ESFANDIARY, A., KRAUT, S., JONAS, F., VEITH, C., ARAS, S., SYDYKOV, A., ALEBRAHIMDEHKORDI, N., GIEHL, K., HECKER, M., BRANDES, R. P., SEEGER, W., GRIMMINGER, F., GHOFRANI, H. A., SCHERMULY, R. T., GROSSMAN, L. I. & WEISSMANN, N. 2017. Mitochondrial Complex IV Subunit 4 Isoform 2 Is Essential for Acute Pulmonary Oxygen Sensing. *Circ Res,* 121**,** 424-438.

STEA, A. & NURSE, C. A. 1991. Whole-cell and perforated-patch recordings from O2-sensitive rat carotid body cells grown in short- and long-term culture. *Pflugers Arch,* 418**,** 93-101.

STEBBINS, C. E., KAELIN, W. G., JR. & PAVLETICH, N. P. 1999. Structure of the VHL-ElonginC-ElonginB complex: implications for VHL tumor suppressor function. *Science,* 284**,** 455-61.

STROWD, R. E., ELLINGSON, B. M., WEN, P. Y., AHLUWALIA, M. S., PIOTROWSKI, A. F., DESAI, A. S., CLARKE, J. L., LIEBERMAN, F. S., DESIDERI, S., NABORS, L. B., YE, X. & GROSSMAN, S. A. 2019. Safety and activity of a first-in-class oral HIF2-alpha inhibitor, PT2385, in patients with first recurrent glioblastoma (GBM). *https://doi.org/10.1200/JCO.2019.37.15_suppl.2027*.

SUBRAMANIAN, A. & MAKER, V. K. 2006. Organs of Zuckerkandl: their surgical significance and a review of a century of literature. *Am J Surg,* 192**,** 224-34.

SULLIVAN, L. B., GUI, D. Y. & VANDER HEIDEN, M. G. 2016. Altered metabolite levels in cancer: implications for tumour biology and cancer therapy. *Nat Rev Cancer,* 16**,** 680-693.

SUYAMA, K., SILAGI, E. S., CHOI, H., SAKABE, K., MOCHIDA, J., SHAPIRO, I. M. & RISBUD, M. V. 2016. Circadian factors BMAL1 and RORalpha control HIF-1alpha transcriptional activity in nucleus pulposus cells: implications in maintenance of intervertebral disc health. *Oncotarget,* 7**,** 23056-71.

TAKEDA, K., HO, V. C., TAKEDA, H., DUAN, L. J., NAGY, A. & FONG, G. H. 2006. Placental but not heart defects are associated with elevated hypoxia-inducible factor alpha levels in mice lacking prolyl hydroxylase domain protein 2. *Mol Cell Biol,* 26**,** 8336-46.

TALBOT, N. P., BALANOS, G. M., ROBBINS, P. A. & DORRINGTON, K. L. 2008. Intravenous endothelin-1 and ventilatory sensitivity to hypoxia in humans. *Adv Exp Med Biol,* 605**,** 57-62.

TALBOT, N. P., SMITH, T. G., BALANOS, G. M., DORRINGTON, K. L., MAXWELL, P. H. & ROBBINS, P. A. 2017. Cardiopulmonary phenotype associated with human PHD2 mutation. *Physiol Rep,* 5.

TALKS, K. L., TURLEY, H., GATTER, K. C., MAXWELL, P. H., PUGH, C. W., RATCLIFFE, P. J. & HARRIS, A. L. 2000. The expression and distribution of the hypoxia-inducible factors HIF-1alpha and HIF-2alpha in normal human tissues, cancers, and tumor-associated macrophages. *Am J Pathol,* 157**,** 411-21.

TATSUMI, K., PICKETT, C. K. & WEIL, J. V. 1995. Possible role of dopamine in ventilatory acclimatization to high altitude. *Respir Physiol,* 99**,** 63-73.

TAYLOR, M. S. 2001. Characterization and comparative analysis of the EGLN gene family. *Gene,* 275**,** 125-32.

THOMPSON, R. J., JACKSON, A. & NURSE, C. A. 1997. Developmental loss of hypoxic chemosensitivity in rat adrenomedullary chromaffin cells. *J Physiol,* 498 (Pt 2)**,** 503-10.

TIAN, H., HAMMER, R. E., MATSUMOTO, A. M., RUSSELL, D. W. & MCKNIGHT, S. L. 1998. The hypoxia-responsive transcription factor EPAS1 is essential for catecholamine homeostasis and protection against heart failure during embryonic development. *Genes Dev,* 12**,** 3320-4.

TIBURCIO, P. D., CHOI, H. & HUANG, L. E. 2014. Complex role of HIF in cancer: the known, the unknown, and the unexpected. *Hypoxia (Auckl),* 2**,** 59-70.

TOLEDO, R. A., QIN, Y., SRIKANTAN, S., MORALES, N. P., LI, Q., DENG, Y., KIM, S. W., PEREIRA, M. A., TOLEDO, S. P., SU, X., AGUIAR, R. C. & DAHIA, P. L. 2013. In vivo and in vitro oncogenic effects of HIF2A mutations in pheochromocytomas and paragangliomas. *Endocr Relat Cancer,* 20**,** 349-59.

TOMITA, S., SINAL, C. J., YIM, S. H. & GONZALEZ, F. J. 2000. Conditional Disruption of the Aryl Hydrocarbon Receptor Nuclear Translocator (*Arnt*) Gene Leads to Loss of Target Gene Induction by the Aryl Hydrocarbon Receptor and Hypoxia-Inducible Factor 1α. *Molecular Endocrinology,* 14**,** 1674-1681.

TORRES-TORRELO, H., ORTEGA-SAENZ, P., MACIAS, D., OMURA, M., ZHOU, T., MATSUNAMI, H., JOHNSON, R. S., MOMBAERTS, P. & LOPEZ-BARNEO, J. 2018. The role of Olfr78 in the breathing circuit of mice. *Nature,* 561**,** E33-E40.

TRENT, C., TSUING, N. & HORVITZ, H. R. 1983. Egg-laying defective mutants of the nematode Caenorhabditis elegans. *Genetics,* 104**,** 619-47.

TUBEK, S., NIEWINSKI, P., RECZUCH, K., JANCZAK, D., RUCINSKI, A., PALECZNY, B., ENGELMAN, Z. J., BANASIAK, W., PATON, J. F. & PONIKOWSKI, P. 2016. Effects of selective carotid body stimulation with adenosine in conscious humans. *J Physiol,* 594**,** 6225-6240.

TURNER, P. J. & BUCKLER, K. J. 2013. Oxygen and mitochondrial inhibitors modulate both monomeric and heteromeric TASK-1 and TASK-3 channels in mouse carotid body type-1 cells. *J Physiol,* 591**,** 5977-98.

UHLEN, M., FAGERBERG, L., HALLSTROM, B. M., LINDSKOG, C., OKSVOLD, P., MARDINOGLU, A., SIVERTSSON, A., KAMPF, C., SJOSTEDT, E., ASPLUND, A., OLSSON, I., EDLUND, K., LUNDBERG, E., NAVANI, S., SZIGYARTO, C. A., ODEBERG, J., DJUREINOVIC, D., TAKANEN, J. O., HOBER, S., ALM, T., EDQVIST, P. H., BERLING, H., TEGEL, H., MULDER, J., ROCKBERG, J., NILSSON, P., SCHWENK, J. M., HAMSTEN, M., VON FEILITZEN, K., FORSBERG, M., PERSSON, L., JOHANSSON, F., ZWAHLEN, M., VON HEIJNE, G., NIELSEN, J. & PONTEN, F. 2015. Proteomics. Tissue-based map of the human proteome. *Science,* 347**,** 1260419.

URENA, J., FERNANDEZ-CHACON, R., BENOT, A. R., ALVAREZ DE TOLEDO, G. A. & LOPEZ-BARNEO, J. 1994. Hypoxia induces voltage-dependent Ca2+

entry and quantal dopamine secretion in carotid body glomus cells. *Proc Natl Acad Sci U S A,* 91**,** 10208-11.

VERHOFSTAD, A. A., COUPLAND, R. E. & COLENBRANDER, B. 1989. Immunohistochemical and biochemical analysis of the development of the noradrenaline- and adrenaline-storing cells in the adrenal medulla of the rat and pig. *Arch Histol Cytol,* 52 Suppl**,** 351-60.

VIDRUK, E. H., OLSON, E. B., LING, L. & MITCHELL, G. S. 2001. Responses of single-unit carotid body chemoreceptors in adult rats. *J Physiol,* 531**,** 165-70.

VOOIJS, M., JONKERS, J. & BERNS, A. 2001. A highly efficient ligand-regulated Cre recombinase mouse line shows that LoxP recombination is position dependent. *EMBO Rep,* 2**,** 292-7.

WALDMANN, J., FENDRICH, V., HOLLER, J., BUCHHOLZ, M., HEINMÖLLER, E., LANGER, P., RAMASWAMY, A., SAMANS, B., WALZ, M. K., ROTHMUND, M., BARTSCH, D. K. & SLATER, E. P. 2010. Microarray analysis reveals differential expression of benign and malignant pheochromocytoma. *Endocr Relat Cancer,* 17**,** 743-56.

WALLACE, E. M., RIZZI, J. P., HAN, G., WEHN, P. M., CAO, Z., DU, X., CHENG, T., CZERWINSKI, R. M., DIXON, D. D., GOGGIN, B. S., GRINA, J. A., HALFMANN, M. M., MADDIE, M. A., OLIVE, S. R., SCHLACHTER, S. T., TAN, H., WANG, B., WANG, K., XIE, S., XU, R., YANG, H. & JOSEY, J. A. 2016. A Small-Molecule Antagonist of HIF2alpha Is Efficacious in Preclinical Models of Renal Cell Carcinoma. *Cancer Res,* 76**,** 5491-500.

WANG, F., GAO, J. X., MIMURA, J., KOBAYASHI, A., SOGAWA, K. & FUJII-KURIYAMA, Y. 1998. Structure and expression of the mouse AhR nuclear translocator (mArnt) gene. *J Biol Chem,* 273**,** 24867-73.

WANG, H., CUI, J., YANG, C., ROSENBLUM, J. S., ZHANG, Q., SONG, Q., PANG, Y., FANG, F., SUN, M., DMITRIEV, P., GILBERT, M. R., EISENHOFER, G., PACAK, K. & ZHUANG, Z. 2019. A Transgenic Mouse Model of Pacak(-)Zhuang Syndrome with An Epas1 Gain-of-Function Mutation. *Cancers (Basel),* 11.

WANG, Z. Y. & BISGARD, G. E. 2002. Chronic hypoxia-induced morphological and neurochemical changes in the carotid body. *Microsc Res Tech,* 59**,** 168-77.

WARNECKE, C., ZABOROWSKA, Z., KURRECK, J., ERDMANN, V. A., FREI, U., WIESENER, M. & ECKARDT, K. U. 2004. Differentiating the functional role of hypoxia-inducible factor (HIF)-1alpha and HIF-2alpha (EPAS-1) by the use of RNA interference: erythropoietin is a HIF-2alpha target gene in Hep3B and Kelly cells. *FASEB J,* 18**,** 1462-4.

WEHN, P. M., RIZZI, J. P., DIXON, D. D., GRINA, J. A., SCHLACHTER, S. T., WANG, B., XU, R., YANG, H., DU, X., HAN, G., WANG, K., CAO, Z., CHENG, T., CZERWINSKI, R. M., GOGGIN, B. S., HUANG, H., HALFMANN, M. M., MADDIE, M. A., MORTON, E. L., OLIVE, S. R., TAN, H., XIE, S., WONG, T., JOSEY, J. A. & WALLACE, E. M. 2018. Design and Activity of Specific Hypoxia-Inducible Factor-2alpha (HIF-2alpha) Inhibitors for the Treatment of Clear Cell Renal Cell Carcinoma: Discovery of Clinical Candidate (S)-3-((2,2-Difluoro-1-hydroxy-7-(methylsulfonyl)-2,3-dihydro-1 H-inden-4-yl)oxy)-5-fluorobenzonitrile (PT2385). *J Med Chem,* 61**,** 9691-9721.

WEIL, J. V., BYRNE-QUINN, E., SODAL, I. E., FRIESEN, W. O., UNDERHILL, B., FILLEY, G. F. & GROVER, R. F. 1970. Hypoxic ventilatory drive in normal man. *J Clin Invest,* 49**,** 1061-72.

WEIL, J. V. & ZWILLICH, C. W. 1976. Assessment of ventilatory response to hypoxia: methods and interpretation. *Chest,* 70**,** 124-8.

WEISKOFF, R. B. & GABEL, R. A. 1975. Depression of ventilation hypoxia in man. *J Appl Physiol,* 39**,** 911-5.

WELANDER, J., ANDREASSON, A., BRAUCKHOFF, M., BACKDAHL, M., LARSSON, C., GIMM, O. & SODERKVIST, P. 2014. Frequent EPAS1/HIF2alpha exons 9 and 12 mutations in non-familial pheochromocytoma. *Endocr Relat Cancer,* 21**,** 495-504.

WENGER, R. H., ROLFS, A., MARTI, H. H., GUENET, J. L. & GASSMANN, M. 1996. Nucleotide sequence, chromosomal assignment and mRNA expression of mouse hypoxia-inducible factor-1 alpha. *Biochem Biophys Res Commun,* 223**,** 54-9.

WEST, J. B. 2004. The birth of clinical body plethysmography: it was a good week. *J Clin Invest,* 114**,** 1043-5.

WEST, J. B. 2012. Centenary of the Anglo-American high-altitude expedition to Pikes Peak. *Exp Physiol,* 97**,** 1-9.

WICKS, E. E. & SEMENZA, G. L. 2022. Hypoxia-inducible factors: cancer progression and clinical translation. *J Clin Invest,* 132.

WIESENER, M. S., JURGENSEN, J. S., ROSENBERGER, C., SCHOLZE, C. K., HORSTRUP, J. H., WARNECKE, C., MANDRIOTA, S., BECHMANN, I., FREI, U. A., PUGH, C. W., RATCLIFFE, P. J., BACHMANN, S., MAXWELL, P. H. & ECKARDT, K. U. 2003. Widespread hypoxia-inducible expression of HIF-2alpha in distinct cell populations of different organs. *FASEB J,* 17**,** 271-3.

WONG, B. W., KUCHNIO, A., BRUNING, U. & CARMELIET, P. 2013. Emerging novel functions of the oxygen-sensing prolyl hydroxylase domain enzymes. *Trends Biochem Sci,* 38**,** 3-11.

WONG, D. L. 2003. Why is the adrenal adrenergic? *Endocr Pathol,* 14**,** 25-36.

WU, D., SU, X., LU, J., LI, S., HOOD, B. L., VASILE, S., POTLURI, N., DIAO, X., KIM, Y., KHORASANIZADEH, S. & RASTINEJAD, F. 2019. Bidirectional modulation of HIF-2 activity through chemical ligands. *Nat Chem Biol,* 15**,** 367-376.

WYATT, C. N. & BUCKLER, K. J. 2004. The effect of mitochondrial inhibitors on membrane currents in isolated neonatal rat carotid body type I cells. *J Physiol,* 556**,** 175-91.

WYATT, C. N., MUSTARD, K. J., PEARSON, S. A., DALLAS, M. L., ATKINSON, L., KUMAR, P., PEERS, C., HARDIE, D. G. & EVANS, A. M. 2007. AMP-activated protein kinase mediates carotid body excitation by hypoxia. *J Biol Chem,* 282**,** 8092-8.

XU, R., WANG, K., RIZZI, J. P., HUANG, H., GRINA, J. A., SCHLACHTER, S. T., WANG, B., WEHN, P. M., YANG, H., DIXON, D. D., CZERWINSKI, R. M., DU, X., GED, E. L., HAN, G., TAN, H., WONG, T., XIE, S., JOSEY, J. A. & WALLACE, E. M. 2019. 3-[(1S,2S,3R)-2,3-Difluoro-1-hydroxy-7-methylsulfonylindan-4-yl]oxy-5-fluorobenzo nitrile (PT2977), a Hypoxia-Inducible Factor 2alpha (HIF-2alpha) Inhibitor for the Treatment of Clear Cell Renal Cell Carcinoma. *J Med Chem,* 62**,** 6876-6893.

YAMAMOTO, Y., KUMMER, W., ATOJI, Y. & SUZUKI, Y. 2002. TASK-1, TASK-2, TASK-3 and TRAAK immunoreactivities in the rat carotid body. *Brain Res,* 950**,** 304-7.

YANG, C., ZHUANG, Z., FLIEDNER, S. M., SHANKAVARAM, U., SUN, M. G., BULLOVA, P., ZHU, R., ELKAHLOUN, A. G., KOURLAS, P. J., MERINO, M., KEBEBEW, E. & PACAK, K. 2015. Germ-line PHD1 and PHD2 mutations detected in patients with pheochromocytoma/paraganglioma-polycythemia. *J Mol Med (Berl),* 93**,** 93-104.

YOKOYAMA, T., NAKAMUTA, N., KUSAKABE, T. & YAMAMOTO, Y. 2015. Serotonin-mediated modulation of hypoxia-induced intracellular calcium responses in glomus cells isolated from rat carotid body. *Neurosci Lett,* 597**,** 149-53.

YOST, C. S. 2006. A new look at the respiratory stimulant doxapram. *CNS Drug Rev,* 12**,** 236-49.

YUAN, G., PENG, Y. J., REDDY, V. D., MAKARENKO, V. V., NANDURI, J., KHAN, S. A., GARCIA, J. A., KUMAR, G. K., SEMENZA, G. L. & PRABHAKAR, N. R. 2013. Mutual antagonism between hypoxia-inducible factors 1alpha and 2alpha regulates oxygen sensing and cardio-respiratory homeostasis. *Proc Natl Acad Sci U S A,* 110**,** E1788-96.

ZAMPONI, G. W. & CURRIE, K. P. 2013. Regulation of Ca(V)2 calcium channels by G protein coupled receptors. *Biochim Biophys Acta,* 1828**,** 1629-43.

ZHOU, J., MOROI, K., NISHIYAMA, M., USUI, H., SEKI, N., ISHIDA, J., FUKAMIZU, A. & KIMURA, S. 2001. Characterization of RGS5 in regulation of G protein-coupled receptor signaling. *Life Sci,* 68**,** 1457-69.

ZHOU, T., CHIEN, M. S., KALEEM, S. & MATSUNAMI, H. 2016. Single cell transcriptome analysis of mouse carotid body glomus cells. *J Physiol,* 594**,** 4225-51.

ZHUANG, Z., YANG, C., LORENZO, F., MERINO, M., FOJO, T., KEBEBEW, E., POPOVIC, V., STRATAKIS, C. A., PRCHAL, J. T. & PACAK, K. 2012. Somatic HIF2A gain-of-function mutations in paraganglioma with polycythemia. *N Engl J Med,* 367**,** 922-30.